2019-08-01

The Investigation of Secondary Particle Formation Initiated by Non-Prototypical Sources and the role of Amines in the Atmosphere

Emily Burrell
Brigham Young University

The Investigation of Secondary Particle Formation Initiated by Non-Prototypical Sources and the Role of Amines in the Atmosphere

Emily Louise Burrell

A dissertation submitted to the faculty of
Brigham Young University
in partial fulfillment of the requirements for the degree of

Doctor of Philosophy

Jaron C. Hansen, Chair
David V. Dearden
Daniel E. Austin
James E. Patterson
Daniel H. Ess

Department of Chemistry and Biochemistry

Brigham Young University

ABSTRACT

The Investigation of Secondary Particle Formation Initiated by Non-Prototypical Sources and the Role of Amines in the Atmosphere

Emily Louise Burrell
Department of Chemistry and Biochemistry, BYU
Doctor of Philosophy

This dissertation is a collection of works that investigate non-prototypical sources leading to new particle formation in the atmosphere. Particles play a major role in atmospheric chemistry. For example, particles are a component of smog and are commonly found in high concentrations under conditions of atmospheric inversions. In order to reconcile the difference between measured and modeled particle concentrations new mechanisms from non-prototypical sources for particle formation need to be determined. Formation of particles has frequently been modeled using classical nucleation theory (CNT). The first step in CNT is the nucleation step where molecular clusters form. In a second step, these clusters grow into particles through coagulation or condensation. First, this research aims to improve the modeling of equilibrium constants for the formation of peroxy radical-water complexes. Failure of the harmonic approximation in the partition function for describing the low frequency vibrational modes of the complexes was explored. Instead the dissociative hydrogen bond mode using a Lennard-Jones 6-3 potential and the other low frequency vibrational modes using one- and two-fold hindered rotors was modeled. It was determined that the contribution of the two-fold hindered rotors is more important than the long-range dipole-dipole potentials and of vibration-rotation coupling.

In related work, the hydroperoxy radical was investigated as a non-prototypical source of particles using high level *ab initio* calculations. The results indicate that the addition of an amine to the dimer increased the overall stability of complex through the increased number and strength of the hydrogen bonds. When compared to prototypical systems, sulfuric acid and methane sulfonic acid, the strength of the complex was found to be similar to the peroxy radical system.

Finally, carboxylic acids, formic acid and acetic acid, were investigated as a source for new particle formation using computational and experimental techniques. Using a slow flow reactor cell particle formation was enhanced by the addition of trimethylamine. High level *ab initio* calculations indicate like the peroxy radicals, carboxylic acids may act as a molecular cluster in particle formation.

Keywords: Secondary Particle Formation, Amines, Carboxylic Acids, Nucleation Theory, Atmospheric Chemistry, Peroxy Radicals, Ab-initio Calculations

ACKNOWLEDGEMENTS

I would like to thank my advisor Jaron Hansen for his constant support and encouragement as I have undertaken my research. I would like to thank Jessica Richards for allowing me to bounce ideas off of her and her support in the lab. I am also grateful for the rest of the Hansen group including: Hanna Burgin, Carson Bateman, Devon Overson, Collin Stocksdale, Nitish Bhardwaj, William Keeton and Kate Thorpe for the learning atmosphere developed in the lab. I would like to thank the BYU chemistry department faculty and support staff for their help throughout my academic career.

Most importantly I am grateful for the support of my family. I am grateful for my parents, Kent and Teresa Burrell; without them I wouldn't be the scientist I am today. They encouraged my curiosity and thirst for knowledge growing up and allowed the messes from my 'experiments'. I am grateful for my brothers, Caleb, Gid, Eph and Josh, and sister, Jessica, who have encouraged me to continue forward in my education. I am grateful for my sister-in-law and friend, Megan, who has always offered support and wisdom. I am thankful for my nieces, Elli, Sophia, Ruby, Hayzlee and nephew, Peter, who have given me unconditional love and support.

Table of Contents

List of Figures

List of Tables

Chapter 1

Introduction

Over the last century there has been an increased interest in the field of atmospheric chemistry. The study of atmospheric chemistry allows for a better understanding of chemical reactions and interactions that occurs in the atmosphere which often leads to the formation of particulate matter, also known as particles. Particles play an important role in not only our health but also climate change. Due to the significant role these particles can play in our everyday life there has been an effort to not only better understand the chemistry behind the formation of particles but also the mechanisms that generate particles.

Despite the broad impact of particles, our current understanding of pathways leading to new particle formation is lacking. Current predictive models underestimate the total concentration of particles in the atmosphere[1]. This underestimation is indicative of unknown pathways leading to particle formation. To better understand potential pathways, this dissertation will delve into understanding particle formation via nucleation and possible non-prototypical sources leading to particle formation.

1.1 Particles

Particles are solids or liquids suspended in the atmosphere with diameters between 0.002 and 100 μm.[2] These particles play a major role in atmospheric chemistry. For example, particles can be a component of smog and are commonly found in high concentrations under conditions of atmospheric inversions.[3] Particles can also be detrimental to our health. When they are smaller than 2.5 μm in diameter they are capable of entering the lungs and blood stream causing breathing related diseases.[3-7]

Particles can also, directly or indirectly impact the climate. They are responsible for cloud formation and depending on the composition of the particle can either absorb or reflect light leading to heating or cooling of the atmosphere.[8] Particles composed primarily of water reflect light leading to cooling of the atmosphere, whereas carbon-based particles absorb light leading to heating of the atmosphere. Particles can also act as cloud condensation nuclei (CCN) and ice nuclei leading to the formation of clouds.[2] The precursors for CCN and ice nuclei impact the occurrence and lifetime of clouds on local, regional and global scales.[9-11]

Particles are divided into two main categories: course and fine particles. Though smaller in size, fine particles account for most of the total number of particles and most of the particle mass.[2, 3, 12, 13] The type of particle formed typically depends on if it comes from a primary or secondary source. A course particle is defined as a particle with a diameter greater than 2.5μm and is typically formed by primary sources or mechanical

processes[2]. Particles from a primary source are emitted or injected directly into the atmosphere[2]. Primary sources can be biogenic or anthropogenic in nature. Some examples of anthropogenic sources include agricultural operations, industrial processes[14-16], grinding, combustion of wood and fossil fuels[17-20], construction and demolition activities and entrainment of road dust[21]. Biogenic sources include windblown dust, erosion and wildfires[22].

While course particles are principally formed via primary sources fine particles are formed by secondary sources. Fine particles are typically formed in the atmosphere by gas-to-particle conversion processes. Secondary sources can be biogenic or anthropogenic in nature. Anthropogenic sources include car and truck emissions, factories and construction sites. Biogenic sources include animal husbandry and emissions from plants.

Unlike course particles, fine particles are further divided into 3 modes: accumulation range, Aitken nuclei range and ultrafine particles (UFPs). The type of mode typically indicates the pathway in that was used to grow the particles. Accumulation range particles typically have diameters ranging from 0.08 -2.5 μm and are composed of more organics than course particles and soluble inorganics such as NH_4^+, NO_3^- and SO_4^{2-}. Particles found in the accumulation range are formed by either the condensation of low-volatility vapors or coagulation. This means that either smaller sized particles from the Aitken nuclei range collide with themselves or collide with

particles in the accumulation range to form the accumulation range sized particles. Accumulation range particles present only a small portion of the total number of particles (~5%) but contain a significant portion of total particle mass (~50%).

The Aitken nuclei range contains particles with diameters ranging from 0.01-0.08 μm and are formed either by gas to particle nucleation or the condensation of low-vapor pressure gaseous species, also known as homogenous nucleation. As mentioned before, often the Aitken nuclei particles will grow in diameter via coagulation to accumulation range particles. Though smaller in size, Aitken range particles and ultrafine particles make up the majority of the particles in the atmosphere but account for very little of the mass.

Ultrafine particles (UFPs) contain particles with diameters less than 0.01 μm and are formed by gas to particle conversion processes which theories will be discussed in a later section. Unlike the accumulation range or Aitken nuclei range particles it contains the smallest amount of total mass but contains a significant number of the total particles.

1.2 Nucleation Theories

Secondary particle formation occurs through gas to particle conversion processes, however these processes are not fully understood, and many molecular scale theories have been formed to describe the process in which new particle formation

occurs under atmospheric conditions. Some of these theories include classical nucleation theory (CNT) and dynamical nucleation theory (DNT).

1.2.1 Classical nucleation theory

CNT has historically been the widely accepted theory for describing new particle formation [23] and was first proposed by Becker, Döring and Frenkel using a spherical droplet approximation[24, 25]. CNT has the advantage of including the thermodynamic and kinetic components through the evaluation of Gibbs free energy of formation and calculating the nucleation rate.

The thermodynamic approach to CNT theory describes the nucleation process through a change in Gibbs free energy upon the formation of a molecular cluster (eq 1).

$$\Delta G = -ikT\ lnS + 4\pi r^2\sigma \qquad \text{(eq. 1)}$$

$$i = \frac{\left(\frac{4}{3}\right)\pi r^3}{v_1} \qquad \text{(eq. 2)}$$

Where S stands for the saturation ratio, k is the Boltzmann constant, i stands for the number of molecules transferred from the vapor phase to a cluster with a radius r where v_1 is the volume of a single molecule and σ represents the surface tension. Equation 1 can be simplified into the Gibbs free energy of the bulk (ΔG_{bulk}; eq. 3a) on the left-side of the equation and the Gibbs free energy of the surface ($\Delta G_{surface}$; eq. 3b) on the right-hand side of the equation. (eq 3.)

$$\Delta G = \Delta G_{bulk} + \Delta G_{surface} \qquad \text{(eq 3)}$$

$$\Delta G_{bulk} = -ikT\ lnS \qquad \text{(eq. 3a)}$$

$$\Delta G_{surface} = 4\pi r^2 \sigma \qquad \text{(eq. 3b)}$$

The first term ΔG_{bulk} represents the energy decrease upon transition from a gas to a particle and is dependent on the saturation ratio. When the S < 1, ΔG_{bulk} is positive and condensation from a gas to a particle is prohibited. However, when S> 1, meaning the system is supersaturated, the ΔG_{bulk} is negative favoring condensation and overcome $\Delta G_{surface}$. $\Delta G_{surface}$ represents the loss of entropy due to the high fraction of surface molecules at the gas/particle interface and is always positive. In smaller diameter molecules the increase $\Delta G_{surface}$ due to the addition of surface molecules at the interface dominates ΔG_{bulk} which results in a nucleation energy barrier, ΔG^*. The absorption/ desorption of molecules off the surface of the particle continues until this barrier reaches its peak at the critical cluster radius (r*) where ΔG_{bulk} dominates $\Delta G_{surface}$. Once the critical radius (r*), has been reached the formation of the cluster is thermodynamically favorable and will continue to grow in diameter.

The kinetics element of CNT includes calculating the nucleation rate. The nucleation rate *J* can be defined as the number of particles that grow past the critical radius size per unit volume per unit time (eq 4).

$$J = J_0 \exp(-\frac{\Delta G^*}{kT}) \qquad \text{(eq. 4)}$$

$$\Delta G^* = \frac{16\pi}{3} \frac{\sigma^3 v_1^2}{(kT\, lnS)^2} \qquad \text{(eq. 5)}$$

J_0 represents the pre-exponential factor, and ΔG^* represents the free energy barrier height (eq. 5). The rate of nucleation has a negative exponential dependence on ΔG^*. ΔG^* is dependent on the saturation ratio. As the saturation ratio increases there is a decrease in ΔG^* which results in a faster nucleation rate. Research has also shown that this barrier is lower for highly polar species such as ions. Thus, ion-induced nucleation is more thermodynamically favored compared to nucleation involving non-polar species.

The main advantage of CNT is in its simplicity and its ability to accurately predict thermodynamic data and nucleation rates under supersaturated conditions. However, under non-supersaturated and extreme temperature conditions, CNT fails to predict measured nucleation rates by an order of magnitude or higher. Another weakness with CNT is the prescribed system must be supersaturated for nucleation to occur. Recent research however, has shown that the addition of an amine allows for an increased stability in the critical cluster leading to particle formation in non-saturated systems[282].

Sulfuric acid (H_2SO_4, ambient concentrations of 10^5-10^6 molecules cm^{-3}) has historically been used as a prototypical system for describing new particle formation using CNT. A polar molecule, such as H_2SO_4, interacts with surrounding water molecules to form a molecular cluster, also known as a nucleating seed. This nucleating seed further interacts with additional water molecules until it reaches the critical cluster

diameter, 1 nm (Figure 1.1). Once the critical cluster overcomes ΔG^* the H_2SO_4-$(H_2O)_n$ (n>1)cluster grows to become an aerosol particle. Once it has surpassed the critical cluster energy barrier it is thermodynamically favorable for the critical cluster to continue adding water molecules to form a larger diameter aerosol. Larger diameter particles are formed when low volatility organics and water vapor condense on the nucleating seed.

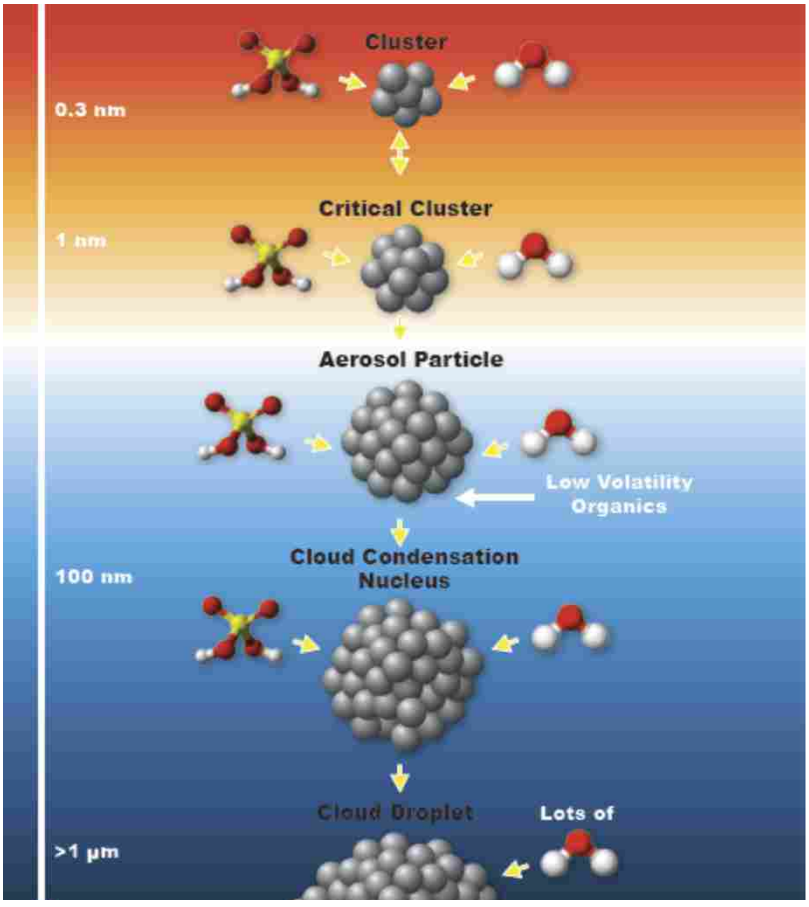

Figure 1.1 Classical nucleation theory described using H_2SO_4, H_2O and VOCs

Computational methods such as Density Functional Theory (DFT), Hartree-Fock (HF) method, Møller-Plesset (MP) methods, DFT hybrid functionals (M0-62X, B3LYP etc.) and couple clustered calculations with single and double excitations (CCSD) are used as a predictive approach to new particle nucleation. For example, DFT is a quantum modeling method that is used to study the structure of a multi-body system. DFT uses functionals of the electron density.

DFT calculations have the advantage of allowing the study of more complex systems at a low cost. The more complex the system the longer it takes for the calculations to converge. Despite the advantages of DFT on a computational level it has difficulties in properly describing intermolecular interaction, charge transfer excitations and transitions states.

The use of computational approaches provide predictive measurements, including thermodynamic data, dipole moments, energy of the molecule or complex, vibrational frequencies and optimized geometries. Based upon these calculations the likelihood of a complex acting as a nucleating site for new particle formation is determined.

1.2.2 Dynamical nucleation theory (DNT)

DNT treats gas to particle nucleation as a multistep binary collision process between the nucleating molecules and clusters. In DNT the reactant states are separated from the product states which allows for each stage of the kinetic process to

be separately evaluated. The interaction energies of these states may come from analytic potential or high-level ab initio calculations. DNT emphasizes the evaluation and approximation of the decomposition rate constant of the particles.

While all of these models have advantages and disadvantages, CNT in conjunction with DFT first principle calculations can provide a relatively accurate prediction of possible new particle formation nucleating seeds. Even though new particle formation pathways are modeled to predict the total number of particles in the atmosphere, CNT and other models are insufficient in accounting for the total concentration of particles in the atmosphere. Additional non-prototypical pathways need to be explored to better predict measured concentrations in the atmosphere.

1.3 Non-Prototypical Sources

A non-prototypical source is defined as a nonstandard source that lead to particle formation. For example, a prototypical source for particle formation is the complexation of HS_2O_4 and H_2O vapor into a nucleating site. As mentioned above, H_2SO_4 is one of the most studied pathways for particle formation however, it is unable to account for the high concentration of particles often measured in the atmosphere. As such it has become necessary to look towards more uncommon sources leading to particle formation. My research has primarily focused on carboxylic acids and radicals complexing with H_2O vapor to form nucleating seeds which are enhanced by the incorporation of an amine or ammonia leading to particle formation.

1.3.1 Amines

An amine is a nitrogen containing group typically found in atmosphere concentrations ranging between 1-10 ppt. Amines are usually 1-3 orders of magnitude lower concentrations in the atmosphere than ammonia (NH_3, ambient concentrations of 1-10 ppb) in the atmosphere[19]. Extensive laboratory results and computational studies have shown that amines enhance new particle formation in prototypical systems and are more effective than NH_3 in enhancing particle formation and may enhance non-prototypical systems[9,20-23].

The most common amines found in the atmosphere are the low-molecular weight aliphatic amines, such as methylamine (MA), dimethylamine (DMA) and trimethylamine (TMA). These amines have both biogenic and anthropogenic sources. Some anthropogenic sources include animal husbandry, the food industry, fish processing, chemical manufacturing, other manufacturing processes (corn starch manufacturing, leather manufacturing, etc.), composting operations, automobiles, sewage, cooking, charbroiling, and tobacco smoke[26-29]. Two of the most important sources of TMA include animal husbandry and food processing. In animal husbandry there are many sources of amines including the formation of amines by decarboxylation reaction with anaerobic bacteria in the gastrointestinal tract. Another source from

animal husbandry is cattle and swine waste which were found to emit MA, DMA and TMA. In the food industry amines, particularly TMA, are emitted through meat rendering and fish processing. Fish processing is an important source for TMA as fresh fish has an TMA emission factor of 0.15 kg t^{-1} $year^{-1}$ while stale fish has a TMA emission factor of 1.75 kg t^{-1} $year^{-1}$.

Biogenic sources of amines include the ocean, biomass burning, vegetation and geological sources[28, 30-32]. It was determined that methylamine contributed up to 20% of the total measured basic compounds found over the ocean. During biomass burnings MA, DMA and TMA were detected in the gaseous emissions and a higher proportion of these gaseous amine emissions were detected during smoldering. Through vegetation, TMA is the predominantly emitted amine however, MA and other amines have also been detected. The fixation of nitrogen in the soil due to microorganisms leads to a natural source of soil nitrogen and amines. In particular MA has been found in soil samples and can enter into the atmosphere due to dust storms or agricultural activities.

Many sources of NH_3 like amines are produced by the decomposition of uric acid, urea and undigested proteins. Uric acid is decomposed by microbial action with oxygen and water to produce carbon dioxide and NH_3. Urea is decomposed through urease activity to produce carbon dioxide and ammonia. Undigested proteins are decomposed by both uricase and urease enzymes to produce NH_3. The eventual

formation of NH_3 (g, air) depends on the chemical equilibrium governed by Henry's law.[33, 34]

These NH_3 emissions react with molecules in the atmosphere to form NH_3 - complexes. In a prototypical system ammonia will complex with sulfuric acid and water vapor to form particles. Swartz et. al.[35] showed that sulfuric acid condenses both onto preexisting particles and into new particles when it reacts with ammonia to form $(NH_4)_2SO_4$. NH_4SO_4 acts as a nucleation site when exposed to water (eq 6-8). [35]

$$SO_2 + OH \longrightarrow HSO_3 \quad \text{(eq 6a)}$$

$$HSO_3 + O_2 \longrightarrow SO_3 + HO_2 \quad \text{(eq 6b)}$$

$$SO_3 + 2H_2O \longrightarrow H_2SO_4 + H_2O \quad \text{(eq 6c)}$$

$$H_2SO_4 + 2NH_3 \longrightarrow (NH_4)_2SO_4 \quad \text{(eq 7)}$$

$$(NH_4)_2SO_4 + nH_2O \longrightarrow PM_{2.5} \quad \text{(eq 8)}$$

NH_3 and H_2O react with H_2SO_4 to form new particles (eq 7-8). In a likewise manner amines and NH_3 stabilize methanesulfonic acid (MSA, CH_3SO_3H) and H_2O (eq 9-12)

$$MSA + H_2O \longrightarrow MSA \bullet H_2O \quad \text{(eq 9)}$$

$$MSA \bullet H_2O + \text{Amine}/NH_3 \longrightarrow \text{cluster} \quad \text{(eq 10)}$$

$$\text{Clusters} + \text{Clusters} \longrightarrow PM_{2.5} \quad \text{(eq 11)}$$

$$\text{Clusters} + H_2O \longrightarrow PM_{2.5} \quad \text{(eq 12)}$$

TMA, NH_3 and other amines play an important role in determining the overall acidity of precipitation, cloud water and airborne particulate matter [36, 37] . Recent

studies[38] have analyzed the role of amines and NH_3 in enhancing new particle formation in prototypical systems, such as H_2SO_4 and MSA. The addition of an amine or NH_3 to these prototypical systems enhanced the rate of particle formation 2-1000 times. Though amines have a lower concentration in the atmosphere than NH_3, amines increased particle formation 2-35 times more than NH_3.[39-41] In another example, experiments using the CLOUD chamber at CERN have demonstrated that dimethylamine concentrations exceeding 3 pptv are able to increase particle formation rates by more than 3 orders of magnitude relative to that seen with NH_3.[9] It is also important to note that the addition of an amine into a prototypical system decrease the relative humidity needed in the environment for particles to form thus more easily overcoming the critical cluster nucleation energy barrier. [39, 42]

There have been many mechanisms proposed for new particle formation via amines, including: amines forming salts with low vapor pressures under acidic conditions [43]; a heterogeneous reaction with acidic substances in the presence of low relative humidity [44]; and the stepwise addition of amines, MSA and H_2O to the nucleation cluster.[38] While the exact pathway in which amines enhance new particle formation has yet to be determined it has been concluded that amines and NH_3 increase the overall production of new particles. While the addition of an amine or NH_3 to the MSA and H_2SO_4 systems have increased our understanding of new particle formation additional mechanisms for new particle formation, need to be investigated. Rather than

systems with MSA or H_2SO_4, we need to look at the use of ammonia or amines in particle formation with non-prototypical sources, such as carboxylic acids and radicals.

1.3.2 Carboxylic Acids

Recent research has emphasized the importance of carboxylic acids contribution to particle formation.[6,14] While monocarboxylic acids tend to have a high vapor pressure and are often overlooked as a source of new particle formation recent field studies have detected monocarboxylic acids in aerosol particulates highlighting their contribution to new particle formation(NPF)[25-31]. For example, in the urban environment of New Mexico City, Mexico HCOOH and CH_3COOH were predominantly detected in the particulate phase.[32] On average, 53% of particles contained HCOOH and 67% of particles contained CH_3COOH. In addition to the detection of monocarboxylic acids in the particulate phase it is also important to note that the vapor pressure of monocarboxylic acids is higher, by a factor of 10^2 to 10^4 than that of the corresponding dicarboxylic acids,[24] their higher vapor pressures suggest that monocarboxylic acids should play a smaller role in NPF and not be found in particles. However recent field measurements, such as those in Mexico, indicate additional mechanisms that allow monocarboxylic acids to play a bigger role in the NPF then previously thought. Additionally, other carboxylic acids such as oxalic acid[18] were found to contribute to NPF[45,46].

Likewise, part of my research focuses on HCOOH and CH_3COOH enhanced by amines as a source of NPF.

Formic acid

As previously stated, formic acid (HCOOH) has been found in particulate matter around the world and as such it has become necessary to better understand the role of HCOOH atmospheric chemistry. There are many anthropogenic and biogenic sources emitting HCOOH in to the atmosphere. Some primary anthropogenic sources include biomass and biofuel burning and fossil fuel combustion (0.4 Tg yr^{-1}). Primary biogenic sources include direct emission from vegetation, soils and agriculture (8.6 Tg yr^{-1})[47]. However, a major source of HCOOH in the atmosphere occurs not from direct emission but from photochemical oxidation of volatile organic compounds (VOCs) emitted into the atmosphere (51.0 Tg yr^{-1})[47-50]. There are many photochemical oxidations that occur, however six main processes will be briefly discussed. These processes include the multistep ozonolysis of monoterpenes (eq 13-17) which leads to the formation of HCOOH and HCHO[51-55]

$O_3 + C_2H_4 \longrightarrow$ 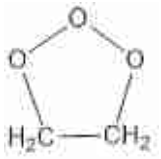 (eq 13)

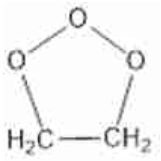 $\longrightarrow$ $HCHO + [CH_2OO]^*$ (eq 14)

$$[CH_2OO^*] + M \longrightarrow CH_2OO + M \quad \text{(eq 15)}$$

$$CH_2OO + H_2O \longrightarrow HOCH_2OOH \quad \text{(eq 16)}$$

$$HOCH_2OOH \longrightarrow HCOOH + H_2O \quad \text{(eq 17)}$$

Another source of HCOOH in the atmosphere is alkyne oxidation[56-58] (eq 18-19) in which C_2H_2 dominates non-biogenic precursors[56, 59-62]

$$RCCH + OH \longrightarrow OO(R)CC(H)OH \quad \text{(eq 18)}$$

$$OO(R)CC(H)OH \longrightarrow RCO + OO(R)CC(H)OH \quad \text{(eq 19)}$$

Isoprene oxidation by OH[49, 59, 62-64] (eq 20-24) is another leading source of formic acid in the atmosphere

$$Isoprene + OH + 2NO + O_2 \longrightarrow HCHO + PRODUCTS \quad \text{(eq 20)}$$

$$HCHO + HO_2 \longrightarrow O_2CH_2OH \quad \text{(eq 21)}$$

$$O_2CH_2OH + HO_2 \longrightarrow HCOOH + H_2O + O_2 \quad \text{(eq 22)}$$

$$O_2CH_2OH + NO + O_2 \longrightarrow HCOOH + NO_2 + HO_2 \quad \text{(eq 23)}$$

$$O_2CH_2OH + O_2CH_2OH \longrightarrow 2HCOOH + 2HO_2 \quad \text{(eq 24)}$$

The reaction of CH_3O_2 with the hydroxy radical (OH)[65, 66] (eq 25-27)

$$CH_3O_2 + OH \longrightarrow CH_2OO + H_2O \quad \text{(eq 25)}$$

$$CH_2OO + H_2O \longrightarrow HOCH_2OOH \quad \text{(eq 26)}$$

$$HOCH_2OOH \longrightarrow HCOOH + H_2O \quad \text{(eq 27)}$$

In low NOx systems the reaction of formaldehyde, radicals and acetate (eq 28-30) become the dominate sources of HCOOH[66-68]

$$HCHO + HO_2 \longrightarrow HOCH_2OO \quad \text{(eq 28)}$$

$$HOCH_2OO \longrightarrow HCOOH + \text{products} \quad \text{(eq 29)}$$

$$CH_3O_2 + OH \longrightarrow HCOOH + \text{products} \quad \text{(eq 30)}$$

A recent paper by Heard et al emphasized the phototautomerization of acetaldehyde[48, 69-71] as a major source of HCOOH over the oceans. (eq 31-34)

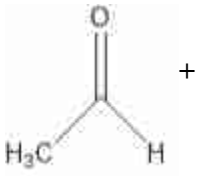

+ hν ⟶

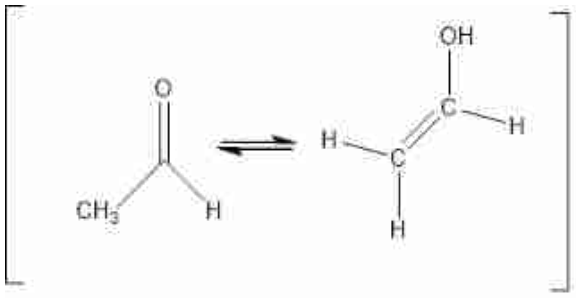

(eq 31)

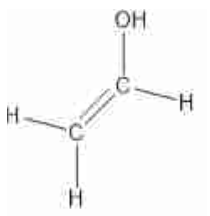

+ OH ⟶ $CH_2\text{-}CH(OH)_2$ (eq 32)

$$CH_2\text{-}CH(OH)_2 + O_2 \longrightarrow OOCH_2\text{-}CH(OH)_2 \quad \text{(eq 33)}$$

$$OOCH_2\text{-}CH(OH)_2 \longrightarrow OH + CH_2O + HCOOH \quad \text{(eq 34)}$$

With the inclusion of the phototautomerization of acetaldehyde into atmospheric model's, formic acid concentrations increased up to 50% particularly over marine areas[48]. This indicates that HCOOH may play a larger role in particle formation than previously thought.

Acetic Acid

Acetic acid (CH_3COOH) like HCOOH, has been found in particulate matter and as such it has become increasingly important toward understanding secondary particle formation in the atmosphere. Measured concentrations of CH_3COOH in the atmosphere range from 75 Tg yr^{-1} to 120 Tg yr^{-1} [49]. The large discrepancy between these concentrations indicates a need for better understanding CH_3COOH formation and sources. There are many anthropogenic and biogenic sources of CH_3COOH in the atmosphere. Anthropogenic sources include commercial and domestic solvents and aerosols, automobile exhaust, and biomass burning[72-75]. Biomass burning is an important direct source for CH_3COOH and can have concentrations upwards to 5000 ppbv[76]. Biogenic sources include soil emissions, vegetable emissions and ocean surfaces[77-84]. Photochemical oxidation of biogenic volatile organic sources is also a major source of CH_3COOH. Some of these processes include ozone reacting with alkenes such as olefins, isoprene and monoterpenes emitted from biogenic sources[53, 58, 85, 86] (eq 35-38).

$O_3 + RCH{=}CH_2 \longrightarrow$ 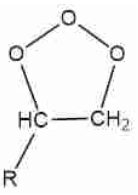 (eq 35)

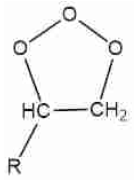 $\longrightarrow$ $RCOH + CH_2COO$ (eq 36)

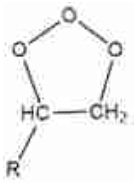 $\longrightarrow$ $HCOH + CH_3COO$ (eq 37)

$CH_3COO + H_2O \longrightarrow CH_3COOH + \text{fragments}$ (eq 38)

Another source includes the acetylperoxy radical reacting with the hydroperoxy radical[87, 88](eq 39-40), primary (1°) or secondary (2°) peroxy radicals[89] (eq 43-45) and CH_3CO[90] (eq 44-45).

$CH_3CO_2 + HO_2 \longrightarrow CH_3COH + O_3$ (eq 39)

$CH_3CO_2 + HO_2 \longrightarrow CH_3COOH + O_2$ (eq 40)

$CH_3CO_2 + CH_3CO \longrightarrow CH_3COOH + O_2 + HCOH$ (eq 41)

$CH_3CO_2 + CH_3CO \longrightarrow CH_3 + CO_2 + O_2 + CH_3$ (eq 42)

$CH_3CO_2 + 1°/2°$ peroxy radical $\longrightarrow CH_3COO_2 + RR`CHO_2$ (eq 43)

$CH_3COO_2 + RR`CHO_2 \longrightarrow CH_3COOH + O_2 + RCOR`$ (eq 44)

$CH_3COO_2 + RR`CHO_2 \longrightarrow CH_3 + CO_2 + O_2 + RR`CHO$ (eq 45)

Another reaction leading to CH_3COOH is acetone reacting with OH[91, 92] (eq 46-48)

$CH_3COCH_3 + OH \longrightarrow CH_3COCH_2 + H_2O$ (eq 46)

$CH_3COCH_3 + OH \longrightarrow (CH_3)_2C(OH)O^*$ (eq 47)

$(CH_3)_2C(OH)O^* \longrightarrow CH_3COOH + CH_3$ (eq 48)

Some CH_3COOH sinks include wet and dry deposition. Wet and dry deposition can account for upwards of 90% loss in the gas phase in some areas of the globe[93]. Another CH_3COOH sink includes the reaction of CH_3COOH with OH which degrades to CO_2, H_2O, HCOH, OH and CH_3[93]. These are just a few sources and sinks of CH_3COOH in the atmosphere and due to large discrepancies in CH_3COOH

concentrations there is a need to better understand sources and sinks of CH_3COOH in the atmosphere.

1.3.3 Radicals

Radicals like carboxylic acids have been detected in the atmosphere and may play a role in new particle formation. The hydroperoxy radical (HO_2, ambient concentrations of 10^8 molecules cm^{-3})[2, 94] and hydroxyl radical (OH, ambient concentrations of 10^6 molecules cm^{-3})[2, 94] are the most abundant radicals found in the atmosphere with concentrations comparable with H_2SO_4 (10^{5-7} molecules cm^{-3})[40, 95-99] and MSA.[38, 45, 46, 100, 101] Due to its high concentration and stronger complexation with water (6.8 kcal/mol),[102-104] HO_2 may play a more vital role in new particle formation than OH.

Atmospheric photochemistry is the main sources of the HO_2 radical however due to HO_2 being closely coupled to the HO_x (HO/ HO_2), NO_x (NO/ NO_2) and O_3 systems, a more complex system of sources and sinks for the HO_2 molecules needs to be taken into consideration when understanding HO_2 sources[2, 105, 106]. Figure 1.2 shows an overall interaction of HO_2 and HO in the atmosphere.

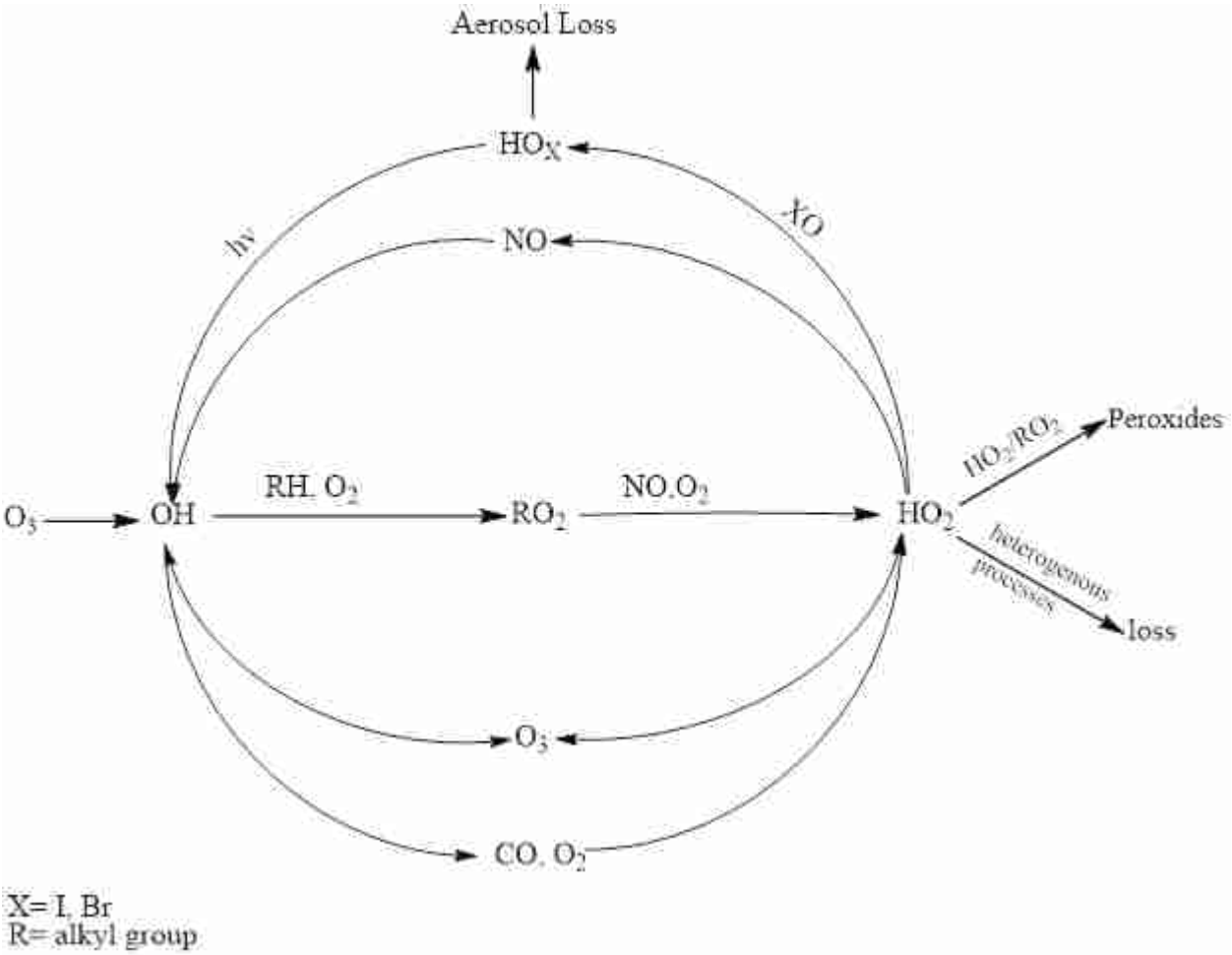

Figure 1.2 The HOx Cycle. (Author Original)

Even though HO and HO_2 sources are dependent there are conditions in which HO_2 is formed without the loss of HO. For example, olefinic hydrocarbons from biogenic and anthropogenic source can react with O_3 to form HO_2 [107-116](eq 49-52)

$$O_3 + \equiv \longrightarrow H^{\bullet} + OH + HCO + H_2O + CO_x + H_2 + HC(O)OH \quad \text{(eq 49)}$$

$$HCO + O_2 \longrightarrow HO_2 + CO \quad \text{(eq 50)}$$

$$H^{\bullet} + O_2 + M \longrightarrow HO_2 + M \quad \text{(eq 51)}$$

$$OH + CO + O_2 \longrightarrow HO_2 + CO_2 \quad \text{(eq 52)}$$

Another source of HO_2 is as a byproduct formed from the photolysis of acetaldehyde (eq 53-56)

$$CH_3CHO + h\nu \longrightarrow CH_3^{\bullet} + HCO^{\bullet} \quad \text{(eq 53)}$$

$$CH_3^{\bullet} + O_2 \longrightarrow CH_3O_2^{\bullet} \quad \text{(eq 54)}$$

$$HCO^{\bullet} + O_2 \longrightarrow H^{\bullet} + CO \quad \text{(eq 55)}$$

$$H^{\bullet} + O_2 \longrightarrow HO_2^{\bullet} \quad \text{(eq 56)}$$

As discussed previously above, ion-induced nucleation has a lower nucleation energy barrier in which particle formation with an ion occurs more quickly and is more stable than a neutral molecule, such as H_2SO_4 and MSA. Radicals, like ions, may have an overall polar nature which in a similar manner may decrease the nucleation energy barrier leading to particle formation. The lifetime of HO_2 is also influenced by water molecules by forming the HO_2-H_2O complex. [117] The formation of the HO_2-H_2O complex leads to an increase stability of HO_2 by forming a hydrogen bond with H_2O when the HO_2-H_2O complex is formed. [103, 118-120] The addition of the hydrogen bond to a radical, like an ion, should increase the thermodynamic stability of the complex [121] and

laboratory results have shown the formation of the HO_2-H_2O complex[102-104] under atmospheric conditions. Particle formation in the atmosphere from the HO_2-H_2O complex like many prototypical systems, may also be enhanced by the addition of an amine or NH_3. However, since there is minimal information on how TMA influences particle formation with a radical-water cluster in order to better understand the possible reactions of TMA with H_2O and HO_2, rather than with MSA or H_2SO_4, we need to look at the use of ammonia in particle formation with non-prototypical sources, such as carboxylic acids and radicals.

1.4 Organization of Dissertation

This dissertation contains research for previously dismissed non-prototypical sources that can lead to new particle formation. Chapters 2, 3 and 4 are published works, while chapter 5 is currently in the process of being submitted for publication. Chapter 2 details collaborative work concerning formation of the hydroxyethylperoxy - water (HEP-H_2O) complex. Chapter 3 details computational results of particle formation initiated by HO_2, water vapor and amines or NH_3. Chapter 4 details the experimental results of particle formation initiated by formic acid, water vapor and trimethylamine and a corresponding computational section. Chapter 5 details the experimental results of particle formation initiated by acetic acid, water vapor and trimethylamine and a corresponding computational section analyzing acetic acid, water vapor and amines acting as a nucleating site. Chapter 6 details the

conclusion and future work. The appendix contains the supplemental information for chapters 2-5 and a source apportionment, positive matrix factorization (PMF) paper.

Chapter 2

An Improved Model to Calculate Equilibrium Constants for Formation of Peroxy Radical-Water Complexes

2.1 Disclaimer

The following chapter is presented in its entirety (with minor changes) from the published version of the paper in Theoretical Chemistry Accounts. Randall B. Shirts,* Sambhav R. Kumbhani, Emily Burrell, and Jaron C. Hansen. An improved model to calculate equilibrium constants for formation of peroxy radical-water complexes. *Theo. Chem. Acct.* **2018**, 137:96. Dr. Sambhav R. Kumbhani and I performed the computations and helped analyzed the computational data. Dr. Randall B. Shirts wrote the paper and performed the modeling calculations. Dr Jaron C. Hansen reviewed and edited the work.

2.2 Abstract

Recent experimental results show that the kinetics of some radical-radical reactions important for atmospheric pollution formation are faster when a radical-molecule complex forms as one step in the reaction mechanism. Calculated radical-molecule equilibria are needed to accurately describe the concentrations of complexes formed in these experiments as well as in the atmosphere. Here we report calculation of the equilibrium constant for complexation of hydroperoxy (HO_2·) and 2-

hydroxyethylperoxy radicals ($HOCH_2CH_2O_2\cdot$) with one water molecule by directly calculating the canonical partition function of the reactant and product species. We demonstrate the accuracy of the calculation using formation of the water dimer as a test case. *Ab initio* calculations provide the binding energy, rotational constants, and vibrational frequencies of both monomers and complexes. We demonstrate the failure of the harmonic approximation in the partition function for describing the low frequency vibrational modes of the complexes. Instead, we model one dissociative hydrogen bond mode using a Lennard-Jones 6-3 potential and the other low frequency vibrational modes using one- and two-fold hindered rotors. The contributions of weakly bound states of the long-range dipole-dipole potential (Lennard-Jones 6-3) and of vibration-rotation coupling are not as important as the contribution of two-fold hindered rotors. We also discuss methods for including multiple hydrogen-bonding configurations (local minima) when calculating equilibrium constants for formation of complexes.

2.3 Introduction

Volatile organic compounds (VOC) can be oxidized in the atmosphere to form organic nitrates that can serve as nucleating seeds for particle formation[122]. VOC emissions are estimated at over a billion metric tons per year, mostly composed of the biogenic emission of isoprene and terpenes[123]. These, as well as anthropogenic

emissions, are oxidized by OH·, Cl·, O_3, or NO_3 to form an alkyl radical, R·, which then reacts with O_2 to form a peroxy radical, RO_2[124, 125]. For example,

$$RH + OH\cdot \rightarrow R\cdot + H_2O \quad (1)$$

$$R\cdot + O_2 \rightarrow ROO\cdot \quad (2)$$

Peroxy radicals then react with NO to produce NO_2 or organic nitrates, which can either nucleate particle formation or go on to produce tropospheric ozone[122].

We seek to understand the formation of atmospheric particulates and ozone in urban environments where ozone and $PM_{2.5}$ (particulate matter under 2.5 μm in diameter) are major contributors to human respiratory and cardiovascular disease[126]. Measured tropospheric particulate concentrations are greater than current atmospheric models predict[127], and we seek to identify the mechanisms through which these additional particles are formed to improve atmospheric models, inform air pollution abatement policies, and ultimately reduce particulate levels to improve human health. Classical nucleation theory (CNT)[128] is commonly invoked to model new particle formation. The first step in forming a particle using CNT is formation of a critical cluster, and peroxy radical-water complexes may serve as the nucleating seed for cluster formation and consequently new particle formation[129].

Several studies have demonstrated that some hydroperoxy radicals react faster in the presence of water molecules than in dry air[125, 130-134]. Furthermore, a recent study[135]

showed a significant enhancement in the kinetics of the self-reaction of 2-hydroxyethylperoxy (HEP) radical as the concentration of water vapor increased. The enhancement in reaction kinetics was hypothesized to be due to the formation of a radical-water complex as one step in the reaction mechanism. This effect might be because the hydrogen-bonded complex has a lower reaction transition-state energy[136] and/or because the hydrogen-bonded complex has multiple low frequency vibrational modes that act as energy sinks, quenching the reaction complex and allowing the activated complex to progress towards products as opposed to dissociating back to reactants[135].

Standard statistical mechanics can be used to calculate the equilibrium constant for the formation of a radical-water complex at any water vapor concentration and temperature[137]

$$K_c = \frac{[complex]}{[water][radical]} = \frac{\tilde{q}_c}{\tilde{q}_w \tilde{q}_r} \quad (3)$$

where c is the complex, r is the radical, w is water, and $\tilde{q} = q/V$, and where q is the canonical partition function. The water vapor concentration is determined by temperature and humidity, and if we know the radical concentration, the complex concentration can be calculated using Eq. (3). To calculate K_C as a function of temperature, we calculated the partition function of the peroxy radical, water, and complex, which, for any species, is given by

$$q = \sum_{states} e^{-E_i/kT} \quad . \tag{4}$$

Often, this calculation is split into standard parts[137]

$$q = q_{trans} q_{vibrot} q_{nuc} q_{elec} \quad , \tag{5}$$

where

$$q_{trans} = \tilde{q}_{trans} V = \left(\frac{2\pi mkT}{h^2}\right)^{3/2} V \tag{6}$$

where q_{nucl} depends on the spin statistics of the nuclei, and

$$q_{elec} = g_i e^{-E_i/kT} \tag{7}$$

Here, g_i is 1 for closed shell molecules and 2 for radicals with an unpaired spin, and E_i is the electronic energy of the ground electronic state. Care is required to refer all energies to the same energy reference, which we choose as the rotationless zero-point energy of separated water and peroxy radicals

The factor q_{vibrot} can sometimes be factored into the rotational part, often approximated by rigid rotor energy levels whose partition function is well known[137], and a product of normal mode vibrations, which can be treated as separate harmonic oscillator, Morse oscillator, or other modes. Additional energy terms that describe interactions between normal modes and between rotational and vibrational degrees of freedom can also be included. Even though this complication requires adding up individual state contributions to the partition function rather than factoring the

partition function into a rotational term and individual terms from each vibrational mode, this calculation is easily summed in fractions of a second on a personal computer.

2.4 Proposed Model for Partition Function Evaluation

The partition function of water is accurately known by direct state count[138-140], so we only need to calculate the vibrational and rotation energy levels of various peroxy radicals and their complexes with water. This was done for hydroperoxy ($HO_2\cdot$) and 2-hydroxyethylperoxy ($HOCH_2CH_2O_2\cdot$ or HEP), two of the simplest and most common peroxy radicals in the troposphere. Figure 2.1 shows the computed equilibrium geometry of the two complexes. Geometries were optimized and normal modes calculated by Gaussian 09[141] using the B3LYP/aug-cc-pVDZ method/basis set combination for both complexes and monomers. For $HO_2\cdot$, single point energy was calculated at the CCSD(T)/aug-cc-pVTZ level of theory/basis set using the optimized geometries computed at the CCSD(T)/aug-cc-pVDZ level. For HEP the single-point energies were calculated at the CCSD(T)/aug-cc-pVDZ level using B3LYP/aug-cc-pVDZ optimized geometry. Geometry optimization at the CCSD(T)/aug-cc-pVDZ level for HEP and HEP-water complex was not successful due to computer system limitations.

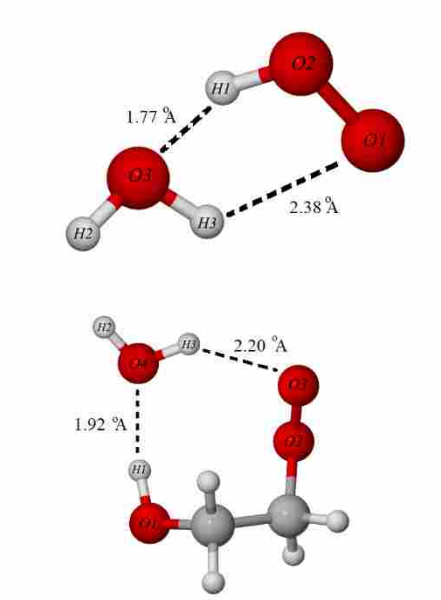

Figure 2.1 Computed equilibrium geometries for the complexes: hydroperoxy–water complex (top), and HEP–water complex (bottom). The lines and numbers indicate a hydrogen bond and its associated interatomic distance in Angstroms. Three higher energy conformations of HEP–water complex are pictured in figure 2 of Ref. 134 .

These complexes with water are each bound by two hydrogen bonds, stabilizing the complex by twice as much as a complex with only one hydrogen bond. The computed binding energy (D_e) of the hydroperoxy-water complex is 9.49 kcal/mol, consistent with what has been reported previously[142, 143]. The binding energy of the HEP-water complex is 8.58 kcal/mol. In addition, the HEP complex has three additional local minima, one with a different set of HEP torsion angles, one with a longer hydrogen bond to the inner peroxy oxygen instead of the outer oxygen, and one with an internal hydrogen bond plus a hydrogen bond from the water to the hydroxyl oxygen (the additional three geometries are shown in Ref[135].134 , Fig, 2). The computed energy difference forms the major contribution to the enthalpy of formation of the complex.

This stabilization gives a large contribution to the electronic partition function of the complex and is the primary driving factor towards complexation. However, the vibrational and rotational terms contribute an entropy term that is also important.

Most of the vibrational modes of the complex can be identified as only slightly changed from those of the radical or of water. Many of these are high frequency modes, above 1000 cm^{-1}, that are not thermally accessible at typical ambient temperatures, and even lower frequency modes tend to cancel out from nearly identical terms in both the numerator (complex) and the denominator (water or radical) of Eq. (3).

However, each complex has 6 new vibrational modes not present in the reactants that grow out of relative motions. One mode is dissociative, correlating to the distance between molecular centers-of-mass. The potential energy for this mode behaves as R^{-3} at long distances as it can be described as a dipole-dipole attraction[144]. The other five modes are soft, anharmonic modes that are thermally accessible and represent rotations of the water with respect to the radical such as hydrogen atom exchange or similar motions. The harmonic oscillator approximation is not appropriate for any of these new vibrational modes. We will show that the usual harmonic oscillator approximation seriously undercounts the accessible states in the partition function of these complexes.

We propose to treat the vibrational mode that correlates with the separation of the molecular centers-of-mass as a Lennard-Jones 6-3 potential, corresponding to the R^{-3}

dependence of the dipole-dipole force. If a harmonic oscillator has N states below a given dissociation energy, a Morse oscillator with the same harmonic frequency has exactly $2N$ bound states because of the quadratic anharmonicity. Similarly, Born-Sommerfeld quantization arguments show that a Lennard-Jones 12-6 potential with the same harmonic frequency has $2.863N$ bound states (instead of twice as many) because the longer-range potential R^{-6} approaches zero slower than the exponential in the Morse potential. Moreover, a Lennard-Jones 6-3 potential with the same harmonic frequency, with an even longer-range attractive potential, has $5.522N$ bound states. Some of the extra states not counted in the harmonic oscillator approximation could be highly excited states of this mode. However, the $5.522N$ states will not all count equally because most are near dissociation and will have lower Boltzmann weight. The energy eigenvalues for a Lennard-Jones 6-3 potential were calculated using Numerov's numerical method[145] and then fit to a functional form for the energy levels of a Lennard-Jones m-n potential developed by R. B. Shirts to be published separately, where the number of bound states discussed earlier in this paragraph is also derived.

The highly excited eigenfunctions of the Lennard-Jones 6-3 potential have large probabilities at very large distances. For states near dissociation, the quantity $\langle R^2 \rangle / R_e^2$ becomes increasingly large, and consequently, the rotational constants affected by this mode will be significantly reduced. This suggests that vibration-rotation coupling may affect the partition function. Figure S1 in the Supplemental information shows the v =

30 vibrational wave function (of 55 bound states) for a Lennard-Jones 6-3 potential with $D_e = 10$ □. The energy of this state is about 99% of dissociation. The probability for this state is large just inside the classical turning point of 6.2 R_e, and the quantity $\langle R^2 \rangle / R_e^2$ is about 25 for this state (where it is about 1 for the ground state). This state will have a rotational constant about 1/25 of the ground state. For a radical-water complex, this means that the *B* and *C* axis moments of inertia become very large for this type of excited state due to a large intermolecular distance, which means the *B* and *C* rotational constants become very small for these highly excited states. This effect will lower the rotational energy and make some rotational states more thermally accessible. The rotational constants for the Lennard-Jones 6-3 potential plus the centrifugal potential were calculated by solving for eigenvalues numerically including terms up through $[J(J+1)]^5$ and then adjusting the *B* and *C* rotational constants using this contribution to the moment of inertia for the intermolecular distance, assuming the contribution from the rest of the molecule was unchanged.

We propose to treat the other five soft modes in the complex as hindered rotors. When two hydrogen atoms in the water molecule are interchanged in a soft mode, that mode is a two-fold hindered rotor. This motion usually has a relatively low barrier. The eigenstates of the two-fold rotor potential are either symmetric or antisymmetric with respect to reflection through the barrier. The lower energy, symmetric states can only support singlet proton spin functions and have an occupancy of ¼ for consistency

with the usual astrophysical convention[138-140]. The higher energy antisymmetric states support only triplet proton spin functions and have an occupancy of 3/4.

When a normal mode consists of rotating an OH bond that breaks a hydrogen bond of the complex but returns to the same configuration after a 2π rotation, that mode is treated as a one-fold rotor with a higher barrier. In either the one-fold or two-fold case, the Schrödinger equation can be transformed to the Mathieu equation for which the eigenvalues are well known and easily calculated[146, 147].

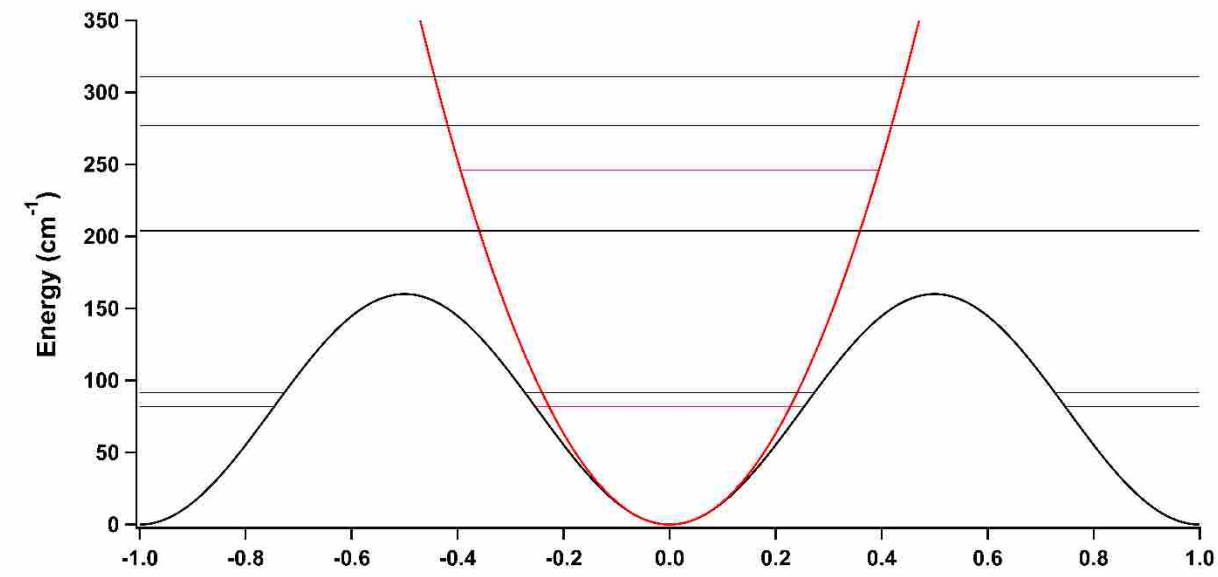

Figure 2.2 Energy levels of a twofold hindered rotor (black) compared to those of a harmonic oscillator (red). Low-energy hindered rotor levels are split by tunneling. Higher energy rotor levels correspond to revolving above the barrier

Figure 2.2 plots a two-fold rotor modeling the rotation of two water hydrogen atoms whose O atom is a proton acceptor in a hydrogen bond. The two lowest energy states are states that tunnel between the wells, and the tunneling rate, or rate of

hydrogen exchange, is inversely proportional to the splitting between the energies. However, a hindered rotor also has states above the barrier. These describe states where the hydrogen atoms are revolving, some clockwise and some counterclockwise. The barrier is often low enough that the energies of several revolving states are lower than the dissociation energy of the complex, so they should be included in the partition function. The Appendix describes how the hindered rotor energy levels are treated.

This proposed model with one Lennard-Jones 6-3 dissociative mode and five hindered rotors (LJ63+5HR model) is simple in that it neglects any coupling between modes and in that it uses energy levels of well-known functional form; however, it should be more accurate than the harmonic approximation. It also includes tunneling of water protons between equivalent positions, a phenomenon not included in the usual rigid rotor/harmonic oscillator model.

2.5 Test of the LJ63+5HR Model for Water Dimer

We first examine how successful the LJ63+5HR model is in treating the water dimer. This species exists in equilibrium with water vapor at any temperature and has been the recent subject of both experiments and theoretical calculations. The dimer partition function is known quite accurately from engineering measurements described by Ruscic[148]. An accurate potential surface in all 12 dimensions has been developed by Bowman and collaborators[149-151], and rovibrational energies have been calculated by

Leforestier and others[152, 153]. This system has many of the same complications as radical-water complexes, so we can compare our results with known results to test the accuracy of the LJ63+5HR model. However, we are interested in an approximate method that we can extend to peroxy radical-water complexes without having to explore the full dimensionality of the potential energy surface.

The geometry of the water dimer was calculated at the B3LYP/aug-cc-pVDZ method/basis set level (the computed structure is displayed in Fig. S2 in the supplementary information). It has one hydrogen bond, twelve vibrational modes, and is almost, but not quite, a prolate symmetric top, the O-O bond axis being the rotational axis with the large rotational constant (A).

Six of the calculated vibrational modes of the complex are easily identified as symmetric and antisymmetric combinations of the vibrational modes of water monomer. The other six modes are soft modes and are described in Table 2.1. In this discussion, computed data from Ref[149]. 149 is used. One of the modes correlates to the O-O stretch coordinate and has a harmonic frequency of 181 cm^{-1}. The dissociation energy for this mode is the computed binding energy, D_e, of the complex, 1739 cm^{-1}, which we model with a Lennard-Jones 6-3 potential.

Table 2.1. Soft modes of the water dimer using data from Ref. 148. Units are cm^{-1}. NA indicates not applicable. Energy splittings calculated in this work using the LJ63+5HR model are in parentheses.

Mode	Harmonic Frequency	Dissociation Energy or Barrier	Splitting	*n*
O-O stretch	181	1739	NA	NA
Acceptor proton exchange (AT)	140	185	12 (4.1)	2
Water exchange (I)	149	354	0.7 (0.1)	2
Donor Proton exchange (DT)	125	629	0.1 ($<10^{-5}$)	2
In-plane bend	352	1739	NA	1
Out-of-plane bend	611	1739	NA	1

One of the low frequency modes (labeled *AT*) leads to the interchange of the two hydrogen atoms of the proton acceptor water. The harmonic frequency of this motion is 140 cm^{-1}, but the barrier to hydrogen exchange is only 185 cm^{-1}, showing the extreme anharmonicity of the potential. The barrier is so low because the motion only involves rotating the proton acceptor molecule without breaking the hydrogen bond. This exchange leads to a splitting of about 12 cm^{-1} between the energy levels of the two-fold hindered rotor. The singlet-triplet occupancy discussed in the previous section applies to the proton spins in this mode.

A second low-frequency motion (labeled *DT*) corresponds to exchange of the two protons of the proton donor water. The harmonic frequency of this motion is about 125 cm^{-1}. This exchange has a higher barrier than the *AT* mode, 629 cm^{-1}, because exchange

involves partially breaking the hydrogen bond, leading to a smaller splitting of about 0.1 cm^{-1}. The same relation to the proton donor spin singlet and triplet wavefunctions applies as in the *AT* mode,

A more complicated low frequency motion (labeled *I*) interchanges the proton donor and the proton acceptor water molecules. The barrier is intermediate, about 354 cm^{-1}, with a harmonic frequency of 149 cm^{-1} and an intermediate experimental splitting of about 0.7 cm^{-1}. Here we must deal with nuclear spin functions of four fermion proton spins together with two boson O nuclei. The full permutation-inversion group of the dimer is G_{16} and involves 8 equivalent energy minima[154]. Luckily, the splittings are small, and we are satisfied with a subgroup that treats this as three independent two-fold hindered rotors. The statistical weights for the two *I* states of ½ and ½ reproduce the overall occupancy obtained by taking into account all of the irreducible representations of the full symmetry group.

The other two low-frequency motions correspond to rotating one molecule with respect to the other, breaking the hydrogen bond, and these are one-fold hindered rotors.

The foregoing information was used as input to the LJ63+5HR model to test its performance. Notice in Table I that the computed *AT* splitting was 4.1 cm^{-1} compared to the experimental 12 cm^{-1}, in reasonable agreement considering the assumption of a

separable, single cosine potential. The complicated *I* splitting is 0.1 cm^{-1} compared to the experimental value of 0.7 cm^{-1}. The *DT* splitting is less than 10^{-5} cm^{-1} compared to the experimental value of 0.1 cm^{-1}. These splittings are in reasonable agreement with experiment because tunneling splittings are exponentially dependent on the potential energy function, and we have made an extreme simplification of the tunneling potential. Disagreement with experimental tunneling splittings should have negligible effect on the partition function.

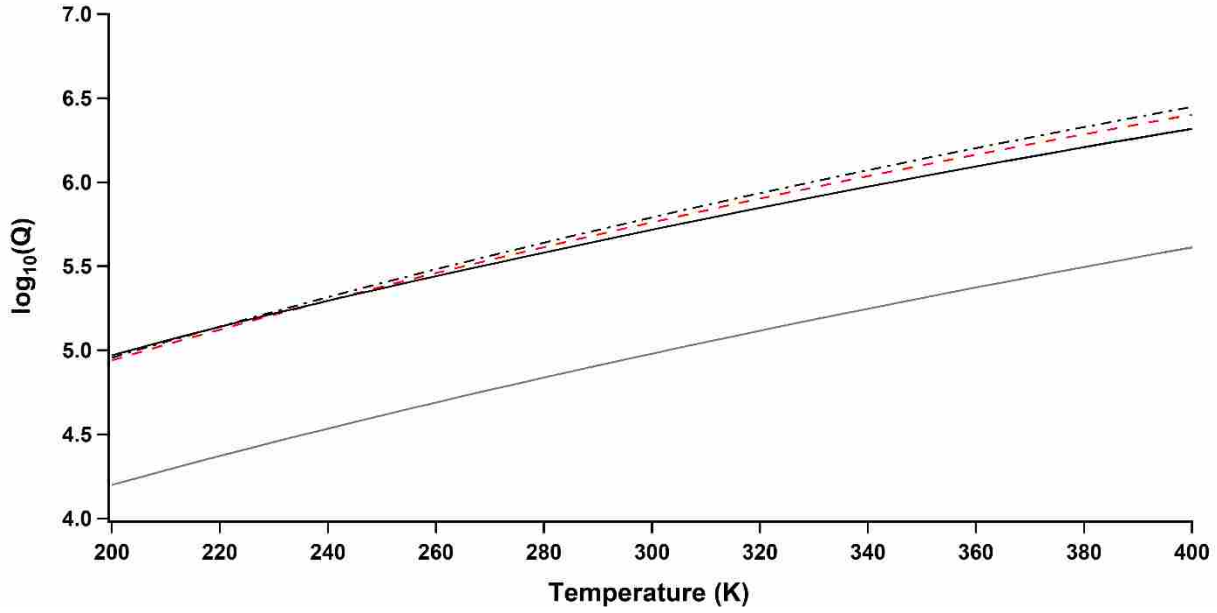

Figure 2.3 Vibration–rotation partition function of water dimer. The black solid line is extracted from Ref.147 by dividing out the translational, nuclear, and electronic parts and represents the experimental value. The dashed curve is from using the LJ63 + 5HR model discussed in the text. The dotted curve is without rotation–vibration coupling in the O–O stretch mode. The gray curve is the harmonic oscillator/rigid rotor approximation

Figure 2.3 compares plots of the vibration-rotation partition function of the water dimer calculated using the LJ63+5HR model with one obtained by treating all the modes as independent harmonic oscillators and the rotations as a rigid symmetric top (HORR

approximation). The HORR result (gray line) is considerably below the experimental curve, by about a factor of 6. In the HORR model, the permutation-inversion symmetry of the dimer with its eight symmetric minima and four spin ½ protons (sixteen spin states) is simulated by dividing by two. The underestimation by a factor of six indicates that many states accessible to the dimer are not included in the HORR model.

The overall partition function obtained using the LJ63+5HR model (dashed curve) is in much better agreement with experiment but is now slightly too large at high temperature compared to the experimental result derived from Ref[148]. 139. Detailed examination of the calculation reveals which aspects of the model contribute to improvement:

1. The use of the anharmonic Lennard-Jones 6-3 potential increased the partition function by 10% at 200 K and increasing to 30% at 400 K over the contribution of that mode in the HORR approximation. Thus, the highly excited O-O stretch states do not contribute the major part of the newly accessible states. These states near dissociation are too high in energy to contribute, and it is only the first three or four vibrational states that are important. For example, a Lennard-Jones 8-4 or Lennard-Jones 7-3 O-O stretch potential, both give about the same agreement. Nevertheless, the anharmonicity of these lower states is a measurable, but less important, factor.

2. Implementing vibration-rotation coupling with decreasing *B* and *C* rotation constants with O-O stretch excitation does not affect the partition function at 200 K but *decreases* the partition function slightly by a factor of 5% at 400 K (see dotted line using rigid rotor rotations in figure 2.5). This decrease is presumably because the increase of the partition function due to the decreasing rotational constant is offset by the fact that our explicit sum of rotational states does not include states above dissociation, whereas the rigid rotor approximation includes all rotational states. The inclusion of higher-order centrifugal distortion, however, is unimportant.

3. The use of the hindered rotor model for the two higher frequency, one-fold hindered rotors increases the partition function above the harmonic oscillator model by 2% at 200 K increasing to 8% at 400 K; thus, this aspect of the model is not an important effect. These two modes incorporate very little correction over the HORR approximation because the frequencies are so high.

4. The hindered rotor model for the three two-fold rotor modes contributes a factor which varies from about 5.3 to 5.1 across the temperature range of interest. This is the major correction implemented in the LJ63+5HR model. In fact, substituting for a harmonic oscillator with a hindered rotor with the same harmonic frequency will always increase the vibrational partition function because the hindered rotor anharmonicity parameter is negative. For the same reason, this substitution will additionally increase the electronic part of the partition function of the complex (and

therefore the equilibrium constant) by lowering the zero-point energy of the complex. The *AT* and *DT* two-fold hindered rotors incorporate somewhat larger corrections than the two one-fold hindered rotors, but that is mitigated by the occupation numbers (¼ and ¾ for symmetric and antisymmetic states respectively) that arise from the nuclear spin symmetries for interchanging identical nuclei on the same molecule. This state reduction arises in the water monomer in the rotational partition function due to the symmetry number, and these normal modes of the complex correlate directly to water rotations.

5. The major correction arises because there are *eight* equivalent potential minima for the complex instead of just four expected from the monomer rotations. These eight minima require a third two-fold hindered rotor mode that, to zero-order, doubles the number of accessible states, and then increases to a factor greater than two due to the low frequency of the mode and then even more from the anharmonicity of the mode due to the low barrier.

The hindered rotor model could be improved by going beyond the assumption that the hindered rotor vibrational modes are factorable into independent partition functions. Important coupling between the modes is obvious in the transition state documented in Ref. 148 for interchanging the donor and acceptor (*I*). More motions than just one normal mode are required, and the approach to the barrier also passes through an intermediate local maximum (see stationary points #4 and #5 in Ref. 148).

The LJ63+5HR model approximates the potential by a simple cosine potential with one barrier at a predetermined position, not the position of the real barrier.

Thus, calculations on the water dimer could be improved by taking more of the available potential surface information into account, but others have already done that very well[149-153], and our goal is to extend the method to more complicated complexes for which extended potential information is not available. However, we hope that our model will give the partition function to within 20–30%, much better than the order of magnitude errors found with the harmonic oscillator-rigid rotor model.

For other peroxy complexes, we do not have the luxury of comparing with results from accurate ab initio calculations and multidimensional potential surfaces. To test if output from standard Gaussian files could give us reasonable accuracy, an older B3LYP functional[155, 156] and a newer MO6-2X functional from Truhlar's group[157] were both tried. Results were within ±30% of experimental values using either of these methods. Figure S3 in the supplementary information plots the ratio of computed partition function to experimental values using Gaussian 09 output energies, harmonic frequencies, effective masses, and force constants rather than experimentally adjusted numbers

2.6 Equilibrium Constant Results for Formation of Hydroperoxy-Water Complex

The equilibrium constant for the formation of an HO_2·-water complex has been measured experimentally at four temperatures by Kanno *et al* [158] and is shown by diamonds in Figure 2.4, where $\log_{10}K_C$ is plotted versus $1000/T$. In 1997, prior to the experiments, Aloisio and Francisco[142] did a HORR calculation, and using their published data from Tables 2, 3 and 4 of Ref[142]. 141, we calculated the dotted curve, which is a factor of about 28 below the experimental numbers. Figure 2 in Aloisio and Francisco's paper contains a curve from a HORR calculation that agrees very well with the later experimental data, and the dot-dash curve represents a digital extraction of data from their figure 2. The original data does not exist, making it impossible to explain the discrepancy between the two curves, but we believe their curve, reproduced as the dot-dash curve, should be more like the dotted curve. The gray line in figure 2.4 plots the HORR equilibrium constant using data from our Gaussian calculation. It is approximately a factor of 2.5 below the HORR calculation using Aloisio and Francisco's data, mostly because their lowest two vibrational modes have lower frequencies and, thus, have higher excited state populations. In both these HORR calculations, we have multiplied by two in the partition function of the complex because there are two equivalent minima that differ by interchanging water hydrogen atoms (water rotation)

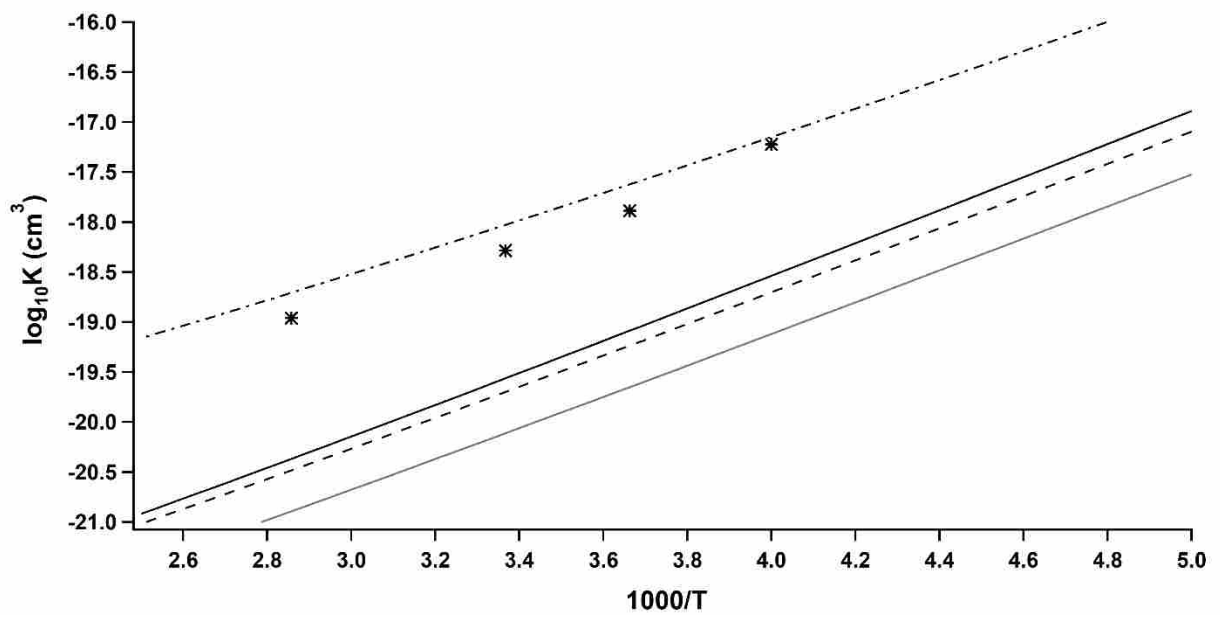

Figure 2.4 Plot of $\log_{10}K_C$ for formation of the HO_2–H_2O complex versus 1000/T. Black solid line is the proposed LJ63 + 5HR model of this work. Dashed line is the HORR model using data from Ref. [141]. Dot–dash line is extracted graphically from Ref. [141], but the present authors believe it should be more like the dashed line. The gray line is calculated using the HORR approximation but using Gaussian frequencies and rotational constants from the same calculation as the solid line. Parameters for the soft modes are summarized in Table 2.2. The diamonds are experimental values at four temperatures from Ref. [157]

and then divided by four because of the four proton spin functions that are divided out in the water partition function by convention.[138-140]

The calculated equilibrium constant using the proposed LJ63+5HR model is plotted as the black line in figure 2.4. In this case, for the soft modes, we used one Lennard-Jones 6-3 mode for the dissociative motion, one two-fold hindered rotor describing the motion that exchanges hydrogen atoms with a barrier of 206 cm^{-1} taken from Suma et al.[159]. We also used four one-fold hindered rotors (see Table 2.2). One of these has a barrier of 215 cm^{-1}, according to Suma et al.[159] for the motion of the

nonbonding hydrogen atom perpendicular to the plane of the other five atoms. This motion was not treated as two separate minima because the barrier is only slightly above the zero-point energy of the harmonic motion. The rigid rotor approximation was used for the rotational part of the partition function.

Table 2.2. Soft modes of the OOH-H2O complex. Units are cm-1. Results are from Gaussian 09 harmonic frequency calculation. NA indicates not applicable.

Potential Model	Harmonic Frequency	Dissociation Energy or Barrier	Calculated Splitting	*n*
Lennard-Jones 6-3	262.3	3314	NA	NA
Hindered rotor	200.5	206[a]	15.9	2
Hindered rotor	108.5	1657[b]	NA	1
Hindered rotor	301.3	215[a]	NA	1
Hindered rotor	471.5	1657[b]	NA	1
Hindered rotor	686.9	1657[b]	NA	1
[a] from Ref. 158. [b] barrier is half of dissociation energy. Units are cm^{-1}				

The equilibrium constant calculated using the LJ63+5HR model is in better agreement with the experimental data than the HORR approximation by a factor of about 4, but the curve is still approximately a factor of 12 below the experimental data. This result still demonstrates that the HORR undercounts accessible quantum states for

weakly bound complexes and that the LJ63+5HR model is a substantial improvement. However, in this case, the improvement comes in about equal amounts from excitation of the low frequency states of the two-fold hindered rotor and a decrease in the zero-point energy of the complex. At room temperature and 50% humidity, the LJ63+5HR model predicts that about 1% of hydroperoxy radicals would be complexed with water molecules.

The remaining discrepancy between the experimental data and the LJ63+5HR model probably lies in the treatment of the two dimensional surface explored by Suma *et al.* [159] describing motions of water hydrogen atoms. This surface is poorly described by the two hindered rotors with low barriers. In particular, the motion of the hydrogen atom not involved in the hydrogen bond is better described by a double well than a hindered rotor. Indeed, this whole surface lies within 350 cm^{-1} of the four equivalent minima according to figure 2 of Ref. 158. Extending our model beyond the separable hindered rotor model is probably the best route for improvement but has not been attempted. Alternatively, a factor of 12 increase in the equilibrium constant could also be achieved by a 15% increase in the computed binding energy, D_e, but we expect more accurate computations would actually lower the binding energy since we have observed the CCSD(T) binding energy to decrease as one moves from double-zeta to triple-zeta to quadruple-zeta basis sets.

2.7 Results for HEP-Water Complex

Experimental data on the observed rate of the HEP self-reaction has been published previously [135]. This rate is a sum of rates with and without bound water. To tease out the separate contributions requires the equilibrium constant. One complication in this calculation is that HEP has two thermally accessible conformations at room temperature, as shown in figure 1 of Ref. 134. The lowest energy conformation has an internal hydrogen bond. The next higher conformation, a local minimum in the potential surface, has no internal hydrogen bond. However, note that HEP already has three modes of internal rotation before complexation. These torsional motions all break the internal hydrogen bond present in the lowest energy conformation. In fact, the second conformation of figure 1 Ref. 134 differs from the lowest energy conformation by only a change in the angle of the O-O-C-C torsion, and more extensive exploration of this torsion as well as the H-O-C-C torsion suggests that an asymmetric 3-fold rotor potential would be more accurate. However, aiming for the simplicity of the proposed model, we model the three internal rotations as one-fold hindered rotors. Therefore, HEP-water complexes have 8 hindered rotor modes: 3 from monomer HEP and 5 new ones. The hindered rotor frequencies of uncomplexed HEP are shown in Table 2.3. The barriers were all chosen as 1500 cm^{-1}, which is approximately the strength of an internal hydrogen bond. Two lower frequency modes at 329.4 cm^{-1} and 398.4 cm^{-1} were identified as Morse-type modes rather than hindered rotor modes by their predicted

high dissociation energy based on the calculated Gaussian *X*-matrix diagonal anharmonicities.

Table 2.3. Soft modes of HEP. Units are cm^{-1}. Results are from Gaussian 09 harmonic frequency calculation. NA indicates not applicable.

Potential Model	Harmonic Frequency	Dissociation Energy or Barrier	*n*
Hindered rotor	85.7	1500[a]	1
Hindered rotor	167.3	1500[a]	1
Hindered rotor	458.3	1500[a]	1
[a] estimated hydrogen bond strength			

As mentioned in Section 2, the HEP-water complex has four different thermally accessible conformations (shown in figure 1 and in figure 2 of Ref. 134). However, these are not as obviously accessible by simple internal rotation. The lowest two have the water hydrogen bonded to the outer peroxy oxygen atom. The third conformation has the water hydrogen bonded to the inner peroxy oxygen atom, and the fourth conformation simply adds one hydrogen bond between the water and the hydroxyl oxygen without disturbing the internal hydrogen bond of the uncomplexed HEP. How should we treat these multiple conformations? One alternative is to calculate equilibrium constants separately for the four different reactions forming four complexes from the reactants and then use Boltzmann weighting to adjust the populations.

However, the simplest and easiest way to treat multiple conformations is as additional states to be added to the partition function sum of states—with the proper energy reference giving the correct Boltzmann weighting. We have adopted this method. Another way would be to recognize that conformations are just local minima in rotations about internal axes that can be described by existing normal modes. However, to accurately describe these states would require extensive information about the barriers in the multidimensional potential surface rather than just local information about the local minima. Treating the conformations as separate species when the internal rotations are not otherwise included by the separable hindered rotor model already described should get equivalent results.

Note that in addition to the conformations in shown in figure 1 and in figure 2 of Ref. 134, each conformation has a mirror image that represents a separate set of accessible conformations. However, we explicitly deal only with those conformations which have a +-*gauche* O-C-C-O torsion angle, since the doubling occurs in both

Table 2.4. Soft modes of the HEP-H_2O complex. Units are cm^{-1}. Results are from Gaussian 09 harmonic frequency calculation. NA indicates not applicable.

Potential Model	Complex #	Harmonic Frequency	Dissociation Energy or Barrier	Calculated Splitting	*n*
Lennard-Jones 6-3	1	154.4	3001	NA	NA
Hindered rotor	1	162.4	600[a]	0.0007	2
Hindered rotor	1	66.8	3001[c]	NA	1
Hindered rotor	1	100.5	1500[b]	NA	1
Hindered rotor	1	106.4	3001[c]	NA	1
Hindered rotor	1	194.0	1500[b]	NA	1
Hindered rotor	1	269.4	1500[b]	NA	1
Hindered rotor	1	413.1	1500[b]	NA	1
Hindered rotor	1	668.1	1500[b]	NA	1
Lennard-Jones 6-3	2	144.0	2741	NA	NA
Hindered rotor	2	189.8	600[a]	0.0069	2
Hindered rotor	2	67.9	1371[b]	NA	1
Hindered rotor	2	92.2	1371[b]	NA	1
Hindered rotor	2	117.8	1371[b]	NA	1
Hindered rotor	2	226.6	1371[b]	NA	1
Hindered rotor	2	331.2	1371[b]	NA	1
Hindered rotor	2	705.9	1371[b]	NA	1
Hindered rotor	2	417.6	2741[c]	NA	1
Lennard-Jones 6-3	3	101.3	2593	NA	NA
Hindered rotor	3	173.0	600[a]	0.002	2
Hindered rotor	3	54.7	1293[b]	NA	1
Hindered rotor	3	59.3	1293[b]	NA	1
Hindered rotor	3	287.9	1293[b]	NA	1
Hindered rotor	3	369.1	1293[b]	NA	1
Hindered rotor	3	133.9	2968[c]	NA	1
Hindered rotor	3	195.6	2741[c]	NA	1
Hindered rotor	3	657.6	2741[c]	NA	1
Lennard-Jones 6-3	4	161.4	2689	NA	NA
Hindered rotor	4	143.6	600[a]	1×10^{-4}	2
Hindered rotor	4	38.9	1344[b]	NA	1
Hindered rotor	4	70.3	1344[b]	NA	1
Hindered rotor	4	96.0	1344[b]	NA	1
Hindered rotor	4	207.9	1344[b]	NA	1
Hindered rotor	4	387.5	1344[b]	NA	1
Hindered rotor	4	498.2	2689[c]	NA	1
Hindered rotor	4	656.7	2689[c]	NA	1

[a] estimated barrier similar to water dimer *DT* mode. [b] barrier is half of dissociation energy.
[c] barrier is equal to dissociation energy

uncomplexed and complexed HEP and will cancel out of the equilibrium constant with

equal factors of two in denominator and numerator of Eq. (3). *Anti* conformations of the O-C-C-O torsion are not favorable for hydrogen bonding and will be thermally inaccessible.

The assignment of soft modes in the LJ63+5HR model for the four conformations of HEP-water complex is summarized in Table 2.4. Each conformation has one dissociative mode modeled by a Lennard-Jones 6-3 potential with an accompanying dissociation energy (D_e) as calculated by Gaussian (different for each conformation). Each conformation has one two-fold hindered rotor corresponding to the motion leading to interchange of the two water hydrogen atoms. For all four conformations, the barrier for this motion was chosen to be 600 cm^{-1} in analogy to the value for the *DT* motion of water dimer, which has a similar transition state. Each conformation also has seven one-fold hindered rotors. The barrier for each of these motions was chosen to be half the dissociation energy if one hydrogen bond was broken by the motion or the full dissociation energy if both hydrogen bonds were broken.

Figure 7 in Ref. 126 shows the net rate constant for the HEP self-reaction increasing with higher water vapor concentration. This effect is higher at low temperature where the equilibrium constant is larger. Figure 2.5 shows a plot of $\log_{10}K_C$ calculated using the proposed model versus 1000/*T* as well as the value using the HORR approximation. The equilibrium constant calculated using the proposed LJ63+5HR model varies from a factor of 3 higher than the HORR approximation predicts at low

temperature raising to a factor of 3.5 higher at high temperature. The improvement comes partly from the lowered hindered-rotor zero-point energy of the complex, but

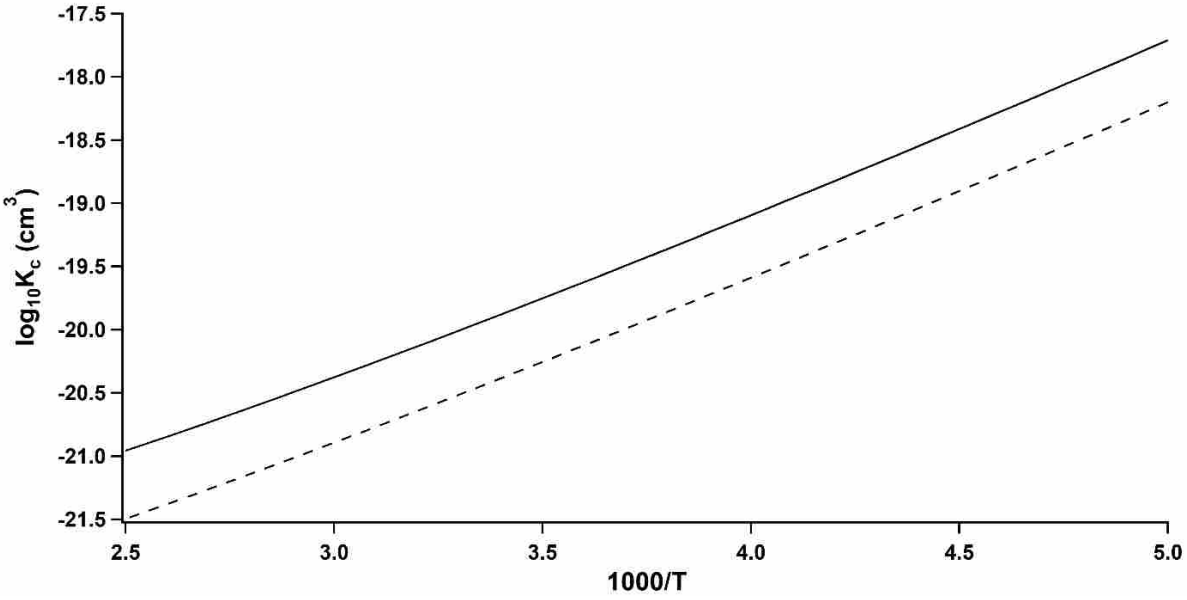

Figure 2.5 Plot of $\log_{10}K_C$ for formation of the HEP–water complex versus 1000/T. Solid line is the proposed LJ63 + 5HR model of this work. Dashed line is the HORR model. Parameters for soft modes are summarized in Table 3 for HEP and in Table 4 for HEP–water complex

there is some contribution from increased vibrational partition function of the complex by the two-fold hindered rotor. For most of the other vibrational modes, the difference is small. It is interesting to note that the electronic partition function of the third conformation of the HEP-complex is larger than for the fourth conformation (with a hydrogen bond to an external water) because of lower zero-point energy in spite of the higher calculated D_e value of the fourth conformation. A linear fit of the calculated $\log_{10}K_{eq}$ plot in Figure 2.5 is given by $\log_{10}K_{eq} = -24.16 + 1259/T$ where K_{eq} is in cm^3.

In this calculation, a Morse oscillator approximation for the non-hindered rotor modes was used. To do this, we calculated the equilibrium geometry using the Gaussian anharmonic option, which reports *X*-matrix anharmonicities as well as harmonic frequencies. To give a Morse oscillator approximation, only the diagonal anharmonicities were used. The Morse oscillator model gives a slightly lower zero-point energy than a harmonic oscillator model, but, independently, this process was quite useful in identifying the hindered-rotor modes. For example, HEP is large enough to have three low-frequency skeletal torsions in the same frequency range as hydrogen-bonded hindered rotors. However, the mode dissociation energy predicted by the Morse oscillator model was higher for skeletal modes (several tens of thousands of cm^{-1}) than for hindered rotors modes (only a few thousand cm^{-1}). Once these are distinguished, using a harmonic model for non-soft mode vibrations was virtually identical to using the Morse oscillator model.

Given the calculated equilibrium constant, we can calculate the extent of complexation in a given water concentration. In particular, at T = 295 K, K_P is 0.3, and the vapor pressure of water is 0.026 atm. This means that about 0.4% of the radicals are complexed at 100% humidity. At 275 K, K_P increases to about 0.7, but the vapor pressure of water is only about 0.007 atm. This means that only 0.25% of the radicals are complexed at 100% humidity. However, figure 7 of Ref. 14 shows that the effect of water on the rate constant is larger at the lower temperature, meaning the rate constant

for the complexed species (k_5 in Ref. 126) may be over 100 times as great (see Fig. 8 of Ref. 126) below 275 K.

2.8 Discussion and Conclusions

The lowest energy configuration of HEP + H_2O complex shown in figure 2.1 is lower in energy than the configuration believed to be the global minimum in Ref. 126 by almost 1 kcal/mol. The other three configurations as discussed in Ref. 126 were discovered by positioning a water molecule around the lowest conformation of HEP. The conformation of the HEP + H_2O complex shown in figure 2.1 results from positioning a water molecule near a higher energy conformation of bare HEP, but results in a lower energy for the complex.

Calculations with more than one complexing water molecule have not been attempted. Each new water molecule adds 6 new soft modes to the complex. This means a complex of $HO_2\cdot$ with two waters has two dissociative modes and 10 hindered rotor modes. Such complications become severe very quickly. Future work may need to address the complications associated with the introduction of the two waters and the associated new soft modes and their effect on K_{eq}. However, the linear dependence of observed rate constant with water concentration in figure 7 of Ref. 126 for HEP and figure 6 of Ref.[131] 122 for $HO_2\cdot$[158], suggests that the complex with two waters is not

important for reaction kinetics. However, additional water may well be important for nucleation of particle formation.

Although the partition function of water has been calculated accurately[138-140], we have elected not to use it. Using the rigid rotor approximation and rotational constants calculated using Gaussian results in a rotational partition function that is approximately 1% lower than that of Ref. 139 in the range 200 K to 400 K. This agreement is within the accuracy we expect to be able to obtain in the vibrational part, although further corrections could be implemented if required[160]. Furthermore, by using the same calculation method for rotational constants and the rotational partition functions of the radical and the complex, we expect some cancellation of error.

Note that the rigid rotor rotational partition function of water contains a symmetry number of 2 in the denominator[137]. This effectively divides the actual state count (occupation numbers of 1 and 3, averaging to 2) by four and is equivalent at sufficiently high temperature to the astrophysical convention[138-140] of using ¼ and ¾ for the occupation numbers for singlet and triplet spin function-allowed vibrational states. This convention requires that we use similar occupation numbers of ¼ and ¾ for the symmetric and antisymmetric states of the two-fold rotors in OOH-water and HEP-water complexes. Likewise, consistency requires multiplication by ½ in the HORR of OOH-water and HEP-water complexes (multiplication by 2 for two minima and dividing by 4 for the four spin functions). The group theory of the water dimer is more

complicated but was discussed in Section 3. Neglecting to divide by four may explain part of the discrepancy between the dot-dash and dotted lines in Figure. 4.

Discovery of the lower energy configuration of HEP-water since publication of Ref. 126 renders obsolete the K_{eq} values calculated in Ref. 126 (see Fig. 8 of Ref. 126). In addition, Ref. 126 did not include the spin-symmetry factor of 4 discussed in the previous paragraph. Moreover, we have found that HEP has a lower energy at the CCSD(T) level of theory than we had previously calculated. The net result is that our updated K_{eq} values documented here are actually slightly lower than plotted in Fig. 8 of Ref. 126 by a factor of approximately two.

The two-fold hindered rotor modes we used include tunneling between equivalent positions for water protons. Tunneling is automatically included in the Mathieu eigenvalues, although for a simplified potential surface consisting of a single cosine. Even so, care must be taken to include occupancies in the calculated states that are consistent with the spin degeneracies of the monomers. Tunneling is not needed for proton tunneling between hydrogen donor and hydrogen acceptors in the hydrogen bonding Lennard-Jones 6-3 modes because H_3O^+ - OH^- -like structures where a proton is exchanged are significantly higher in energy and thermally inaccessible.

Tables of coordinates for the calculated equilibrium geometries of all calculated species, as well as tables of calculated normal mode frequencies, effective masses, and

force constants are included in supplemental information. Diagonal *X*-matrix elements for HEP and its water complexes are also included.

The question of whether to include resonances (rotation-vibration states with energies above dissociation) in the partition function sum has been discussed in the literature[161]. These states have a finite lifetime but may exist to a significant degree in any dynamic equilibrium. In our calculation, it does not matter if excited vibrational states of high frequency modes are included because these almost exactly cancel between numerator and denominator. However, these states are routinely included as part of the harmonic oscillator approximation, which includes states with energy up to infinity. However, most of these states are too high in energy to contribute, and most do not couple strongly with the low frequency, hindered rotor modes, so, to the extent they *are* populated, they would be expected to persist in an equilibrium mixture. However, we have not included hindered rotor states whose energy is above the dissociation energy because these states couple strongly, and motion in any of these modes would be expected to leak out of the dissociative mode. We have tested the inclusion of rotational states of the dissociative mode that are bound inside the centrifugal barrier and whose energy is greater than the dissociation energy. Including these does not seem to make a significant difference, again because they are too high in energy. Note, however, that by using a separable approximation, we *are* including

combination states (states where two or more modes are excited) that are above dissociation.

We have not included the counterpoise correction for basis set superposition error. Some discussion has appeared in the literature[162, 163] about the accuracy of the counterpoise correction for hydrogen bonded complexes, and doing so always decreases the computed value of D_e, decreasing agreement of computed and measured equilibrium constants.

In conclusion, we have shown that using the HORR approximation gives a partition function too small for these weakly bound complexes. Treating the dissociative mode as a Lennard-Jones 6-3 potential because of the high anharmonicity makes minor improvement, but only the first three or four states are important. Most of the improvement of the LJ63+5HR model comes from treating the remaining soft modes as hindered rotors with appropriate barriers and spin statistics. Some of the improvement also comes from the fact that hindered rotor modes have lower zero-point energies than harmonic modes with the same frequency, and this fact increases the binding energy of the complex and increases the equilibrium constant.

Greater accuracy will require more information about the shape and positions of the barriers and coupling between these modes. However, these envisioned improvements will probably help quantitatively predict equilibrium concentrations of

reactive radical-water complexes. The recent paper by Khan et al.[164] suggested that up to 17% of radicals are complexed with water. Although we did not calculate percentages of complexed radicals quite this high (less than 1%), if these complexes, as suggested by experiments are as much as 100 times more reactive, understanding these effects will be required for informed air pollution policies and improvements in human health.

Although this study has only examined hydrogen-bonded complexes of water with peroxy radicals, the LJ63+5HR model should be applicable to other hydrogen-bonded complexes involving closed shell polar molecules with water and also polar species with ammonia. Moreover, the model is generalizable to ion-molecule or van del Waals complexes by adjusting the LJ *m-n* parameters to match the long-range potential behavior and equilibrium separation.

;

Chapter 3

Computational Study of the Thermodynamics of New Particle Formation Initiated by Complexes of H_2SO_4-H_2O-NH_x, CH_3SO_3H-H_2O-NH_x, and HO_2-H_2O-NH_x

3.1 Disclaimer

The following chapter is presented in its entirety (with minor changes) from the published version of the paper in ACS Earth and Space Chemistry. Burrell, E.; Kar, T. and Hansen, J.C., Computational study of the thermodynamics of new particle formation initiated by complexes of H_2SO_4-H_2O-NH_x, CH_3SO_3H-H_2O-NH_x, and HO_2-H_2O-NH_x. *ACS Earth and Space Chemistry*, **2019**, http://doi.org/10.1021/acsearthspacechem.9b00120. I wrote the paper, performed all computational calculations except for a few electron density maps, and reviewed the paper. Dr. Tapas Kar performed most of the calculations to create the electron density maps. Dr. Jaron C. Hansen reviewed and edited the work.

3.2 Abstract

Exposure to high concentrations of particulate matter has been linked to an increase in asthma, heart problems and death. This link has increased the importance of understanding particle formation and its role in the atmosphere. Research has shown

that measured particle concentrations are often higher than modeled concentrations in the atmosphere. This discrepancy is caused by unknown mechanisms that lead to particle formation. Classical nucleation theory (CNT) is one theory used to explain new particle formation. The first step in forming a particle according to CNT is agglomeration of molecules around a nucleating site. CNT has been successfully applied to modeling new particle formation using sulfuric acid and ions as nucleating sites. This article presents computational support for the use of CH_3SO_3H and HO_2 radical as nucleating sites for new particle formation. Recent studies have shown increased particle formation rates via ions and neutral molecules with the addition of amines to the reaction mixture. We have investigated the reaction of HO_2 radical with four different amines and water vapor. Our results illustrate the stabilizing effect of amines in particle formation. These results suggest that the reaction between CH_3SO_3H and amines as well as HO_2 radical and amines in the presence of water vapor may serve as a viable mechanism for new particle formation in the atmosphere.

3.3 Introduction

Ultrafine particles (UFPs) affect everyday life including air quality, human health, visibility and the earth's radiation balance[3, 4, 8, 165]. Numerically the most abundant type of particle in the atmosphere are UFPS, but they contain the least amount of mass when compared to all other particle types and are generally modeled as having diameters less than 0.01 μm [2]. Evidence suggests that due to the UFPs small

diameters it is possible for them to be inhaled deeply into the lungs and enter into the blood streams leading them to be more toxic than larger diameter particles [3, 7, 166, 167]. Most UFPs precursors are emitted into the atmosphere from both biogenic and anthropogenic sources such as mobile emissions[19, 168-170].

Classical Nucleation Theory (CNT) has historically been used to describe the formation of UFPs from gas phase precursors[11, 23-25, 171, 172] starting with the formation of a molecular cluster, also known as the nucleating site. However, the formation of a molecular cluster can be difficult to understand experimentally on a molecular scale. Several studies have successfully applied high level *ab initio* calculations to better understand the thermodynamics of molecular cluster formation[100, 173, 174]. This computational approach has been used on previous prototypical systems such as H_2SO_4 (sulfuric acid)[175, 176] and CH_3SO_3H (methane sulfonic acid, MSA)[38, 173]complexed with water and amines.

Sulfuric acid (H_2SO_4) is one of the most extensively studied prototypical system for particle formation and upon complexation with water acts as a precursor for formation of particles in the atmosphere[98, 177-181]. Curtius et al. [23] , Becker and Doring et al[24] and others[173, 178, 182] have proposed particle formation via CNT as a viable source in which particles are formed. Specifically, CNT has described particle formation in which H_2SO_4 and other precursors, such as ions, interact with water vapor to form a molecular cluster or nucleation site[183-190]. It has been reported that the thermodynamics of ion-

induced nucleation is more favorable in contrast to neutral molecule induced-nucleation [23]. It is important to note that radicals, such as they hydroperoxy radical (HO_2), have yet to be included in atmospheric models as possible precursors to molecular clusters associated with the CNT model.

Analogous to studies that utilized the H_2SO_4-H_2O cluster as the nucleating site, the MSA-H_2O complex has been observed to successfully serve as a nucleating site for particulate formation[39, 45, 100]. The rate of particle formation in both systems is observed to be influenced by the addition of amines[39-41, 191-194]. In particular, methylamine (MA), dimethylamine (DMA), trimethylamine (TMA) and ammonia (NH_3) were observed to produce a 10+ times increase in the rate of particle formation compared to the rate of particle formation in the absence of these amines or ammonia [38, 41, 193, 195]. When comparing the influence of different amines on the rate of particle formation with the inclusion of trace amounts of ammonia, MA, DMA, TMA, the measured rate enhancement depended on the system[192, 193, 196, 197]. For example, using H_2SO_4 and water vapor, it was observed that DMA and TMA had the greatest influence on the rate of particle formation followed by MA and lastly NH_3[41]. In contrast using MSA and water vapor, MA had the greatest influence on the rate of particle formation followed by DMA, TMA and lastly NH_3. To better understand the change on the rate of particle formation with the addition of amines to the MSA system a mechanism was suggested for particle growth based on a computational analysis that included the binding

energies, Gibbs free energies and enthalpy of formation for formation of the initial molecular complexes[38]. Findings suggest that amines can play a critical role in new particle formation, but with the inclusion of these mechanisms into atmospheric models there still exists a difference between measured and modeled particulate matter concentrations[196, 198, 199]. This has led to the suggestion that other molecules found in the atmosphere could serve as nucleating sites for particle formation.

HO_2 is an abundant radical in the atmosphere with an average ambient air concentration of 10^8 molecules cm^{-3} , and, coupled with its strong binding energy with water [103, 120], is an ideal candidate for serving as the nucleating site for new particle formation. Using the equilibrium constant measured by Kanno et al.[200] for the formation of the HO_2-H_2O complex, coupled with a HO_2 concentration of 10^9 molecules cm^{-3} and a water vapor concentration 9.2 x 10^{17} molecules cm^{-3} (100%, relative humidity at 298 K), 48% of HO_2 is complexed with water vapor, which equates to ~5 x 10^8 molecules cm^{-3} of potential nucleating sites. This calculation represents an upper limit on the ability of the HO_2-H_2O complex to initiate particle formation, but even if only 1% of the complexes form aerosol particles, it would contribute ~5 x 10^6 cm^{-3} of new nucleating sites in the atmosphere.

In an analogous way that the H_2SO_4-H_2O complex and MSA-H_2O complex can serve as nucleating sites for new particle formation, HO_2-H_2O complexed with amines may also serve as the seed for new particle formation. Like the H_2SO_4-H_2O complex and

MSA-H_2O complex, the HO_2-H_2O complex has been detected in laboratory studies[102, 104] and contains a strong binding energy of 31.4 kJmol^{-1}. Although the HO_2-H_2O complex has a smaller binding energy than the H_2SO_4-H_2O and MSA-H_2O complexes the addition of an amine or NH_3 may further stabilize the HO_2-H_2O complex making it competitive as a possible nucleating seed for particle formation. This mechanism is examined in this manuscript

The goal of this work is to better understand secondary particle formation in the atmosphere by extending the use of amines in particle formation from the prototypical systems, H_2SO_4-H_2O and MSA-H_2O to the non-prototypical HO_2-H_2O system. The thermodynamics of particle formation using the atmospherically abundant hydroperoxy (HO_2) radical complexing with water vapor and amines is presented. Data from this computational study provides a better understanding on the molecular scale about the process in which H_2SO_4, MSA and HO_2 in the presence of water vapor and TMA can serve as nucleating sites for new particle formation.

3.4 Computational Method

The Gaussian 09, Revision 5.0.8[201] suite of programs was used for geometry optimizations, vibrational frequency calculations, and high-level configuration interaction molecular energy calculations. Initial optimization of the monomer structures for each complex began with a M06-2X/6-311++G (d,p) level geometry optimization. The M06-2X level is regarded as one of the best density functional

theories involving thermochemistry, kinetics and non-covalent interaction calculations[202, 203]. The purpose of this initial step was to quickly generate initial force constants in the G09 environment and to decrease the overall computation time. The geometry of each monomer structure was then refined at the M06-2X/aug-cc-PVDZ level. The energy of the optimized structure was then refined with a CCSD (T)/aug-cc-PVDZ single-point calculation from the optimized geometries determined using the M06-2X/aug-cc-PVDZ level.

The minimum energy geometry for the global and local minima for each complex was generated and identified by a wide-ranging random constrained sampling (RCS) methodology[204]. The global and local minima for each complex was fully optimized using the M06-2X/aug-cc-PVDZ level and further refined with a CCSD (T)/aug-cc-PVDZ single-point calculation using the optimized geometries determined using the M06-2X/aug-cc-PVDZ method and basis set.

The random constrained sampling (RCS) method was used to generate the HO_2-H_2O-amine, MSA-H_2O-amine and H_2SO_4-H_2O-amine complex geometries. Briefly, the RCS method generates HO_2-H_2O complex geometries by randomly packing a H_2O molecule within a 3.5 Å constrained radius sphere encompassing the entire radical or a user-defined portion of the optimized HO_2 structure. In this work, the overall optimized complex geometries were determined via two iterations of the RCS method. The first iteration generated 1000 HO_2-H_2O geometries by placing a H_2O molecule around a 3.5 Å

radius sphere centered over the entire radical structure. The second iteration produced 1000 HO_2-H_2O-amine complex geometries that involved placing the optimized geometry of an amine or NH_3 around a 3.5 Å radius sphere centered over the entire optimized minimum energy geometry of the HO_2-H_2O complex. Both iterations followed a geometry and energy optimization scheme identical to that used for the identification of the radical lowest energy structure.

The harmonic vibrational frequency calculations were performed from the M06-2X/aug-cc-PVDZ level and confirmed each structure as a minimum. Additional thermodynamic calculations were performed using the optimized geometries identified using the M06-2X/aug-cc-PVDZ level. Binding energies were calculated from the CCSD (T)/aug-cc-PVDZ level. The anharmonic frequency calculations were performed using the M06-2X/aug-cc-PVDZ level.

Electron density maps with a surface resolution of 0.0003 e/au^2 were generated using the results from the M06-2X/aug-cc-pVDZ level for the HO_2-H_2O-amine complexes. HO_2, H_2O and amine monomer electron density maps were subtracted from the electron density map computed for each complex to produce an electron density difference map showing how the electron density is perturbed as a result of complex formation.

3.5 Results and Discussion

3.5.1 Geometry of Complexes and Monomers

Table 3.1: Bond lengths and angles of the complexes.

Complex[a]	Interactions	Bond length(Å)	Angles (°)
H_2SO_4-H_2O (2A)	O-H…O(water)	1.65	163.2
	O-H(water)…O	2.11	129.2
H_2SO_4-H_2O-TMA(3D)	O-H…O(water)	1.45	176.2
	O-H(water)…N	1.68	175.2
HO_2-H_2O(2B)	O-H(radical)…O	1.79	144.5
	O…H-O(water)	2.23	114.3
HO_2-TMA(2F)	O-H(radical)….N	1.61	164.3
HO_2- H_2O TMA (5D)	O-H(water)…O	1.86	175.6
	O-H(radical)…N	1.52	177.5
	C-H…O(water)	2.32	141.7
HO_2-DMA(2E)	O-H(radical)…N	1.62	162.9
HO_2- H_2O DMA (5C)	O-H(water)…O	1.86	167.5
	O-H(radical)…N	1.52	172.4
	N-H…O(water)	2.08	128.7
HO_2-MA(2D)	O-H(radical)…N	1.65	159.6
HO_2- H_2O -MA (5B)	O-H(water)…O	1.87	167.7
	O-H(radical)…N	1.55	169.5
	N-H…O(water)	2.08	127.8
HO_2-NH_3 (2C)	O-H(radical)…N	1.70	157.6
	N-H…O(radical)	2.61	84.56
HO_2- H_2O -NH_3- (5A)	O-H(water)…O	1.88	166.4
	O-H(radical)…N	1.61	173.2
	N-H…O(water)	1.98	143.3
MSA-H_2O(2H)	O-H(MSA)…O(water)	1.68	164.1
	O-H(water)…O	1.99	134.5
MSA-H_2O-TMA(4A)	O-H(MSA)…O(water)	1.44	170.8
	O-H(water)…N	1.63	173.7
[a] Structures are shown in Figures 3.2-3.5			

Geometries and rotational constants for each monomer (H_2SO_4, MSA, HO_2, H_2O, NH_3, MA, DMA and TMA) and the Amine-HO_2, H_2SO_4-H_2O, MSA-H_2O, MSA-H_2O-TMA, H_2SO_4-H_2O-TMA, HO_2-H_2O, and HO_2-H_2O-Amine complexes are given in supplemental table 1, table 3.1 and Figures 3.1-3.5. Vibrational frequencies are given in supporting materials. Generally, a range of van der Waal's interactions are responsible for holding the molecular clusters together. In particular hydrogen bonds play an important role in the stability of a molecular cluster. The stronger the hydrogen bond or the increased number of hydrogen bonds in the system increases the overall stability of the molecular cluster. Typically, the closer a hydrogen-bond angle is to 180° the larger the molecular overlap and consequently the stronger the hydrogen bond interaction[205]. The hydrogen bonds in the H_2SO_4-H_2O complex have angles ranging from 129°-163° (Figure 3.2A and Table 3.1). The addition of either an amine or NH_3 to the complex increases these bonding angles, specifically; the addition of TMA increases the binding angles to ~176°. The hydrogen bonds in the MSA-H_2O complex have similar angles ranging from 134-164° (Figure 3.2H and Table 3.1). With the addition of TMA, the binding angles between the O-H of the water and N of TMA increases to 173° (Figure 3.4A). In these prototypical systems the addition of either TMA or NH_3 increases the stability of the hydrogen bonds and overall complex. A similar approach to these prototypical systems was extended to HO_2 complexed to H_2O, an amine and NH_3. The five HO_2 complexes included in this work are: HO_2-TMA, HO_2- DMA, HO_2- MA, HO_2-

NH_3 and HO_2-H_2O. These complexes were analyzed to determine if the starting complex influences the overall stability of the HO_2-H_2O-amine complex. The hydrogen bond angles in the HO_2-TMA complex is 164°(Figure 3.2F and Table 3.1) which is consistent with the H_2SO_4-H_2O and MSA-H_2O prototypical systems. The addition of a H_2O molecule to the HO_2-TMA complex changes the hydrogen bond angle between the nitrogen atom in TMA and the hydrogen in HO_2 in this complex and drives the angle from 175.6°to 177.5°and introduces and additional hydrogen bond. Likewise, the HO_2-

NH_3 complex has a hydrogen bond that forms between the nitrogen of NH_3 and the hydrogen in HO_2. With a bond angle of 157.6° in the dimer with the addition of a water molecule increases the angle to 173.2°. An increase in the hydrogen bond angle is also

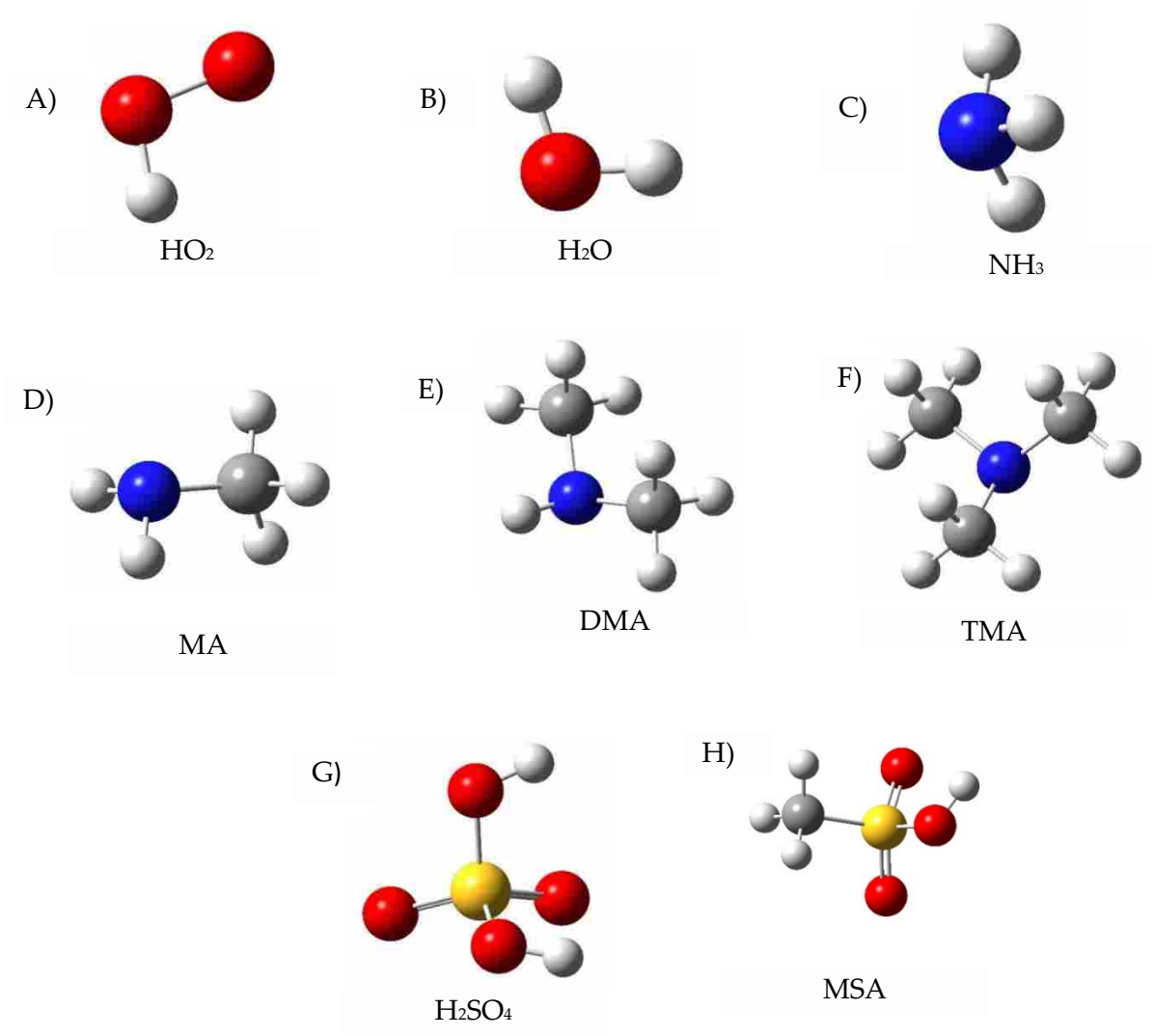

Figure 3.1: Optimized geometries of the monomer at the M062x/aug-cc-pVDZ level. A-Hydroperoxy radical. B-water molecule C- Ammonia molecule D- Methyamine molecule E- Dimethylamine molecule F-Trimethylamine molecule G- Sufuric acid molecule H-Methane sulfonic acid molecule

observed upon addition of H_2O to the HO_2-DMA and HO_2-MA complexes. The hydrogen bond that forms between the nitrogen in DMA and the hydrogen in HO_2 starts with an initial angle of 162.9°and increases to 172.4°with the addition of H_2O. The

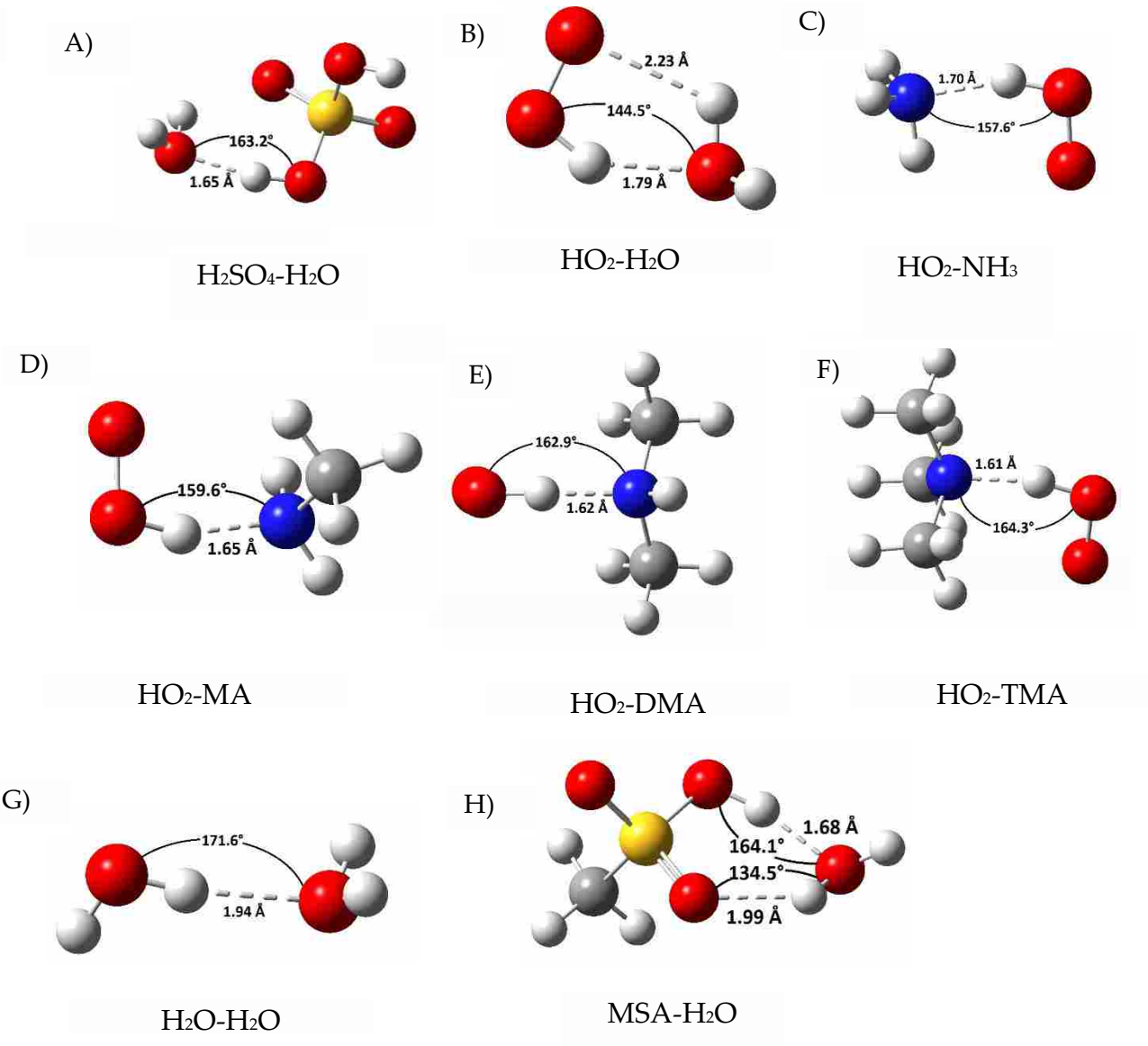

Figure 3.2. Optimized geometry of the dimers at the M062x/aug-cc-pVDZ level: (A) sulfuric acid–water dimer; (B) hydroperoxy radical–water dimer; (C) hydroperoxy radical–ammonia dimer; (D) hydroperoxy radical–methyamine dimer; (E) hydroperoxy radical-dimethylamine dimer; (F) hydroperoxy radical–trimethylamine dimer; (G) water–water dimer; (H) methanesulfonic acid–water dimer

HO_2-MA complex follows this same pattern and starts with a hydrogen bond angle of 159.6° between the nitrogen in MA and the hydrogen in HO_2 and increases to 169.5° with the addition of H_2O to the complex. The hydrogen bond angles in the HO_2-H_2O complex range from 114°-144°. With the addition of an amine or NH_3 to the HO_2-H_2O complex results in the same changes in the hydrogen-bond angles as what is observed in the other complexes. Namely the angle increases to become closer to 180°. The increase in the hydrogen bond angle in each of these complexes has the overall effect of improving the strength of the hydrogen bond which further stabilizes each complex. Stabilization of the complex by addition of an amine suggests that the HO_2-H_2O-amine complexes, like the H_2SO_4-H_2O-amine and MSA-H_2O-amine complexes, have an increased capability of acting as a nucleating site for new particle formation relative to just the HO_2 -amine complexes. Further analysis of binding energies, enthalpy data, dipole moments and electron density maps further corroborate the increased stability of the HO_2-H_2O-amine complexes and possibility of acting as a nucleating site for particle formation.

3.5.2 Thermodynamic Results

Complex Binding Energies

As shown in recent publications, the inclusion of trace concentrations of amines or NH_3 enhances the formation of UFPs using the H_2SO_4-H_2O and MSA-H_2O complexes as nucleating sites[41, 173]. Changes in the hydrogen bond angles with the inclusion of an amine into the H2SO4-H_2O, MSA-H_2O and HO_2-H_2O complexes indicate a stronger hydrogen bond formation which increases binding energies. While the H_2SO_4-H_2O complex has a strong binding energy of 50.8 kJ mol^{-1} the H_2SO_4-H_2O-DMA and H_2SO_4-H_2O-TMA complexes, figure 3.3C and figure 3.3D, have an increase in binding energy

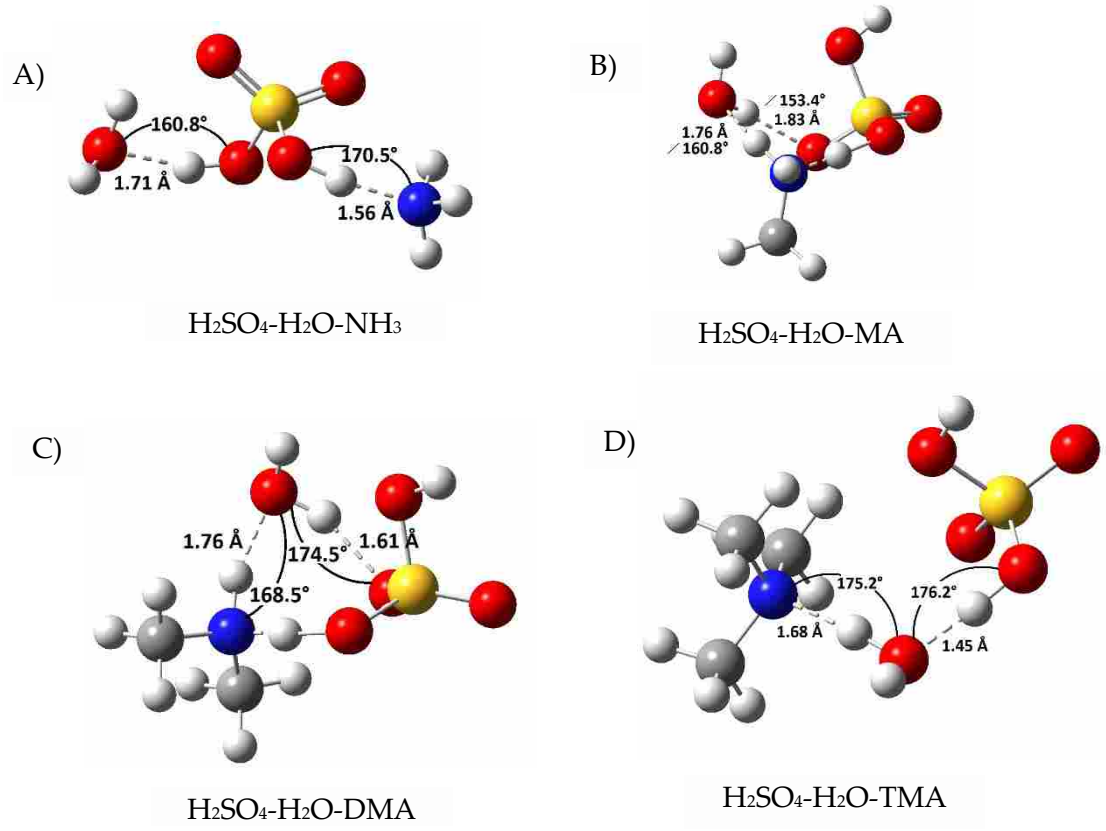

H_2SO_4-H_2O-NH_3 H_2SO_4-H_2O-MA

H_2SO_4-H_2O-DMA H_2SO_4-H_2O-TMA

Figure 3.3: Optimized geometries of H_2SO_4-Amines-H2O complexes at the M062x/aug-cc-pVDZ level. A- Sulfuric acid-water-ammonia complex. B- Sulfuric acid-water-methylamine complex C- Sulfuric acid-water-dimethylamine complex D- Sulfuric acid-water-trimethylamine complex

with the addition of the amines. The complexes are more strongly bound by comparison and have binding energies of 146.5 kJ mol^{-1} (Complex 3.3C) and 139.12 kJ mol^{-1} (Complex 3.3D). Likewise, the MSA-H_2O complex has a binding energy of 44.35 kJ mol^{-1} but the addition of an amine or NH_3increases the overall binding energies. Specifically, the MSA-H_2O-TMA (Figure 3.4A) and MSA-H_2O-DMA (Figure 3.4B) are more strongly bound with binding energies of 103.77 kJ mol^{-1} and 106.7 $kJmol^{-1}$. The increased binding energies of the complexes upon inclusion of an amine can be attributed to the increased hydrogen bonding energies and number of hydrogen bonds.

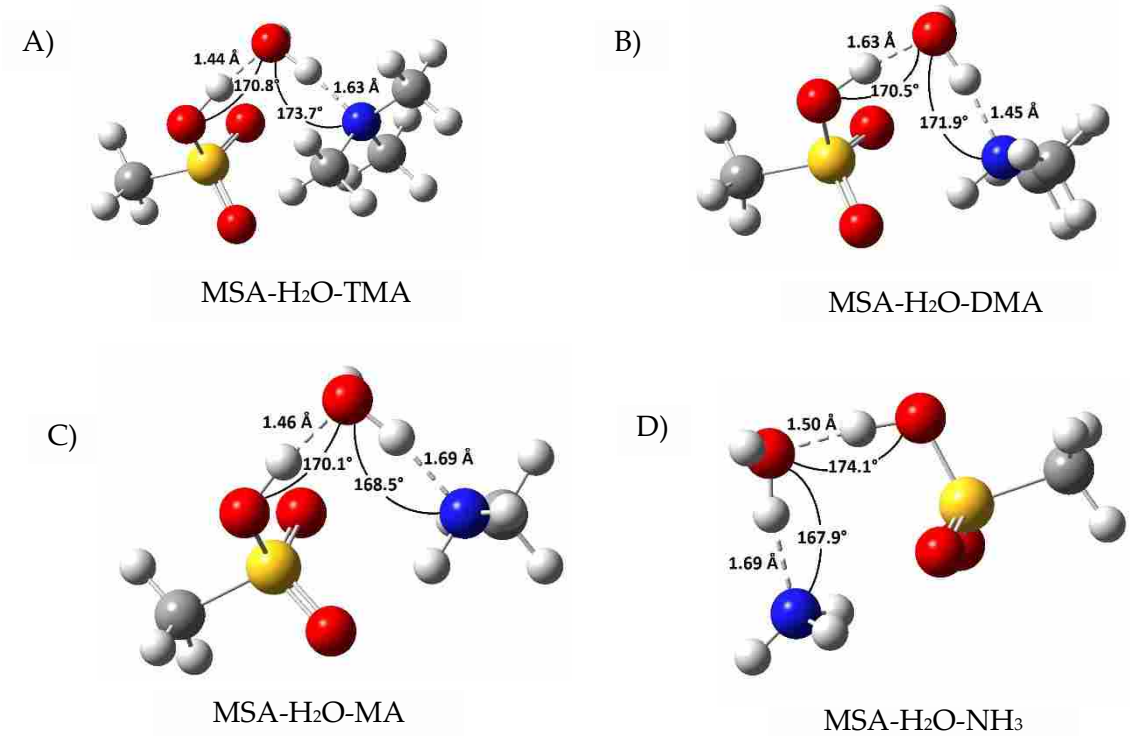

Figure 3.4: MSA-Amines-H_2O complexes at the M062x/aug-cc-pVDZ level. A- Methane sulfonic acid-water-trimethylamine complex. B- Methane sulfonic acid-water-dimethylamine complex C- Methane sulfonic acid-water-methylamine complex D- Methane sulfonic acid-water-ammonia complex

Included in the Glasoe et al.[41] and Finlayson-Pitts et al.[38] studies were a comparison of the binding energies for the following complexes: H_2SO_4-H_2O-TMA, H_2SO_4-H_2O-DMA, H_2SO_4-H_2O-MA, H_2SO_4-H_2O-NH_3 and MSA- H_2O -TMA, MSA- H_2O -DMA, MSA- H_2O -MA, MSA- H_2O -NH_3. A pattern emerges when comparing the binding energies of the H_2SO_4- H_2O-amine/NH_3 complexes to one another (Figures 3.3(A-D)). As the number of methyl groups increase on the central nitrogen atom there is an increase in the binding energies except for the increased binding energy of DMA

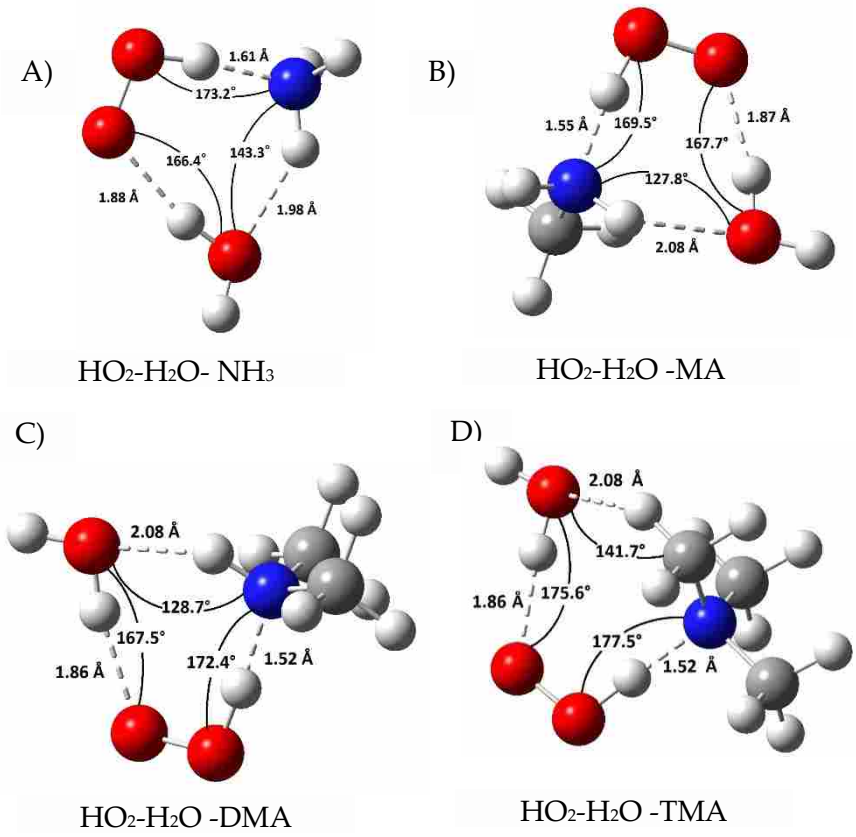

Figure 3.5: HO_2-Amines-H_2O complexes at the M062x/aug-cc-pVDZ level. A- Hydroperoxy radical-water-ammonia complex. B- Hydroperoxy radical-water-methylamine complex C- Hydroperoxy radical-water-dimethylamine complex D- Hydroperoxy radical-water-trimethylamine complex

over TMA. A similar pattern is observed with the MSA-H_2O-amine/NH_3 complexes (Figure 3.4(A-D)) however, it is found that MA and DMA have larger binding energies when compared to complexes formed with TMA and NH_3. Comparison of the H_2SO_4-H_2O-TMA, H_2SO_4-H_2O-DMA, H_2SO_4-H_2O-MA or H_2SO_4-H_2O-NH_3 complex to the analogous MSA-H_2O-TMA, MSA-H_2O-DMA, MSA-H_2O-MA or MSA-H_2O-NH_3 complex shows the H_2SO_4-H_2O-amine/NH_3 complexes all have stronger binding energies than their MSA-H_2O-amine/NH_3 counterpart. This can be attributed to the increased number of hydrogen bonds found in the H_2SO_4-H_2O-amine/ NH_3 complexes that are not formed when complexing with MSA.

Francisco et al[103], reported a binding energy for the H_2O-HO_2 complex to be 25.10 kJ mol^{-1} (Figure 3.2B) which is weaker than the H_2SO_4-H_2O binding energy of 50.8kJ mol^{-1} (Figure 3.2A) and MSA-H_2O binding energy of 44.4 kJ mol^{-1}, but stronger than the H_2O-H_2O binding energy 11.37 kJ mol^{-1} (Figure 2G). Overall the H_2SO_4-H_2O-amine/NH_3 complexes have stronger binding energies than the analogous HO_2-H_2O-amine/NH_3 complexes. When comparing the binding energy trend of the H_2SO_4-H_2O-amine/NH_3 complexes with the HO_2-H_2O-amine/NH_3 complexes a similar trend exists with one exception, TMA.

The trend in binding energies shows that as the number of methyl groups increases in

Table 3.2: Binding energies and corrected binding energies of the dimers HO_2-H_2O-amine/NH_3, MSA-H_2O-amine/NH_3 and H_2SO_4-H_2O-amine/NH_3 complexes.

Complex	Binding Energies (kJ mol^{-1})	Binding Energies with ZPE (kJ mol^{-1})
H_2O-H_2O (2G)	-11.37	-21.97
HO_2-H_2O (2B)	-31.41	-43.61
TMA-HO_2(2F)	-67.49	-57.45
DMA-HO_2(2E)	-65.27	-55.06
MA-HO_2(2D)	-59.37	-50.33
NH_3-HO_2(2C)	-51.92	-40.92
MSA-H_2O(2H)	-55.56	-44.35
H_2SO_4-H_2O(2A)	-61.55	-50.75
HO_2-H_2O-TMA (5D)	-103.68	-85.86
HO_2-H_2O-DMA (5C)	-107.03	-88.95
HO_2-H_2O-MA (5B)	-101.59	-83.30
HO_2-H_2O-NH_3 (5A)	-93.30	-71.55
MSA-H_2O-TMA(4A)	-119.08	-103.76
MSA-H_2O-DMA(4B)	-122.63	-106.69
MSA-H_2O-MA(4B)	-120.65	-105.23
MSA-H_2O-NH_3 (4B)	-113.99	-95.17
H_2SO_4-H_2O-TMA(3D)	-162.59	-139.12
H_2SO_4-H_2O-DMA(3C)	-167.19	-146.52
H_2SO_4-H_2O-MA(3C)	-154.56	-134.01
H_2SO_4-H_2O NH_3 (3C)	-132.47	-114.26

the amine the binding energies with H_2SO_4 and HO_2 also increases with the exception of TMA which only has a slightly stronger binding energy than MA. HO_2-H_2O-TMA has a binding energy of 85.86 kJ mol^{-1} which is only 2.5 kJ mol^{-1} stronger than the HO_2-H_2O-MA complex with a binding energy of 83.30 kJ mol^{-1}. Whereas HO_2-H_2O-DMA has a binding energy of 88.95 kJ mol^{-1}. All of which have stronger binding energies than HO_2-H_2O-NH_3 which has a binding energy of 71.55 kJ mol^{-1}. TMA, DMA and MA have

stronger binding energies than NH_3 due to the methyl groups attached to the nitrogen. These methyl groups are electron donating to the nitrogen. Thus, making the nitrogen on the TMA, DMA and MA more electronegative and consequently forming a stronger hydrogen bond with the hydrogen from HO_2 then NH_3. DMA and MA also have the ability to form additional hydrogen bonds which is lost with the three methyl groups found in TMA (Figure 3.1F) which accounts for the decrease in binding energy of TMA. DMA and MA have stronger binding energies due to the additional H-bond and the CH_3 electron donating groups. Even though TMA has electron donating groups as well the nitrogen does not have the spare hydrogen so HO_2 does not make the additional H-bond instead it makes a weaker CHO bond which leads to a lower binding energy. This loss of hydrogen bonding capability helps to account for the sequentially lower binding energy of TMA in the HO_2-H_2O-amine/NH_3 complex series.

Enthalpy, Entropy and Gibbs Free Energy

The Gibbs free energy ($\Delta G°$) and enthalpy ($\Delta H°$) of formation was calculated for each complex. $\Delta H°$ is related to the binding energies in that the corrected internal energy of the system used to find the binding energies has been adjusted from the Gaussian files. $\Delta H°$ was calculated from the total corrected internal energy of the system and corrected for the Boltzmann constant and temperature (eq. 1)[206]:

$$\Delta H° = \Delta E_{tot} + k_B T \qquad \text{(eq. 1)}$$

The Gibbs free energy data was also mined from the Gaussian files where $\Delta G°$ was calculated from $\Delta H°$, total internal entropy (ΔS_{tot}) and temperature (eq. 2)[206]:

$$\Delta G° = \Delta H° - T\Delta S_{tot} \qquad \text{(eq. 2)}$$

These calculations allow for a better understanding of the potential pathways for new particle formation and allows for a comparison between the Gibb's free energy and enthalpy of formation of prototypical systems (H_2SO_4-H_2O-amine/NH_3 and MSA-H_2O-amine/NH_3) and the HO_2-H_2O-amine/NH_3 system. Table S2 shows that with the addition of an amine to the HO_2-H_2O complex $\Delta G°$ becomes increasingly negative. The thermodynamics of complex formation becomes more favorable with the addition of H_2O, amine/NH_3 or radical and results in driving particle formation. The enthalpy of H_2SO_4-H_2O complex formation is -54.49 kJ mol^{-1} which is a factor of 3.24 larger than the enthalpy of formation of H_2SO_4-TMA (-16.82 kJ mol^{-1}). When an amine or H_2O molecule is added to the H_2SO_4-TMA complex, the enthalpy of formation increases to -107.04 kJ mol^{-1}. The Gibbs free energy for the H_2SO_4-TMA and H_2SO_4-H_2O dimers are significantly lower, -22.64kJ mol^{-1} and -12.26 kJ mol^{-1} respectively. Indicating that particle formation via the H_2SO_4-H_2O-TMA complex is enthalpically driven. In comparison $\Delta H°$ of the MSA-H_2O dimer is -48.12 kJ mol^{-1} which is approximately

double of the enthalpy of formation of MSA-TMA (-28.11 kJ mol^{-1}). However, the addition of a trimethylamine or H_2O molecule to the MSA-H_2O complex increases the overall ΔH to -108.10 kJ mol^{-1}. $\Delta G°$ of the MSA- H_2O and MSA-TMA dimers are significantly lower, -6.41 kJ mol^{-1}, and -17.92 kJ mol^{-1} respectively. Extending this trend to the non-prototypical HO_2-H_2O-amine/NH_3 system, the $\Delta H°$ of the HO_2-H_2O is -35.55 kJ mol^{-1} and -59.20 kJ mol^{-1} for the HO_2-TMA dimer. Upon addition of an amine or H_2O molecule to the complex $\Delta H°$ increases to -89.47 kJ mol^{-1}, a gain of approximately 29.29 kJ mol^{-1} and consequently further stabilizing the complex. The $\Delta G°$ of the HO_2-TMA and HO_2-H_2O dimers are significantly smaller, -14.39 kJ mol^{-1} and 3.28 kJ mol^{-1} respectively. Even though $\Delta G°$ for HO_2-H_2O indicates particle formation in unfavorable it is interesting to note that with the addition of an amine or NH_3 new particle formation becomes favorable. Like the H_2SO_4 and MSA systems, particle formation via the HO_2-H_2O-TMA complex is enthalpically driven. However, when compared to MSA and H_2SO_4, $\Delta G°$ of formation is less favorable unless an amine or NH_3 is present. This can be attributed to the increased polarity and hydrogen bonding strength which influences $\Delta G°$ for the reaction resulting in the formation of a more thermodynamically favorable nucleating site. From the enthalpy and Gibbs free energy data the entropy of complex formation can be calculated (table 3.4). Evaluation of the entropy of complex formation data indicates as expected that complex formation is an entropically unfavorable reaction.

To refine the calculated enthalpy, entropy and Gibb's free energy of HO_2-H_2O-amine/NH_3 complex formation, anharmonic calculations were performed for the HO_2-H_2O-amine/NH_3 complexes including local and global minima (SI Fig 1) using the M06-2X-aug-cc-PVDz method and basis set. Anharmonic frequency calculations were

Table 3.3: Anharmonic calculations of Gibbs free energy, Entropy and Enthalpy of the complex at the global and local minima's

Complexes	ΔG (kJ mol^{-1})	ΔH (kJ mol^{-1})	ΔS (kJ mol^{-1} K)
HO_2-H_2O (2B)	2.21	-35.89	-0.13
HO_2-TMA (2F)	-14.95	-59.35	-0.15
HO_2-DMA (2E)	-15.10	-59.42	-0.15
HO_2-MA (2D)	-13.63	-56.21	-0.14
NH_3-HO_2(2C)	-10.75	-49.07	-0.13
HO_2-H_2O-TMA _475	-6.61	-89.24	-0.28
HO_2-H_2O-TMA _664	-8.74	-89.44	-0.27
HO_2-H_2O-TMA _274	-3.22	-84.16	-0.27
HO_2-H_2O-TMA _301	-2.24	-79.99	-0.26
HO_2-H_2O-DMA _264	-15.20	-97.63	-0.28
HO_2-H_2O-DMA _345	-6.15	-87.45	-0.27
HO_2-H_2O-DMA _892	-1.35	-82.26	-0.27
HO_2-H_2O-DMA _941	-18.96	-98.29	-0.27
HO_2-H_2O-MA _280	6.00	-88.06	-0.28
HO_2-H_2O-MA _561	-13.47	-95.08	-0.27
HO_2-H_2O-MA _58	-10.36	-90.87	-0.27
HO_2-H_2O-MA _739	-1.65	-83.38	-0.27
HO_2-H_2O-NH_3_136	-0.42	-80.92	-0.27
HO_2-H_2O-NH_3_365	2.93	-72.16	-0.25
HO_2-H_2O-NH_3_408	-5.58	-86.00	-0.27
HO_2-H_2O-NH_3_608	-4.75	-84.44	-0.27

performed to account for the increase in populated vibrational energy levels. Harmonic $\Delta G°$ for the HO_2-H_2O-TMA complex were found to range from -0.64 to -7.12 kJ mol^{-1} whereas the $\Delta G°$ calculated using the anharmonic calculated frequencies increased in range from -2.24 to -8.74 kJ mol^{-1}. Harmonic $\Delta G°$ for the HO_2-H_2O-DMA complex were

found to range from 0.70 to -16.33 kJ mol^{-1} which is larger when compared to the TMA complexes range. A similar pattern was found for the HO_2-H_2O-DMA complex ΔG° calculated using anharmonic frequencies which increased the range from -1.35 to -17.97 kJ mol^{-1}. This pattern of increased spontaneity as seen in ΔG° using the anharmonic frequencies is seen with the NH_3 and MA complexes (table 3.3).

To further understand the overall increase of ΔG° the harmonic and anharmonic calculations of ΔH° and ΔS° of the complexes were analyzed and compared. Harmonic ΔH° for the HO_2-H_2O-TMA complex were found to range from -79.70 to -89.13 kJ mol^{-1} whereas the anharmonic ΔH° increased in range from -79.99 to -89.44 kJ mol^{-1}. Harmonic ΔH° for the HO_2-H_2O-DMA complex were found to have an increased harmonic range from -81.76 to -97.81 kJ mol^{-1} compared to the TMA complexes range. A similar pattern was found for the HO_2-H_2O-DMA Anharmonic ΔH° which increased in range from -82.26 to -98.29 kJ mol^{-1}. A similar pattern is seen with the MA complex where the anharmonic ΔH° has an increased negative value when compared to the harmonic calculations (table 3.3 and 3.4). Unlike MA, TMA and DMA the NH_3 complexes showed no change in the enthalpy.

Like ΔG° and ΔH° the amine-radical-water complexes had a similar pattern for ΔS° where the anharmonic calculations increased in comparison to the harmonic calculations (table

3.4). As expected, the anharmonic vibrational frequencies are more populated then the harmonic vibrational frequencies leading to an increased stability of the complexes.

The addition of these compounds leads to an increased stability which is highlighted by the decrease in the overall enthalpy of the complex. However, it should be noted that even though these complexes appear stable until the critical diameter size is met there will be an adsorption/desorption of the compounds and not all subsequent complexes are increasingly stable. As shown with the HO_2-amine/NH_3 intermediate complex the loss of water decreases the overall stability of the complex and makes this

Table 3.4: Harmonic calculations of Gibbs free energy, Entropy and Enthalpy of the complex at the global and local minima's

Complex	ΔG° (kJ mol^{-1})	ΔH° (kJ mol^{-1})	ΔS° (kJ mol^{-1} K)
HO_2-H_2O (2B)	3.28	-35.55	-0.13
HO_2-TMA (2F)	-14.39	-59.20	-0.15
HO_2-DMA (2E)	-14.59	-59.18	-0.15
HO_2-MA (2D)	-13.06	-55.25	-0.14
HO_2-NH_3 (2C)	-10.53	-49.04	-0.13
HO_2-H_2O-TMA _475	-1.13	-21.27	-0.07
HO_2-H_2O-TMA _664	-1.70	-21.30	-0.07
HO_2-H_2O-TMA _274	-0.15	-20.08	-0.07
HO_2-H_2O-TMA _301	-0.19	-19.05	-0.06
HO_2-H_2O-DMA _264	-3.05	-23.20	-0.07
HO_2-H_2O-DMA _345	-1.05	-20.82	-0.07
HO_2-H_2O-DMA _892	0.17	-19.54	-0.07
HO_2-H_2O-DMA _941	-3.90	-23.38	-0.07
HO_2-H_2O-MA _280	-1.06	-20.77	-0.07
HO_2-H_2O-MA _561	-2.59	-22.40	-0.07
HO_2-H_2O-MA _58	-1.94	-21.41	-0.07
HO_2-H_2O-MA _739	0.05	-19.63	-0.07
HO_2-H_2O-NH_3_136	0.18	-19.34	-0.07
HO_2-H_2O-NH_3_365	1.08	-17.25	-0.06
HO_2-H_2O-NH_3_408	-0.99	-20.55	-0.07
HO_2-H_2O-NH_3_608	-0.79	-20.18	-0.07

process less favorable from an enthalpy perspective. However, this intermediate complex can re-hydrate and continue to grow in size with the further adsorption of H_2O, an amine, NH_3 or HO_2.

3.5.3 Dipole Moments

To better understand why MSA, H_2SO_4, and HO_2 can serve as good nucleating agents the dipole moments of the individual monomers and complexes were calculated. The H_2SO_4 monomer has a dipole moment of 3.82 Debye with the positive end of the dipole centered on the sulfur atom and the negative end of the dipole moving towards the oxygen atoms. Figure 3.6 shows H_2SO_4 with its computed dipole moment. The length of the dipole vector is proportional to the magnitude of the dipole moment. When H_2O is added to H_2SO_4 the dipole strength increases to 4.0 Debye. Forming a complex with TMA further increases the dipole moment to 9.0 Debye. With the inclusion of a H_2O molecule to the H_2SO_4-TMA complex to form the H_2SO_4-H_2O-TMA complex the dipole moment decreases to 7.0 Debye. By comparison MSA has a dipole moment of 3.9 Debye. Upon addition of a H_2O molecule to form the MSA-H_2O complex the dipole moment decreases to 3.3 Debye. The addition of H_2O to MSA to form the MSA-H_2O dimer thus decreases the dipole moment by 0.6 Debye while inclusion of H_2O to H2SO4 to form the H_2SO_4-H_2O complex increases the dipole moment by 0.2 Debye indicating that H_2O plays a greater role in increasing the polarity of the H_2SO_4-H_2O complex than it does by complexing with MSA. The addition of TMA to MSA to form

the MSA-TMA dimer also decreases the dipole moment to 3.1 Debye. With the inclusion of a H_2O molecule to the MSA-TMA dimer to form the MSA-H_2O-TMA complex the dipole moment increases to 5.9 Debye. Unlike the H_2SO_4-H_2O-TMA complex the MSA-H_2O-TMA complex has a dipole moment that is larger than the MSA-H_2O and MSA-TMA complexes. By comparison to the prototypical systems the HO_2 radical has a dipole moment of 2.2 Debye. Upon addition of a H_2O molecule to form the HO_2-H_2O complex the dipole moment increases to 3.0 Debye. The addition of H_2O to HO_2 to form the HO_2-H_2O complex thus increases the dipole moment by 0.8 Debye while inclusion of H_2O to H2SO4 to form the H_2SO_4-H_2O complex only increases the dipole moment by 0.2 Debye but decreases the dipole moment for the MSA-H_2O dimer. This indicates that H_2O plays a greater role in increasing the polarity of the HO_2-H_2O complex than it does by complexing with H_2SO_4 or MSA. The addition of TMA to HO_2 to form the HO_2-TMA complex doubles the dipole moment to 4.5 Debye. Like the H_2SO_4-H_2O-TMA complex the HO_2-H_2O-TMA complex has a dipole moment that lies between the HO_2-H_2O and HO_2-TMA complexes. The increase in dipole strength and subsequent polarity with the inclusion of either H_2O or TMA to form complexes with H_2SO_4, MSA and HO_2 indicates

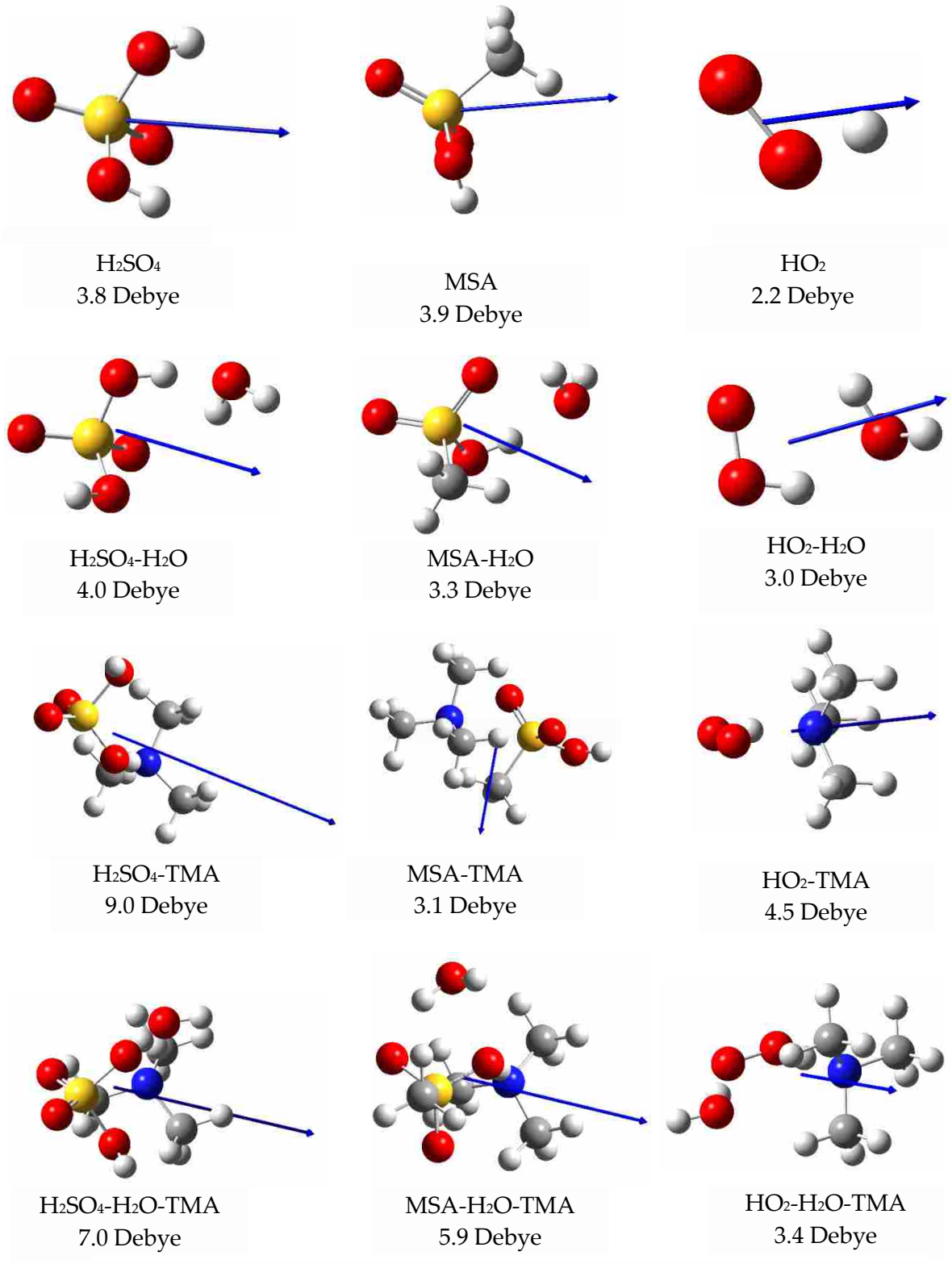

Figure 3.6: H_2SO_4 MSA, HO_2 and complexes with dipole moments and dipole strength

that subsequent growth of the complex by addition of H_2O molecules will not only be

enthalpically favorable but also impact the reaction rate.

3.5.4 Electron Density Maps

To provide additional information about the ability of complexes of HO_2 to serve as a nucleating site for particle formation, the change in electron density as a function of complex formation was computed. Change in electron density maps have been successfully used to show formation of hydrogen bonds in complexes[207]. Electron density difference maps were generated using a contour of 0.0003 e/au^3 with the M06-2X/aug-cc-pVDZ method/basis set[208]. The blue shaded regions in Figure 3.7(A-D) represent areas of electron density gain and red shaded regions represent areas of electron loss as a result of complex formation. A prototypical hydrogen bond is evidenced by a region of electron density redistribution between the hydrogen atom and corresponding atom. Correspondingly, along the axis of the hydrogen bond a region of electron density loss is typically observed around the bridging proton. In the HO_2-H_2O-amine complex's it is expected that a number of hydrogen bonds will form between HO_2 and H_2O, HO_2 and TMA and TMA and H_2O. Prototypical hydrogen bond formation is observed in the HO_2-H_2O-DMA, HO_2-H_2O-MA and HO_2-H_2O-NH_3 complexes. Interestingly, the electron density difference maps (Figure 7(A-D)) indicate a weak interaction between TMA and water.

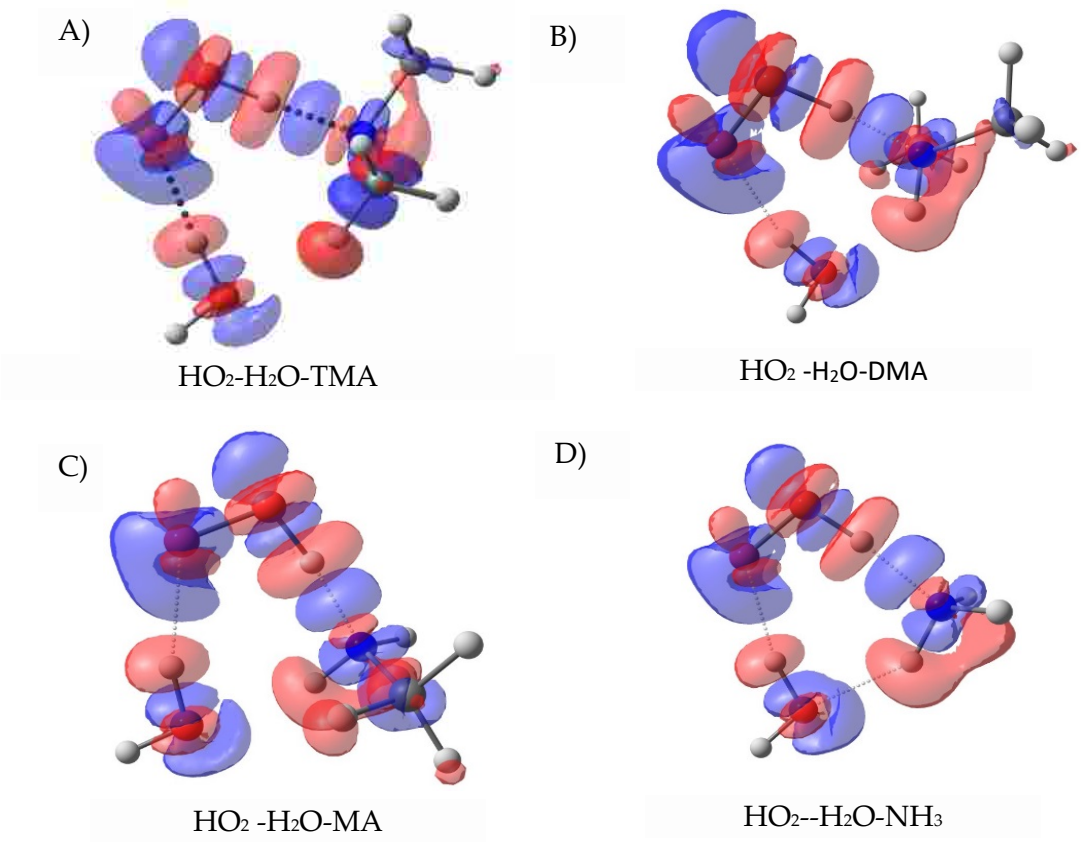

Figure 3.7: Electron density maps of HO_2 -H_2O-Amines complexes A- Hydroperoxy radical-water-trimethylamine complex. B- Hydroperoxy radical-water-dimethylamine complex C- Hydroperoxy radical-water-methylamine complex D- Hydroperoxy radical-water-ammonia complex

3.6 Conclusion

Radicals have been overlooked as a possible pathway for particle formation however the Gibbs free energy of HO_2-H_2O-amine complex formation is favorable and consequently this complex could serve as a nucleating site for particle formation. This is reinforced by comparison of the binding energies, dipole moment strengths and electron density maps for the prototypical systems H_2SO_4-H_2O and MSA-H_2O to HO_2-

H_2O. The HO_2-H_2O-amine complex may not contribute as much to particle formation as complexes involving MSA and H_2SO_4, complexes of HO_2 may play a larger role in particle formation especially in more rural areas where higher concentrations of amines are present.

Chapter 4

Molecular Insights Into Organic Particulate Formation

4.1 Disclaimer

The following chapter is presented in its entirety (with minor changes) from the published version of the paper in Communications Chemistry. Kumar, M.; Burrell, E.;Hansen , J.C.; and Francisco, J.S.; Molecular insights into organic particulate formation. *CommsChem* **2019**. Dr. Manoj Kumar performed the computational calculations and wrote the introduction and computational sections. I performed the experimental measurements, wrote the experimental methods, results and contributed to the atmospheric implication sections. Dr. Joseph S. Francisco and Dr. Jaron C. Hansen reviewed and edited the work

4.2 Abstract

Carboxylic acids have been detected in particles collected in various regions of the world. Experiments and Born-Oppenheimer molecular dynamics simulations have been completed to better understand the mechanism of particle formation from gas phase mixtures of formic acid (HCOOH), $(CH_3)_3N$, and water vapor. A flow reaction cell coupled to two scanning mobility particle sizers was used to measure particle size, absolute number of particles and kinetics of particle formation. Experimental results show that the addition of $(CH_3)_3N$ to a mixture of HCOOH and water vapor results in a

dramatic increase in particle formation. Simulation results indicate that ion-pair formation on the water surface involves direct proton transfer between HCOOH and $(CH_3)_3N$. The $HCOO^-\cdot\cdot(CH_3)_3NH^+$ ion-pair remains at the air-water interface due to hydrogen bonding and the interfacial hydration shell. This experiment-theory study aids in the understanding of the role of organics in haze and cloud droplet formation and nanoparticle growth.

4.3 Introduction

Atmospheric aerosols affect air quality, human health, urban visibility, and the Earth radiation balance.[209-211] By acting as cloud condensation nuclei (CCN) and ice nuclei, aerosols impact frequency of occurrence, and lifetime of clouds on local, regional, and global scales.[10, 212-214] Despite their broad impact, the exact formation pathways for the atmospheric particles remain largely unknown.[176] Sulfuric acid (H_2SO_4) is recognized as perhaps the most important nucleating species in the atmosphere.[99, 215, 216] However, binary homogenous nucleation of H_2SO_4 and water (H_2O) is insufficient to explain the nucleation events under actual atmospheric conditions,[217] suggesting that other species may also participate in nucleation events.[187, 218, 219]

Amines and carboxylic acids are an important class of compounds that have recently been found to contribute to the particle formation under certain conditions.[176, 220] It is noted that molecules with high vapor pressures, which includes certain carboxylic

acids, would be unlikely to contribute to new particle formation however, recent field studies from a variety of locations around the world have found evidence of carboxylic acids contributing to new particle formation. For example, alkylaminium ions and carboxylate ions are seen in the mass spectra obtained for nanoparticles collected during new particle formation events in Hyytiala, Finland.[221] Measurements in Tecamac, Mexico also predict an important role of organic species in the particle growth.[13] Zhang et al. observed marked increase in the particle concentration when benzoic, *p*-toluic, *m*-toluic, or *cis*-pinonic acid vapor was added to the H_2SO_4-H_2O vapor system.[222, 223] Additional measurements in Shanghai, China observed increased rates of particle formation containing markers for the sulfuric acid dimer, H_2SO_4-dimethylamine (DMA) clusters and H_2SO_4-DMA-H_2O nucleation.[224] Recently, Arquero et al.[46] experimentally examined the role of oxalic acid in particle formation from vapor phase methanesulfonic acid, methylamine, and H_2O. The addition of water to the mixture of oxalic acid and methylamine was found to enhance particle formation by an order of magnitude. Although amines have concentrations 1-3 orders of magnitude lower than that of NH_3 in the atmosphere,[28] laboratory experiments demonstrate that amines are more effective than NH_3 in enhancing particle formation.[11,41, 225-227] For example, experiments using the CLOUD chamber at CERN have demonstrated that dimethylamine concentrations exceeding three parts per trillion by volume are able to increase particle formation rates by more than 3 orders of magnitude relative to that seen with NH_3.[11] The vapor pressure

of monocarboxylic acids is higher, by a factor of 10^2 to 10^4 than that of the corresponding dicarboxylic acids,[228] suggesting that the latter is likely to play a bigger role in the new particle formation. Despite that, monocarboxylic acids have been detected in aerosol particles collected in various regions of the world.[73, 79, 229-233] Supplementary Table 1 summarizes the concentration of HCOOH and CH_3COOH measured in air samples collected in a variety of environments. In the urban environment of New Mexico City, HCOOH and CH_3COOH were predominantly detected in the particulate phase.[234] On average, 53% of HCOOH and 67% of CH_3COOH were present in particulate matter. The presence of particulate organic salts was also raised as a possible explanation for the relatively high aerosol hygroscopicity and CCN concentrations observed in the Amazon basin.[235]

Despite being ubiquitous in diverse environments, the mechanism of organic particulate formation is yet to be fully established. Specifically, identifying key organic species and the underlying chemical mechanisms responsible for the nucleation and growth of atmospheric particles remains a significant challenge. Our current understanding about the role of organics in initial atmospheric nucleation events is based on quantum chemical calculations,[8,100, 175, 236-239] which are typically limited to few atom clusters. This hampers the generalization of gas-phase results to the water surfaces, such as fog, snow, clouds and water microdroplets, which are present in the troposphere and are believed to impact the chemistries occurring there.[114, 240-245]

We have performed experiments and BOMD simulations to explore the particle formation from HCOOH, TMA ($(CH_3)_3N$) and water. The BOMD simulations and performed experiments provide a further understanding as to the mechanism behind high vapor pressure molecules contributing to new particle formation. The results of this experiment-theory study also help in understanding the role of organics in both haze and cloud droplet formation, and to nanoparticle growth in urban, rural and remote regions.

4.4 Results

4.4.1 Experimental results of particle formation enhanced by trimethylamine.

Experiments were conducted by flowing gas mixtures of formic acid, water vapor, and TMA in a flow reaction cell. The instrumental set-up is shown in Supplementary Fig. 1. Three sets of conditions were analyzed for each precursor, which resulted in 27 conditions (Supplementary Table 2), each analyzed at 6 different reaction times (8, 16, 24, 32, 40 and 48 seconds). The analysis of the 8 minimal and maximal concentrations are discussed in the following figures. However, it should be noted that the additional 19 conditions agree with the minimal and maximal results. The size distribution and total number of particles at each reaction time under each reaction condition was measured. Figure 4.1a compares particle formation and particle size distributions as a result of flowing a mixture of formic acid (140 ppm) and water vapor (630 ppm) in the absence and presence of 200 ppb TMA. The total number of particles and particle size distribution is plotted for both 8- and 48-seconds reaction times. Figure

4.1b offers a closer look at particle concentrations vs particle diameters ranging from 300-500 nm. Figure 4.1c shows particle concentrations vs diameter from 0-100 nm. No particles are observed while flowing only N_2, 630 ppm H_2O, 140 ppm formic acid or 200 ppb TMA. Particles did form as a result of flowing a mixture of formic acid (140 ppm) and water vapor (630 ppm); however, with the addition 200 ppb of TMA to the mixture, there is a dramatic increase in the formation of smaller particles at both reactions. The mixture of formic acid (140 ppm) and water vapor (630 ppm) without any TMA, generated a maximum of $3.3\pm0.3 \times 10^6$ particles cm^{-3} at a diameter of 1.29 nm and a total number of particles of $7.2\pm0.3 \times 10^6$ particles ranging in diameter from 1.09-498 nm. 99.4 % of the particles were < 40 nm in diameter and 0.6% of particles were > 40 nm. Inclusion of 200 ppb TMA to this formic acid/water vapor mixture resulted in an increase in the total number of particles to $7.1\pm0.05 \times 10^7$ particles between 1.09-498 nm in diameter with a maximum of $3.4\pm0.3 \times 10^6$ particles cm^{-3} generated at a diameter of 1.09 nm at 8 s of reaction time .The percentage of particles formed at 8 s with a diameter of <40 nm decreased to 98.7 % while the percentage of particles with a diameter of >40 nm rose to 1.3%. With an increase of reaction time to 48 s, the total number of particles rose to $4.1\pm0.11 \times 10^8$ particles with a maximum concentration of $7.3\pm0.9 \times 10^6$ particles cm^{-3} generated at a diameter of 1.54 nm. The percentage of particles formed <40 nm in diameter dropped to 98.6 % while the percentage of particles > 40 nm rose to 1.4%. By comparison, the formic acid/water vapor mixture containing 200 ppb TMA shows an

increased formation of both smaller diameter particles, < 40 nm, and larger diameter particles (> 300 nm), compared to the formic acid/water vapor mixture without TMA. The difference in the number of total particles and formation of particles (>300 nm) increases with longer reaction times for mixtures that include TMA.

Table 4.1. Conditions probed for each trial and the measured rate of particle formation.

Initial Concentration	**A**	**B**	**C**	**D**	**E**	**F**	**G**	**H**
Formic Acid, ppm	140	140	140	140	540	540	540	540
Water Vapor*, ppm	630	1550	630	1550	630	1550	630	1550
TMA, ppb	200	200	400	400	200	200	400	400
*comparison graphs for change in water vaper are given in **Supplementary Fig. 2**								

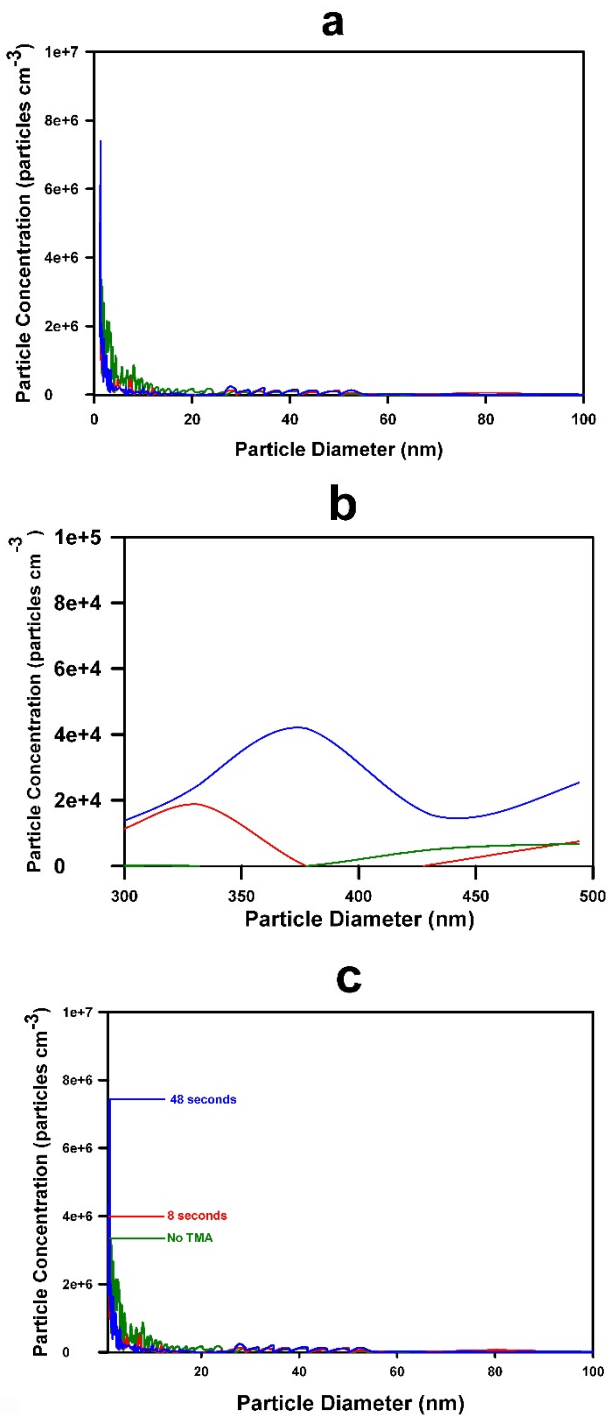

Figure 4.1 Particle formation initiated by the addition of 140 ppm formic acid, 630 ppm water vapor, 200 ppm trimethylamine (TMA) at different reaction times (no TMA, 8 and 48 seconds). a- Overall comparison of particle concentration vs particle diameter (0.8-500 nm). b- Comparison of larger diameter particle concentration vs particle diameter (300-500 nm) at different times (blue- 48 seconds, red- 8 seconds, green-no TMA) . c- Comparison of smaller diameter particle concentration vs particle diameter (0.8-100 nm). Numerical values are given in Supplementary Table 3.

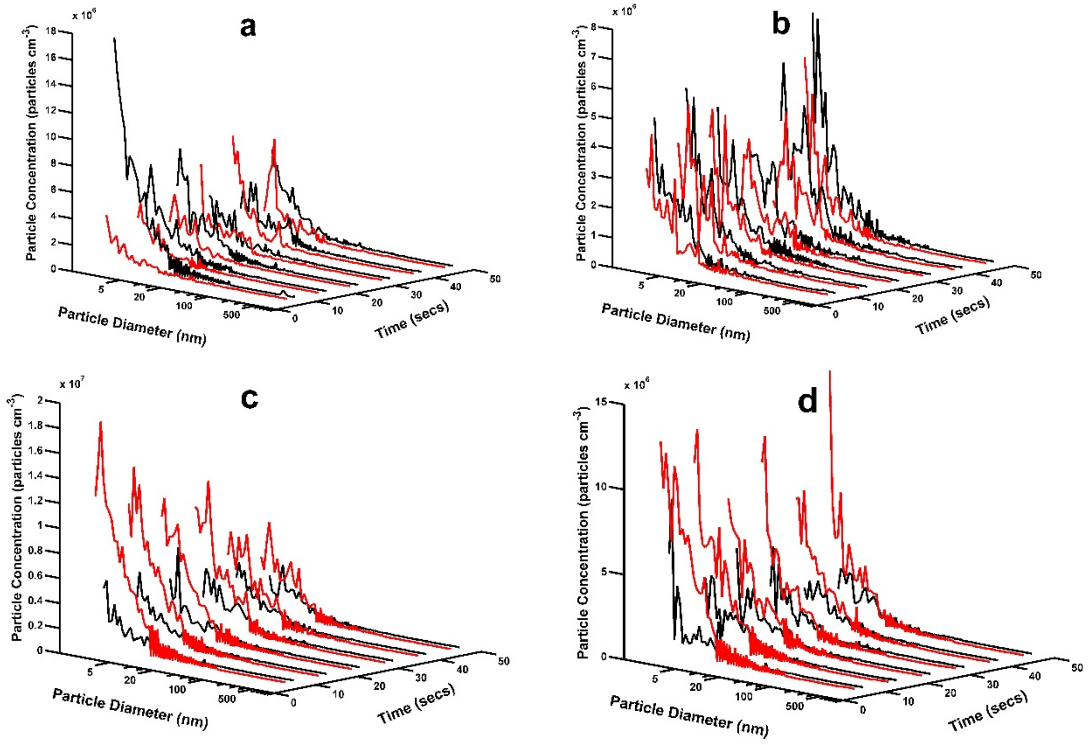

Figure 4.2 Inclusion of TMA into the formic acid water vapor system is shown to increase particle formation. Comparison of particle size distribution measured by an SMPS with different concentrations of formic acid, H_2O and TMA. A-concentrations A(red) vs C(black); b-concentrations B(red) vs D(black); c-concentrations E(red) vs G(black); d-concentrations F(red) vs H(black).

Table 4.1 lists the conditions probed for each trial and the measured rate of particle formation. Figure 4.2 compares particle formation as a function of initial formic acid, water vapor and TMA concentrations. Additional comparisons of Table 4.1 conditions are found in the supplemental data. See Supplementary Figure 2 and Supplementary Note 1. Figure 4.2a shows that the particle formation occurs even at the lowest concentration of formic acid (140 ppm), water vapor (630 ppm) and TMA (200 ppb) in the

reaction cell shown in red compared to increased TMA concentration (400 ppb) shown in black. The rate of particle formation under these conditions is measured to be 1.0±.02x10^{6} particles cm^{-3} s^{-1}. The rate of particle formation under higher concentrations could not be determined due to the aggregation of smaller sized particles leading to an increased concentration of larger particles, which skewed the calculations needed to determine the rate of particle formation. Figure 4.2a compares trials A and C (shown in black) with lower formic acid concentrations and an increase concentration of TMA from 200 ppm to 400 ppm, which shows a definite increase in the smaller particles at the shorter reaction times. Increasing the TMA concentration by a factor of 2 results in a 6.6% increase in the number of particles formed with diameters < 20 nm at 8 seconds. A shift in the size distribution of smaller particles (<20 nm) and increase in the number of particles > 40 nm is also observed. In figure 4.2b, trials B (red) and D (black) are shown. The formic acid (140 ppm) and higher water vapor (1550 ppm) concentrations were kept constant but the concentration of TMA was double in trial D compared to B. The total number of particles grown in trial D at 8 seconds was 36% larger compared to that in B. In addition, evaluation of the particle size distribution shows 3.9% of the total particles in B are > 20 nm in diameter but upon doubling of the concentration of TMA the total number of particles >20 nm in trial D increased to 4.2%. figure 4.2c, which shows trials E (red) and G (black), the formic acid (540 ppm) and water concentrations (630 ppm) were kept constant but the TMA concentration was double in trial G compared to E. The total

number of particles in trial G at 8 seconds was 17% smaller compared to that in E. In addition, evaluation of the particle size distribution shows that 3.1% of the total particles in E are > 20 nm in diameter but upon increasing the concentration of TMA, the total number of particles >20 nm in trial G increased to 3.3%. In figure 4.2c, which shows trials F (red) and H (black), the formic acid (540 ppm) and water concentrations (630 ppm) were kept constant but the TMA concentration was double in trial H compared to F. The total number of particles grown in trial F at 8 seconds was 4.8% larger compared to that in H. In addition, evaluation of the particle size distribution shows that 4.1% of the total particles in F are > 20 nm in diameter but upon increasing the concentration of TMA, the total number of particles >20 nm in trial H increased to 4.5%. Comparison of figure 4.2a-d (Supplementary Table 4) indicate an increase in the concentration of TMA increases the rate of particle formation and perturbs the particle size distribution a table of the values is found in supplemental materials. However, due to the high concentrations of formic acid and TMA in these trials, nucleation was not the only mechanism contributing to particle formation as is discussed later.

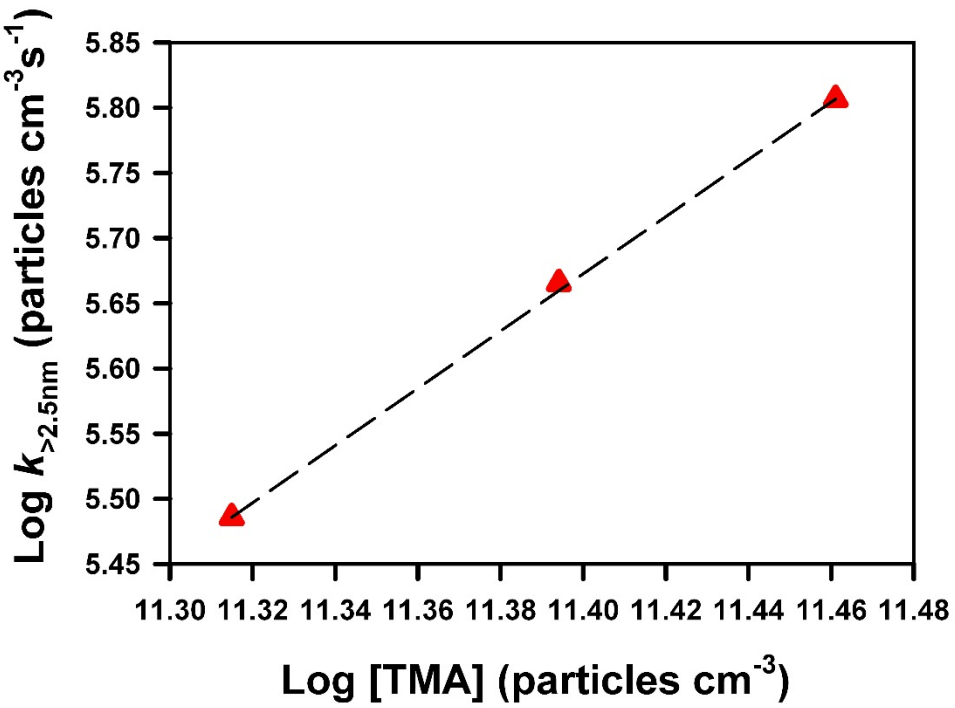

Figure 4.3 Addition of TMA to formic acid and water vapor system increased the rate of particle formation. Comparative rates of particle formation at 60 ppm formic acid, 630 ppm H_2O and different TMA concentrations.

The effect of TMA on the kinetics of particle formation was next measured by changing the TMA concentrations and comparing the changed rates of particle formation. To overcome a secondary mechanism via aggregation and to determine the rate of particle formation via nucleation, the formic acid and TMA concentrations were decreased minimizing aggregation in the flow cell. A gas mixture of 60 ppm formic acid and 630 ppm water vapor with varying concentrations of TMA was introduced into the reaction cell. The concentration of TMA was varied in the reaction mixture between 12-20 ppb and the total number of particles >2.5 nm in diameter was measured at reaction

times ranging between 8-48 seconds. These experiments allowed for measurement of the reaction rate coefficient, $k_{>2.5\ nm}$, for new particle formation. The rate of particle formation was determined by finding the linear slope between the reaction times (8-48 seconds) and the total number of particles. Figure 4.3 shows a comparison of $k_{>2.5\ nm}$ for three different formic acid, water vapor, TMA mixtures. A linear relationship between total number of particles formed >2.5nm in diameter and increasing concentration of TMA is observed. The rate of particle formation is observed to increase with the TMA concentration. The only anomaly observed in these series of experiments occurred when 200-400 ppb of TMA was introduced into the reaction cell. Under these conditions, the total number of particles formed, and shift in the particle size distribution did not follow the linear trend (Figure 4.4), but instead, a decrease in rate of particle formation was measured. This rate decrease can be associated to the inability to measure particles with a diameter > 500 nm using the SMPS's used in this project. Figure 4.4a compares formation of particles >300 nm in diameter as a function of the reaction time under conditions of flowing 140 ppm formic acid, 630 ppm water vapor and 200 ppb TMA. At 8 seconds, the shortest reaction time probed, particle concentration peaks at $1.9\pm0.4\text{x}10^{4}$ particles cm^{-3} at 332 nm in diameter. As the reaction time increases to 24 seconds, the maximum concentration increases to $4.7\pm0.1\text{x}10^{4}$ particles cm^{-3} at a particle diameter of 332 nm. A long, shallow tail is observed in the observed particle diameters for both reac/tion times, 8 and 24 seconds. As the reaction time increases to 32 seconds the previously observed maximum

in particle concentration observed in reaction times 8 and 24 seconds at 332 nm disappears, and a strong, broad distribution of particles >375 nm forms. At 48 seconds reaction time, a large peak in concentration is measured at 375nm and a second broad tail is observed rising from 440 nm in diameter. Fine particles are classified into three distinct ranges: the ultrafine particle range (<10 nm), the transient nuclei range (10-100 nm) and the accumulation range (100 nm-1.2 μm)[246]. Figure 4.4b separates particle diameters for each reaction time into these three modes versus particle concentration. At the earliest reaction time, there is a high particle concentration for the ultrafine particle range and a constant particle concentration for the accumulation range with an increase in reaction time. However, at the next shortest reaction time, there is an unexpected decrease in particle concentration in the ultrafine particle range followed by a slow increase in the ultrafine particle concentration with an increase in reaction time. In contrast, there is still an increase in the total number of particles in the accumulation range. The sudden decrease and subsequent increase in smaller diameter particles (<10 nm) along with the continuous increase in larger diameter particles indicates a two-fold nature of particle growth occurring in the reaction cell via nucleation and aggregation. To better comprehend the influence of TMA and H_2O on the two-fold mechanism of particle growth, Figure 4.5 compares the change in particle diameter distribution versus either a change in TMA or H_2O concentration. Figure 4.5a analyzes particle concentration versus particle diameter distribution with 140 ppm formic acid, 630 ppm water vapor, 200 ppb

TMA. Figure 4.5b shows a change in particle distribution with an increase in TMA. While Figure 4.5c shows the change in particle distribution with an increase in H_2O. The concentrations of H_2O and TMA were respectively increased from 630 ppm to 1550 ppm, and 200 ppb to 400 ppb. Figure 4.5b indicates that with increased TMA concentrations particles with a diameter between 2.5-10 nm decreased and increased the number of particles with diameters between 100-500 nm six-fold at 8 seconds. Compared with Figure 4.5c, there is a decrease in the number of particles with in diameter range diameters between 2.5-10 nm and a three-fold increase in particles with diameters between 100-500 nm at 8 seconds. Increased reaction times show the expected decrease

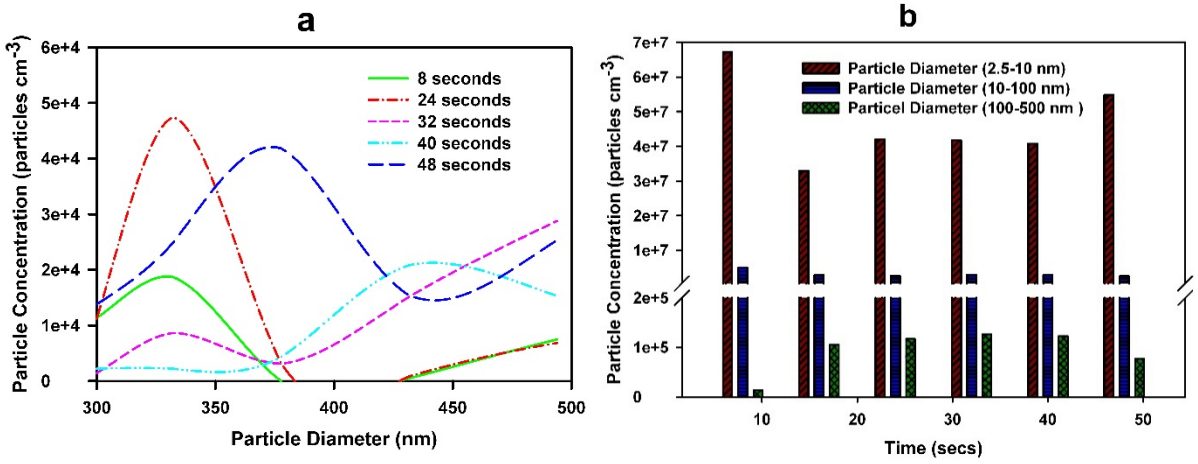

Figure 4.4 Inclusion of TMA into the formic acid and water vapor system increased the formation of larger diameter particles. Comparison of particle formation with 140 ppm formic acid, 630 ppm water vapor, 200 ppb TMA at different reaction times. A particle concentration vs particle diameter (300-493 nm) b bar graph comparing concentration to particle diameter sized (2.5-10 nm, 10-100 nm and 100-493 nm) numerical values are given in Supplementary Table 5-6.

in the overall particle concentration followed by an increase in the larger sized particles. The overall decrease is attributed to the inability to measure particles large than 500 nm

in diameter. The aggregation of smaller sized particles leading to the formation particles with diameters 100-500 nm may be enhanced by the dipole moment caused by the TMA complexing with formic acid which in turn forms a hydrophobic/hydrophilic interaction as stated in the computational section. A similar enhancement may occur with increased H_2O concentration, however to a lesser extent due to the smaller dipole moment. Ultrafine particles are formed as formic acid/water/TMA clusters grow with increasing reaction time in the cell. As the concentration of these particles increases the probability that these particles will collide with one another and aggregate to form a larger diameter particle increases. Aggregation of particles in the ultrafine and accumulation size range results in a decrease in the total number of these particles but increase in the formation of particles >100 nm in diameter. We see both particle growth as water adheres to the nucleating site but also observe aggregation as small particles collide into one another to produce larger diameter particles.

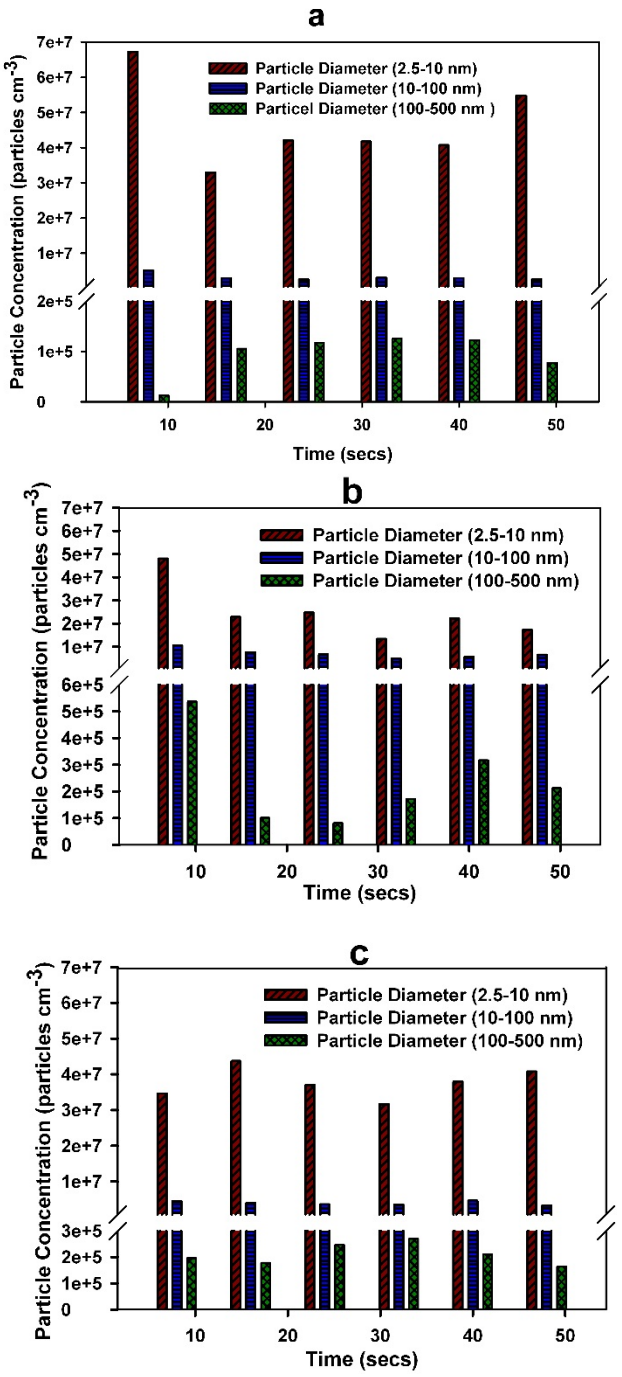

Figure 4.5 Increased water vapor or TMA concentrations increased the formation of larger diameter particles. Bar graph comparing concentration to particle diameter sized (2.5-10 nm, 10-100 nm and 100-493 nm) a particle formation with 140 ppm formic acid, 630 ppm water vapor, 200 ppb TMA; b particle formation with 140 ppm formic acid, 630 ppm water vapor, 400 ppb TMA; c particle formation with 140 ppm formic acid, 1550 ppm water vapor, 200 ppb TMA). Numerical values are given in Supplementary Table 5.

4.4.2 Simulation Evidence of the Formic acid-TMA Interaction at Air-Water Interface.

The BOMD simulations provide useful information into the time scale, molecular mechanism of the ion-pair formation as well as the dynamic behavior of the ion-pair formed on the aqueous surface. In a recent experimental study,[48] Eugene et al. observed interfacial proton transfer from simpler carboxylic acids. The BOMD simulations were performed on a water droplet of 191 H_2O molecules probing the nature of interaction between HCOOH and $(CH_3)_3N$. The details of simulation procedure are provided in **Method section**. We initiated BOMD simulations from hydrogen-bonded and non-hydrogen-bonded complexes of HCOOH with $(CH_3)_3N$. Surprisingly, only the hydrogen-bonded configurations resulted in the ion-pair formation on the water surface, implying that the formation of hydrogen-bonded HCOOH··$(CH_3)_3N$ complex in the gas-phase constitutes a crucial step in the particle formation on the water surface. The initial configuration of the HCOOH··$(CH_3)_3N$ complex adsorbed on the water droplet surface are given in Supplementary Figure 3. Though the role of gas-to-particle partitioning in the particle formation has been speculated before,[8] our simulations provide a mechanistic rationale why the gas-to-particle conversion is actually required for the particle formation.

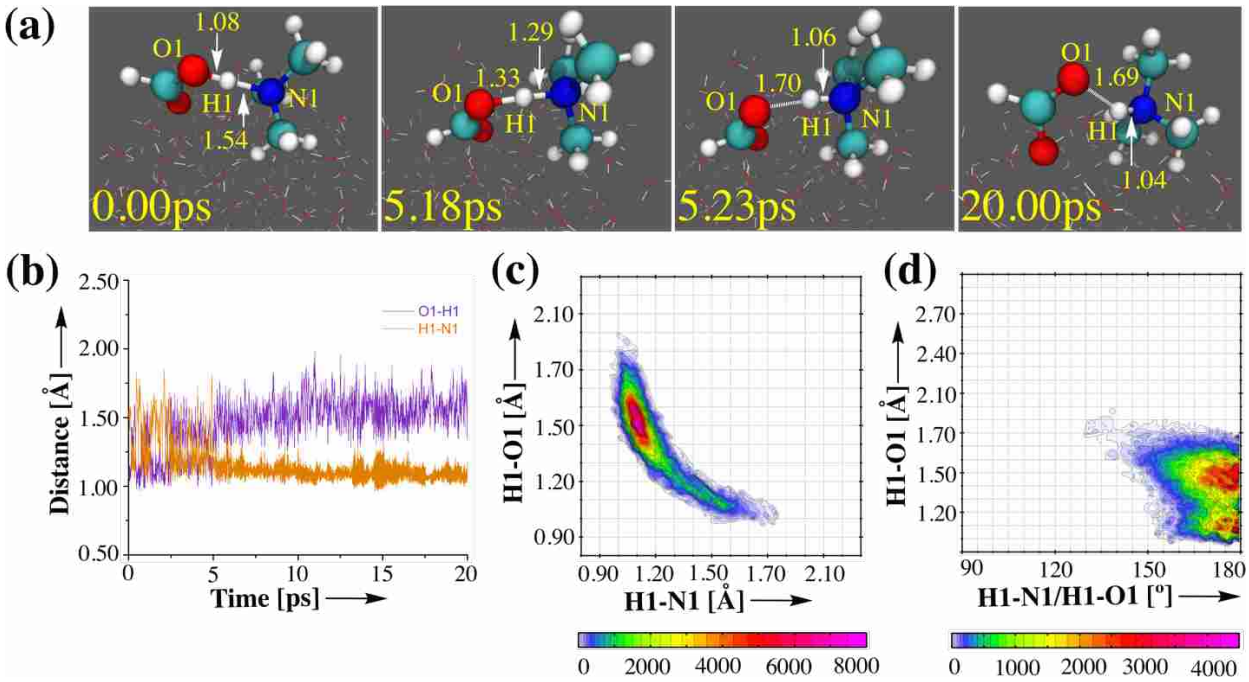

Figure 4.6 The simulation results detailing the interfacial proton transfer between formic acid and TMA ($(CH_3)_3N$). (a) Snapshot structures taken from the BOMD simulations of the reaction of formic acid with $(CH_3)_3N$, which illustrates the formation of $HCOO^-\cdot\cdot(CH_3)_3NH^+$ ion-pair on the water droplet. (b) Time evolution of key bond distances, O1-H1 and H1-N1 involved in the $HCOO^-\cdot\cdot(CH_3)_3NH^+$ ion-pair forming reaction. (c) Combined radial/radial distribution function involving H1-O1 and H1-N1 bond distances in the $HCOO^-\cdot\cdot(CH_3)_3NH^+$ ion-pair. (d) Combined distribution function involving an angular distribution function between H1-O1 and H1-N1 vectors and a radical distribution function between O1 and H1 bond distance in the $HCOO^-\cdot\cdot(CH_3)_3NH^+$ ion-pair.

The $HCOOH\cdot\cdot(CH_3)_3N$ interaction follows a typical trajectory of acid-base chemistry and involves a proton transfer between HCOOH and $(CH_3)_3N$ without the direct involvement of surface water molecules. This results in the formation of $HCOO^-\cdot\cdot(CH_3)_3NH^+$ ion-pair on a picosecond (ps) time scale (Figure 4.6). As just described, Eugene et al. have recently also observed interfacial proton transfer from simpler carboxylic acids that can play an important role in aerosol formation.[48] The role of water

droplet here is to stabilize the ion-pair particle by forming a hydration shell around it. These findings are consistent with field measurements, predicting that aminium salts could be formed in aged organic carbon particles in Riverside, California,[247] and in the Central Valley region of California[248]. A laboratory study of the reactive uptake of NH_3 onto slightly soluble organic acid particle also found that this process can significantly enhance the CCN activity and hygroscopic growth of these particles.[249] For the reaction between HCOOH and $(CH_3)_3N$, the transition state like complex is formed at 5.18 ps (Figure 4.6a and Supplementary Movie 1). In this complex, the hydroxyl proton of HCOOH is partially dissociated and transferred towards $(CH_3)_3N$, i.e., the O1-H1 bond is 1.33 Å long whereas the H1-N1 bond is 1.29 Å long. This complex is converted into the $HCOO^{-}\cdot\cdot(CH_3)_3NH^{+}$ ion pair at 5.23 ps. The O1-H1 bond is now lengthened to 1.70 Å, indicative of a hydrogen bonding interaction whereas the H1-N1 bond has become a true covalent bond (H1-N = 1.06 Å).

4.4.3 Dynamic Behavior of HCOO—··(CH3)3NH+ Ion-Pair at the Air-Water Interface.

To gain deeper insights into the dynamic behavior of the $HCOO^{-}\cdot\cdot(CH_3)_3NH^{+}$ ion-pair, we next analyzed its locus on the water droplet. Supplementary Fig. 4 shows the distance between the center of mass of the ion-pair and that of the water droplet as a function of the simulation time. The $HCOO^{-}\cdot\cdot(CH_3)_3NH^{+}$ ion-pair is situated at 10-13 Å distance from the center of the water droplet, implying that it preferentially resides at the

air-water interface. There are two main interactions responsible for the interfacial locus of the $HCOO^{-}\cdot\cdot(CH_3)_3NH^{+}$ ion-pair: (i) intraparticle hydrogen bonding (O1··H1-N1), and (ii) interfacial hydration shell. The intraparticle hydrogen bond in $HCOO^{-}\cdot\cdot(CH_3)_3NH^{+}$ ion-pair is quite strong as is evidenced from the combined distribution functions shown in Figure 4.6c-d, respectively. The calculated average number of hydrogen bonds formed by the $HCOO^{-}\cdot\cdot(CH_3)_3NH^{+}$ ion-pair with interfacial water molecules provides useful insight into its interfacial hydration shell. Our model specified a hydrogen bond between a formate oxygen and H_2O, if the O1/O2··H-O or O··H1-N1 distance was <2.5 Å and the ∠O1/O2··H-O or ∠O··H1-N1 hydrogen bond angle was >150°. The COO^{-} group forms 1.9 hydrogen bonds whereas the aminium proton does not form any hydrogen bond with H_2O molecules. The hydrophobicity of trimethyl group in the $HCOO^{-}\cdot\cdot(CH_3)_3NH^{+}$ ion-pair prevents any interaction between the aminium proton and interfacial water molecules. To deeply understand the solvation structure of $HCOO^{-}\cdot\cdot(CH_3)_3NH^{+}$ ion-pair at the air-water interface, we next identified key [m,n] configurations and calculated their probabilities (Figure 4.7). Here m and n are the number of interfacial H_2O molecules bound to the $HCOO^{-}$ and $(CH_3)_3NH^{+}$ respectively. The configurations, in which only the $HCOO^{-}$ group of $HCOO^{-}\cdot\cdot(CH_3)_3NH^{+}$ ion-pair binds to one, two and three interfacial H_2O molecules, are the most probable ones and account for 31%, 38% and 26% of the total configurations, respectively (Figure 4.7). Since there remains significant uncertainty about the exact composition of the particle in air,[8,37-42] our results may play a crucial role

in revealing a fundamental yet vital piece of information on the particle formation on the water surfaces.

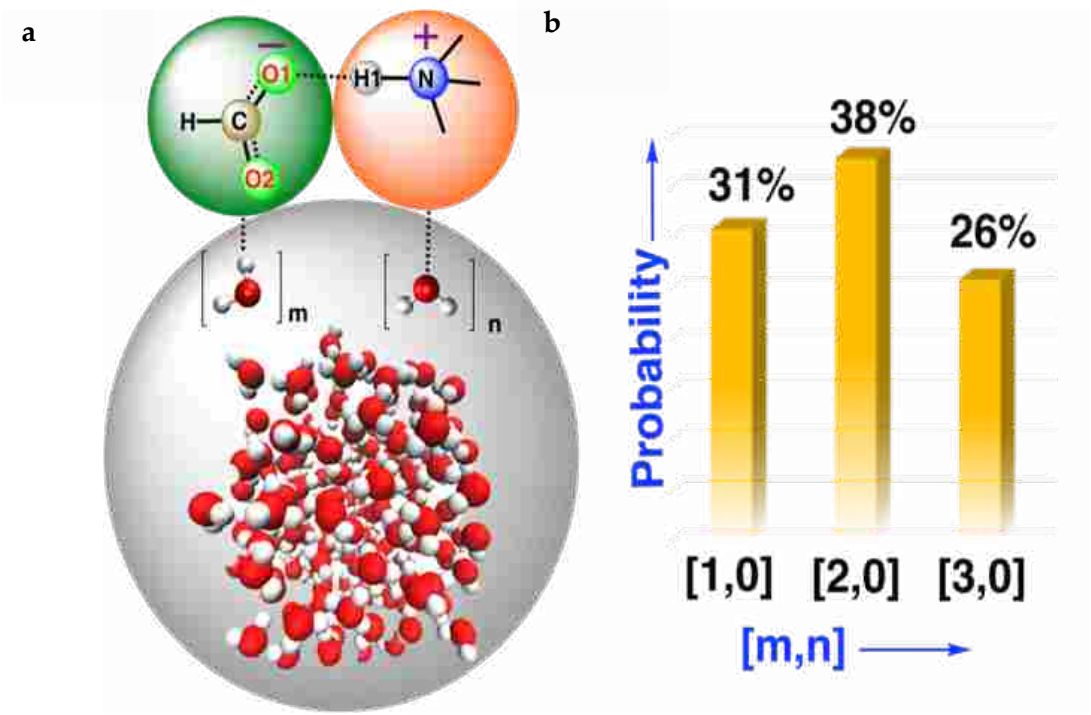

Figure 4.7 Simulation results on the hydration behavior of the $HCOO^{-}\cdot\cdot(CH_3)_3NH^{+}$ ion-pair on the water surface. a schematic showing the [m,n] interfacial waters forming hydrogen bonds with oxygens and aminium protons and of $HCOO^{-}\cdot\cdot(CH_3)_3NH^{+}$ where m and n are the number of interfacial water molecules bound to $HCOO^{-}$ and $(CH_3)_3NH^{+}$, respectively. b histograms of probabilities of different [m,n] configurations for $HCOO^{-}\cdot\cdot(CH_3)_3NH^{+}$.

4.5 Atmospheric Implications

Direct condensation of organic vapors of low volatility, such as organic acids, was initially thought to be a potential additional mechanism for the growth of atmospheric nanoparticles.[250] However, the high saturation pressure of organic acids over

nanoparticles[251] rules out the possibility of direct condensation mechanism. On contrary, thermal desorption chemical ionization mass spectrometry (TDCIMS) measurements of the composition of ambient 10-33 nm diameter particles formed from nucleation in Tecamac, Mexico show the presence of carboxylic and hydroxycarboxylic organic acids,[13] suggesting that organics play a dominant role in the nanoparticle growth.

Our experimental and theoretical results may help in resolving the discrepancy in the role of organic acids in nanoparticle growth. The current BOMD simulations suggest a new gas-to-particle partitioning mechanism for the formation of organic particles that involves two steps: (i) formation of hydrogen-bonded complexes of organic acids with amines in the gas-phase, and their adsorption on the aqueous surface, and (ii) subsequent proton transfer between hydrogen-bonded entities. The mechanistic beauty of this new mechanism lies in the fact that it does not require direct condensation of organic acids, but rather involves hydrogen bonding between organic acids and amines. The organic-amine salts formed in this mechanism will have reduced volatility, as has been pointed out in a recent thermodynamic modeling study[252]. This new mechanism is supported by combined laboratory investigation and field measurements using TDCIMS and ultrafine hygroscopicity tandem differential mobility analyzer (TDMA) confirming that carboxylate-alkylaminium salts contribute to the growth of particles as small as 8-10 nm in atmosphere.[17] Additional support for this mechanism comes from the study of Dinar

et al. showing that the reactive uptake of NH_3 on slightly soluble organic acid particles increases their CCN activity and hygroscopic growth.[53]

Our BOMD simulations suggest that the carboxylate-aminium ion-pair remained stable on the water surface over the simulated time scale of 20 ps. This is again consistent with a recent measurement of the volatility of alkylaminium carboxylate salts that shows high thermal stability from the organic acid-amine reactions: the measured vapor pressure of alkylaminium dicarboxylate salts is 10^{-6} Pa, and the vaporization enthalpy ranges from 73 to 134 kJ mol^{-1}.[253]

4.6 Discussion

Our experiments show the nanoparticle formation under conditions that are typically outside what is expected if you use classical nucleation theory to describe particle formation. That is to say, we see nanoparticle growth under conditions of < 100% RH. Under the classical nucleation model, it is suggested that 100% RH is necessary for particle formation and growth to occur. We speculate that by adding trace amounts of amines and/or formic acid, we may "seed" a cloud to increase the rate of particle formation. Our experimental results are consistent with what is observed around the world in terms of measuring carboxylic acids in particles as shown in the Sao Paulo, Brazil and Tecama, Mexico studies. The conclusions from our work could be used to better understand the role of other monocarboxylic acids such as CH_3COOH, and dicarboxylic

acids such as oxalic acid and malonic acid in the particle formation under diverse environmental conditions, including semiurban sites in the northeastern United States,[254] urban environments,[75, 255, 256] and remote locations[257].

Though considered unlikely due to their high vapor pressures atmospheric gaseous- and particle-phase carboxylic acids have been measured in the urban environment of Sao Paulo, Brazil.[20] Carboxylic acids accounted for a fraction of 7% of the total organic carbon in the particle phase, with formate and oxalate being two of the most abundant carboxylates. Though the major source of these carboxylate is suggested to be traffic emissions, the comprehensive insights into their emission source are still lacking. Our results suggest that the acid-base chemistries between organic acids and organic nitrogens could be an overlooked source of organic particulate in urban air. The organic nitrogens could be transported from the rural agricultural sites to the urban regions where they react with organic acids and result in the particulate formation. These new findings may help in improving the accuracy of existing atmospheric models.

4.7 Methods

4.7.1 Experimental Details

A flow cell set-up was used to experimentally verify the formation of particles initiated by formic acid, water vapor and TMA. Supplementary Fig. 1 shows the experimental setup, a 180 cm long Pyrex flow cell (5.1 cm i.d.) was connected to two

aluminum boxes (26.5 cm x 26.5 cm x 26.5 cm) that allowed for UV light to pass through the flow cell for detection of formic acid and TMA. Formic acid, water vapor, and N_2 were separately introduced at the top of the cell. TMA was introduced at varying points in the flow cell by a Teflon coated shower ring. Particle size distribution with particle diameter sizes ranging from 1.09 nm to 493.95 nm were analyzed using two Grimm Aerosol Technik scanning mobility particle sizer (SMPS, model: 5.710) each consisting of a differential mobility analyzer (DMA) Electrostatic Classifier (Vienna/Reishl type, model 55-u; 55-100) and a faraday cup electrometer (FCE, model 5.705).

Prior to each experiment, the flow cell was cleaned out with ozone, N_2 (2 SLM) and O_2 (100 sccm) for 1 hour between experiments and overnight. This allowed for the complete removal of any formic acid or TMA that had been introduced in previous experiments. The flow cell was kept at a constant temperature (22±1 °C) and pressure (650±5 Torr). In all experiments, formic acid and water vapor were introduced separately into the flow cell by bubbling N_2 (100-300 sccm) through 88% proof formic acid and purified water. Additional N_2 was introduced into the flow cell for a total flow rate of 3.125 SLM. As previously mentioned, TMA (25-125 sccm) was introduced at varying points in the flow cell by a Teflon coated shower ring. The shower ring (i.d. 4.5 cm) with pin holes was attached to a stainless-steel rod which allowed for movement up and down the flow cell. This method of introducing TMA allows for reaction times varying from 8 s to 48 s. A range of concentrations for formic acid and TMA were varied by varying the

flow of gases and subsequently using UV absorption spectroscopy to determine formic acid and TMA concentrations. Using Beer's Law and previously published cross sections from 220.16 to 250.9 nm the concentrations of TMA were determined to be 200 and 400 ppb. Using previously published formic acid cross sections from 210.88 to 230.86 nm the formic acid concentrations were determined to be 140 and 540 ppm. A water vapor calibration curve was determined by introducing known concentrations of water vapor via a syringe pump (KD Scientific KDS-100 Syringe Pump) at known flow rates. Water was introduced into a stainless-steel tee packed with glass wool heated to 150 °C. N_2 (3.1 SLM) passed through the glass wool into the flow cell and the absorption from the water concentration was determined by dithering an IR diode over 1380.47 nm to 1384.6 nm and the area under the desired peak was integrated for the known concentration of water vapor. Water vapor concentrations used were 630 and 1550 ppm.

4.7.2 Computational Details

Born-Oppenheimer molecular dynamics (BOMD) simulations were performed based on a density functional theory (DFT) method implemented in the CP2K[258] code. In the BOMD simulation, the droplet system contained 191 water molecules, one HCOOH molecule and one $N(CH_3)_3$ molecule. We have explored a total number of 10 different trajectories, in which five of them started from non-hydrogen-bonded configurations of HCOOH and $N(CH_3)_3$ whereas the other five started from hydrogen-bonded configurations. The dimension of the simulation box is x = 35 Å, y = 35 Å, z = 35 Å, which

is large enough to neglect interactions between adjacent periodic images of the water droplet. Prior to the BOMD simulation, the system was fully relaxed using a DFT method, in which the exchange and correlation interaction is treated with the Becke-Lee-Yang-Parr (BLYP) functional[156, 259]. The Grimme's dispersion correction method is applied to account for the weak dispersion interaction[260, 261]. A double-ζ Gaussian basis set combined with an auxiliary basis set and the Goedecker-Teter-Hutter (GTH) norm-conserved pseudopotentials were adopted to treat the valence electrons and the core electrons, respectively[262, 263]. An energy cutoff of 280 Rydberg was set for the plane-wave basis set and 40 Rydberg for the Gaussian basis set. The BOMD simulations were carried out in the constant volume and temperature (NVT) ensemble, with the Nose-Hoover chain method for controlling the temperature (300 K) of the system. The integration step was set as 1 fs, which had been proven to achieve sufficient energy conservation for the water system.

Chapter 5

Secondary Particle Formation Initiated by Mixtures of Acetic Acid, Water Vapor and Trimethylamine

5.1 Disclaimer

The following chapter is presented in its entirety (with minor changes) from the pre-submitted version of the paper. Burrell, E.;and Hansen, J.C; Secondary Particle Formation initiated by Mixtures of Acetic Acid, Water Vapor and Trimethylamine. Dr. Emily Burrell performed the experimental measurements, the computational calculations and analysis, and wrote the manuscript. Dr. Jaron C. Hansen reviewed and edited the work

5.2 Abstract

Carboxylic acids have been detected in particulate matter around the world and as such it has become increasingly important to better understand the role of carboxylic acids in secondary particle formation. A slow flow reaction cell coupled with two scanning mobility particle sizers were used to measure the particle size distribution, absolute number of particles and kinetics of particle formation. The experimental results suggest that even though particles are formed as a result of flowing a mixture of acetic

acid (22 ppm) and water vapor (630 ppm), the addition 35 ppb of $(CH_3)_3N$ to the mixture results in a dramatic increase in the formation of ultrafine particles.

5.3 Introduction

Ultrafine particles (UFPs) affect everyday life including air quality, human health, visibility and the earth's radiation balance[3, 4, 8, 165]. Additionally, UFPs act as cloud condensation nuclei impacting the frequency of occurrence and lifetime of clouds [212, 264, 265]. Despite UFPs impact the exact pathways leading to their formation remains mostly unknown[176]. For example, one of the most recognized pathways for particle formation is the nucleation of sulfuric acid (H_2SO_4) complexed with water (H_2O)[40, 99, 266-270]. However this pathway is insufficient to explain measured particle concentrations under atmospheric conditions[196] which suggests alternative species may be participating in particle formation.[187, 198, 219]

Some of these potential species include amines and carboxylic acids.[76, 176, 234, 256, 257, 271-276] Low amine concentrations (ppt) have shown to significantly increase the rate of ultrafine particle formation. One step in the mechanism in forming new particles from mixtures of carboxylic acids, water vapor and amines is the formation of alkylaminium ions.[221] Carboxylate ions along with alkylaminium ions were measured in particles collected in Hyytiala, Finland.[221] Formic acid (HCOOH, FA) and acetic acid (CH_3COOH, AA) have been measured in particulate matter collected in Mexico City,

Mexico. On average, 53% of HCOOH and 67% of CH_3COOH were found present in particulate matter[234]. Additional measurements in Tecamac, Mexico have predicted an important role for these organic species in particle growth.[198, 235] Recently, Kumar et al. experimentally and computationally examined the role of formic acid in particle formation from mixtures of vapor phase formic acid, trimethylamine, and water vapor. The addition of trimethylamine to the mixture of formic acid and water was found to enhance particle formation by an order of magnitude. Although amines have concentrations 1-3 orders of magnitude lower than that of NH_3 in the atmosphere[28], laboratory experiments demonstrate that amines are more effective than NH_3 in enhancing particle formation.[41, 46, 97, 191, 216, 277, 278] In another example, Finlayson-Pitts et al.[38, 100, 173] demonstrated the efficiency of amines compared with NH_3 in a system containing methane sulfonic acid (MSA) and H_2O. It was shown that amines increased the rate of particle formation even under conditions of low relativity humidity. For example, classical nucleation theory[11, 23, 97, 279] requires >100% RH for particle formation and growth to occur. Under this constraint, in a typical low relative humidity environment commonly found in the atmosphere, MSA and H_2O would be unable to produce significant concentration of particles[173]. However, with the addition of methylamine to this environment a significant increase in particle formation was demonstrated.

As shown in recent studies our current understanding of the role of carboxylic acids and amines in atmospheric nucleation events is limited and as such, we have performed experiments to explore particle formation from mixtures of CH_3COOH, trimethylamine ($(CH_3)_3N$, TMA) and water vapor. The conclusions from our work can be used to better understand the role of other monocarboxylic acids such as CH_3COOH, and dicarboxylic acids such as oxalic acid and malonic acid in particle formation under various environmental conditions, including semi-urban sites[76, 254], urban environments[75, 255, 256], and remote locations[233, 275, 280, 281].

5.4 Experimental Set-Up

A slow flow reaction cell set-up was used to experimentally verify the formation of particles initiated by mixtures of acetic acid, water vapor and TMA. Figure 1 shows the experimental setup, a 180 cm long Pyrex flow cell (5.1 cm i.d.) was connected to two aluminum boxes (26.5 cm x 26.5 cm x 26.5 cm) that allowed for UV light to pass through the flow cell for detection of acetic acid and TMA. Acetic acid, water vapor, and N_2 were separately introduced at the top of the cell. TMA was introduced at varying points in the flow cell by a Teflon coated shower ring. Particle size distribution with particle diameter sizes ranging from 1.09 nm to 493.95 nm were analyzed using two Grimm Aerosol Technik scanning mobility particle sizer (SMPS, model: 5.710) each consisting of a differential mobility analyzer (DMA) Electrostatic Classifier (Vienna/Reishl type, model 55-u; 55-100) and a faraday cup electrometer (FCE, model 5.705).

Prior to each experiment, the flow cell was flushed with ozone, N_2 (2 SLM) and O_2 (100 sccm) for at least 1 hour between experiments. This allowed for the complete removal of any acetic acid or TMA that had been introduced in previous experiments from the cell. The flow cell was kept at a constant temperature (22±1 °C) and pressure (650±5 Torr). In all experiments, acetic acid and water vapor were introduced separately into the flow cell by bubbling N_2 (20-60 sccm) through 99.7% proof acetic acid and 18 MΩ purified water. Additional N_2 was introduced into the flow cell to produce a total flow rate of 3.125 slm. As previously mentioned, TMA (15-25 sccm) was introduced at varying points in the flow cell by a Teflon coated shower ring. The shower ring (i.d. 4.5 cm) with

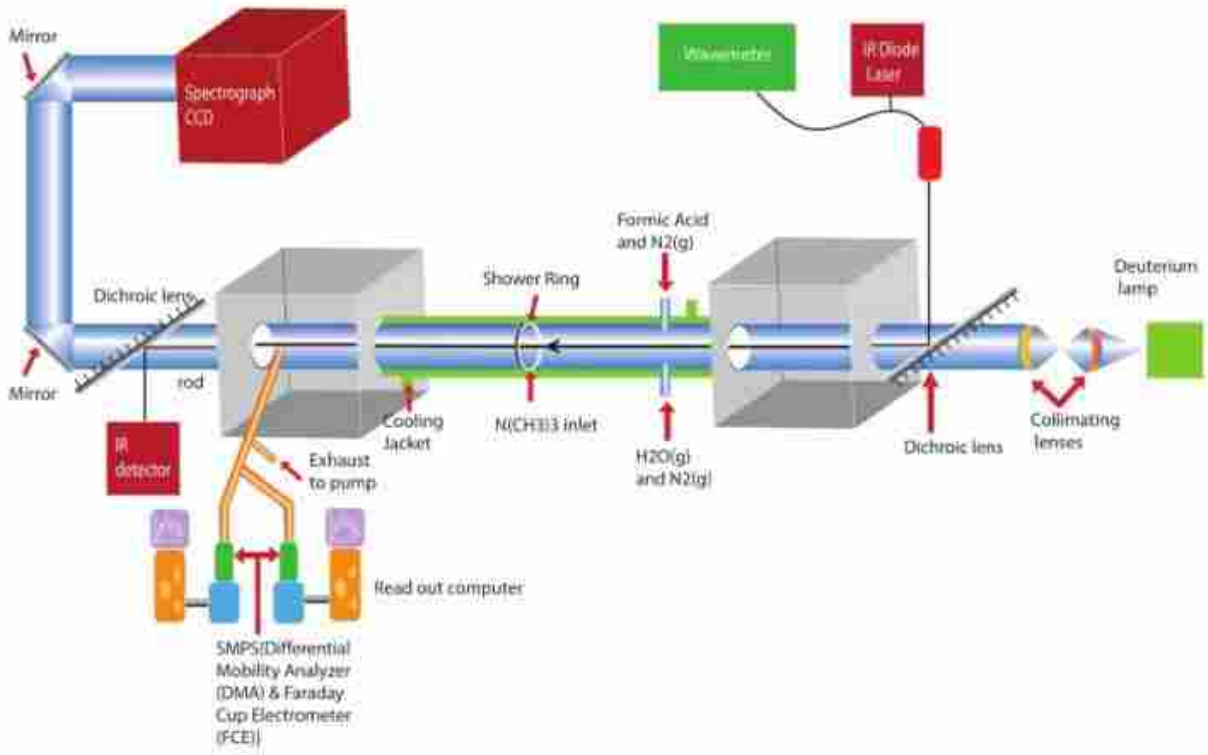

Figure 5.1 Instrument Set-Up

pin holes was attached to a stainless-steel rod which allowed for movement up and down the flow cell. This method of introducing TMA allows for reaction times varying from 8 s to 48 s. A range of concentrations for acetic acid and TMA were varied by varying the flow of gases and subsequently using UV absorption spectroscopy to determine acetic acid and TMA concentrations. Using Beer's Law and previously published cross sections from 220.16 to 250.9 nm were fit to measured absorption spectra. The concentrations of TMA were determined to range between 35 and 70 ppb. Using previously published acetic acid cross sections from 210 to 230 nm the acetic acid concentrations were determined to range between 22 and 73 ppm. A water vapor calibration curve was determined by introducing known concentrations of water vapor via a syringe pump (KD Scientific KDS-100 Syringe Pump) at known flow rates. Water was introduced into a stainless-steel tee packed with glass wool heated to 150 °C. N_2 (3.1 slm) passed through the glass wool into the flow cell and the absorption from the water concentration was determined by dithering an IR diode over 1380.47 nm to 1384.6 nm and the area under the desired peak was integrated for the known concentration of water vapor. Water vapor concentrations used were 630 and 1550 ppm.

5.5 Computational Method

The Gaussian 09, Revision 5.0.8[201] suite of programs was used for geometry optimizations, vibrational frequency calculations, and high-level configuration interaction molecular energy calculations. Initial optimization of the monomer

structures for each complex began with a M06-2X/6-311++G (d,p) level geometry optimization. The M06-2X level is regarded as one of the best density functional theories involving thermochemistry, kinetics and non-covalent interaction calculations[202, 203]. The purpose of this initial step was to quickly generate initial force constants in the G09 environment and to decrease the overall computation time. The geometry of each monomer structure was then refined at the M06-2X/aug-cc-PVDZ level. The energy of the optimized structure was then refined with a CCSD (T)/aug-cc-PVDZ single-point calculation from the optimized geometries determined using the M06-2X/aug-cc-PVDZ level.

The minimum energy geometry for the global and local minima for each complex was generated and identified by a wide-ranging random constrained sampling (RCS) methodology[204]. The global and local minima for each complex was fully optimized using the M06-2X/aug-cc-PVDZ level and further refined with a CCSD (T)/aug-cc-PVDZ single-point calculation using the optimized geometries determined using the M06-2X/aug-cc-PVDZ method and basis set.

The random constrained sampling (RCS) method was used to generate the HO_2-H_2O-amine, MSA-H_2O-amine and H_2SO_4-H_2O-amine complex geometries. Briefly, the RCS method generates HO_2-H_2O complex geometries by randomly packing a H_2O molecule within a 3.5 Å constrained radius sphere encompassing the entire radical or a user-defined portion of the optimized HO_2 structure. In this work, the overall optimized

complex geometries were determined via two iterations of the RCS method. The first iteration generated 1000 HO_2-H_2O geometries by placing a H_2O molecule around a 3.5 Å radius sphere centered over the entire radical structure. The second iteration produced 1000 HO_2-H_2O-amine complex geometries that involved placing the optimized geometry of an amine or NH_3 around a 3.5 Å radius sphere centered over the entire optimized minimum energy geometry of the HO_2-H_2O complex. Both iterations followed a geometry and energy optimization scheme identical to that used for the identification of the radical lowest energy structure.

The harmonic vibrational frequency calculations were performed from the M06-2X/aug-cc-PVDZ level and confirmed each structure as a minimum. Additional thermodynamic calculations were performed using the optimized geometries identified using the M06-2X/aug-cc-PVDZ level. Binding energies were calculated from the CCSD (T)/aug-cc-PVDZ level. The anharmonic frequency calculations were performed using the M06-2X/aug-cc-PVDZ level.

Electron density maps with a surface resolution of 0.0003 e/au^2 were generated using the results from the M06-2X/aug-cc-pVDZ level for the HO_2-H_2O-amine complexes. HO_2, H_2O and amine monomer electron density maps were subtracted from the electron density map computed for each complex to produce an electron density difference map showing how the electron density is perturbed as a result of complex formation.

5.6 Results and Discussion

5.6.1 Experimental Results

Experiments were conducted by flowing gas mixtures of acetic acid, water vapor, and TMA in a slow flow reaction cell. The instrumental set-up is shown in Figure 5.1. Three sets of conditions were analyzed for each precursor, which resulted in 27 conditions (Table S1), each analyzed at 6 different reaction times (8 secs, 16 secs, 24 secs, 32 secs, 40 secs, 48 secs). The size distribution and total number of particles at each reaction time under each reaction condition was measured. Figure 5.2 compares particle formation and particle size distributions as a result of flowing a mixture of acetic acid (22 ppm) and water vapor (630 ppm) in the absence and presence of 35 ppb TMA. The total number of particles and particle size distribution is plotted for both 8 secs and 48 secs reaction times. No particles are observed while flowing only N_2, 630 ppm H_2O, 22 ppm acetic acid or 35 ppb TMA. Particles did form as a result of flowing a mixture of acetic acid (22 ppm) and water vapor (630 ppm); however, with the addition 35 ppb of TMA to the mixture there is a dramatic increase in the formation of smaller particles at both reactions. The mixture of acetic acid (22 ppm) and water vapor (630 ppm) without any TMA generated a maximum of $1.5\pm0.3 \times 10^5$ particles cm^{-3} at a diameter of 1.83 nm and a total number of particles of $1.87\pm0.3 \times 10^6$ particles ranging in diameter from 1.09-498 nm. 98.3 % of the particles were < 40 nm in diameter and 1.7 % of particles were > 40. Inclusion of 35 ppb TMA to this acetic acid/water vapor mixture resulted in an increase in the total

Table 5.1. Conditions probed for each trial

Initial Concentration	A	B	C	D	E	F	G	H
Acetic Acid, ppm	22	22	22	22	73	73	73	73
Water Vapor, ppm	630	1550	630	1550	630	1550	630	1550
TMA, ppb	35	35	70	70	35	35	70	70

number of particles to 3.8±0.05 x 10^7 particles between 1.09-498 nm in diameter with a maximum of 5.9±0.3 x 10^6 particles cm^{-3} generated at a diameter of 1.09 nm at 8 s of reaction time. The percentage of particles formed at 8 s with a diameter of <40 nm increased to 99.1 % while the percentage of particles with a diameter of >40 nm decreased to 0.8%. With an increase of reaction time to 48 s, the total number of particles rose to 7.1±0.11 x 10^7 particles with a maximum concentration of 6.5±0.9 x 10^6 particles cm^{-3} generated at a diameter of 1.09 nm. The percentage of particles formed <40 nm in diameter increased to 99.4 % while the percentage of particles >40 nm decreased to 0.6%. By comparison, the acetic acid/water vapor mixture containing 35 ppb TMA shows an increased formation of both smaller diameter particles, < 40 nm, and larger diameter particles (> 300 nm), compared to the acetic acid/water vapor mixture without TMA. The difference in the number of total particles and formation of particles (>300 nm) increases with longer reaction times for mixtures that include TMA.

Table 5.1 lists the conditions probed for each trial Figures 5.3-5.5 and Figure S1 compares particle formation as a function of initial acetic acid, water vapor and TMA concentrations. In Figure 5.3a when trial A (22 ppm acetic acid, 630 ppm water vapor, 35 ppb TMA) is compared to trial C (22 ppm acetic acid, 630 ppm water vapor, 70 ppb TMA), a shift in the size distribution of smaller particles (<20 nm), 97.1% to 96.2%, and an increase in the number of particles > 40 nm, 0.8% to 1.7%, is observed. In Figure 5.3b, trials B (red) and D (black) are shown. The acetic acid and water vapor concentrations were kept constant, but the concentration of TMA was double in trial D (22 ppm acetic acid, 1550 ppm water vapor, 70 ppb TMA) compared to B (22 ppm acetic acid, 1550 ppm water vapor, 35 ppb TMA). Unexpectedly, the total number of particles grown in trial D at 8 secs was 5.6% smaller compared to that in B. In addition , evaluation of the particle size distribution showed 3.4% of the total particles in B are > 20 nm in diameter but upon doubling of the concentration of TMA the total number of particles >20 nm in trial D slightly decreases to 3.0%. Previous research has shown that experiments run in

a slow flow reactor cell have two mechanisms contributing to particle growth. These two mechanisms can be used to explain the decrease in both larger and smaller

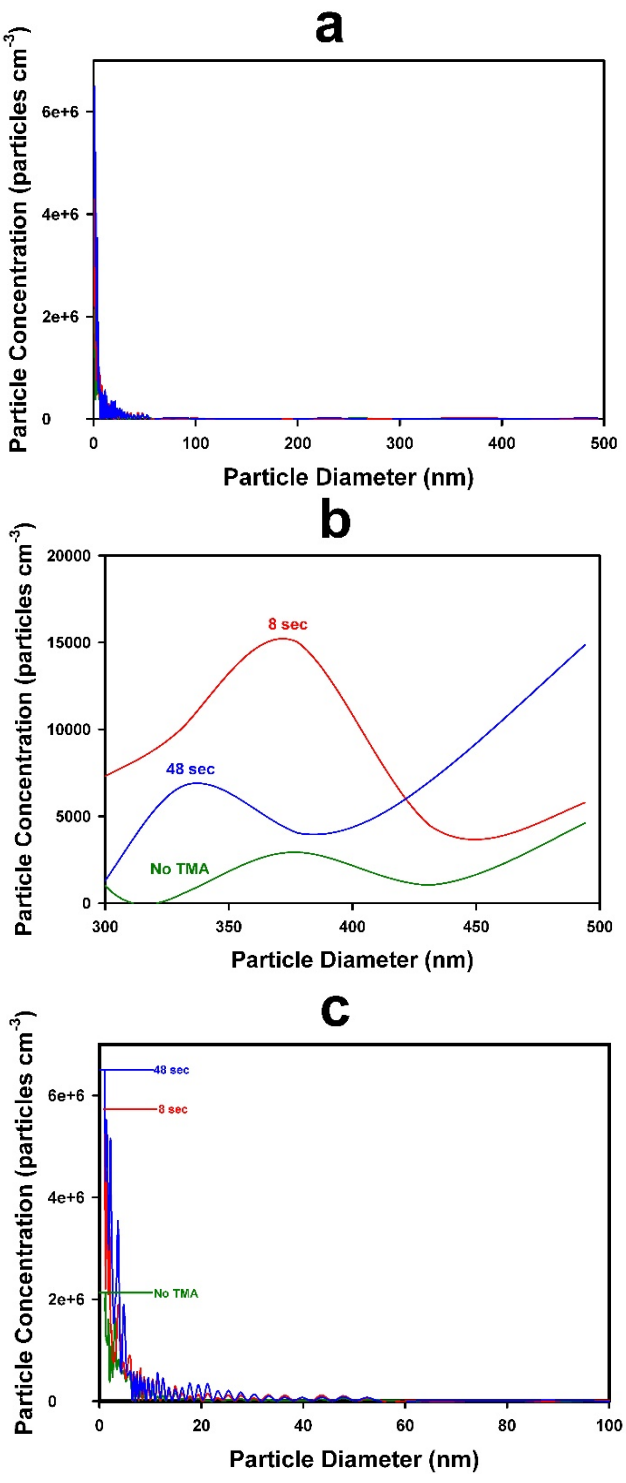

Figure 5.2: Comparison of particle formation initiated by the addition of 22 ppm acetic acid, 630 ppm water vapor, 35 ppb TMA at different reaction times.

diameter particles in higher concentration experiments. Comparison of the data in Figure 5.3a and 5.3b indicates that the concentration of water vapor in the system effects particle formation however, an increase in the concentration of TMA increases the rate of particle formation and perturbs the particle size distribution. However, due to the high concentrations of acetic acid and TMA in these trials, nucleation was not the only mechanism contributing to particle formation as is seen in Figure 5.3c, which shows

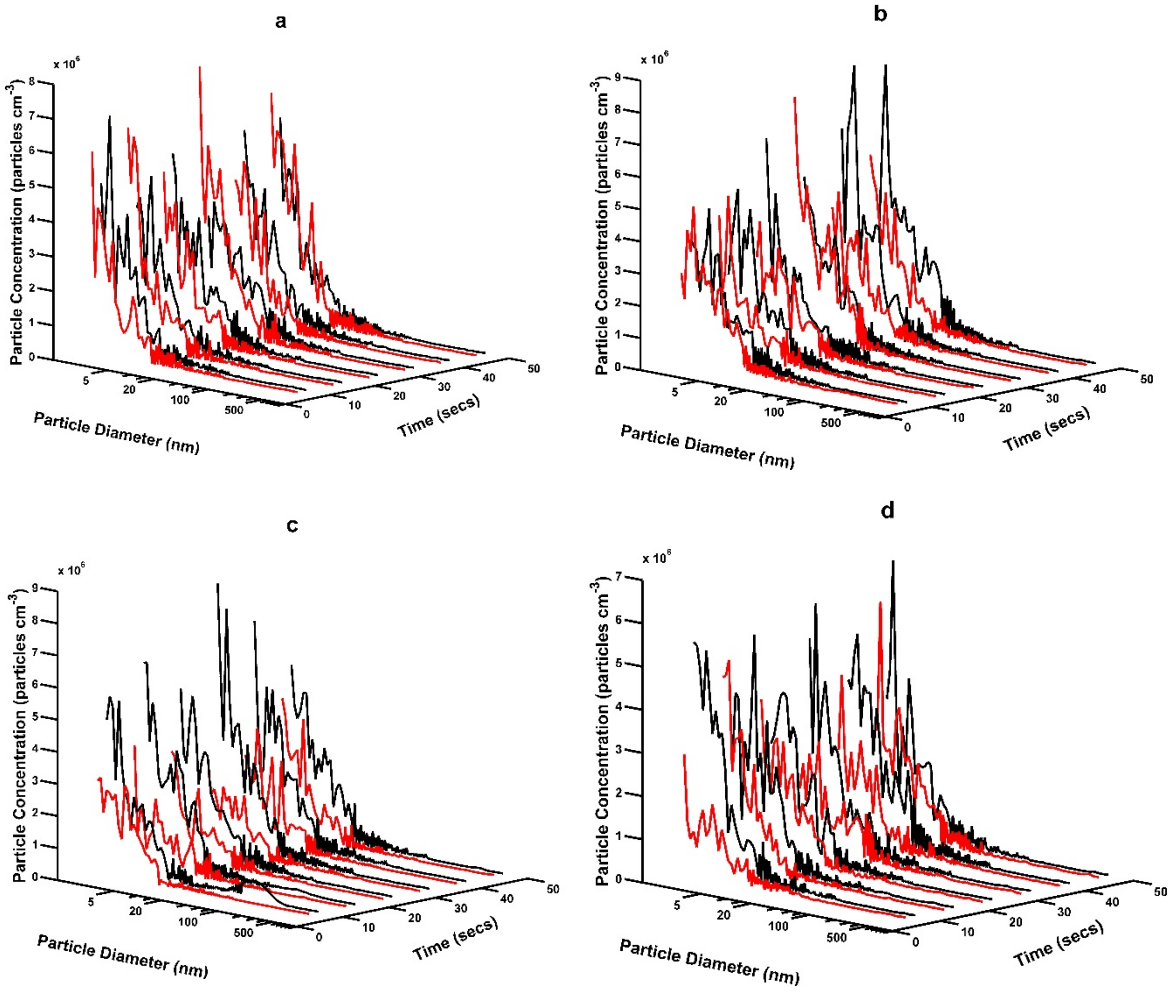

Figure 5.3. Comparison of particle size distribution measured by an SMPS with different concentrations of acetic acid, H_2O and TMA: 3A-concentrations A(red) vs C(black);3B-concentrations B(red) vs D(black); 3C- concentrations E(red) vs G(black); 3D- concentrations G(red) vs H(black).

trials E (red) and G (black), the acetic acid (73 ppm) and water concentrations (630 ppm) were kept constant but the TMA concentration was double in trial G compared to E. The total number of particles grown in trial G at 8 secs was 35.1% smaller compared to that in E. In addition, evaluation of the particle size distribution shows that 2.6% of the total particles in E are > 20 nm in diameter but upon increasing the concentration of water, the total number of particles >20 nm in trial G grows to 4.0%. In Figure 5.3d, which shows trials G (red) and H (black), the acetic acid (73 ppm) and TMA (75 ppm) concentrations were kept constant but the water concentration was doubled in trial H compared to G. The total number of particles grown in trial H at 8 s was 58% larger compared to that in G. In addition, evaluation of the particle size distribution shows that 3.9% of the total particles in G are >20 nm in diameter but upon increasing the concentration of water, the total number of particles >20 nm in trial H decreases to 3.2%. The severe drop in total particles can be accounted to the loss of larger sized particles due to our inability to detect particles >494 nm. The dependence of the concentration of TMA on the kinetics of particle formation was measured by changing the TMA concentrations and comparing the changed rates of particle formation.

To overcome particle growth via aggregation and to determine the rate of particle formation via nucleation, the acetic acid and TMA concentrations were decreased minimizing aggregation in the flow cell. A gas mixture of 22 ppm acetic acid and 630 ppm water vapor with varying concentrations of TMA was introduced into the reaction cell. The concentration of TMA was varied in the reaction mixture between 28-53 ppb and the total number of particles <2.5 nm in diameter was measured at reaction times ranging between 8-48 secs. These experiments allowed for measurement of the reaction rate coefficient, $k_{<2.5\ nm}$, for new particle formation. The rate of particle formation was

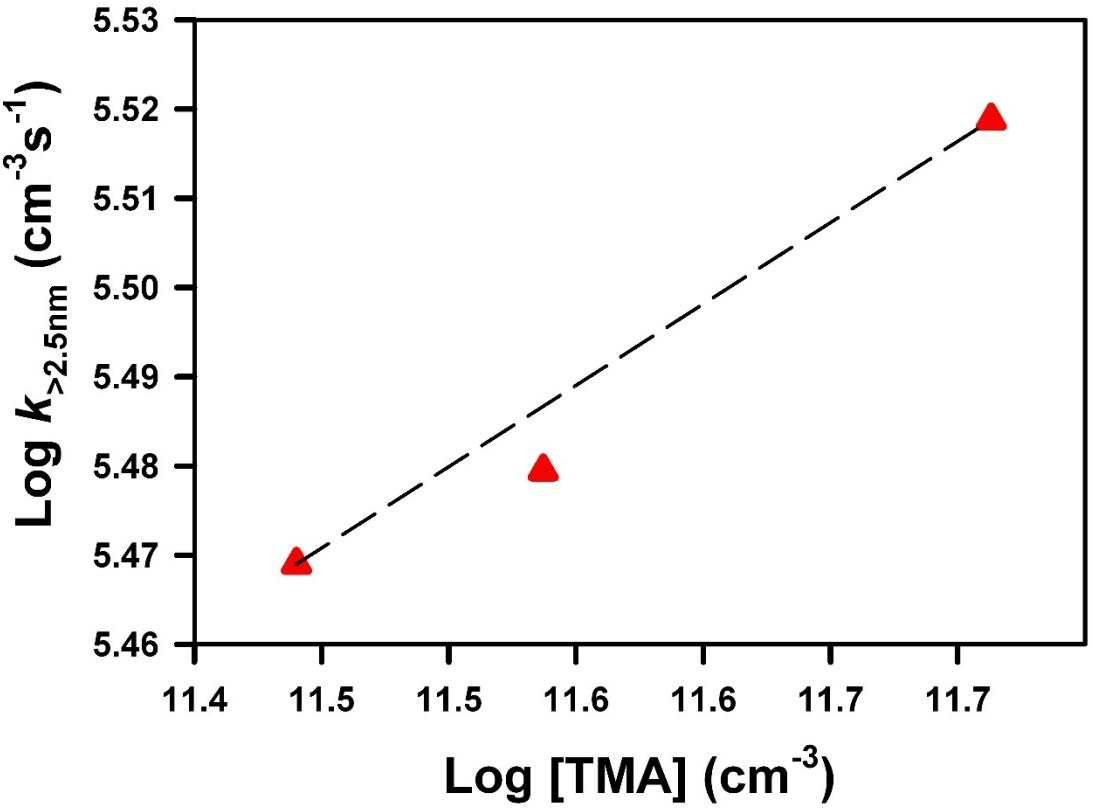

Figure 5.4: Comparative rates of particle formation at 60 ppm acetic acid, 630 ppm H_2O and different TMA concentrations.

determined by finding the linear slope between the reaction times (8-48 secs) and the total number of particles. Figure 5.4 shows a comparison of $k_{<2.5\ nm}$ for three different acetic acid, water vapor, TMA mixtures. A linear relationship between total number of particles formed <2.5nm in diameter and increasing concentration of TMA is observed. The rate of particle formation is observed to increase with the TMA concentration. The only anomaly observed in these series of experiments occurred when 35-70 ppb of TMA was introduced into the reaction cell. Under these conditions, the total number of particles formed, and shift in the particle size distribution did not follow the linear trend (Figure 5.5), but instead, a decrease in rate of particle formation was measured. This rate decrease can be associated to the inability to measure particles with a diameter > 500 nm using the SMPS's available for use in this project. Figure 5.5A compares formation of particles >300 nm in diameter as a function of the reaction time under conditions of flowing 22 ppm acetic acid, 630 ppm water vapor and 35 ppb TMA. At 8 secs, the shortest reaction time probed, particle concentration peaks at $1.5\pm0.4x10^4$ particles cm^{-3} at 377 nm in diameter. As the reaction time increases to 16 seconds there is a downward shift to 332 nm with a concentration of $1.85\pm0.4x10^4$ followed by and increased reaction time of 24 secs, where the maximum concentration increases to $1.2\pm0.1x10^4$ particles cm^{-3} at a particle diameter of 431 nm and a decrease in concentration at 377 nm and 332nm. At 32 secs there is a significant increase in larger sized particles at 431 nm ($1.94\pm0.3x10^4$ particles cm^{-3}) and 332 nm ($1.29\pm0.1x10^4$ particles cm^{-3}) before a long tail begins to taper off indicating additional

undetected larger sized particles. As the reaction time increases to 40 secs the previously observed maximum in particle concentration observed reaction times 8, 16 and 32 secs at 332 nm decreases, and a strong, broad distribution of particles at 431 nm forms with a concentration of 2.66±0.3x10^4 particles cm^{-3}. At the 48 secs reaction time, a peak with a concentration of 6.78±0.3x10^3 particles cm^{-3} is measured at 331 nm and a second peak is observed at 431 nm with a concentration of 1.49±0.3x10^4 particles cm^{-3}. Fine particles are classified into three distinct ranges: the ultrafine particle range (<10 nm), the transient nuclei range (10-100 nm) and the accumulation range (100 nm-1.2 μm). [41] Figure 5.5B separates particle diameters for each reaction time into these three modes versus particle concentration. At the earliest reaction time, 8 seconds, there is a high particle concentration of the ultrafine particle range and a constant particle concentration for the accumulation range with an increase in reaction time. at 16 seconds, there is a minimal

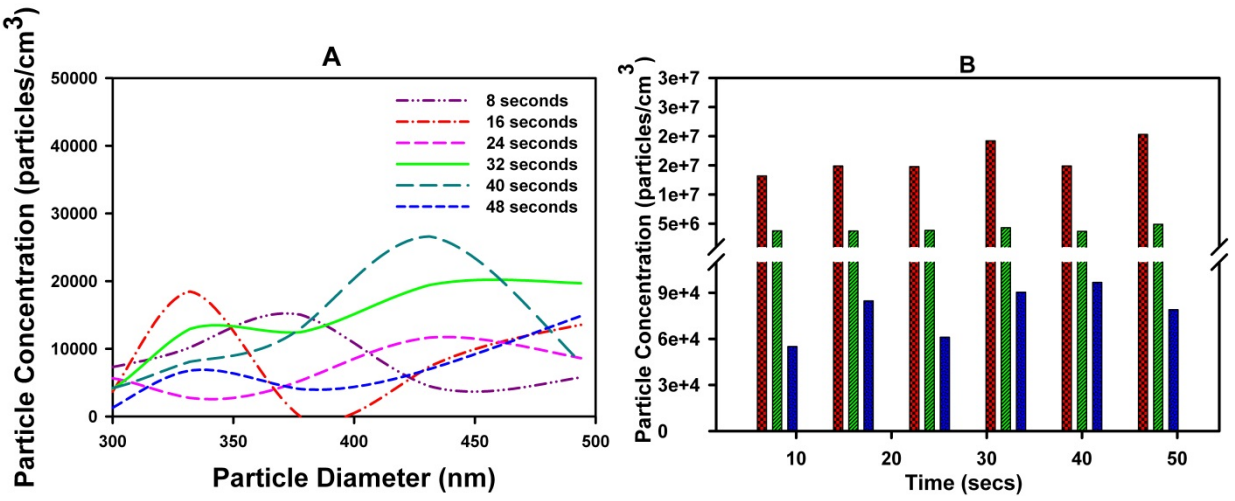

Figure 5.5: Comparison of particle formation with 22 ppm acetic acid, 630 ppm water vapor, 70 ppb TMA at different reaction times. A-particle concentration vs particle diameter (300-493 nm) B-Bar graph comparing concentration to particle diameter sized (2.5-10 nm, 10-100

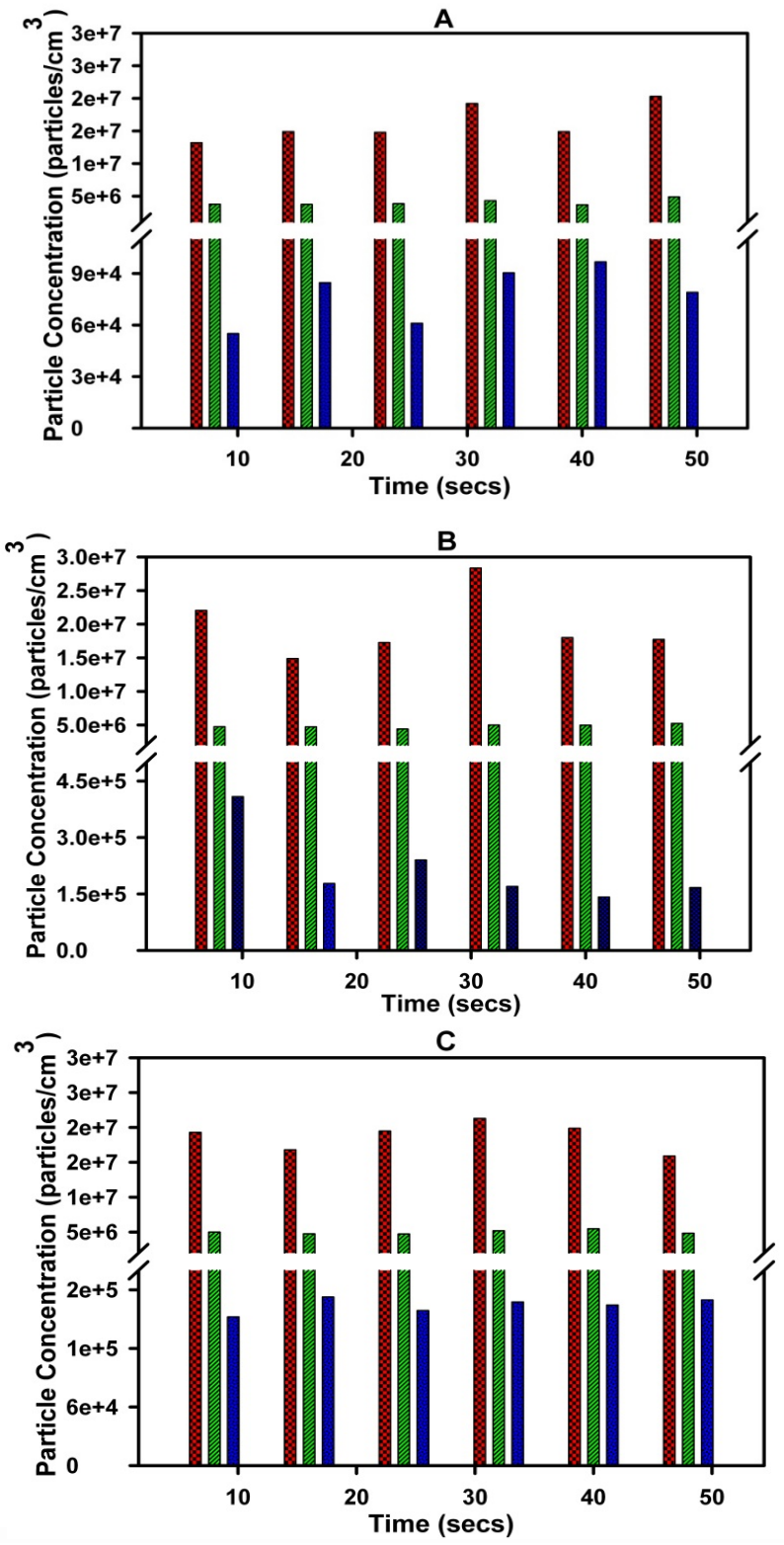

Figure 5.6: Bar graph comparing concentration to particle diameter sized (2.5-10 nm, 10-100 nm and 100-493 nm) A-Particle formation with 22 ppm acetic acid, 630 ppm water vapor, 35 ppb TMA; B- particle formation with 22 ppm acetic acid, 630 ppm water vapor, 70 ppb TMA; C- particle formation with 22 ppm acetic acid, 1550 ppm water vapor, 35 ppb TMA

increase in the ultrafine particle range- concentration and an increase in the ultrafine particle concentration. In contrast, there is still an increase in the total number of particles in the accumulation range. The decrease and subsequent increase in smaller diameter particles (<10 nm) along with the semi-continuous increase in larger diameter particles indicates a two-fold nature of particle growth occurring in the reaction cell via nucleation and aggregation. To better understand the influence of TMA and H_2O on the two-fold particle growth mechanisms, nucleation and aggregation, Figure 5.6A compares increased TMA and H_2O concentrations in Figure 5.6B and Figure 5.6C. The concentrations of H_2O and TMA were increased respectively from 630 ppm to 1550 ppm, and 35 ppb to 75 ppb. In Figure 5.6B the concentration of TMA was doubled in comparison to Figure 5.6A. At 8 secs the number of particles with diameters that range between 2.5-10 nm increased by ~1.5x whereas the larger sized particles increased ~7.5x in concentration. At increased reaction times there is a sharp decrease in larger sized particles which indicates that we are unable to detect the larger sized particles. When Figure 5.6A is compared with Figure 5.6C, there is a similar increase in the number of particles with diameters that range between 2.5-10 nm and a three-fold increase in particles with diameters between 100-500 nm at 8 seconds. Increased reaction times show the expected decrease in the overall particle concentration followed by an increase in the larger sized particles. The overall decrease is attributed to the inability to measure particles large than 500 nm in diameter. The aggregation of smaller sized particles

leading to the formation particles with diameters 100-500 nm may be enhanced by a dipole moment caused by the TMA complexing with acetic acid which in turn may forms an ion-dipole interaction shown with formic acid, TMA and water vapor.[282] A similar enhancement may occur with increased H_2O concentration, however to a lesser extent due to the smaller dipole moment. Ultrafine particles are formed as acetic acid/water/TMA clusters grow with increasing reaction time in the cell. As the concentration of these particles increases the probability that these particles will collide with one another and aggregate to form a larger diameter particle increases. Aggregation of particles in the ultrafine and accumulation size range results in a decrease in the total number of these particles but increase in the formation of particles >100 nm in diameter. We see both particle growth as water adheres to the nucleating site but also observe aggregation as small particles collide into one another to produce larger diameter particles.

5.6.2 Computational Results

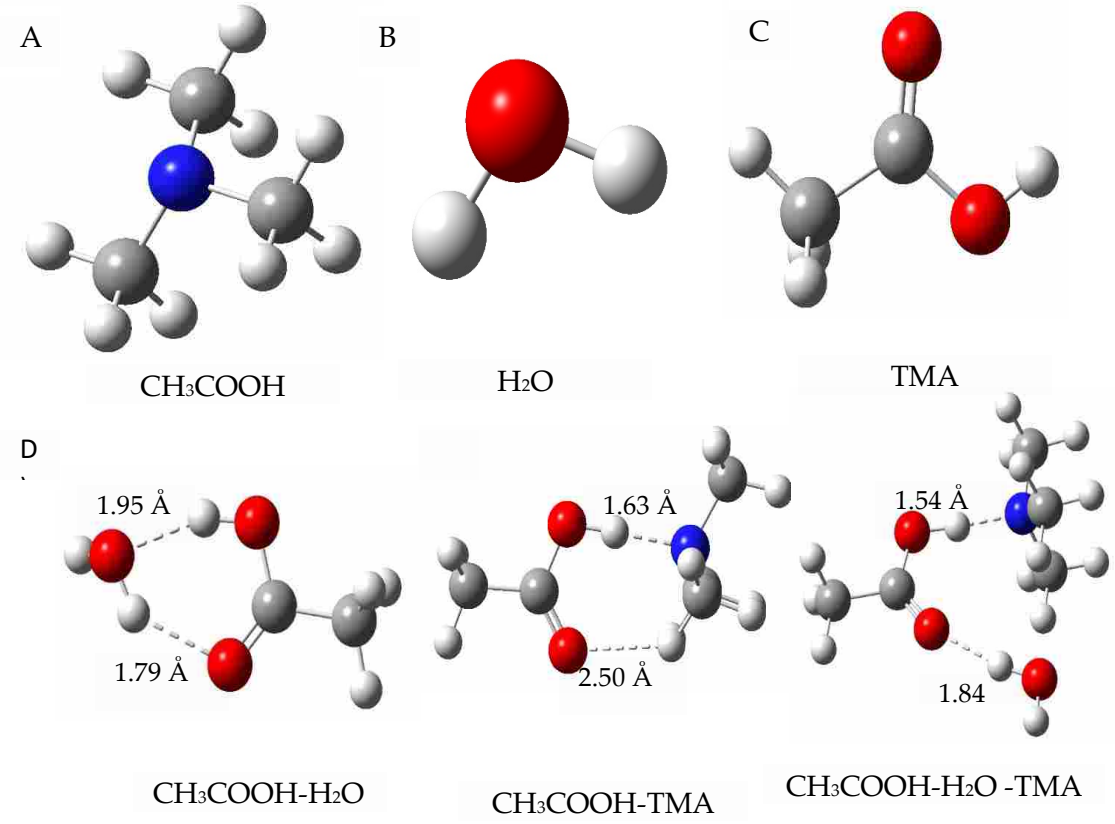

Figure 5.7: Optimized geometries of monomers, CH_3COOH-H_2O dimer, CH_3COOH-TMA dimer and CH_3COOH-H_2O-TMA complex at the M062x/aug-cc-pVDZ level

To better understand the mechanics of particle formation the binding energies and geometries of the acetic acid-water dimer (CH_3COOH-H_2O) and the acetic acid-trimethylamine-water complex (CH_3COOH-H_2O-TMA) were analyzed (Figure 5.7). Binding energies were determined by calculating the difference between the complex and the monomers energies. The binding energy of acetic acid-water dimer is 8.75 kcal mol^{-1} (table 5.2). While lower than the binding energy of H_2SO_4-H_2O, 12.13 kcal mol^{-1}, still

provides stability to act as a nucleation site. However, like with H_2SO_4-H_2O-TMA (33.25 kcal mol^{-1}) the addition of an amine to the CH_3COOH-H_2O dimer increases the binding energy of the CH_3COOH-H_2O-TMA complex to 19.76 kcal mol^{-1} thus increasing the stability of the nucleating complex.

Table 5.2: Binding energies of dimers and complexes at M062X/aug-cc-PVDZ level

	Binding energy (kcal mol^{-1})	Binding Energy (kJ mol^{-1})
H_2O-H_2O	5.25	21.97
H_2SO_4-H_2O	12.13	50.75
H_2SO_4-H_2O-TMA	33.25	139.24
CH_3COOH-TMA	12.92	54.07
CH_3COOH-H_2O	8.75	36.62
CH_3COOH-H_2O-TMA	19.76	82.68

Further evidence to the increased stability of the nucleation site is indicated in the strengthening of the hydrogen bonds by more favorable bond lengths and bond angles (table 3). Ideally, a hydrogen bond has an angle of 180° and bond lengths that range between 1.5-2.5 Å (ref). The CH_3COOH-H_2O dimer has two hydrogen bonds that form. The weaker of the two hydrogen bonds lies between the oxygen on the acetic acid and the hydrogen on the water with a bond angle of 138.2° and a bond length of 1.95 Å. The second hydrogen bond is formed between the oxygen of water and the hydrogen on acetic acid with a bond angle of 156.7° and a bond length of 1.79 Å. With the addition of TMA there is an increase in bond angles and bond lengths along with a shift in the placement of the hydrogen bonds. A hydrogen bond forms between the nitrogen in TMA

and the hydrogen on CH_3COOH and has a bond angle of 175.1° and a bond length 1.54 Å. A second hydrogen bond forms between the oxygen in acetic acid and the hydrogen in water with a bond angle of 170.5° and a bond length of 1.84 Å.

Table 5.3: Bond lengths and angles of the complexes and dimers

Complex	Interactions	Bond length (Å)	Angles (°)
H_2SO_4-H_2O[a]	O-H…O(water)	1.65	163.2
	O-H(water)…O	2.11	129.2
H_2SO_4-H_2O-TMA[a]	O-H…O(water)	1.45	176.2
	O-H(water)…N	1.68	175.2
CH_3COOH-H_2O	O(AA)…H-O(water)	1.95	138.2
	O-H…O(water)	1.79	156.7
CH_3COOH-TMA	O-H…N(TMA)	1.63	177.6
	C-H…O(AA)	2.5	125.2
CH_3COOH-H_2O-TMA	O-H(AA)…N	1.54	175.1
	O-H(water)…O	1.84	170.5

Enthalpy, Entropy and Gibbs Free Energy

The Gibbs free energy (ΔG°), enthalpy (ΔH°) and entropy (ΔS°) of formation was calculated for each complex (table 4). ΔH° was calculated from the total corrected internal energy of the system and corrected for the Boltzmann constant and temperature (eq. 1)[206]:

$$\Delta H° = \Delta E_{tot} + k_B T \qquad \text{(eq. 1)}$$

The Gibbs free energy data was mined from the Gaussian output files where $\Delta G°$ was calculated from $\Delta H°$, total internal entropy ($\Delta S°_{tot}$) and temperature (eq. 2)[206]:

$$\Delta G° = \Delta H° - T\Delta S°_{tot} \qquad \text{(eq. 2)}$$

These calculations allow for a better understanding of the potential pathways for new particle formation. $\Delta G°$ of the CH_3COOH-H_2O dimer is 0.56 kcal mol^{-1}(table 4), $\Delta H°$ of the dimer is -9.50 kcal mol^{-1} while $\Delta G°$ of the CH_3COOH-TMA dimer is -1.67 kcal mol^{-1}, $\Delta H°$ of the dimer is -12.96 kcal mol^{-1}. With the addition of either a TMA molecule or H_2O molecule the complex has a decreased $\Delta G°$ (0.03 kcal mol^{-1}) and an increased $\Delta H°$ (-20.07 kcal mol^{-1}). The addition of either TMA or H_2O to the system increased the enthalpy and either decreased or increased the Gibbs free energy dependent on the added molecule. This indicates that the addition of TMA to the CH_3COOH-H_2O dimer increases the stability of the dimer allowing for it to stay longer in the atmosphere leading to particle formation. This can be attributed to the increased polarity and hydrogen bonding strength which influences $\Delta G°$ for the reaction resulting in the formation of a more thermodynamically favorable nucleating complex. From the enthalpy and Gibbs free energy data the entropy of complex formation can be calculated (table 4). Evaluation of the entropy of complex formation data indicates that complex formation is an entropically unfavorable reaction.

Anharmonic Calculations

To refine the calculated enthalpy, entropy and Gibb's free energy of CH_3COOH-H_2O-TMA complex formation, anharmonic calculations were performed for the CH_3COOH-H_2O-TMA complex including local and global minima (SI Fig 1) using the M06-2X-aug-cc-PVDz method and basis set. Anharmonic frequency calculations were performed to account for the increase in populated vibrational energy levels that arise from treatment of the vibrational modes as anharmonic oscillators. Harmonic $\Delta G°$ for the CH_3COOH-H_2O-TMA complex were found to range from 0.03 to 2.22 kcal mol^{-1} whereas the $\Delta G°$ calculated using the anharmonic calculated frequencies increased in range from 0.004 to 2.11 kcal mol^{-1}.

Table 5.4: Harmonic and anharmonic calculations of Gibbs free energy, entropy and enthalpy of the complex.

	$\Delta G°$ (kcal mol^{-1})		$\Delta H°$ (kcal mol^{-1})		$\Delta S°$ (kcal mol^{-1} K)	
	Harmonic	Anharmonic	Harmonic	Anharmonic	Harmonic	Anharmonic
CH_3COOH-H_2O	0.56	0.39	-9.50	-9.56	-0.034	-0.033
CH_3COOH-TMA	-1.67	-1.69	-12.96	-12.96	-0.038	-0.38
CH_3COOH-H_2O-TMA	0.03	0.004	-20.07	-20.08	-0.067	-0.067

To further understand the overall decrease of $\Delta G°$ the harmonic and anharmonic calculations of $\Delta H°$ and $\Delta S°$ of the complexes were analyzed and compared. Harmonic

$\Delta H°$ for the CH_3COOH-H_2O-TMA complex were found to range from -18.39 to -20.07 kcal mol^{-1} whereas the anharmonic $\Delta H°$ increased in range from -18.44 to -20.08 kcal mol^{-1}.

The addition of these molecules leads to an increased stability which is highlighted by the decrease in the overall enthalpy of the complex. As shown with the CH_3COOH-H_2O intermediate complex the loss of TMA decreases the overall stability of the complex and makes this process less favorable from an enthalpy perspective. However, this intermediate complex can re-hydrate and continue to grow in size with the further adsorption of H_2O, TMA or CH_3COOH.

5.6.3 Dipole Interactions

To better understand why CH_3COOH complexed with TMA and H_2O can serve as good nucleating agents the dipole moments of the individual monomers and complexes were calculated. The CH_3COOH monomer has a dipole moment of 3.82 Debye with the positive end of the dipole centered on the nitrogen atom and the negative end of the dipole moving towards the oxygen atoms. The H_2O monomer has a dipole moment of 1.89 Debye and the TMA monomer has a dipole moment of 0.62 Debye. Figure 8 shows CH_3COOH with its computed dipole moment. The length of the dipole vector is proportional to the magnitude of the dipole moment. When H_2O is added to CH_3COOH the dipole strength decreases to 1.26 Debye. Forming a complex with TMA increases the dipole moment to 2.21 Debye. With the inclusion of a H_2O molecule to the CH_3COOH-TMA complex to form the CH_3COOH-H_2O-TMA complex the dipole moment decreases

to 1.65 Debye. The increase in dipole strength and subsequent polarity with the inclusion of either H_2O or TMA to form complexes with CH_3COOH indicates that subsequent growth of the complex by addition of H_2O molecules will not only be enthalpically favorable but also impact the reaction rate.

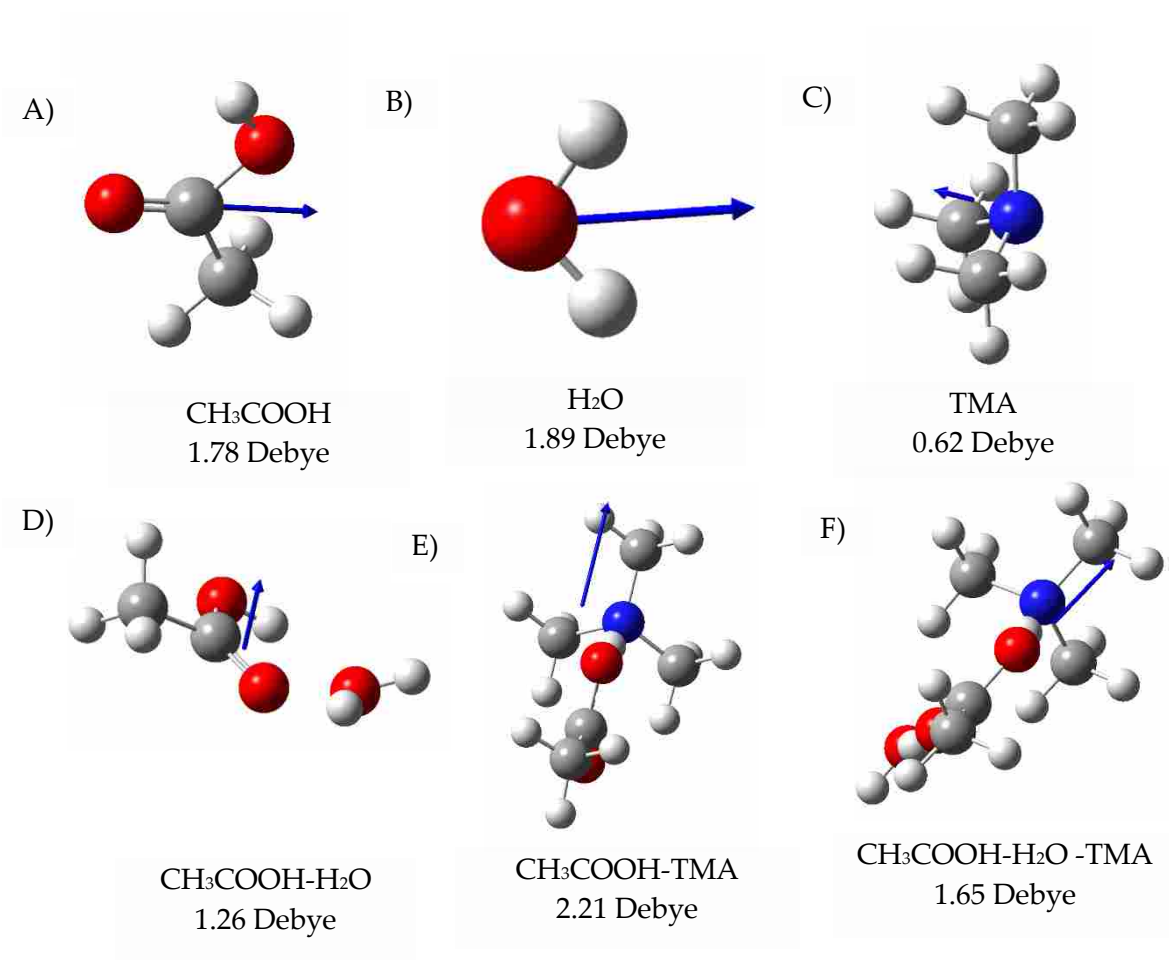

Figure 5.8: Dipole moments of monomers and complexes. A-acetic acid, B- water, C-trimethylamine, D- acetic acid -water dimer, E-acetic acid-trimethylamine dimer and F-acetic acid-water-trimethylamine complex

5.6.4 Electron Density Maps

To further understand the molecular interactions of the complex and dimer electron energy density maps were computed to provide additional information about the ability of the complex and dimer to serve as a nucleating site for particle formation. The change in electron density maps have been successfully used to show formation of

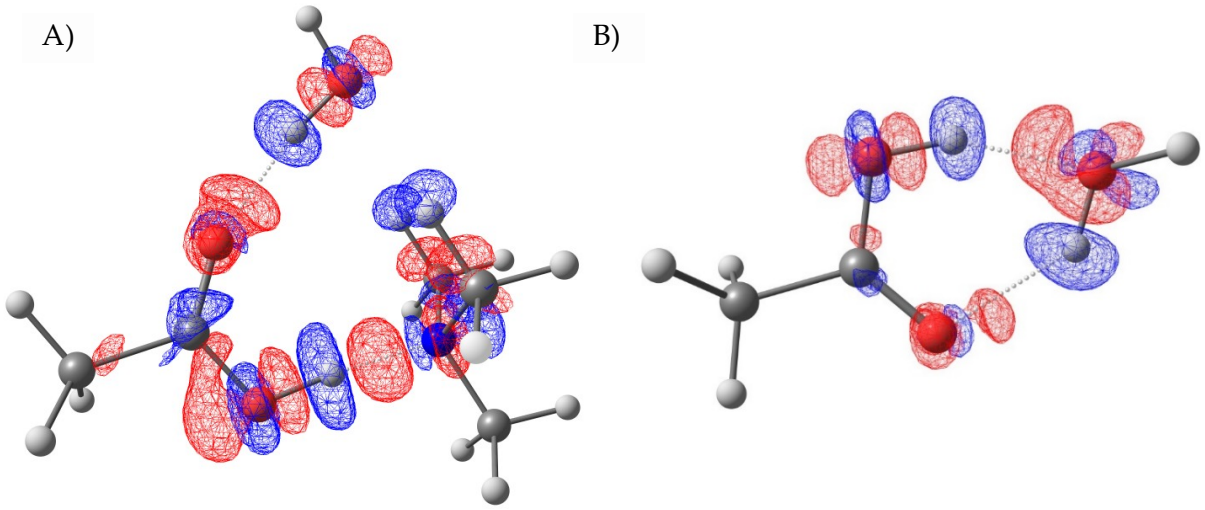

Figure 5.9: Electron density maps of A- CH3COOH-H2O-TMA complex and B- CH3COOH-H2O dimer

hydrogen bonds in complexes.[207] Additional hydrogen bonds provide added stability to the complex and/or dimer allowing for them to act as nucleating sites. Electron density difference maps were generated using a contour of 0.0003 e/au^3 with the M06-2X/aug-cc-pVDZ method/basis set[208]. The blue shaded regions in Figure 9 represent areas of electron density gain and red shaded regions represent areas of electron loss as a result of the complex formation. A prototypical hydrogen bond is evidenced by a region of electron density redistribution between the hydrogen atom and corresponding atom.

Correspondingly, along the axis of the hydrogen bond a region of electron density loss is typically observed around the bridging proton. In the CH_3COOH-H_2O-amine complex it is expected that several hydrogen bonds will form between CH_3COOH and H_2O, CH_3COOH and TMA and TMA and H_2O. As shown, there are prototypical hydrogen bonds formed between the CH_3COOH and H_2O, and CH_3COOH and TMA. However, there is a weak interaction between TMA and H_2O but should not be characterized as a prototypical hydrogen bond. In contrast, the CH_3COOH-H_2O complex shows two prototypical hydrogen bonds forming between CH_3COOH and H_2O. As previously noted, an ideal hydrogen bond has a 180° bond angle. The addition of TMA to the CH_3COOH-H_2O complex pushes the bond angle closer to 180°. This increase in bond angle further strengthens the stability of the complex and ability to act as a nucleating seed.

5.7 Conclusion

Ultrafine particles (UFPs) play an important role in the atmosphere and affect everyday life. As such pathways leading to UFP formation have become an increasingly important research focus. For example, one of the most recognized pathways for particle formation is the binary homogenous nucleation of sulfuric acid (H_2SO_4) complexed with water (H_2O). However, this pathway is insufficient to explain measured particle concentrations under atmospheric conditions which suggests alternative species may be participating in particle formation. As previously stated, measurements of the composition of ambient 10-33 nm diameter particles formed from

nucleation in Tecamac, Mexico shows the presence of carboxylic and hydroxycarboxylic organic acids, [11] indicating that organics play a dominant role in the nanoparticle growth. Our experiments have shown nanoparticle formation under conditions that are typically outside what is expected if classical nucleation theory is used to describe particle formation. Classical Nucleation Theory suggests that >100% relative humidity is necessary for particle formation and growth to occur however; our experiments conditions were always run under <100% relative humidity and still produced a large number of particles. Our computational results indicate that the addition of TMA to the CH_3COOH-H_2O complex increases the stability of the complex and its ability to act as a nucleating site.

Chapter 6

6.1 Conclusions

The gap between modeled and measured particle concentrations has become an increasingly important topic in the atmospheric chemistry community. The purpose of this dissertation is to identify non-prototypical sources that lead to particle formation that should be included in atmospheric models. The first study focused on providing an improved model to calculate the equilibrium constants for the formation of peroxy radical-water complexes. This was achieved by examining the hydrogen-bonded complexes of water with the hydroxyethyl peroxy radical (HEP) in conjunction with an improved LJ63+5HR model for quantifying the vibrational partition function used in calculation of the equilibrium constant for formation of the H_2O-HEP complex. It was shown that using the HORR approximation gives an underestimated partition function for weakly bound complexes. Instead improvements made to the LJ63+5HR model comes from treating the soft modes in the complex as hindered rotors with appropriate barriers and spin statistics.

Two subsequent follow-up studies (computational and experimental) investigated the role of carboxylic acids complexed with water vapor and enhanced by amines to serve as nucleating seeds for new particle formation under atmospheric conditions. The experimental studies of formic acid and acetic acid showed an increased

rate of particle nucleation with the addition of trace amounts of trimethylamine to the gas mixture. The experimental work on these two systems was complemented by computational studies which presented a mechanism by which these gases combine to grow to form ultrafine particles. In the formic acid study, it was shown that the $HCOO^{-}\cdot\cdot(CH_3)_3NH^{+}$ ion-pair interacted with water vapor to increase the stability of the nucleating cluster thereby leading to particle growth. The addition of trimethylamine to the formic acid/water vapor system using a slow flow reactor cell increased the rate of new particle formation. It was shown that not only was there an increase in smaller diameter particles, due to the large quantity of new particles being formed, but there was an increase in larger diameter particles due aggregation. In a similar manner, the acetic acid-water complex was also enhanced by the addition of trimethylamine. In the computational study of this system it was found that the addition of trimethylamine increased the overall binding energy of the complex, consistent with what was observed for formic acid, hydroperoxy radical and methanesulfonic acid complexes with water. The computational results of the acetic acid-water-amine system suggested that an experimental investigation of this system would produce similar results to that of formic acid. It was found that the slightly higher binding energy of acetic acid-water-amine system compared to the formic acid-water-amine system provides greater stability to the nucleation cluster which transferred to the experimental results. Using lower concentrations of acetic acid and trimethylamine than in the formic acid study led

to a larger increase in the concentration of smaller diameter particles and the aggregation of larger diameter particles. The implications of these findings indicate the necessity to research additional carboxylic acids as sources of new particle formation.

The carboxylic acid studies served as a catalyst for studying radical molecule-water complex induced particle formation. The final study included the computational analysis of the hydroperoxy radical complexed with water vapor and enhanced by amines or ammonia. It was determined that the addition of an amine to the hydroperoxy radical-water complex increased the stability of the nucleation complex. The increased stability came from the formation of additional hydrogen bonds with the addition of amines or ammonia as shown by changes in electron density. It was determined that trimethylamine and dimethylamine had the greatest stabilizing factor followed by methylamine and lastly ammonia. When compared to prototypical systems, such as sulfuric acid and methanesulfonic acid complexed with water and amines, the hydroperoxy radical-water vapor-trimethylamine nucleation complex had binding energies either equal to or slightly less than those systems. Comparison of prototypical systems to the non-prototypical systems presented in this dissertation show that carboxylic acids and hydroperoxy radical may serve as significant sources of new particle formation in the atmosphere.

6.2 Future Work

The next step in this research is to apply the carboxylic acid experimental set-up to investigation of hydroperoxy radical as a possible nucleating seed for particle formation under atmospheric conditions. The implications of the computational findings of hydroperoxy radical serving as a nucleating seed in conjunction with water vapor and trace amounts of amines indicate the necessity to further research the role of additional peroxy radicals in particle formation.

Peroxy radicals (RO_2) have a vital role in atmospheric chemistry particularly the formation and degradation of NO_x[2, 283, 284]and O_3. However, the role of RO_2 in new particle formation has yet to be considered. Like the HO_2 (10^8 molecules cm^{-3}, lifetime ~1.3 ms[88, 94, 115, 285-288]), RO_2 have a total concentration ranging from 10^{8-9} molecules cm^{-3} [283, 289-292] and have lifetimes ranging from 1 to 100 seconds[289, 293]. RO_2 are formed from volatile organic compounds (VOCs) and hydrocarbons (RH) found in the atmosphere. Hydrocarbons will react with the hydroxyl radical (OH), chlorine radical (Cl) or nitrate radical (NO_3) to form RO_2 (eq 1- 2)

$$RH + OH/Cl/NO_3 \longrightarrow R\bullet + H_2O/HCl/HNO_3 \qquad \text{(eq. 1)}$$

$$R\bullet + O_2 + M \longrightarrow RO_2 + M \qquad \text{(eq. 2)}$$

Another source includes the oxidation of olefins with ozone (O_3) which can lead to nighttime formation of RO_2[288]. Research previously done in the Hansen lab indicated that a RO_2-water complex with a binding energy greater than 5 kcal/mol may act as a nucleating site[204, 294]. These RO_2-water complexes may then be enhanced by the addition of an amine. Further research on RO_2 includes computational analysis of an amine enhancement followed by experimental research. Using the same computational and experimental process the discovered results may produce additional pathways for new particle formation from RO_2 complexed with water enhanced by amines. These pathways can then be applied to predictive models to improve their accuracy.

References

1. Carslaw, K. S., Cosmic rays, clouds and climate. *Nature* **2009,** *460*, 332-333.

2. Finlayson-Pitts, B. J.; Pitts, J. N., *Upper and Lower Atmosphere*. Academic Press: San Diego, 2000.

3. Particles, H. R. P. o. U., Understanding the Health Effects of Ambient Ultrafine Particles. In *HEI Perspective 3*, Health Effects Institute: Boston,MA, 2013; pp 1-122.

4. Morawska, L., Moore, M.R., Ristovski, Z.D. , *Health Impacts of Ultrafine Particles*. Commonwealth of Australia

Australia 2004; p 291.

5. Mater, P., *Environmental Outlook to 2050: The Consequences of Inaction: Key Findings on Health and Environment*. 2012.

6. Pope, C. A.; Dockery, D. W., Health Effects of Fine Particulate Air Pollution: Lines That Connect. *J. Air Waste Manage. Assoc.* **2006,** *56*, 709.

7. Dockery, D. W.; Pope, C. A., Acute Respiratory Effects of Particulate Air-Pollution. *Annu. Rev. Public Health* **1994,** *15*, 107.

8. Solomon, S., Qin, D, Manning, M., Chen, Z., Marquis, M., Averyt, K.B., Tignor, M., Miller, H.L., Eds.; *Contribution of Working Group I to the Fourth Assessment Report of*

the Intergovernmental Panel on Climate Change; Cambridge University Press, Cambridge, United Kingdom, 2007.

9. Fan, J. W.; Zhang, R. Y.; Li, G. H.; Tao, W. K.; Li, X. W., Simulations of Cumulus Clouds Using a Spectral Microphysics Cloud-Resolving Model. *J. Geophys. Res.* **2007,** *112*, D04201.

10. Zhang, R., Getting to the Critical Nucleus of Aerosol Formation. *Science* **2010,** *328* (5984), 1366.

11. Zhang, R.; Khalizov, A.; Wang, L.; Hu, M.; Xu, W., Nucleation and Growth of Nanoparticles in the Atmosphere. *Chemical Reviews* **2012,** *112* (3), 1957-2011.

12. Poschl, U., Atmospheric Aerosols: Composition, Transformation, Climate and Health Effects. *Angew. Chem., Int. Ed.* **2005,** *44*, 7520.

13. Kulmala, M.; Kerminen, V.-M., On the formation and growth of atmospheric nanoparticles. *Atmospheric Research* **2008,** *90* (2), 132-150.

14. Brock, C. A.; Trainer, M.; Ryerson, T. B.; Neuman, J. A.; Parrish, D. D.; Holloway, J. S.; Nicks, D. K.; Frost, G. J.; Hübler, G.; Fehsenfeld, F. C.; Wilson, J. C.; Reeves, J. M.; Lafleur, B. G.; Hilbert, H.; Atlas, E. L.; Donnelly, S. G.; Schauffler, S. M.; Stroud, V. R.; Wiedinmyer, C., Particle Growth in Urban and Industrial Plumes in Texas. *J. Geophys. Res.* **2003,** *108*.

15. Zhang, R. Y.; Lei, W. F.; Tie, X. X.; Hess, P., Industrial Emissions Cause Extreme Diurnal Urban Ozone Variability. *Proc. Natl. Acad. Sci. U.S.A.* **2004,** *101*, 6346.

16. Almanza, V. H.; Molina, L. T.; Li, G.; Fast, J.; Sosa, G., Impact of External Industrial Sources on the Regional and Local SO2 and O3 Levels of the Mexico Megacity. *Atmos. Chem. Phys.* **2014,** *14*, 8483.

17. Miguel, A. H.; Kirchstetter, T. W.; Harley, R. A.; Hering, S. V., On-Road Emissions of Particulate Polycyclic Aromatic Hydrocarbons and Black Carbon from Gasoline and Diesel Vehicles. *Environmental science & technology* **1998,** *32* (4), 450-455.

18. Chan, T. L.; Ning, Z.; Wang, J. S.; Cheung, C. S.; Leung, C. W.; Hung, W. T., Gaseous and Particle Emission Factors from the Selected On-Road Petrol/Gasoline, Diesel, and Liquefied Petroleum Gas Vehicles. *Energy & Fuels* **2007,** *21* (5), 2710-2718.

19. Takahama, S.; Russell, L. M.; Shores, C. A.; Marr, L. C.; Zheng, J.; Levy, M.; Zhang, R.; Castillo, E.; Rodriguez-Ventura, J. G.; Quintana, P. J. E.; Subramanian, R.; Zavala, M.; Molina, L. T., Diesel Vehicle and Urban Burning Contributions to Black Carbon Concentrations and Size Distributions in Tijuana, Mexico, during the Cal-Mex 2010 Campaign. *Atmos. Environ.* **2014,** *88*, 341.

20. Mkoma, S. L.; da Rocha, G. O.; Regis, A. C. D.; Domingos, J. S. S.; Santos, J. V. S.; de Andrade, S. J.; Carvalho, L. S.; de Andrade, J. B., Major ions in PM2.5 and PM10 released from buses: The use of diesel/biodiesel fuels under real conditions. *Fuel* **2014,** *115*, 109-117.

21. Shi, J. P.; Harrison, R. M., Investigation of Ultrafine Particle Formation during Diesel Exhaust Dilution. *Environmental science & technology* **1999,** *33* (21), 3730-3736.

22. Carslaw, K. S.; Lee, L. A.; Reddington, C. L.; Pringle, K. J.; Rap, A.; Forster, P. M.; Mann, G. W.; Spracklen, D. V.; Woodhouse, M. T.; Regayre, L. A.; Pierce, J. R., Large contribution of natural aerosols to uncertainty in indirect forcing. *Nature* **2013,** *503* (7474), 67-71.

23. Curtius, J., Nucleation of atmospheric aerosol particles. *Comptes Rendus Physique* **2006,** *7* (9-10), 1027-1045.

24. Becker, R.; Doring, W., Kinetic treatment of the nucleation of supersaturated vapors. *Ann. Phys.-Berlin* **1935,** *24*, 719.

25. Frenkel, J., Statistical Theory of Condensation Phenomena. *J. Chem. Phys.* **1939,** *7*, 200.

26. Szulejko, J. E.; Kim, K.-H., A review of sampling and pretreatment techniques for the collection of airborne amines. *TrAC Trends in Analytical Chemistry* **2014,** *57*, 118-134.

27. Sintermann, J.; Schallhart, S.; Kajos, M.; Jocher, M.; Bracher, A.; Münger, A.; Johnson, D.; Neftel, A.; Ruuskanen, T., Trimethylamine emissions in animal husbandry. *Biogeosciences* **2014,** *11* (18), 5073-5085.

28. Ge, X. L.; Wexler, A. S.; Clegg, S. L., Atmospheric Amines-Part I. A review. *Atmos. Environ.* **2011,** *45* (3), 524-546.

29. Ge, X.; Wexler, A. S.; Clegg, S. L., Atmospheric amines – Part II. Thermodynamic properties and gas/particle partitioning. *Atmospheric Environment* **2011,** *45* (3), 561-577.

30. Kuhn, U.; Sintermann, J.; Spirig, C.; Jocher, M.; Ammann, C.; Neftel, A., Basic biogenic aerosol precursors: Agricultural source attribution of volatile amines revised. *Geophysical Research Letters* **2011,** *38* (16), n/a-n/a.

31. Gibb, S. W.; Mantoura, R. F. C.; Liss, P. S., Ocean-atmosphere exchange and atmospheric speciation of ammonia and methylamines in the region of the NW Arabian Sea. *Global Biogeochemical Cycles* **1999,** *13* (1), 161-178.

32. Facchini, M. C.; Decesari, S.; Rinaldi, M.; Carbone, C.; Finessi, E.; Mircea, M.; Fuzzi, S.; Moretti, F.; Tagliavini, E.; Ceburnis, D.; O'Dowd, C. D., Important Source of Marine Secondary Organic Aerosol from Biogenic Amines. *Environmental science & technology* **2008,** *42* (24), 9116-9121.

33. Behera, S. N.; Sharma, M.; Aneja, V. P., Ammonia in the atmosphere: A review on emission sources, atmospheric chemistry and deposition on terrestrial bodies. *Environ Sci Pollut Res* **2013**, 8092-9131.

34. Behera, S. N.; Betha, R.; Liu, P.; Balasubramanian, R., A study of diurnal variations of $PM_{2.5}$ acidity and related chemical species using a new thermodynamic equilibrium model. *Sci Total Environ* **2013,** (452), 286-295.

35. Swartz, E.; Shi, Z.; Davidovits, P.; Jayne, J. T.; Worsnop, D. R.; Kolb, C. E., Utpake of gas-phase ammonia, 2. Uptake by sulfuric acid surfaces. *The journal of physical chemistry. A* **1999,** *103* (8824-8833).

36. Xue, J.; Lau, A. K.; YU, J. Z., A Study of Acidity on PM2.5 in Hong Kong using onling ionic chemical composition measurements. *Atmos. Environ.* **2011,** *39* (45), 7081-7088.

37. Behera, S. N.; Sharma, M., Transformation of atmospheric ammonia and acid gases into components of $PM_{2.5}$: an environmental chamber study. *Environ Sci Pollut Res Int* **2012,** *4* (19), 1187-1197.

38. Chen, H.; Ezell, M. J.; Arquero, K. D.; Varner, M. E.; Dawson, M. L.; Gerber, R. B.; Finlayson-Pitts, B. J., New particle formation and growth from methanesulfonic acid, trimethylamine and water. *Physical chemistry chemical physics : PCCP* **2015,** *17* (20), 13699-709.

39. Chen, H.; Ezell, M. J.; Arquero, K. D.; Varner, M. E.; Dawson, M. L.; Gerber, R. B.; Finlayson-Pitts, B. J., New particle formation and growt from methanesulfonic acid, trimethylamin and water. *Physical chemistry chemical physics : PCCP* **2015,** *17*, 13699-13709.

40. Zollner, J. H.; Glasoe, W. A.; Panta, B.; Carlson, K. K.; McMurry, P. H.; Hanson, D. R., Sulfuric Acid Nucleation: Power Dependencies, Variation with Relative Humidity, and Effect of Bases. *Atmos. Chem. Phys.* **2012,** *12*, 4399.

41. Glasoe, W. A.; Volz, K.; Panta, B.; Freshour, N.; Bachman, R.; Hanson, D. R.; McMurry, P. H.; Jen, C., Sulfuric acid nucleation: An experimental study of the effect of seven bases. *Journal of Geophysical Research: Atmospheres* **2015,** *120* (5), 1933-1950.

42. Jen, C. N.; McMurry, P. H.; Hanson, D. R., Stabilization of sulfuric acid dimers by ammonia, methylamine, dimethylamine, and trimethylamine. *Journal of Geophysical Research: Atmospheres* **2014,** *119* (12), 7502-7514.

43. Neitola, K.; Brus, D.; Makkonen, U.; Sipila, M.; Lihavainen, H.; Kulmala, M., Effect of addition of four base compounds on sulphuric-acid-water new partical formation: a laboratory study. *Boreal Env. Res.* **2014,** *19* ((suppl. B)), 257-274.

44. Murphy, S. M.; Sorooshian, A.; Kroll, J. H.; Ng, N. L.; Chhabra, P.; Tong, C.; Surratt, J. D.; Knipping, E.; Flagan, R. C.; Seinfeld, J. H., Secondary aerosol formation from atmospheric reactions of aliphatic amines. *Atmospheric Chemistry and Physics* **2007,** *7*, 2343-2337.

45. Arquero, K. D.; Xu, J.; Gerber, R. B.; Finlayson-Pitts, B. J., Particle formation and growth from oxalic acid, methanesulfonic acid, trimethylamine and water: a combined experimental and theoretical study. *Physical Chemistry Chemical Physics* **2017,** *19* (41), 28286-28301.

46. Arquero, K. D.; Gerber, R. B.; Finlayson-Pitts, B. J., The Role of Oxalic Acid in New Particle Formation from Methanesulfonic Acid, Methylamine, and Water. *Environmental science & technology* **2017,** *51* (4), 2124-2130.

47. Millet, D. B.; Bassandor, M.; Farmer, D. K.; Thornton, J. A.; Baumann, K.; Brophy, P.; Chaliyakunnel, S.; de Gouw, J. A.; Graus, M.; Hu, L.; Koss, A.; Lee, B. H.; Lopez-Hilfiker, F. D.; Neuman, J. A.; Paulot, F.; Peischl, J.; Pollack, I. B.; Ryerson, T. B.; Warneke, C.; Williams, B. J.; Xu, J., A large ubiquitous source of atmospheric formic acid. *Atmos. Chem. Phys.* **2015,** *15*, 6283-6304.

48. Shaw, M. F.; Stztaray, B.; Whalley, L. K.; Heard, D. E.; Millet, D. B.; Jordan, M. J. T.; Osborn, D. L.; Kable, S. H., Photo-tautomerization of acetaldehyde as a photocheical source of formic acid in the troposphere. *Nature Communications* **2018,** *9*, 2584-2591.

49. Paulot, F.; Wunch, D.; Crounse, J. D.; Toon, G. C.; Millet, D. B.; DeCarlo, P. F.; Vigouroux, C.; Deutsher, N. M.; Gonzalez, A.; Notholt, J.; Warneke, T.; Hannigan, J. W.; Warneke, C.; de Gouw, J. A.; Dunlea, E. J.; De Maziere, M.; Griffith, D.; Bernath, W. T.; Jimenez, P.; Wennberg, P. O., Importance of secondary sources in the atmospheric budgets of formic and acetic acids. *Atmos. Chem. Phys.* **2011,** *11*, 1989-2013.

50. Millet, D. B.; Donahue, N. M.; Pandis, S. N.; Polidori, A.; Stanier, C. O.; Turpin, B. J.; Goldstein, A. H., Atmospheric Volatile Organic Compound Measurements during the Pittsburgh Air Quality Study: Results, Interpretation, and Quantification of Primary and Secondary Contributions. *J. Geophys. Res.* **2005,** *110*.

51. Atkinson, R.; Baulch, D. L.; Cox, R. A.; Crowley, J. N.; Hampson, R. F.; Hynes, R. G.; Jenkin, M. E.; Rossi, M. J.; Troe, J., Evaluated Kinetic and Photochemical Data for Atmospheric Chemistry: Volume I—Gas Phase Reactions of Ox, HOx, NOx and SOx Species. *Atmos. Chem. Phys.* **2004,** *4*, 1461.

52. Atkinson, R.; Baulch, D. L.; Cox, R. A.; Crowley, J. N.; Hampson, R. F.; Hynes, R. G.; Jenkin, M. E.; Rossi, M. J.; Troe, J.; Subcommittee, I., Evaluated kinetic and photochemical data for atmospheric chemistry: Volume II – gas phase reactions of organic species. *Atmos. Chem. Phys.* **2006,** *6*, 3625-4055.

53. Hasson, A. S.; Orzechowska, G.; Paulson, S. E., Production of stabilized Criegee intermediates and peroxides in the gas phase ozonolysis of alkenes: 1. Ethene,trans-2-butene, and 2,3-dimethyl-2-butene. *J. Geophys. Res.* **2001,** *106* (34131-34142).

54. Neeb, P.; Horie, O.; Moortgat, G. K., Gas-phase ozonolysis of ethene in the presence of hydroxylic compounds. *Int. J. Chem. Kinet.* **1996,** *28*, 721-730.

55. Neeb, P.; Sauer, F.; Horie, O.; Moortgat, G. K., Formation of hydroxymethyl hydroperoxide and formic acid in alkene ozonolysis in the presence of water vapour. *Atmos. Environ.* **1997,** *31* (1417-1423).

56. Bohn, B.; Siese, M.; Zetzschn, C., Bohn, B., Siese, M., and Zetzschn, C. *J. Chem. Soc., Faraday Trans.*, **1996,** *92*, 1459-1466.

57. Hatakeyama, S.; Washida, N.; Akimoto, H., Rate constants and mechanisms for the reaction of OH (OD) radicals with acetylene, propyne, and 2-butyne in air at 297 ± 2 K. *J. Phys. Chem.* **1986,** *90* (173-178).

58. Hatakeyama, S.; Akimoto, H., Reactions of Criegee intermediates in the gas phase. *Res. Chem. Intermed* **1994,** *20*, 503-524.

59. Paulot, F.; Crounse, J. D.; Kjaergaard, H. G.; Kurten, A.; Clair, J. M.; Seinfeld, J. H.; Wennberg, P. O., Unexpected Epoxide Formation in the Gas-Phase Photooxidation of Isoprene. *Science* **2009,** *325*, 730.

60. Paulot, F.; Henze, D. K.; Wennberg, P. O., Impact of the isoprene photochemical cascade on tropical ozone. *Atmospheric Chemistry and Physics* **2012,** *12* (3), 1307-1325.

61. Paulot, F.; Jacob, D. J., Hidden cost of U.S. agricultural exports: particulate matter from ammonia emissions. *Environmental science & technology* **2014,** *48* (2), 903-8.

62. Crounse, J. D.; Paulot, F.; Kjaergaard, H. G.; Wennberg, P. O., Peroxy radical isomerization in the oxidation of isoprene. *Physical chemistry chemical physics : PCCP* **2011,** *13* (30), 13607-13.

63. Paulot, F.; Crounse, J. D.; Kjaergaard, H. G.; Kroll, J. H.; Seinfeld, J. H.; Wennberg, P. O., Isoprene photooxidation: new insights into the production of acids and organic nitrates. *Atmos. Chem. Phys.* **2009a,** *9*, 1479-1501.

64. Crounse, J. D.; Knap, H. C.; Ornso, K. B.; Jorgensen, S.; Paulot, F.; Kjaergaard, H. G.; Wennberg, P. O., Atmospheric fate of methacrolein. 1. Peroxy radical isomerization following addition of OH and O2. *J. Phys. Chem. A* **2012,** *116*, 5756-5762.

65. Archibald, A. T.; Petit, A. S.; Percival, C. J.; Harvey, J. N.; Shallcross, D. E., On the importance of the reaction between OH and RO2 radicals. *Atmos. Sci. Lett.* **2009,** *10* (102-109).

66. Bossolasco, A.; Faragó, E. P.; Schoemaecker, C.; Fittschen, C., Rate constant of the reaction between CH3O2 and OH radicals. *Chem. Phys. Lett.* **2014,** *593*, 7-13.

67. Singh, H. B.; Brune, W. H.; Crawford, J. H.; Jacob, D. J.; Russell, P. B., Overview of the summer 2004 intercontinental chemical transport experiment – North America (INTEX-A). *J. Geophys. Res.* **2006,** *111*, D24S01.

68. Singh, H. B.; Brune, W. H.; Crawford, J. H.; Flocke, F.; Jacob, D. J., Chemistry and transport of pollution over the Gulf of Mexico and the Pacific: spring 2006 INTEX-B campaign overview and first results. *Atmos. Chem. Phys.* **2009,** *9*, 2301-2318.

69. Andrews, D. U.; Heazlewood, B. R.; Maccarone, A. T.; Conroy, T.; Payne, R. J.; Jordan, M. J. T.; Kable, S. H., Photo-Tautomerization of Acetaldehyde to Vinyl Alcohol: A Potential Route to Tropospheric Acids. *Science* **2012,** *337* (6099), 1203-1206.

70. Archibald, A. T.; McGillen, M. R.; Taatjes, C. A.; Percival, C. J.; Shallcross, D. E., Atmospheric transformation of enols: A potential secondary source of carboxylic acids in the urban troposphere. *Geophys. Res. Lett.* **2007,** *34*, L21801.

71. So, S.; Wille, U.; da Silva, G., Atmospheric chemistry of enols: A theoretical study of the vinyl alcohol + OH + O2 reaction

mechanism. *Environ. Sci. Technol.* **2014,** *48* (6694-6701).

72. Goode, J. G.; Yokelson, R. J.; Ward, D. E.; Susott, R. A.; Babbitt, R. E.; Davies, M. A.; Hao, W. M., Measurements of excess O3, CO2, CO, CH4, C2H4, C2H2, HCN, NO, NH3, HCOOH, CH3COOH, HCHO, and CH3OH in 1997 Alaskan biomass burning plumes by airborne Fourier transform infrared spectroscopy *J. Geophys. Res.* **2000,** *105* (D17), 22147-22166.

73. Kawamura, K.; Steinberg, S.; Kaplan, I. R., Homologous series of C1–C10 monocarboxylic acids and C1–C6 carbonyls in Los Angeles air and motor vehicle exhausts. *Atmospheric Environment* **2000,** *34* (24), 4175-4191.

74. Kawamura, K.; Ng, L. L.; Kaplan, I. R., Determination of organic acids (C•-C•o) in the atmosphere, motor exhaust and engine oils,. *Environ. Sci. Technol.* **1985,** *19*, 1081-1086.

75. Kawamura, K.; Kaplan, I. R., Motor exhaust emissions as a primary source for dicarboxylic acids in Los Angeles ambient air. *Environmental science & technology* **1987,** *21* (1), 105-110.

76. Talbot, R. W.; Mosher, B. W.; Heikes, B. G.; Jacob, D. J.; Munger, B. C.; Daube, B. C.; Keene, W. C.; Maben, J. R.; Artz, R. S., Carboxylic acids in the rural continental atmosphere over the eastern United States during the Shenandoah Cloud and Photochemistry Experiment. *J. Geophys. Res.* **1995,** *100* (D5), 9335-9343.

77. Sanhueza, E.; Figueroa, L.; Santana, M., Atmospheric formic and acetic acids in Venezuela. *Atmos. Environ.* **1996,** *30* (1861-1873).

78. Sanhueza, E.; Andreae, M. O., Emmission of formic acid and acetic acid from tropical savanna soils *Geophys. Res. Lett.* **1991,** *18*, 1707-1710.

79. Andreae, M. O.; Talbot, R. W.; Andreae, T. W.; Harris, R. C., Formic and acetic acid over the central Amazon region, Brazil: 1. Dry season. *J. Geophys. Res.* **1988,** *93* (D2), 1616-1624.

80. Enders, G.; Dlugi, R.; Steincrecher, R.; Clement, B.; Daiber, R.; Eijik, J. V.; Gab, S.; Haziza, M.; Helas, G.; Hermann, U.; Kessel, M.; Kesselmeier, J.; Kotzias, D.; Kourtidis, K.; Kurth, H. H.; McMillen, R. T.; Roider, G.; Schurmann, W.; Teichmann,

U.; Torres, L., Biosphere/atmosphere interactions: integrated research in a European forest ecosystem. *Atmos. Environ.* **1992,** *26a* (171-189).

81. Keene, W. C.; Galloway, J. N., The biogeochemical cycling of formic and acetic acids through the troposphere: an overview of current understanding. *Tellus, Ser. B: Chem. Phys. Meteorol.* **1988,** *40* (5), 322-334.

82. Talbot, R. W.; Andreae, M. O.; Berresein, H.; Jacob, D. J.; Beecher, K. M., Sources and sinks of formic, acetic, and pyruvic acids over central Amazonia. 2. Wet season. *J. Geophys. Res.* **1990,** *95* (D10), 16799-16811.

83. Staudt, M.; Wolf, A.; Kesselmeir, J., Influence of environmental factors on the emissions of gaseous formic and acetic acids from orange (Citrus sinensis L.) foliage. *Biogeochemistry* **2000,** *48*, 199-216.

84. Kesselmeir, J.; Staudt, M., Biogenic volatile organic compounds (VOC): An overview on emission, physiology and ecology. *J. Atmos. Chem.* **1999,** *33*, 23-88.

85. Ying, Q.; Cureño, I. V.; Chen, G.; Ali, S.; Zhang, H.; Malloy, M.; Bravo, H. A.; Sosa, R., Impacts of Stabilized Criegee Intermediates, Surface Uptake Processes and Higher Aromatic Secondary Organic Aerosol Yields on Predicted PM2.5 Concentrations in the Mexico City Metropolitan Zone. *Atmos. Environ.* **2014,** *94*, 438.

86. Welz, O.; Savee, J. D.; Osborn, D. L.; Vasu, S. S.; Percival, C. J.; Shallcross, D. E.; Taatjes, C. A., Direct Kinetic Measurements of Criegee Intermediate (CH2OO) Formed by Reaction of CH2I with O2. *Science* **2012,** *335*, 204.

87. Niki, H.; Maker, P. D.; Savage, C. M.; Breitenbach, L. P., FTIR study of the kinetics and mechanism for chlorine-atom-initiated reactions of acetaldehyde. *J. Phys. Chem.* **1985,** *89* (4), 588-591.

88. Moortgat, G. K.; Veyret, B.; Lesclaux, R., Kinetics of the reaction of hydroperoxo (HO2) with peroxyacetyl [CH3C(O)O2] in the temperature range 253-368 K. *Chem. Phys. Lett.* **1989,** *160* (4), 443-447.

89. Madronich, S.; Calvert, J. G., Permutation reactions of organic peroxy radicals in the troposphere. *J. Geophys. Res.* **1990,** *95* (D5), 5697-5715.

90. Moortgat, G. K.; Veyret, B.; Lesclaux, R., Absorption spectrum and kinetics of reactions of the acetylperoxy radical. *J. Phys. Chem.* **1989,** *93* (6), 2362-2368.

91. Wollenhaupt, M.; Crowley, J. N., Kinetic Studies of the Reactions CH_3 + NO2 → Products, CH3O + NO2 → Products, and OH + CH3C(O)CH3 → CH3C(O)OH + CH3, over a Range of Temperature and Pressure. *J. Phys. Chem. A* **2000,** *104*, 6429-6438.

92. Wollenhaupt, M.; Carl, S. A.; Horowitz, A.; Crowley, J. N., Rate Coefficients for Reaction of OH with Acetone between 202 and 395 K. *J. Phys. Chem. A.* **2000,** *104*, 2695-2705.

93. Khare, P.; Kumar, N.; Kumari, K.; S. Srivastava, S., *Atmospheric formic and acetic acids: An overview*. 1999; Vol. 37, p 227-248.

94. Stone, D.; Whalley, L. K.; Heard, D. E., Tropospheric OH and HO2 radicals: field measurements and model comparisons. *Chemical Society reviews* **2012,** *41* (19), 6348-404.

95. Jefferson, A.; Tanner, D. J.; Eisele, F. L.; Berresheim, H., Sources and sinks of H2SO4in the remote Antarctic marine boundary layer. *Journal of Geophysical Research: Atmospheres* **1998,** *103* (D1), 1639-1645.

96. Olin, M.; Alanen, J.; Palmroth, M. R. T.; Rönkkö, T.; Dal Maso, M., Inversely modeling homogeneous H2SO4-H2O nucleation rate in exhaust-related conditions. *Atmospheric Chemistry and Physics* **2019,** *19* (9), 6367-6388.

97. Zollner, J. H.; Glasoe, W. A.; Panta, B.; Carlson, K. K.; McMurry, P. H.; Hanson, D. R., Sulfuric acid nucleation: power dependencies, variation with relative humidity, and effect of bases. *Atmospheric Chemistry and Physics* **2012,** *12* (10), 4399-4411.

98. Zhao, J.; Smith, J. N.; Eisele, F. L.; Chen, M.; Kuang, C.; McMurry, P. H., Observation of neutral sulfuric acid-amine containing clusters in laboratory and ambient measurements. *Atmospheric Chemistry and Physics* **2011,** *11* (21), 10823-10836.

99. Sipilä, M.; Berndt, T.; Petäjä, T.; Brus, D.; Vanhanen, J.; Stratmann, F.; Patokoski, J.; Mauldin, R. L.; Hyvärinen, A.-P.; Lihavainen, H.; Kulmala, M., The Role of Sulfuric Acid in Atmospheric Nucleation. *Science* **2010,** *327* (5970), 1243.

100. Xu, J.; Finlayson-Pitts, B. J.; Gerber, R. B., Proton Transfer in Mixed Clusters of Methanesulfonic Acid, Methylamine, and Oxalic Acid: Implications for Atmospheric Particle Formation. *The Journal of Physical Chemistry A* **2017,** *121* (12), 2377-2385.

101. Schweitzer, F.; Magi, L.; Mirabel, P.; George, C., Uptake Rate Measurements of Methanesulfonic Acid and Glyoxal by Aqueous Droplets. *J. Phys. Chem. A* **1998,** *102*, 593.

102. Alolsio, S.; Francisco, J. S.; Friedl, R. R., Experimental Evidence for the Existence of the HO2-H2O Complex. *The journal of physical chemistry. A* **2000,** *104* (28), 6597-6601.

103. Alolsio, S.; Francisco, J. S., Existence of a Hydroperoxy and Water (HO2*H20) Radical Complex. *J Phys Chem* **1998,** *102* (11), 1899-1902.

104. Suma, K.; Sumiyoshi, Y.; Endo, Y., The Rotational Spectrum of the Water-Hydroperoxy Radical (HO2-H2O) Complex. *Science* **2006,** *311*, 1278-1280.

105. Albrecht, S. R.; Novelli, A.; Hofzumahaus, A.; Kang, S.; Baker, Y.; Mentel, T.; Wahner, A.; Fuchs, H., Measurements of hydroperoxy radicals (HO₂) at atmospheric concentrations using bromide chemical ionisation mass spectrometry. *Atmospheric Measurement Techniques* **2019,** *12* (2), 891-902.

106. Hornbrook, R. S.; Crawford, J. H.; Edwards, G. D.; Goyea, O.; Mauldin Iii, R. L.; Olson, J. S.; Cantrell, C. A., Measurements of tropospheric HO₂ and RO₂ by oxygen dilution modulation and chemical ionization mass spectrometry. *Atmospheric Measurement Techniques* **2011,** *4* (4), 735-756.

107. Piccot, S. D.; Watson, J. J.; Jones, J. W., A global inventory of volatile organic compound emissions from anthropogenic sources. *Journal of Geophysical Research: Atmospheres* **1992,** *97* (D9), 9897-9912.

108. Guenther, A.; Hewitt, C. N.; Erickson, D.; Fall, R.; Geron, C.; Graedel, T.; Harley, P.; Klinger, L.; Lerdau, M.; Mckay, W. A.; Pierce, T.; Scholes, B.; Steinbrecher, R.; Tallamraju, R.; Taylor, J.; Zimmerman, P., A global model of natural volatile

organic compound emissions. *Journal of Geophysical Research: Atmospheres* **1995,** *100* (D5), 8873-8892.

109. Finlayson-Pitts, B. J.; Pitts, J. N. J., *Atmospheric chemistry. Fundamentals and experimental techniques*. United States, 1986.

110. Donahue, N. M.; Kroll, J. H.; Anderson, J. G.; Demerjian, K. L., Direct observation of OH production from the ozonolysis of olefins. *Geophysical Research Letters* **1998,** *25* (1), 59-62.

111. J., R. F.; Ha, T. K.; Gunthard, H. H., DETECTION AND IDENTlFlCATlON OF FREE RADICALS IN THE GASEOUS-PHASE MICROREACTOR-MATRIX OZONOLYSIS OF ETHYLENE: ESR SPECTROSCOPY. *Chem Phys* **1983,** *74*, 273-299.

112. Atkinson, R., Gas-Phase Tropospheric Chemistry of Volatile Organic Compounds: 1. Alkanes and Alkenes. *Journal of Physical and Chemical Reference Data* **1997,** *26* (2), 215-290.

113. Peeters, J.; Nguyen, T. L.; Vereecken, L., HOx radical regeneration in the oxidation of isoprene. *Physical chemistry chemical physics : PCCP* **2009,** *11* (28), 5935-9.

114. Zhu, C.; Kumar, M.; Zhong, J.; Li, L.; Francisco, J. S.; Zeng, X. C., New Mechanistic Pathways for Criegee–Water Chemistry at the Air/Water Interface. *Journal of the American Chemical Society* **2016,** *138* (35), 11164-11169.

115. Mihelcic, D.; Heitlinger, M.; Kley, D.; Müsgen, P.; Volz-Thomas, A., Formation of hydroxyl and hydroperoxy radicals in the gas-phase ozonolysis of ethene. *Chemical Physics Letters* **1999,** *301* (5), 559-564.

116. Fang, Y.; Barber, V. P.; Klippenstein, S. J.; McCoy, A. B.; Lester, M. I., Tunneling effects in the unimolecular decay of (CH3)2COO Criegee intermediates to OH radical products. *J Chem Phys* **2017,** *146* (13), 134307.

117. Du, S.; Francisco, J. S., Interaction between OH Radical and the Water Interface. *J Phys Chem* **2008,** *112* (21), 4826-4835.

118. Clark, J.; English, M. A.; Hansen, J. C., Computational Study of the Existence of Organic Peroxy Radical-Water Complexex (RO2*H2)). *J. Phys. Chem. A* **2008,** *112* (7), 1587-1595.

119. Belair, S. D.; Herndandez, H.; Francisco, J. S., The Orgin of Sticking between a Hydroperoxy Radical and a Water Surface. *J. Am. Chem. Soc* **2004,** *126* (10), 3024-3025.

120. Alolsio, S.; Francisco, J. S., Experimental Evidence for the Existence of the HO2-H2O Complex. *J Phys Chem* **2000,** *104* (28), 6597-6601.

121. Riva, M.; Budisulistiorini, S. H.; Zhang, Z.; Gold, A.; Surratt, J. D., Chemical characterization of secondary organic aerosol constituents from isoprene ozonolysis in the presence of acidic aerosol. *Atmospheric Environment* **2015**.

122. Lightfoot, P. D.; Cox, R. A.; Crowley, J. N.; Destriau, M.; Hayman, G. D.; Jenkin, M. E.; Moortgat, G. K.; Zabel, F., Organic Peroxy radicals: Kinetics, spectroscopy, and tropospheric chemistry. *Atmos. Environ.* **1992,** *26A*, 1805-1961.

123. Guenther, A.; Hewitt, C. N.; Erickson, D.; Fall, R.; Geron, C.; Graedel, T.; Harley, P.; Klinger, L.; Lerdau, M.; McKay, W. A., A global model of natural volatile organic compound emissions. *Journal of Geophysical Research: Atmospheres* **1995,** *100* (D5), 8873-8892.

124. Blanksby, S. J.; Ramond, T. M.; Davico, G. E.; Nimlos, M. R.; Kato, S.; Bierbaum, V. M.; Lineberger, W. C.; Ellison, G. B.; Okumura, M., Negative-ion photoelectron spectroscopy, gas-phase acidity, and thermochemistry of the peroxyl radicals CH3OO and CH3CH2OO. *Journal of the American Chemical Society* **2001,** *123* (39), 9585-9596.

125. Kircher, C. C.; Sander, S. P., Kinetics and mechanism of hydroperoxo and hydroperoxo-d disproportionations. *Journal of Physical Chemistry* **1984,** *88* (10), 2082-2091.

126. Dockery, D. W.; Pope, C. A.; Xu, X.; Spengler, J. D.; Ware, J. H.; Fay, M. E.; Ferris, B. G.; Speizer, F. E., An Association between Air Pollution and Mortality in Six U.S. Cities. *New England J of Med* **1993,** *329* (24), 1753-1759.

127. Stocker, T. F.; Qin, D.; Plattner, G.-K.; Tignor, M. M.; Allen, S. K.; Boschung, J.; Nauels, A.; Xia, Y.; Bex, V.; Midgley, P. M., *Climate Change 2013: The physical science basis. contribution of working group I to the fifth assessment report of IPCC the intergovernmental panel on climate change*. Cambridge University Press: 2014.

128. Kaschiev, D., *Nucleation: Basic Theory With Applications.* . Oxford: Butterworth Heinemann: 2000.

129. Kumbhani, S. R., *Peroxy Radical-Water Complexes: Their Role in the Atmosphere*. Brigham Young University: Provo, Utah, 2015.

130. Hamilton, E. J.; Lii, R. R., The Dependence on H2O and on NH3 of the Kinetics of the self-reaction of HO2 in the gas-phase formation of HO2· H2O and HO2· NH3 complexes. *International Journal of Chemical Kinetics* **1977,** *9* (6), 875-885.

131. Sander, S. P.; Peterson, M.; Watson, R. T.; Patrick, R., Kinetics studies of the HO_2 + HO_2 and DO_2 + DO_2 reactions at 298 K. *J. Phys. Chem.* **1982,** *86* (8), 1236-1240.

132. DeMore, W. B., Reaction of HO_2 with O_3 and the effect of water-vapor on HO_2 kinetics. *J. Phys. Chem.* **1979,** *83*, 1113-1118.

133. Cox, R. A.; Burrows, J. P., Kinetics and mechanism of the disproportionation of hydroperoxyl radical in the gas phase. *Journal of Physical Chemistry* **1979,** *83* (20), 2560-2568.

134. Lii, R.-R.; Sauer Jr, M. C.; Gordon, S., Temperature dependence of the gas-phase self-reaction of hydroperoxo in the presence of water. *Journal of Physical Chemistry* **1981,** *85* (19), 2833-2834.

135. Kumbhani, S. R.; Cline, T. S.; Killian, M. C.; Clark, J. M.; Keeton, W. J.; Hansen, L. D.; Shirts, R. B.; Robichaud, D. J.; Hansen, J. C., Water vapor enhancement of rates of peroxy radical reactions. *International Journal of Chemical Kinetics* **2015,** *47* (6), 395-409.

136. Zhu, R.; Lin, M. C., Ab initio study of the catalytic effect of H 2 O on the self-reaction of HO 2. *Chemical physics letters* **2002,** *354* (3), 217-226.

137. McQuarrie, D. A., *Statistical Mechanics. Chapter 8-9*. Harper & Row: New York, 1976.

138. Harris, G. J.; Viti, S.; Mussa, H. Y.; Tennyson, J., Calculated high-temperature partition function and related thermodynamic data for H 2 16 O. *Journal of chemical physics* **1998,** *109* (17), 7197-7204.

139. Partridge, H.; Schwenke, D. W., The determination of an accurate isotope dependent potential energy surface for water from extensive ab initio calculations and experimental data. *Journal of Chemical Physics* **1997,** *106* (11), 4618-4639.

140. Vidler, M.; Tennyson, J., Accurate partition function and thermodynamic data for water. *Journal of Chemical Physics* **2000,** *113* (21), 9766-9771.

141. Frisch, M.; Trucks, G.; Schlegel, H.; Scuseria, G.; Robb, M.; Cheeseman, J.; Scalmani, G.; Barone, V.; Mennucci, B.; Petersson, G.; et., a. l., *Gaussian 09, revision B. 01*. Gaussian, Inc.: Wallingford CT, 2010.

142. Aloisio, S.; Francisco, J. S., Existence of a Hydroperoxy and Water (HO2⊙ H2O) Radical Complex. *Journal of Physical Chemistry A* **1998,** *102* (11), 1899-1902.

143. Alongi, K. S.; Dibble, T. S.; Shields, G. C.; Kirschner, K. N., Exploration of the Potential Energy Surfaces, Prediction of Atmospheric Concentrations, and Prediction of

Vibrational Spectra for the HO2⊙⊙⊙(H2O) n (n= 1− 2) Hydrogen Bonded Complexes. *Journal of Physical Chemistry A* **2006,** *110* (10), 3686-3691.

144. Cooksy, A., *Qunatam Chemistry and Molecular Interactions*. Pearson Boston, MA, 2014.

145. Levine, I. N., *Quantum Chemistry. 6th ed*. Pearson: Upper Saddle River, N. J., 2009.

146. Shirts, R. B., The computation of eigenvalues and solutions of Mathieu's differential equation for noninteger order. *ACM Trans on Math Soft (TOMS)* **1993,** *19* (3), 377-390.

147. Shirts, R. B., Algorithm 721: MTIEU1 and MTIEU2: two subroutines to compute eigenvalues and solutions to Mathieu's differential equation for noninteger and integer order. *ACM Trans on Math Soft (TOMS)* **1993,** *19* (3), 391-406.

148. Ruscic, B., Active thermochemical tables: Water and water dimer. *Journal of Physical Chemistry A* **2013,** *117* (46), 11940-11953.

149. Shank, A.; Wang, Y.; Kaledin, A.; Braams, B. J.; Bowman, J. M., Accurate ab initio and "hybrid" potential energy surfaces, intramolecular vibrational energies, and classical ir spectrum of the water dimer. *Journal of chemical physics* **2009,** *130* (14), 144314.

150. Huang, X.; Braams, B. J.; Bowman, J. M., Ab initio potential energy and dipole moment surfaces of (H2O) 2. *Journal of Physical Chemistry A* **2006,** *110* (2), 445-451.

151. Huang, X.; Braams, B. J.; Bowman, J. M.; Kelly, R. E.; Tennyson, J.; Groenenboom, G. C.; van der Avoird, A., New ab initio potential energy surface and the vibration-rotation-tunneling levels of (H 2 O) 2 and (D 2 O) 2. *Journal of chemical physics* **2008,** *128* (3), 034312.

152. Scribano, Y.; Goldman, N.; Saykally, R. J.; Leforestier, C., Water dimers in the atmosphere III: equilibrium constant from a flexible potential. *Journal of Physical Chemistry A* **2006,** *110* (16), 5411-5419.

153. Leforestier, C., Water dimer equilibrium constant calculation: A quantum formulation including metastable states. *Journal of chemical physics* **2014,** *140* (7), 074106.

154. Bunker, P. R.; Jensen, P., *Fundamentals of Molecular Symmetry*. Institute of Physics: Bristol, 2005.

155. Becke, A. D., A new mixing of Hartree–Fock and local density-functional theories. *Journal of chemical physics* **1993,** *98* (2), 1372-1377.

156. Lee, C.; Yang, W.; Parr, R. G., Development of the Colle-Salvetti correlation-energy formula into a functional of the electron density. *Physical Review B* **1988,** *37* (2), 785-789.

157. Zhao, Y.; Truhlar, D. G., The M06 suite of density functionals for main group thermochemistry, thermochemical kinetics, noncovalent interactions, excited states, and transition elements: two new functionals and systematic testing of four M06-class functionals and 12 other functionals. *Theo Chem Acc: Theo, Comp, and Mod (Theoretica Chimica Acta)* **2008,** *120* (1), 215-241.

158. Kanno, N.; Tonokura, K.; Koshi, M., Equilibrium constant of the HO2-H2O complex formation and kinetics of HO2+HO2-H2O: Implications for tropospheric chemistry. *J Geophys Res-Atm* **2006,** *111*, D20312.

159. Suma, K.; Sumiyoshi, Y.; Endo, Y., The rotational spectrum of the water-hydroperoxy radical (H2O-HO2) complex. *Science* **2006,** *311* (5765), 1278-1281.

160. Stripp, K. F.; Kirkwood, J. G., Asymptotic expansion of the partition function of the asymmetric top. *Journal of Chemical Physics* **1951,** *19* (9), 1131-1133.

161. Schenter, G. K.; Kathmann, S. M.; Garrett, B. C., Equilibrium constant for water dimerization: analysis of the partition function for a weakly bound system. *Journal of Physical Chemistry A* **2002,** *106* (8), 1557-1566.

162. Mentel, Ł. M.; Baerends, E. J., Can the counterpoise correction for basis set superposition effect be justified? *J. Chem. Theo. Comput.* **2013,** *10* (1), 252-267.

163. DiLabio, G. A.; Johnson, E. R.; Otero-de-la-Roza, A., Performance of conventional and dispersion-corrected density-functional theory methods for hydrogen bonding interaction energies. *Physical Chemistry Chemical Physics* **2013,** *15* (31), 12821-12828.

164. Khan, M. A. H.; Cooke, M. C.; Utembe, S. R.; Archibald, A. T.; Derwent, R. G.; Jenkin, M. E.; Morris, W. C.; South, N.; Hansen, J. C.; Francisco, J. S.; Percival, C. J.; Shallcross, D. E., Global analysis of peroxy radicals and peroxy radical-water complexation using the STOCHEM-CRI global chemistry and transport model. *Atmospheric Environment* **2015,** *106*, 278-287.

165. Matus, K.; Nam, K. M.; Selin, N. E.; Lamsal, L. N.; Reilly, J. M.; Paltsev, S., Health Damages from Air Pollution in China. *Global Environ. Change* **2012,** *22*, 55.

166. Gauderman, W. J.; Avol, E.; Gilliland, F.; Vora, H.; Thomas, D.; Berhane, K.; McConnell, R.; Kuenzli, N.; Lurmann, F.; Rappaport, E.; Margolis, H.; Bates, D.; Peters, J., The Effect of Air Pollution on Lung Development from 10 to 18 Years of Age. *N. Engl. J. Med.* **2004,** *351*, 1057.

167. Huang, R. J.; Zhang, Y. L.; Bozzetti, C.; Ho, K. F.; Cao, J. J.; Han, Y. M.; Daellenbach, K. R.; Slowik, J. G.; Platt, S. M.; Canonaco, F.; Zotter, P.; Wolf, R.; Pieber, S. M.; Bruns, E. A.; Crippa, M.; Ciarelli, G.; Piazzalunga, A.; Schwikowski, M.; Abbaszade, G.; Schnelle-Kreis, J.; Zimmermann, R.; An, Z. S.; Szidat, S.; Baltensperger, U.; El Haddad, I.; Prevot, A. S. H., High Secondary Aerosol Contribution to Particulate Pollution during Haze Events in China. *Nature* **2014,** *514*, 218.

168. Abbatt, J. P.; Lee, A. K.; Thornton, J. A., Quantifying trace gas uptake to tropospheric aerosol: recent advances and remaining challenges. *Chemical Society reviews* **2012,** *41* (19), 6555-81.

169. Vogt, R.; Scheer, V.; Casati, R.; Benter, T., On-Road Measurement of Particle Emission in the Exhaust Plume of a Diesel Passenger Car. *Environmental science & technology* **2003,** *37* (18), 4070-4076.

170. May, A. A.; Presto, A. A.; Hennigan, C. J.; Nguyen, N. T.; Gordon, T. D.; Robinson, A. L., Gas-Particle Partitioning of Primary Organic Aerosol Emissions: (2) Diesel Vehicles. *Environ. Sci. Technol.* **2013,** *47*, 8288.

171. Volmer, M.; Weber, A., Nucleus Formation in Supersaturated Systems. *Z. Phys. Chem., Stochiom. Verw.* **1926,** *119*, 277.

172. Farkas, L., Velocity of nucleation in supersaturated vapors. *Z. Phys. Chem., Stochiom. Verw.* **1927,** *125*, 236.

173. Dawson, M. L.; Varner, M. E.; Perraud, V.; Ezell, M. J.; Gerber, R. B.; Finlayson-Pitts, B. J., Simplified Mechanism for New Particle Formation from Methanesulfonic Acid, Amines, and Water via Experiments and ab Initio Calculations. *Proc. Natl. Acad. Sci. U.S.A.* **2012,** *109*, 18719.

174. Pankow, J. F., An Absorption-Model of the Gas Aerosol Partitioning Involved in the Formation of Secondary Organic Aerosol. *Atmos. Environ.* **1994,** *28*, 189.

175. Zhang, R.; Wang, G.; Guo, S.; Zamora, M. L.; Ying, Q.; Lin, Y.; Wang, W.; Hu, M.; Wang, Y., Formation of Urban Fine Particulate Matter. *Chemical Reviews* **2015,** *115* (10), 3803-3855.

176. Zhang, R.; Khalizov, A.; Wang, L.; Hu, M.; Xu, W., Nucleation and Growth of Nanoparticles in the Atmosphere. *Chem. Rev.* **2012,** *112*, 1957.

177. Ball, S. M., Hanson, D.R., Eisele, F.L., McMurry,P.H., Laboratory Studies of Particle Nucleation: Initial Results for H_2SO_4, H_2O and NH_3. *J Geophys. Res.* **1999,** *104*, 23709-23718.

178. Benson, D. R., Erupe, M.E., Yu, J.H., Markovich, A., Lee, S.H., Atmospheric Homogenous Nucleation of H_2SO_4 and H_2O. *Atmos. Chem. Phys. Discuss* **2010,** *10*, 29051-29073.

179. Molina, M. J.; Zhang, R.; Wooldridge, P. J.; McMahon, J. R.; Kim, J. E.; Chang, H. Y.; Beyer, K. D., Physical Chemistry of the H2SO4/HNO3/H2O System: Implications for Polar Stratospheric Clouds. *Science* **1993,** *261*, 1418.

180. Wooldridge, P. J.; Zhang, R.; Molina, M. J., Phase Equilibria of H2SO4, HNO3, and HCl Hydrates and the Composition of Polar Stratospheric Clouds. *J. Geophys. Res.* **1995,** *100*, 1389.

181. Erupe, M. E.; Viggiano, A. A.; Lee, S. H., The Effect of Trimethylamine on Atmospheric Nucleation Involving H2SO4. *Atmos. Chem. Phys.* **2011,** *11*, 4767.

182. Lv, S. S.; Miao, S. K.; Ma, Y.; Zhang, M. M.; Wen, Y.; Wang, C. Y.; Zhu, Y. P.; Huang, W., Properties and Atmospheric Implication of Methylamine-Sulfuric Acid-Water Clusters. *The journal of physical chemistry. A* **2015,** *119* (32), 8657-66.

183. Castleman, A. W.; Holland, P. M.; Keesee, R. G., The properties of ion clusters and their relationship to heteromolecular nucleation. *The Journal of Chemical Physics* **1978,** *68* (4), 1760-1767.

184. Eisele, F. L.; Tanner, D. J., Identification of ions in continental air. *Journal of Geophysical Research: Atmospheres* **1990,** *95* (D12), 20539-20550.

185. Beig, G.; Brasseur, G. P., Model of tropospheric ion composition: A first attempt. *Journal of Geophysical Research: Atmospheres* **2000,** *105* (D18), 22671-22684.

186. Kulmala, M.; Tammet, H., Finnish-Estonian air ion and aerosol workshops. *Boreal Environment Research* **2007,** *12* (3), 237-245.

187. Kulmala, M.; Kerminen, V.-M., On the formation and growth of atmospheric nanoparticles. *Atmospheric Research* **2008,** *90* (2-4), 132-150.

188. Misaki, M., Mobility spectrums of large ions in the New Mexico semidesert. *Journal of Geophysical Research (1896-1977)* **1964,** *69* (16), 3309-3318.

189. Mohnen, V. A., *Electrical Processes in Atmospheres* **1977,** *80*, 1-17.

190. Parts, T. E.; Luts, A., Observed and simulated effects of certain pollutants on small air ion spectra: I. Positive ions. *Atmospheric Environment* **2004,** *38* (9), 1283-1289.

191. Kurten, T.; Loukonen, V.; Vehkamäki, H.; Kulmala, M., Amines are likely to enhance neutral and ion-induced sulfuric acid-water nucleation in the atmosphere more effectively than ammonia. *Atmospheric Chemistry and Physics* **2008,** *8*, 4095-4103.

192. Silva, P. J. E., M.E.; Price, D.; Elias, J., Trimethlyamine as Precursor to Secondary Organic Aerosol Formation via Nitrate Radical Reaction in the Atmospere. *Environmental science & technology* **2008,** (42), 4689-4696.

193. Kurten, T.; Loukonen, V.; Vehkamäki, H.; Kulmala, M., Amines are likely to enhance neutral and ion-induced sulfuric acid-water nucleation in the atmopshere more effective than ammonia. *Atmospheric Chemistry and Physics* **2008,** *8*, 4095-4103.

194. Erupe, M. E.; Viggiano, A. A.; Lee, S. H., The effect of trimethylamine on atmospheric nucleation involving H2SO4. *Atmospheric Chemistry and Physics* **2011,** *11* (10), 4767-4775.

195. Swartz, E.; Shi, Q.; Davidovits, P.; Jayne, J. T.; Worsnop, D. R.; Kolb, C. E., Uptake of Gas-Phase Ammonia. 2. Uptake by Sulfuric Acid Surfaces. *J. Phys. Chem. A* **1999,** *103*, 8824.

196. Kirkby, J.; Curtius, J.; Almeida, J.; Dunne, E.; Duplissy, J.; Ehrhart, S.; Franchin, A.; Gagne, S.; Ickes, L.; Kurten, A.; Kupc, A.; Metzger, A.; Riccobono, F.; Rondo, L.; Schobesberger, S.; Tsagkogeorgas, G.; Wimmer, D.; Amorim, A.; Bianchi, F.; Breitenlechner, M.; David, A.; Dommen, J.; Downard, A.; Ehn, M.; Flagan, R. C.; Haider, S.; Hansel, A.; Hauser, D.; Jud, W.; Junninen, H.; Kreissl, F.; Kvashin, A.; Laaksonen, A.; Lehtipalo, K.; Lima, J.; Lovejoy, E. R.; Makhmutov, V.; Mathot, S.; Mikkila, J.; Minginette, P.; Mogo, S.; Nieminen, T.; Onnela, A.; Pereira, P.; Petaja, T.; Schnitzhofer, R.; Seinfeld, J. H.; Sipila, M.; Stozhkov, Y.; Stratmann, F.; Tome, A.; Vanhanen, J.; Viisanen, Y.; Vrtala, A.; Wagner, P. E.; Walther, H.; Weingartner, E.; Wex, H.; Winkler, P. M.; Carslaw, K. S.; Worsnop, D. R.; Baltensperger, U.; Kulmala, M., Role of sulphuric acid, ammonia and galactic cosmic rays in atmospheric aerosol nucleation. *Nature* **2011,** *476* (7361), 429-33.

197. DePalma, J. W.; Doren, D. J.; Johnston, M. V., Formation and growth of molecular clusters containing sulfuric acid, water, ammonia, and dimethylamine. *The journal of physical chemistry. A* **2014,** *118* (29), 5464-73.

198. Smith, J. N.; Dunn, M. J.; VanReken, T. M.; Iida, K.; Stolzenburg, M. R.; McMurry, P. H.; Huey, L. G., Chemical Composition of Atmospheric Nanoparticles Formed from Nucleation in Tecamac, Mexico: Evidence for an Important Role for Organic Species in Nanoparticle Growth. *Geophys. Res. Lett.* **2008,** *35*.

199. Kuang, C.; McMurry, P. H.; McCormick, A. V.; Eisele, F. L., An improved criterion for new particle formation in diverse atmospheric environments. *J. Geophys. Res.* **2010,** *113*, D10209.

200. Kanno, N.; Tonokura, K.; Koshi, M., Equilibrium constant of the HO2-H2O complex formation and kinetics of HO2+HO2-H2O: Implications for tropospheric chemistry. *Journal of Geophysical Research-Atmospheres* **2006,** *111* (D20).

201. Frisch, M. J.; Trucks, G. W.; Schlegel, H. B.; Scuseria, G. E.; Robb, M. A.; Cheeseman, J. R.; Montgomery, J. A., Jr.; Vreven, T.; Kudin, K. N.; Burant, J. C.; Millam, J. M.; Iyengar, S. S.; Tomasi, J.; Barone, V.; Mennucci, B.; Cossi, M.; Scalmani, G.; Rega, N.; Petersson, G. A.; Nakatsuji, H.; Hada, M.; Ehara, M.; Toyota, K.; Fukuda, R.; Hasegawa, J.; Ishida, M.; Nakajima, T.; Honda, Y.; Kitao, O.; Nakai, H.; Klene, M.; Li, X.; Knox, J. E.; Hratchian, H. P.; Cross, J. B.; Bakken, V.; Adamo, C.; Jaramillo, J.; Gomperts, R.; Stratmann, R. E.; Yazyev, O.; Austin, A. J.; Cammi, R.; Pomelli, C.; Ochterski, J. W.; Ayala, P. Y.; Moro-kuma, K.; Voth, G. A.; Salvador, P.; Dannenberg, J. J.; Zakrzewski, V. G.; Dapprich, S.; Daniels, A. D.; Strain, M. C.; Farkas, O.; Malick, D. K.; Rabuck, A. D.; Raghavachari, K.; Foresman, J. B.; Ortiz, J.

V.; Cui, Q.; Baboul, A. G.; Clifford, S.; Cioslowski, J.; Stefanov, B. B.; Liu, G.; Liashenko, A.; Piskorz, P.; Komaromi, I.; Martin, R. L.; Fox, D. J.; Keith, T.; Al-Laham, M. A.; Peng, C. Y.; Nanayakkara, A.; Challa-combe, M.; Gill, P. M. W.; Johnson, B.; Chen, W.; Wong, M. W.; Gonzalez, C.; Pople, J. A. *Gaussian 2009*, Revision 5.0.8 Gaussian, Inc.: Wallingford,CT, 2009.

202. Mardirossian, N.; Head-Gordan, M., Thirty years of density functional theory in computational chemistry: an overview and extensive assessment of 200 density functionals. *Molecular Physics* **2017,** *115* (19), 2315-2372.

203. Zhao, Y.; Truhlar, D. G., The M06 suite of density functionals for main group thermochemistry, thermochemical kinetics, noncovalent interactions, excited states, and transition elements: two new functionals and systematic testing of four M06-class functionals and 12 other functionals. *Theor. Chem. Acc.* **2008,** *120*

(1-3), 215-241.

204. Clark, J.; Call, S. T.; Austin, D. E.; Hansen, J. C., Computational Study of Isoprene Hydroxyalkyl Peroxy Radical-Water Complexes

(C5H8(OH)O2-H2O). *The journal of physical chemistry. A* **2010,** *114* (23), 6534-6541.

205. Perrin, C. L.; Nielson, J. B., "STRONG" HYDROGEN BONDS IN CHEMISTRY AND BIOLOGY. *Annual Review of Physical Chemistry* **1997,** *48* (1), 511-544.

206. Ochterski, J. W. Thermochemistry in *Gaussian* 2000, p. 13. http://www.gaussian.com/g_whitepap/thermo.html (accessed 6/15/2010).

207. Scheiner, S.; Kar, T., Underlying source of the relation between polypeptide conformation and strength of NH···O hydrogen bonds. *Journal of Molecular Structure* **2007,** *844-845*, 166-172.

208. A, Z. G.; Andrienko, G. A. *Chemcraft - graphical software for visualization of quantum chemistry computations*, 1.8 (build 164); Ivanovo, Russia, 2016.

209. Solomon, S., et al.; Eds. *IPCC "Intergovernmental Panel on Climate Change. Report*; Cambridge University Press:: Cambridge, U. K., 2007.

210. Pillar-Little, E. A.; Guzman, M. I., An overview of dynamic heterogeneous oxidations in the troposphere. *Environments,* **2018,** *5*, 104.

211. Liu, Z.; Yim, S. H. L.; Wang, C.; Lau, N. C., The impact of the aerosol direct radiative

forcing on deep convection and air quality in the Pearl river delta region. *Geophys. Res. Lett.* **2018,** *45*, 4410.

212. Fan, J. W.; Zhang, R. Y.; Li, G. H.; Tao, W. K., Effects of Aerosols and Relative Humidity on Cumulus Clouds. *J. Geophys. Res.* **2007,** *112*, D14204.

213. Zhang, R.; Li, G.; Fan, J.; Wu, D. L.; Molina, M. J., Intensification of Pacific storm track linked to Asian pollution. *Proceedings of the National Academy of Sciences* **2007,** *104* (13), 5295.

214. Yuan, T. L.; Li, Z. Q.; Zhang, R. Y.; Fan, J. W., Increase of Cloud Droplet Size with Aerosol Optical Depth: An Observation and Modeling Study. *J. Geophys. Res.* **2008,** *113*, D04201.

215. Chen, M.; Titcombe, M.; Jiang, J.; Jen, C.; Kuang, C.; Fischer, M. L.; Eisele, F. L.; Siepmann, J. I.; Hanson, D. R.; Zhao, J.; McMurry, P. H., Acid–base chemical reaction model for nucleation rates in the polluted atmospheric boundary layer. *Proceedings of the National Academy of Sciences* **2012,** *109* (46), 18713.

216. Almeida, J.; Schobesberger, S.; Kürten, A.; Ortega, I. K.; Kupiainen-Määttä, O.; Praplan, A. P.; Adamov, A.; Amorim, A.; Bianchi, F.; Breitenlechner, M.; David, A.; Dommen, J.; Donahue, N. M.; Downard, A.; Dunne, E.; Duplissy, J.; Ehrhart, S.; Flagan, R. C.; Franchin, A.; Guida, R.; Hakala, J.; Hansel, A.; Heinritzi, M.; Henschel, H.; Jokinen, T.; Junninen, H.; Kajos, M.; Kangasluoma, J.; Keskinen, H.; Kupc, A.; Kurtén, T.; Kvashin, A. N.; Laaksonen, A.; Lehtipalo, K.; Leiminger, M.; Leppä, J.; Loukonen, V.; Makhmutov, V.; Mathot, S.; McGrath, M. J.; Nieminen, T.; Olenius, T.; Onnela, A.; Petäjä, T.; Riccobono, F.; Riipinen, I.; Rissanen, M.; Rondo, L.; Ruuskanen, T.; Santos, F. D.; Sarnela, N.; Schallhart, S.; Schnitzhofer, R.; Seinfeld, J. H.; Simon, M.; Sipilä, M.; Stozhkov, Y.; Stratmann, F.; Tomé, A.; Tröstl, J.; Tsagkogeorgas, G.; Vaattovaara, P.; Viisanen, Y.; Virtanen, A.; Vrtala, A.; Wagner, P. E.; Weingartner, E.; Wex, H.; Williamson, C.; Wimmer, D.; Ye, P.; Yli-Juuti, T.; Carslaw, K. S.; Kulmala, M.; Curtius, J.; Baltensperger, U.; Worsnop, D. R.; Vehkamäki, H.; Kirkby, J., Molecular understanding of sulphuric acid–amine particle nucleation in the atmosphere. *Nature* **2013,** *502*, 359.

217. Kirkby, J.; Curtius, J.; Almeida, J.; Dunne, E.; Duplissy, J.; Ehrhart, S.; Franchin, A.; Gagné, S.; Ickes, L.; Kürten, A.; Kupc, A.; Metzger, A.; Riccobono, F.;

Rondo, L.; Schobesberger, S.; Tsagkogeorgas, G.; Wimmer, D.; Amorim, A.; Bianchi, F.; Breitenlechner, M.; David, A.; Dommen, J.; Downard, A.; Ehn, M.; Flagan, R. C.; Haider, S.; Hansel, A.; Hauser, D.; Jud, W.; Junninen, H.; Kreissl, F.; Kvashin, A.; Laaksonen, A.; Lehtipalo, K.; Lima, J.; Lovejoy, E. R.; Makhmutov, V.; Mathot, S.; Mikkilä, J.; Minginette, P.; Mogo, S.; Nieminen, T.; Onnela, A.; Pereira, P.; Petäjä, T.; Schnitzhofer, R.; Seinfeld, J. H.; Sipilä, M.; Stozhkov, Y.; Stratmann, F.; Tomé, A.; Vanhanen, J.; Viisanen, Y.; Vrtala, A.; Wagner, P. E.; Walther, H.; Weingartner, E.; Wex, H.; Winkler, P. M.; Carslaw, K. S.; Worsnop, D. R.; Baltensperger, U.; Kulmala, M., Role of sulphuric acid, ammonia and galactic cosmic rays in atmospheric aerosol nucleation. *Nature* **2011,** *476*, 429.

218. Smith, J. N.; Dunn, M. J.; VanReken, T. M.; Iida, K.; Stolzenburg, M. R.; McMurry, P. H.; Huey, L. G., Chemical composition of atmospheric nanoparticles formed from nucleation in Tecamac, Mexico: Evidence for an important role for organic species in nanoparticle growth. *Geophys. Res. Lett.* **2008,** *35* (L04808).

219. kuang, C.; Riipinen, I.; Sihto, S. L.; Kulmala, M.; McCormick, A. V.; mcmurry, P. H., An improved criterion for new particle formation in diverse atmospheric environments. *Atmos. Chem. Phys.* **2010,** *10*, 8469-8480.

220. Barsanti, K. C.; McMurry, P. H.; Smith, J. N., The potential contribution of organic salts to new particle growth. *Atmos. Chem. Phys.* **2009,** *9* (2949-2957).

221. Smith, J. N.; Barsanti, K. C.; Friedli, H. R.; Ehn, M.; Kulmala, M.; Collins, D. R.; Scheckman, J. H.; Williams, B. J.; McMurry, P. H., Observations of aminium salts in atmospheric nanoparticles and possible climatic implications. *Proceedings of the National Academy of Sciences of the United States of America* **2010,** *107* (15), 6634-9.

222. Zhang, R. Y.; Suh, I.; Zhao, J.; Zhang, D.; Fortner, E. C.; Tie, X. X.; Molina, L. T.; Molina, M. J., Atmospheric New Particle Formation Enhanced by Organic Acids. *Science* **2004,** *304*, 1487.

223. Zhang, R.; Wang, L.; Khalizov, A. F.; Zhao, J.; Zheng, J.; McGraw, R. L.; Molina, L. T., Formation of Nanoparticles of Blue Haze Enhanced by Anthropogenic Pollution. *Proc. Natl. Acad. Sci. U.S.A.* **2009,** *106*, 17650.

224. Yao, L. e. a., Atmospheric new particle formation from sulfuric acid and amines in a Chinese megacity. *Science* **2018,** *361*, 278-281.

225. Kurten, T.; Loukonen, V.; Vehkamäki, H.; Kulmala, M., Amines are likely to enhance neutral and ion-induced sulfuric acid water nucleation in the atmosphere is more effectively than ammonia. *Atmos. Chem. Phys.* **2008,** *8*, 4095-4103.

226. Berndt, T.; Stratmann, F.; Sipila, M.; Vanhanen, J.; Petaja, T.; Mikkila, J.; Gruner, A.; Spindler, G.; Lee Mauldin Iii, R.; Curtius, J.; Kulmala, M.; Heintzenberg, J., Laboratory Study on new particle formation from the reaction OH+SO_2 : influence of experimetnal conditions, H_2O vapour, NH_3 and the amine tert-butylamine on the overall process. *Atmos. Chem. Phys.* **2010,** *10* (7101-7116).

227. Yu, H.; McGraw, R.; Lee, S.-H., Effects of amines on formation of sub-3 nm particles and their subsequent growth. *Geophysical Research Letters* **2012,** *39* (2).

228. Makar, P. A., The estimation of organic gas vapour pressure. *Atmospheric Environment* **2001,** *35* (5), 961-974.

229. Andreae, M. O.; Talbot, R. W.; Li, S.-M., Atmospheric measurements of pyruvic and formic acid. *Journal of Geophysical Research: Atmospheres* **1987,** *92* (D6), 6635-6641.

230. Talbot, R. W.; Harriss, R. C.; Browell, E. V.; Gregory, G. L.; Sebacher, D. I.; Beck, S. M., Distribution and geochemistry of aerosols in the tropical north Atlantic troposphere: Relationship to Saharan dust. *Journal of Geophysical Research: Atmospheres* **1986,** *91* (D4), 5173-5182.

231. Talbot, R. W.; Beecher, K. M.; Harris, R. C.; Cofer, W. R., Atmospheric geochemistry of formic and acetic acids at a mid-latitude temperate site. *J. Geophys. Res.* **1988,** *93*, 1638-1652.

232. Li, S. M.; Winchester, J. W., Geochemistry of organic and inorganic ions of the late winter Arctic aerosol. *Atmos. Environ.* **1989,** *23*, 2401-2416.

233. Baboukas, E. D.; Kanakidou, M.; Mihalopoulos, N., Carboxylic acids in gas and particulate phase above the Atlantic Ocean. *Journal of Geophysical Research: Atmospheres* **2000,** *105* (D11), 14459-14471.

234. Limón-Sánchez, M. T.; Arriaga-Colina, J. L.; Escalona-Segura, S.; Ruíz-Suárez, L. G., Observations of formic and acetic acids at three sites of Mexico City. *Science of The Total Environment* **2002,** *287* (3), 203-212.

235. Mircea, M.; Facchini, M. C.; Decesari, S.; Cavalli, F.; Emblico, L.; Fuzzi, S.; Vestin, A.; Rissler, J.; Swietlicki, E.; Frank, G.; Andreae, M. O.; Maenhaut, W.; Rudich, Y.; Artaxo, P., Importance of the organic aerosol fraction for modeling aerosol

hygroscopic growth and activation: a case study in the Amazon Basin. *Atmos. Chem. Phys.* **2005,** *5*, 3111-3126.

236. Peng, X. Q.; Liu, Y.-R.; Huang, T.; Jiang, S.; Huang, W., Interaction of gas phase oxalic acid with ammonia and its atmospheric implications. *Phys. Chem. Chem. Phys.* **2015,** *17*, 9552-9563.

237. Weber, K. H.; Liu, Q.; Tao, F. M., Theoretical study on stable small clusters of oxalic acid with ammonia and water. *J. Phys. Chem. A* **2014,** *118*, 1451-1468.

238. Xu, W.; Zhang, R., Theoretical Investigation of interaction of dicarboxylic acids with common aerosol nucleation precursors. *J. Phys. Chem. A* **2012,** *116*, 4539-4550.

239. Chen, J. e. a., Interaction of oxalic acid with dimethylamine and its atmospheric implications. *RSC Adv.* **2017,** *7*, 6374-6388.

240. Gerber, R. B.; Varner, M. E.; Hammerich, A. D.; Riikonen, S.; Murdachaew, G.; Shemesh, D.; Finlayson-Pitts, B. J., Computational Studies of Atmospherically-Relevant Chemical Reactions in Water Clusters and on Liquid Water and Ice Surfaces. *Accounts of Chemical Research* **2015,** *48* (2), 399-406.

241. Ravishankara, A. R., Heterogeneous and Multiphase Chemistry in the Troposphere. *Science* **1997,** *276* (5315), 1058-1065.

242. Li, L.; Kumar, M.; Zhu, C.; Zhong, J.; Francisco, J. S.; Zeng, X. C., Near-Barrierless Ammonium Bisulfate Formation via a Loop-Structure Promoted Proton-

Transfer Mechanism on the Surface of Water. *Journal of the American Chemical Society* **2016,** *138* (6), 1816-1819.

243. Zhong, J.; Kumar, M.; Zhu, C. Q.; Francisco, J. S.; Zeng, X. C., Surprising stability of larger Criegee intermediates on aqueous interfaces. *Angew. Chem. Int. Ed.* **2017,** *56*, 7740-7744.

244. J., E. A.; Pillar, E. A.; Colussi, A. J.; Guzman, M. I., Enhanced acidity of acetic and pyruvic Acids on the surface of water. *Langmuir* **2018,** *34*, 9307-9313.

245. J., E. A.; Xia, S. S.; Guzman, M. I., Negative production of acetoin in the photochemistry of aqueous pyruvic acid. *Proc. Natl. Acad. Sci. U. S. A.* **2013,** *110*, E4274-E4275.

246. Whitby, K. T.; Sverdrup, G. M., The aerosol size distribution of Los Angeles smog. *J. Colloid Interface Sci.* **1980,** *8*, 477.

247. Pratt, K. A.; Hatch, L. E.; Prather, K. A., Seasonal Volatility Dependence of Ambient Particle Phase Amines. *Environmental science & technology* **2009,** *43* (14), 5276-5281.

248. Sorooshian, A.; murphy, S. M.; Hersey, S.; Gates, H.; Padro, L. T.; Nenes, A.; Brechtel, F. J.; Jonsson, H.; Flagan, R. C.; seinfeld, J. H., Comprehensive airborne characterization of aerosol from a major bovine source. *Atmos. Chem. Phys.* **2008,** *8*, 5489-5520.

249. Dinar, E.; Anttila, T.; Rudich, Y., CCN Activity and Hygroscopic Growth of Organic Aerosols Following Reactive Uptake of Ammonia. *Environmental science & technology* **2008,** *42* (3), 793-799.

250. Kulmala, M., Atmospheric science. how particles nucleate and grow. *Science* **2003,** *302*, 1000-1001.

251. Zhang, K. M.; Wexler, A. S., A hypothesis for growth of fresh atmospheric nuclei. *J. Geophys. Res.* **2002,** *107* (D21), 4577.

252. Paciga, A. L.; Riipinen, I.; Pandis, S. N., Effect of Ammonia on the Volatility of Organic Diacids. *Environmental science & technology* **2014,** *48* (23), 13769-13775.

253. Lavi, A.; Segre, E.; Gomez-Hernandez, M.; Zhang, R.; Rudich, Y., Volatility of Atmospherically Relevant Alkylaminium Carboxylate Salts. *The Journal of Physical Chemistry A* **2015,** *119* (19), 4336-4346.

254. Khwaja, H. A., Atmospheric concentrations of carboxylic acids and related compunds at 10. a semiurban site. *Atmos. Environ.* **1995,** *29*, 127-139.

255. Kawamura, K.; Ikushima, K., Seasonal changes in the distribution of dicarboxylic acids in the urban atmosphere. *Environmental science & technology* **1993,** *27* (10), 2227-2235.

256. Sempére, R.; Kawamura, K., Comparative distributions of dicarboxylic acids and related polar compounds in snow, rain and aerosols from urban atmosphere. *Atmospheric Environment* **1994,** *28* (3), 449-459.

257. Kawamura, K.; Kasukabe, H.; Barrie, L. A., Source and reaction pathways of dicarboxylic acids, ketoacids and dicarbonyls in arctic aerosols: One year of observations. *Atmospheric Environment* **1996,** *30* (10), 1709-1722.

258. VandeVondele, J.; Krack, M.; Mohamed, F.; Parrinello, M.; Chassaing, T.; Hutter, J., Quickstep: Fast and accurate density functional calculations using a mixed Gaussian and plane waves approach. *Computer Physics Communications* **2005,** *167* (2), 103-128.

259. Becke, A. D., Density-functional exchange-energy approximation with correct asymptotic behavior. *Physical Review A* **1988,** *38* (6), 3098-3100.

260. Grimme, S., Accurate description of van der Waals complexes by density functional theory including empirical corrections. *Journal of Computational Chemistry* **2004,** *25* (12), 1463-1473.

261. Grimme, S., Semiempirical GGA-type density functional constructed with a long-range dispersion correction. *Journal of Computational Chemistry* **2006,** *27* (15), 1787-1799.

262. Goedecker, S.; Teter, M.; Hutter, J., Separable dual-space Gaussian pseudopotentials. *Physical Review B* **1996,** *54* (3), 1703-1710.

263. Hartwigsen, C.; Goedecker, S.; Hutter, J., Relativistic separable dual-space Gaussian pseudopotentials from H to Rn. *Physical Review B* **1998,** *58* (7), 3641-3662.

264. Zhang, R. Y.; Li, G. H.; Fan, J. W.; Wu, D. L.; Molina, M. J., *Proc. Natl. Acad. Sci. U.S.A.* **2007,** *104*, 5295.

265. Fan, J.; Zhang, R.; Tao, W. K.; Mohr, K. I., Effets of aerosol optical properties on deep convective clouds and radiative forcing. *Journal of Geophysical Research* **2008,** *113* (D08209).

266. Sipilä, M.; Berndt, T.; Petäjä, T.; Brus, D.; Vanhanen, J.; Stratmann, F.; Patokoski, J.; Mauldin, R. L.; Hyvärinen, A.-P.; Lihavainen, H.; Kulmala, M., The Role of Sulfuric Acid in Atmospheric Nucleation. *Science* **2010,** *327* (5970), 1243-1246.

267. Chen, M.; Titcombe, M.; Jiang, J.; Jen, C.; Kuang, C.; Fischer, M. L.; Eisele, F. L.; Siepmann, J. I.; Hanson, D. R.; Zhao, J.; McMurry, P. H., Acid–base chemical reaction model for nucleation rates in the polluted atmospheric boundary layer. *Proceedings of the National Academy of Sciences* **2012,** *109* (46), 18713-18718.

268. Almeida, J., Molecular understanding of Sulphuric acid-amine particle nucleation in the atmosphere. *Nature* **2013,** *502* (7471), 359-363.

269. Yue, D. L.; Hu, M.; Zhang, R. Y.; Wang, Z. B.; Zheng, J.; Wu, Z. J.; Wiedensohler, A.; He, L. Y.; Huang, X. F.; Zhu, T., The Roles of Sulfuric Acid in New Particle Formation and Growth in the Mega-City of Beijing. *Atmos. Chem. Phys.* **2010,** *10*, 4953.

270. Vehkamäki, H., An improved parameterization for sulfuric acid–water nucleation rates for tropospheric and stratospheric conditions. *Journal of Geophysical Research* **2002,** *107* (D22).

271. Barsanti, K. C.; McMurry, P. H.; Smith, J. N., The potential contribution of organic salts to new particle growth. *Atmos. Chem. Phys. Discuss* **2009,** *9* (9), 2949-2957.

272. Xue, H. X.; Khalizov, A. F.; Wang, L.; Zheng, J.; Zhang, R. Y., Effects of Coating of Dicarboxylic Acids on the Mass–Mobility Relationship of Soot Particles. *Environ. Sci. Technol.* **2009,** *43*, 2787.

273. Xu, W.; Zhang, R. Y., Theoretical Investigation of Interaction of Dicarboxylic Acids with Common Aerosol Nucleation Precursors. *J. Phys. Chem. A* **2012,** *116*, 4539.

274. Xu, W.; Zhang, R. Y., A Theoretical Study of Hydrated Molecular Clusters of Amines and Dicarboxylic Acids. *J. Chem. Phys.* **2013,** *139*.

275. Servant, J.; Kouadio, G.; Cros, B.; Delmas, R., Carboxylic monoacids in the air of mayombe forest (Congo): Role of the forest as a source or sink. *J. Atmos. Chem.* **1991,** *12*, 367-380.

276. Chebbi, A.; Carlier, P., Carboxylic Acids in the Troposphere, Occurrence, Sources, and Sinks: A Review. *Atmos. Environ.* **1996,** *30*, 4233.

277. Berndt, T.; Stratmann, F.; Sipilä, M.; Vanhanen, J.; Petäjä, T.; Mikkilä, J.; Grüner, A.; Spindler, G.; Lee Mauldin Iii, R.; Curtius, J.; Kulmala, M.; Heintzenberg, J., Laboratory study on new particle formation from the reaction OH + SO₂: influence of experimental conditions, H₂O vapour, NH₃ and the amine tert-butylamine on the overall process. *Atmospheric Chemistry and Physics* **2010,** *10* (15), 7101-7116.

278. Yu, H.; McGraw, R.; Lee, S. H., Effects of Amines on Formation of Sub-3 nm Particles and Their Subsequent Growth. *Geophys. Res. Lett.* **2012,** *39*.

279. Kashchiev, D., *Nucleation: basic theory with applications*. 2000.

280. Sorooshian, A.; Murphy, F. J.; Hersey, S.; Gates, H.; Padro, L. T.; Nenes, A.; Brechtel, F. J.; Jonsson, H.; Flagan, R. C.; Seinfeld, J. H., Comprehensive airborne characterization of aerosol from major bovine sources. *Atmospheric Chemistry and Physics* **2008,** *8*, 5489-5520.

281. Shao-Meng, L.; Winchester, J. W., Geochemistry of organic and inorganic ions of late winter arctic aerosols. *Atmospheric Environment (1967)* **1989,** *23* (11), 2401-2415.

282. Kumar, M.; Burrell, E.; Hansen, J. C.; Francisco, J. S., Molecular insights into organic particulate formation. *Communications Chemistry* **2019,** *2* (1), 87.

283. Carpenter, L. J.; Monks, P. S.; Bandy, B. J.; Penkett, S. A.; Galbally, I. E.; Meyer, C. P. M., A study of peroxy radicals and ozone photochemistry at coastal sites in the northern and southern hemispheres. *Journal of Geophysical Research: Atmospheres* **1997,** *102* (D21), 25417-25427.

284. Zanis, P.; Monks, P. S.; Schuepbach, E.; Penkett, S. A., On the relationship of HO2+ RO2withj(O1D) during the Free Tropospheric Experiment (FREETEX '96) at the Jungfraujoch Observatory(3580 m above sea level) in the Swiss Alps. *Journal of Geophysical Research: Atmospheres* **1999,** *104* (D21), 26913-26925.

285. Tang, Y.; Tyndall, G. S.; Orlando, J. J., Spectroscopic and Kinetic Properties of HO2 radicals and the enhancement of the HO2 Self Reaction by CH3OH and H2O. *The journal of physical chemistry. A* **2010,** *114* (1), 369-378.

286. Lendvay, G., Ab Initio Studies of Complexes of HO_2 radical with NH_3, H_2O and HF. *Zeitschrift fur physikalishe Chemie* **2001,** *215* (3), 377-392.

287. Kanno, N.; Tonokura, K.; Tezaki, A.; Koshi, M., Dependence of the HO2 Self Reaction: Kinetics of the HO2-H2O Complex. *J Phys Chem* **2005,** *109* (14), 3153-3158.

288. Geyer, A.; Bächmann, K.; Hofzumahaus, A.; Holland, F.; Konrad, S.; Klüpfel, T.; Pätz, H.-W.; Perner, D.; Mihelcic, D.; Schäfer, H.-J.; Volz-Thomas, A.; Platt, U., Nighttime formation of peroxy and hydroxyl radicals during the BERLIOZ campaign: Observations and modeling studies. *Journal of Geophysical Research: Atmospheres* **2003,** *108* (D4).

289. Green, T. J.; Reeves, C. E.; Brough, N.; Edwards, G. D.; Monks, P. S.; Penkett, S. A., Airborne measurements of peroxy radicals using the PERCA technique. *Journal of Environmental Monitoring* **2003,** *5* (1), 75-83.

290. Zhang, D.; Zhang, R.; Park, J.; North, S. W., Hydroxy Peroxy Nitrites and Nitrates from OH Initiated Reactions of Isoprene. *J. Am. Chem. Soc.* **2002,** *124*, 9600.

291. Cantrell, C. A.; Shetter, R. E.; Gilpin, T. M.; Calvert, J. G.; Eisele, F. L.; Tanner, D. J., Peroxy radical concentrations measured and calculated from trace gas measurements in the Mauna Loa Observatory Photochemistry Experiment 2. *Journal of Geophysical Research: Atmospheres* **1996,** *101* (D9), 14653-14664.

292. Burkert, J.; Andrés-Hernández, M.-D.; Stöbener, D.; Burrows, J. P.; Weissenmayer, M.; Kraus, A., Peroxy radical and related trace gas measurements in the

boundary layer above the Atlantic Ocean. *Journal of Geophysical Research: Atmospheres* **2001,** *106* (D6), 5457-5477.

293. Praske, E.; Otkjaer, R. V.; Crounse, J. D.; Hethcox, J. C.; Stoltz, B. M.; Kjaergaard, H. G.; Wennberg, P. O., Atmospheric autoxidation is increasingly important in urban and suburban North America. *Proceedings of the National Academy of Sciences of the United States of America* **2018,** *115* (1), 64-69.

294. Clark, J.; English, A. M.; Hansen, J. C., Computational Study of the Existence of Organic Peroxy Radical-Water Complexes (RO_2*H_2O). *The journal of physical chemistry. A* **2008,** *112* (7), 1587-1595.

295. Brunekreef, B.; Janssen, N. A. H.; deHartog, J.; Harssema, H.; Knape, M.; vanVliet, P., Air Pollution from Truck Traffic and Lung Function in Children Living Near Motorways. . *Epidemiology* **1997,** *8*, 298-303.

296. Kozawa, K. H.; Fruin, S. A.; Winer, A. M., Near-Road Air Pollution Impacts of Goods Movement in Communities Adjacent to the Ports of Los Angeles and Long Beach. *atmos. Environ.* **2009,** *43*, 2960-2970.

297. Lin, S.; Munsie, J. P.; Hwang, S. A.; Fitzgerald, E.; Cayo, M. R., Childhood Asthma Hospitalization and Residential Exposure to State Route Traffic. *Environ. Research* **2002,** *88*, 73-81.

298. Perez, L.; Lurmann, F.; Wilson, J.; Pastor, M.; Brandt, S. J.; Kunzli, N.; McConnell, R., Near-Roadway Pollution and Childhood Asthma: Implications for

Developing "Win-Win" Compact Urban Development and Clean Vehicle Strategies. *Environmental Health Perspectives* **2012,** *120*, 1619-1626.

299. Institute, H. E. *Traffic-Related Air Pollution: A Critical Review of the Literature on Emissions, Exposure, and Health Effects*; Institute, H.E: 2010.

300. Venn, A. J.; Lewis, S. A.; Cooper, M.; Hubbard, R.; Britton, J., Living Near a Main Road and the Risk of Wheezing Illness in Children. *American Journal of Respiratory and Critical Care Medicine* **2001,** *164*, 2177-2180.

301. Westerdahl, D.; Fruin, S.; Sax, T.; Fine, P. M.; Sioutas, C., Mobile Platform Measurements of Ultrafine Particles and Associated Pollutant Concentrations on Freeways and Residential Streets in Los Angeles. *Atmos. Environ.* **2005,** *39*, 3597-3610.

302. S., F.; D., W.; T., S.; C., S.; P.M, F., Measurements and Predictors of On-Road Ultrafine Particle Concentrations and Associated Pollutants in Los Angeles. *Atmos. Environ.* **2008,** *42*, 207-219.

303. Kozawa, K. H.; Winer, A. M.; Fruin, S. A., Ultrafine Particle Size Distributions Near Freeways: Effects of Differing Wind Directions on Exposure. *Atmos. Environ.* **2012,** *63*, 250-260.

304. Hansen, L. D.; Cropper, P.; W., K.; Burell, E.; Eatough, D. J.; Cary, R. B.; Farber, R., Concentration, Composition and Light Scattering of PM2.5 Adjacent to the I-710 Freeway in Long Beach, CA. *J. Air & Waste Manag. Assoc.* **2019**.

305. Grover, B. D.; Kleinman, M.; Eatough, N. L.; Eatough, D. J.; Cary, R. A.; Hopke, P. K.; Wilson, W. E., Measurement of Fine Particulate Matter Nonvolatile and Semi-Volatile Organic Material with the Sunset Laboratory Carbon Aerosol Monitor. *J. Air & Waste Manage. Assoc* **2008a,** *58*, 72-77.

306. Grover, B. D.; Eatough, N. L.; Woolwine, W. R.; Eatough, D. J.; Cary, R. A.; Smith, D. F.; Wilson, W. E., Modifications to the Sunset Laboratory Carbon Aerosol Monitor for the Simultaneous Measurement of PM2.5 Nonvolatile and Semi Volatile Organic Material. *J. Air & Waste Manag. Assoc.* **2009,** *59*, 1007-1017.

307. Turpin, B. J.; Lim, H. J., Species Contributions to PM2.5 Mass Concentrations: Revisiting Common Assumptions for Estimating Organic Mass. *Aerosol Science and Technology* **2001,** *35*, 602-610.

308. SCAQMD http://www.aqmd.gov/comply/1118/hotlines.htm.

309. Eatough, D. J.; Grover, B. D.; Woolwine, W. R.; Eatough, N. L.; Long, R.; Farber, R., Source Apportionment of 1h Semi-Continuous Data During the 2005 Study of Organic Aerosols in Riverside (SOAR) Using Positive Matrix Factorization. *Atmos. Environ.* **2008,** *42*, 2706-2719.

310. Grover, B. D.; Eatough, D. J., Source Apportionment of One-Hour Semi-Continuous Data Using Positive Matrix Factorization with Total Mass (Nonvolatile plus Semi-Volatile) Measured by the R&P FDMS Monitor. *Aerosol Sci & Technol* **2008b,** *42*, 28-39.

311. Waldron, K.; Paegle, J.; Horel, J., Sensitivity of a spectrally filtered and nudged limited-area model to outer model options. *Mon. Weather Rev* **1996,** *124*, 529–547.

312. Polissar, A. V.; Hopke, P. K.; Malm, W. C.; Sisler, J. F., Atmospheric Aerosol over Alaska 2. Elemental Composition and Sources. *J. Geophys. Research* **1998,** *103*, 19045-10057.

313. Paatero, P.; Hopke, P. K.; Begum, B. A.; Biswas, S. K., A Graphical Diagnostic Method for Assessing the Rotation in Factor Analytical Models of Atmospheric Pollution. *Atmos. Environ.* **2005,** *38*, 193-201.

314. Lioy, P. J.; Zelenka, M. P.; Cheng, M. D.; Reiss, N. M.; Wilson, W. E., The Effect of Sampling Duration on the Ability to Resolve Source Types Using Factor Analysis. *Atmos. Environ.* **1989,** *23*, 239-254.

315. U.S. Department of Health, E., and Welfare *Atmospheric Emissions from Petroleum Refineries. A Guide for Measurement and Control*; 1960.

316. https://www.mcilvainecompany.com/brochures/refinery_process.htm.

317. Abramowitz, M.; Stegun, I., *Handbook of Mathematical Functions with Formulas, Graphs, and Mathematical Tables*. 10th printing ed.; United States Department of Commerce, National Bureau of Standards. : Washington D.C., 1972.

318. Ma, X.; Sun, Y.; Huang, Z.; Zhang, Q.; Wang, W., A density functional theory study of the molecular interactions between a series of amides and sulfuric acid. *Chemosphere* **2019,** *214*, 781-790.

319. Loukonen, V.; Kurten, T.; Ortega, I. K.; Vehkamäki, H.; Padua, A. A. H.; Sellegri, K.; Kulmala, M., Enhancing effect of dimethylamine in sulfuric acid nucleation in the presence of water - a computational study. *Atmos. Chem. Phys.* **2010,** *10* (10), 4961-4974.

320. kurten, T.; Sundberg, M. R.; Vehkamäki, H.; Noppel, M.; Blomquist, B.; Kulmala, M., Ab Initio and Density Functional Theory Reinvestigation of Gas-Phase Sulfuric Acid Monohydrate and Ammonium Hydrogen Sulfate. *J. Phys. Chem. A* **2006,** *110* (22), 7178-7188.

Appendix

Appendix A-1

Apportionment of $PM_{2.5}$ Adjacent to the I-710 Harbor Freeway in Long Beach, CA

A1.1 Disclaimer The following chapter is presented in its entirety (with minor changes) from the submitted version of the paper to the Journal o the Air and Waste Management Association.

A1.2 Abstract:

During August and September 2012, a study was conducted to determine the sources of PM2.5 adjacent to the I-710 Long Beach Freeway. The sampling site is jointly operated by Southern California Edison and the South Coast Air Quality Management District and is located immediately east of the freeway and just south of the northbound Long Beach Avenue exit. The site is directly affected by the emissions from heavy diesel traffic flowing from major container ports about 10 km south of the sampling site. Hourly average data were obtained for particulate species including PM2.5, black carbon and UV absorbing carbon, EC, fine particulate nonvolatile and semi-volatile organic material, sulfate, nitrate, chloride, ammonium ion and Na ion, for related factors including O3, CO, NOX, SO2, and total traffic flow on the I-710. A total of 520 hourly averaged data sets with 15 measured variables were analyzed by EPA-PMF v5.0.

The data were best described by a 10-factor solution. Based on the composition and diurnal patterns of the factors, they were assigned to 3 diesel related factors (two of which appeared to represent traffic from the Ports and one general freeway diesel factor), a light-duty, spark-ignition vehicle related factor, three secondary factors (one of which was associated with O_3 formation processes), and three factors dominated by sulfate, SO_2 and chloride, respectively. The diurnal patterns for these last three factors are strongly correlated. Meteorological and refinery upset data indicate that they are associated with emissions from a nearby refinery. There is no evidence from these results to suggest sulfur oxide emissions from ships at sea was observable at this site. The use of hourly average data made possible the identification of factors associated with gasoline vehicle emissions and both port and non-port diesel emissions.

A1.3 Introduction:

Past studies have suggested that reduced lung function and the incidence of asthma in children are associated with their exposure to fresh emissions from vehicles and that exposure to heavy-duty diesel emissions may be particularly harmful.[295-300] Exposure to ultrafine particles, black carbon, and NO_x in fresh heavy-duty diesel emissions have all been shown to be associated with each other on freeways in Los Angeles and to be associated with truck traffic.[296, 301-303] The study by Kozawa et al.[296] focused on heavy-duty diesel truck traffic associated with goods movement from the Ports of Los Angeles and Long Beach.

All of the above referenced near roadway studies point to the potential importance of heavy-duty diesel exhaust near a freeway as a risk factor for the development of respiratory morbidity, especially in children. During August and September 2012, a study was conducted to determine the sources of $PM_{2.5}$ adjacent to the I-710 Long Beach Freeway. The site was chosen because of the impact of emissions from diesel traffic flowing from the Port of Long Beach and the Port of Los Angeles about 10 km south of the sampling site. All data obtained in the study were collected on an hourly averaged basis. The details of the sampling techniques, evaluation of the data set and comparison of the results with light scattering data have been published[304]. This manuscript describes the results of a Positive Matrix Factorization (EPA-PMF v5.0) analysis of the data. Results include the description of factors that can be associated with automobile emissions and three difference categories of diesel emissions. The importance of secondary particle production was also elucidated from the results.

A1.4 Experimental:

Data were collected at the Long Beach Boulevard sampling site (AQS Station Code 060374008) shown in Figures 1 and 2 from 1 August 2012 through 2 September 1012.

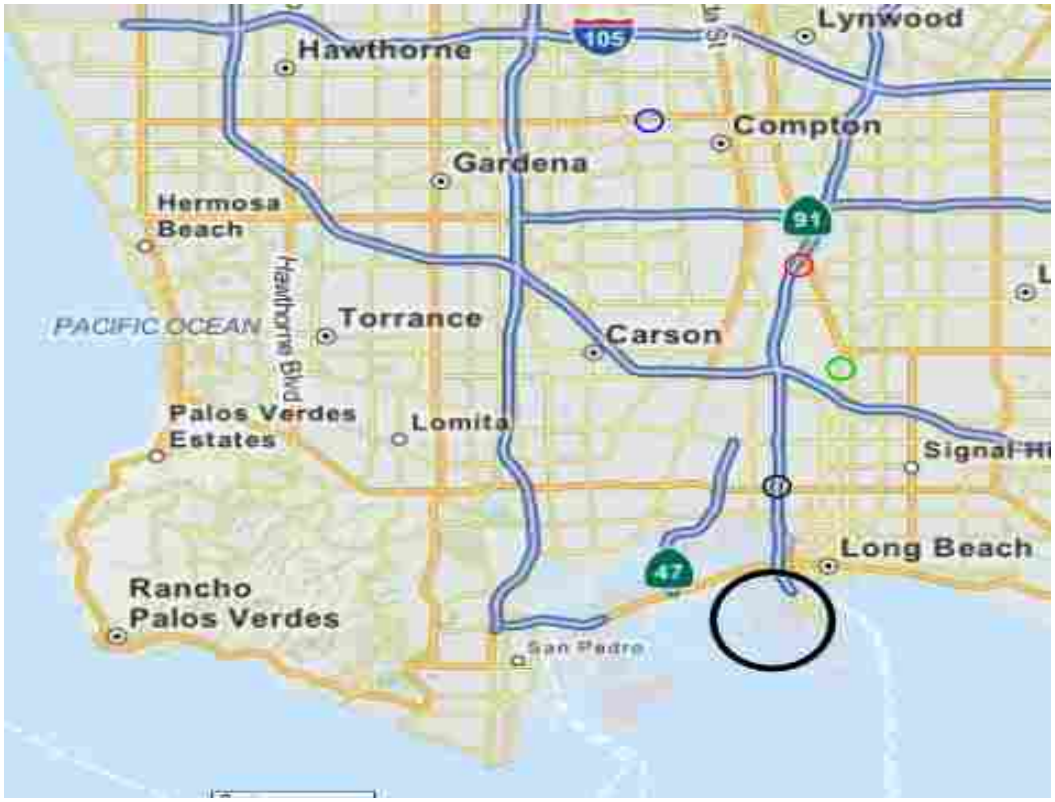

Figure A1.1. Roadway map of the area around the sampling site with the freeways shown in blue. The sampling site is indicated by the red circle. The Long Beach and Los Angeles Harbors are indicated by the larger black circle. The SCAQMD sampling sites at Long Beach and Compton are indicated by the green and blue circles, respectively.

All data were obtained on a 1-hr averaged time basis. Details of the sample collection methods and comparisons of the various results have been previously described[10] and are only outlined here. The following was measured:

A1.4.1 Fine Particulate Mass.

Total fine particulate mass, including the semi-volatile species was measured with an R&P Model 8500 FDMS TEOM. Fine particulate mass was also measured using a conventional TEOM. The size distribution of particulate matter mass (CM Impactor) collected on oscillating crystals with size cuts of 0.10, 0.15, 0.25, 0.4, 0.7, 1.0, 2.5, 4, 7 and 10 microns. Samples were collected immediately east of the freeway by the Long Beach Blvd. exit.

Figure A1.2. Arial view of the sampling site showing the Long Beach Freeway (I710), the Long Beach Blvd. And the sampling location as a black rectangle.

A1.4.2 Fine Particulate Composition.

An URG Model 9000D AIM was used to measure both particulate and gas phase cations and anions. Measured species specifically included in the PMF analysis were ammonium nitrate, ammonium sulfate, and chloride in the particles. Gas phase SO_2 was also measured and used in the PMF analysis. Fine particulate carbonaceous material was measured with a Sunset Laboratory Dual Oven Carbon Monitor[305, 306]. This

instrument gives nonvolatile organic material (NVOC, corrected to NVOM with a factor of 1.6,[307]), EC and semi-volatile organic carbon. However, the second oven to measure the semi-volatile organic material (SVOM) was not functioning well during the study. Thus, SVOM was estimated as the difference between the FDMS TEOM $PM_{2.5}$ mass minus the conventional TEOM $PM_{2.5}$ mass (assumed to represent semi-volatile ammonium nitrate and SVOM) minus the ammonium nitrate. An Andersen Instruments Inc. (Model RTAA-900) Aethalometer was used for the determination of aerosol BC. In addition, 1-h Aethalometer UV absorption data were included in the PMF analysis.

Comparisons of the sum of all measured species and the FDMS TEOM $PM_{2.5}$ measurements were generally in agreement, except for periods when high concentrations of ammonium sulfate or chloride were measured. Comparison of the FDMS TEOM and the CM Impactor data indicated that for these samples a significant fraction of the sulfate and chloride particulate material was found in the 1.0 to 4.0-micron size range. The 2.5 micron cut points of the FDMS TEOM and the URG AIM are not identical with the cut point of the AIM biased towards larger particles such that ammonium sulfate and chloride were not sampled with the same efficiency in the two systems. The majority of these species were sampled by the AIM, but not by the FDMS TEOM (Hansen et al, 2019). To avoid the effects of this difference in the PMF analysis, the $PM_{2.5}$ fit in the PMF analysis was calculated as the sum of all measured fine

particulate components except for ammonium sulfate and chloride (Figure 3). However, the AIM measured ammonium sulfate and chloride (assumed to be NaCl) were used in the PMF analysis.

A1.4.3 Other Components Used in the PMF Analysis.

In addition to the particulate components listed above, other measurements were included in the PMF analysis. These included all measurements related to either $PM_{2.5}$ emissions or to the formation of secondary $PM_{2.5}$. Measurements made at the sampling site by BYU provided concentrations of SO_2 as a precursor to sulfate. Measurements made by the South Coast Air Quality Management District (SCAQMD[308]) related to primary emissions or secondary aerosol formation included gas phase NO_X, NO_2, and the hourly Traffic count on the freeway. This latter number included all vehicles (both gasoline and diesel powered) going in either direction. Two other species that have been shown to be useful in distinguishing between gasoline and diesel powered vehicular traffic or to secondary pollutant formation are CO and O_3, respectively[309, 310]. These species were intended to be measured but for technical reasons, were not. However, ozone was measured by the SCAQMD at their Long Beach and Compton sites (Figure 1). In addition, CO, NO_X, and BC were also measured at the Long Beach site. Ozone is expected to be somewhat regional in nature. Concentrations of ozone at the Long Beach and Compton sites were in good agreement and the average of these two measurements was assumed to represent ozone at the near-freeway

sampling site. The Long Beach sampling site, but not the Compton site, is close to the

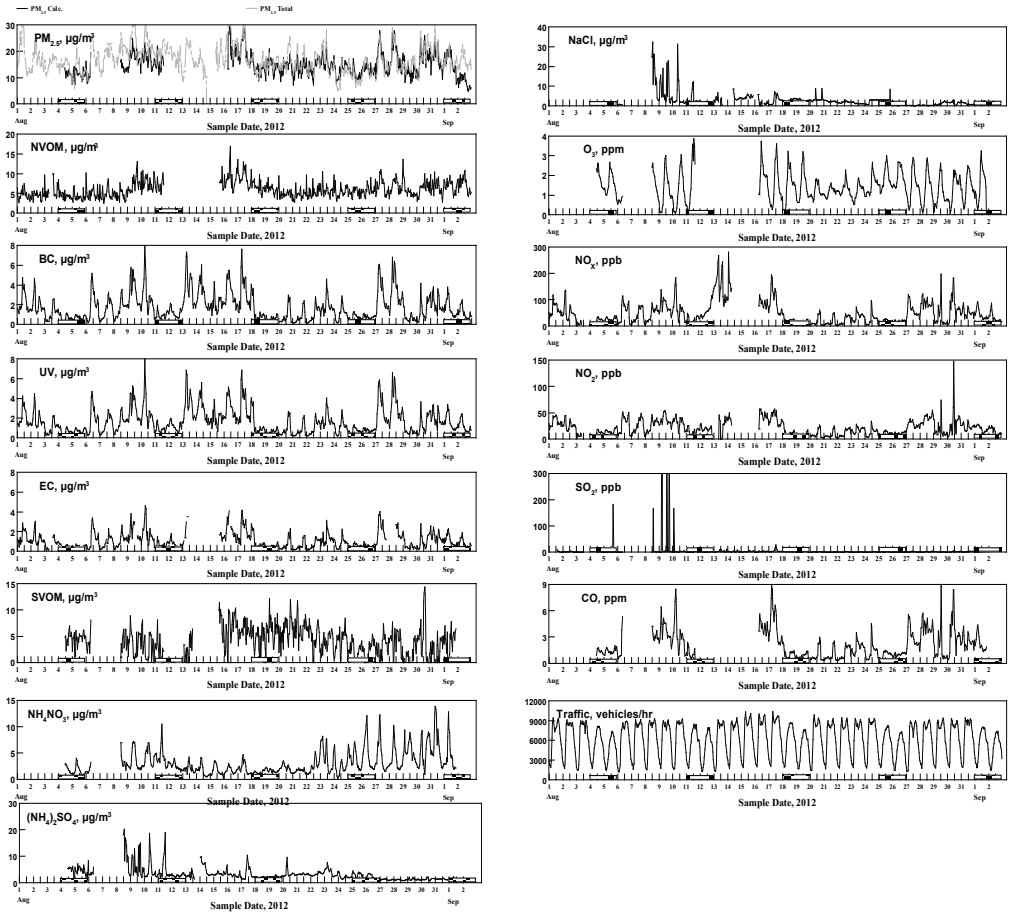

Figure A1.3. Data used in the PMF analysis. The hashed bars on the X axis mark weekends.

intersection of two freeways, including the Harbor Freeway. The useful components in a PMF analysis for distinguishing between diesel and gasoline powered vehicles are CO, NO_X, and BC[309, 310]. Regression analysis of the data from the SCAQMD Long Beach site gave:

$$CO = 0.23 \pm 0.11 + (0.0445 \pm 0.0027)\ NO_X + (0.0161 \pm 0.0096)\ BC,\ n = 684\ R^2 = 0.59 \qquad (1)$$

PMF analysis of the data set without CO did not allow the separation of factors related to gasoline and diesel emissions. Therefore, equation (1) was used to estimate CO at the I-710 sampling site, giving the results shown in Figure 7.3. These CO concentrations were used in the analysis reported here.

A1.4.4 Meteorological Analysis

Interpretation of the PMF analysis was aided using streamlines to identify probable origins of air masses influencing the sampling site for each data point. The LA Basin is populated by approximately 21 million residents. It is bounded on the west and south by the Pacific Ocean. Multiple mountain ranges define the Basin to the north and east. The northern (actually several mountain ranges, Figure 4B) mountains rise from west to east from about 1000 m to 3500 meters. The eastern mountains decrease from north to south from about 3300 meters to 1500 meters. The LA Basin is geographically large, averaging 70 km in width and about 110 km west to east length. Basically, the Basin is landlocked on its northern and eastern sides. These bounds result in frequent strong inversion that still get flushed daily by the sea breeze.

The LA Basin enjoys a Mediterranean climate. The summers are characterized by various high-pressure systems. There is little to no precipitation. The boundary or mixed layer experiences daily late morning through early evening sea-breezes. The average summer ocean temperatures are 20°C while, to the desert to the east of the Basin heats to 40-45°C during the summer. This thermal gradient results in a daily

thermally driven west to east sea breeze, providing natural conditioning to the Basin. A combination of topography and meteorological regimes leads to a stably stratified environment. Marine inversions are often 10°C strong. The average summer mixing height is just 450 meters. It increases little during the day because of sea-breeze divergence which maintains and strengthens the daily inversion. On many days, there is stratus along the coast extending inland about 30 miles during the night. While there

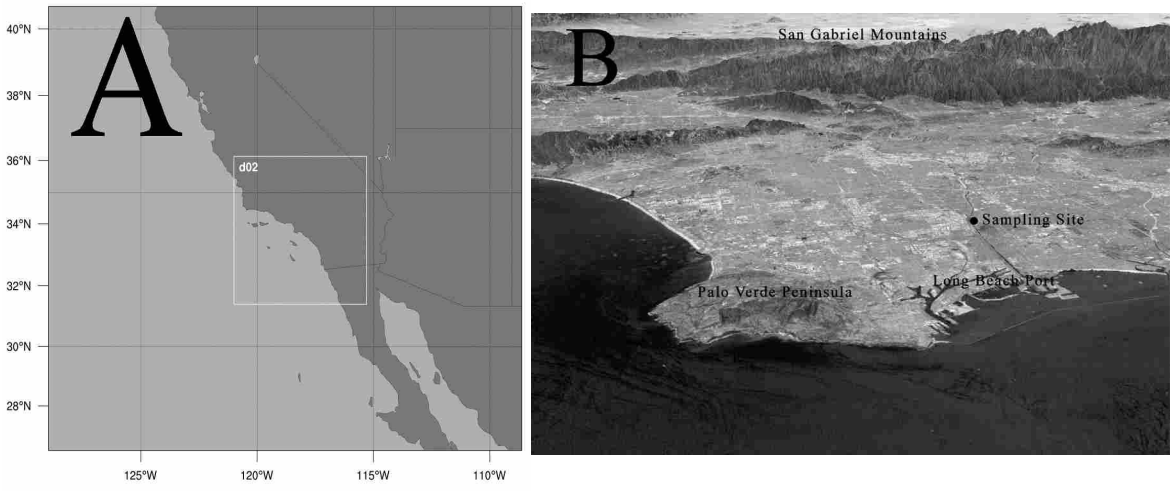

Figure A1.4. (A) A depiction of the two nested domains used for the simulations by the WRF-ARW model. The map area represents the outer domain with a grid cell size of 6 km and the white box labeled "do2" depicts the inner domain with a grid cell size of 2 km. (B) A topographical image of the upper left-hand portion of do2 highlighting the Sampling Site, the Long Beach Port, the Palo Verde Peninsula and the San Gabriel Mountains which form the northern boundary of the Los Angeles Basin.

is a typical 5-8 m/sec diurnal sea breeze, the nights are close to calm. Average summer maximum temperatures at the coast are 24°C, downtown LA 28°C, the inland valleys

35°C. Nighttime minimums are typically 17°C. August 2012 was a hotter than normal month.

From Aug 1 – Sept 3, a total of 34 days, 24 days were above the average maximum temperatures and 25 days were the above average minimums. There were long intervals where the marine/mixed layer was under 300 m. There were only 6 days when the airmass was cooler than normal. There were only 7 days when the stratus emanating from the ocean moved into the basin overnight. On most days, there was little stratus even along the coast. From Aug 1-5, there was a weak upper level trough along the west coast. This situation led to ML heights from 275-730 meters and surface temperatures below normal. The only other trough period was Aug 22-26 when ML heights ranged from 600-700 meters and surface temperatures were below normal. Nearly all other days were dominated by high pressure centered to the east of CA over the "Four Corners" area. Since circulation around a high pressure is clockwise, this southeast flow advected monsoonal moisture from the Gulf of Mexico. This configuration led to high clouds at times, disruption of the marine layer, warm nights, higher relative humidity and warmer than normal days. Another pattern was a drier high-pressure ridge from Sept 1-3. This flow was southwest off the Pacific Ocean. This pattern resulted in warmer days, but normal night temperatures, and a shallow marine layer.

The meteorology associated with the sampling site is interesting. It is in the downwind path of the Palo Verde Peninsula, (Figure 4B), convergence zone. Winds come from Santa Monica Bay to the north of the Peninsula and from the south in the direction of the Long Beach Port activities, Figure 4B. At times, they come from both directions.

Greatly aiding in the meteorological analyses were continuous hourly streamline plots in the boundary layer. AWS Truepower exercised the Weather Research and Forecasting (WRF) model Advanced Research (ARW) version 3.6. The simulated domain is displayed in Figure 4A. the parent domain was 297 x 250 grid points, 50 vertical levels, 6-km horizontal resolution, 1782 km x 1500 km. The inner nested domain (two-way interactive with parent domain) was 250 x 250 grid points, 50 vertical levels 2-km resolution, 500 x 500 km and centered on the Long Beach sampling site. The simulation data was created by one continuous WRF run that began at 0000 UTC on the July 30, 2012 (1700 PDT July 29) and ended at 0600 UTC on September 3, 2012 (2300 PDT September 2) with the first 48 hours used as a spin-up period. The initialization data was based on the GFS analysis data (i.e. 0 hour forecast) at 0.5-degree resolution. The GFS forecast hour 0 data, updated every 6 hours, was also used for lateral boundary conditions for the outer domain as well as for spectral nudging throughout the entire simulation period. The spectral nudging technique[311] is used to keep the extended simulation from drifting from the observed large-scale atmospheric state (as

represented by the GFS 0-hour analysis). The model outputs were saved at 1-hour intervals and the hourly graphical output provided for this analysis included PBL height, surface parameters including sea level pressure (mb), 2-meter temperature (deg C) and 10-meter wind (m/s), 10-meter streamlines with speed (m/s) shaded, 50-meter streamlines with speed (m/s) shaded and 80-meter streamlines with speed (m/s) shaded. Where possible, the modeled results were compared to observations and found to be quite accurate.

A1.5 EPA-PMF v5.0 Analysis

EPA-PMF v5.0 and the algorithm used in the analysis has been previously described (EPA 2014). With PMF, the results are constrained so that factor contributions cannot be negative for any species. One of the advantages to PMF is the ability to account for missing and below detection limit data. The uncertainty in each measurement can be adjusted to account for aberrations in the data set. In this study, error uncertainty estimates were chosen similar to those previously outlined by Grover[310]. Based on peak to peak noise in the data, a higher uncertainty (20%) was assigned to NVOM. For what were determined to be "reliable" data, the concentration values were directly used and the error estimates were assigned as the measurement error plus one third the limit of detection (LOD). In a few instances when the measurement was below the LOD, the error was estimated as 5/6 the LOD. Missing values in the data set were accounted for by taking the geometric mean of the hour

preceding and following the missing data point. SVOM concentrations were obtained as the hourly differences between the FDMS TEOM, conventional TEOM and measured ammonium nitrate. Therefore, the error estimate was performed as mentioned above using the highest LOD of the various measurement techniques. The uncertainty of the fitted parameter, FDMS calculated mass, was taken to be four times the measured value[312].

A1.6 PMF Analysis of Mass and Composition Data

One-hour semi-continuous measurements were made throughout the study period with instruments to measure both $PM_{2.5}$ mass, $PM_{2.5}$ chemical species, and gas phase species with concentrations as summarized above and shown in Figure 3. In performing PMF analysis, the number of factors to be identified is defined by the user. However, a higher order solution does not necessarily contain all the same factors as a lower order solution. Experimentation with the number of factors was performed until the most reasonable results are obtained (i.e. the results describe the data and were meaningful). In this study, a constrained base result is reported with details on the constraints applied to the EPA-PMF base analysis.

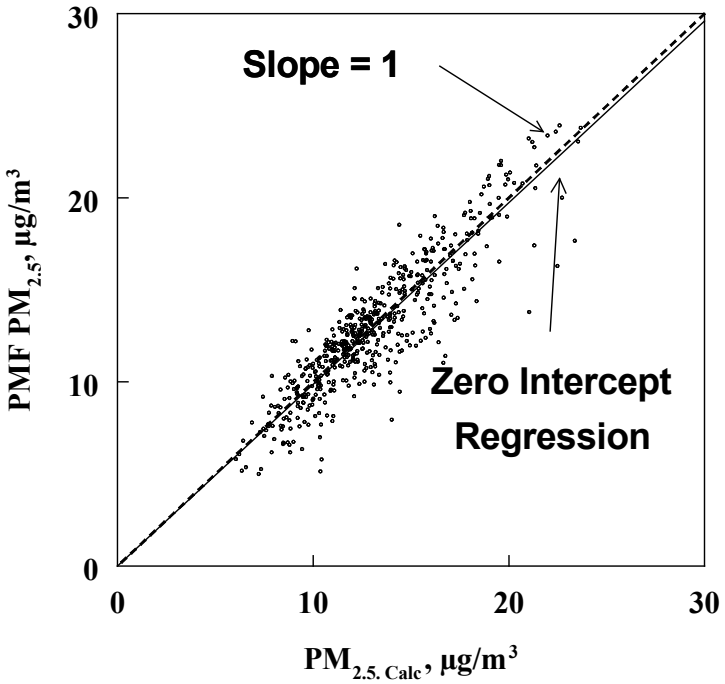

Figure A1.5. A comparison of the PM2.5,Calc used in the PMF analysis and the PMF PM2.5 calculated from the final EPA-PMF v5.0 soluti.on

Fifteen species for 520 1-hr averaged data sets were used in this EPA-PMF v5.0 analysis and ten factors were identified. An evaluation of the quality of the fitted data can be obtained by comparing the degrees of freedom (i.e. the number of data points) with the calculated value of *Q*. If a reasonable fit is obtained, the calculated value of *Q* should be equal to or less than the degrees of freedom. Deviation from the theoretical value suggests that the errors in the model are not well defined. For this study, the degrees of freedom were 7280 and the resultant *Q* value for the base result was 1185. This solution was further evaluated using the "constrained" feature of EPA-PMF and the resulting Q value was 1299. The constraint analysis focused on major species to see

where the profiles could be constrained to more closely match expectations based on the identification of the nature of each factor. The constraints involved minimizing the traffic, BC, and UV contributions to all factors that were unrelated to traffic emissions, maximizing the contributions of NO_X and CO to factors related to traffic, and minimizing the presence of sulfate, SO_2 and chloride in factors other than those in which these poorly measured species were dominant. This last decision was based on the observation that these species were present together only for a limited time period, e.g. August 8-15, Figure 3. The concentrations in the time series of all factors were essentially unchanged by these constraints. Residuals were small and Gaussian in nature. Examination of G-Space edges[313] indicated all factors were independent of each other as detailed below.

Linear regression analysis of the constrained solution calculated $PM_{2.5}$ compared to the input $PM_{2.5}$ resulted in a zero-intercept slope of 0.986 ± 0.005 (R^2 = 0.80, n = 520) and a regression calculated slope of 0.959 ± 0.020 (R^2 = 0.80 and intercept = 0.4 ± 1.6 $\mu g/m^3$) (Figure 5), respectively. As shown in Figure 5, the distribution of the differences between the FDMS mass and the PMF estimated mass inform the EPA-PMF analysis were random with an average deviation of 1.2 $\mu g/m^3$ (average $PM_{2.5}$ = 13.0 $\mu g/m^3$).

A second check on the "fit" of the solution can be made by comparing the sum of the factor contributions to the measured mass, to verify that the measured mass is well defined by the calculated sources. In this case, the sums of the factor contributions were

in good agreement with the measured $PM_{2.5}$ mass values and the individual species used in the factor analysis as shown in Figure 6, with the largest variations being -5.9% for NVOM, +3.5% for SVOM, and less that 2% for all other comparisons. Likewise, all fitted parameters were well accounted for in the analysis (Figure 6). The 3 percent overestimation of SVOM probably results from the higher uncertainty in this species since it was estimated from other measurements and not directly measured. The 5% underestimation of NVOM can be attributed to the higher uncertainly in these experimental values, being about four times higher than that for other species.

The factor profiles and concentrations for the ten identified factors are shown in Figure A1. 7.

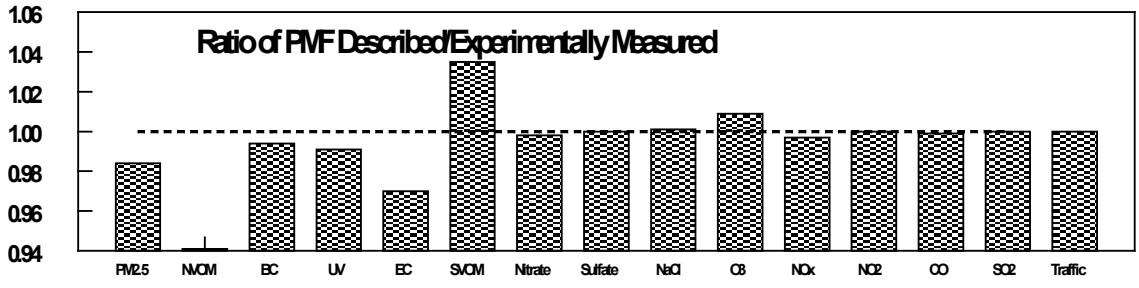

Figure A1.6. Ratio of PMF Described to experimentally determined average concentrations for each of the species used in the PMF analysis.

In source apportionment studies, a priori knowledge of chemical markers that can be attributed to a particular source is needed to identify sources most likely associated with each factor. Relevant time patterns and meteorological stream lines were also used in this study to aid in the identification of the sources associated with

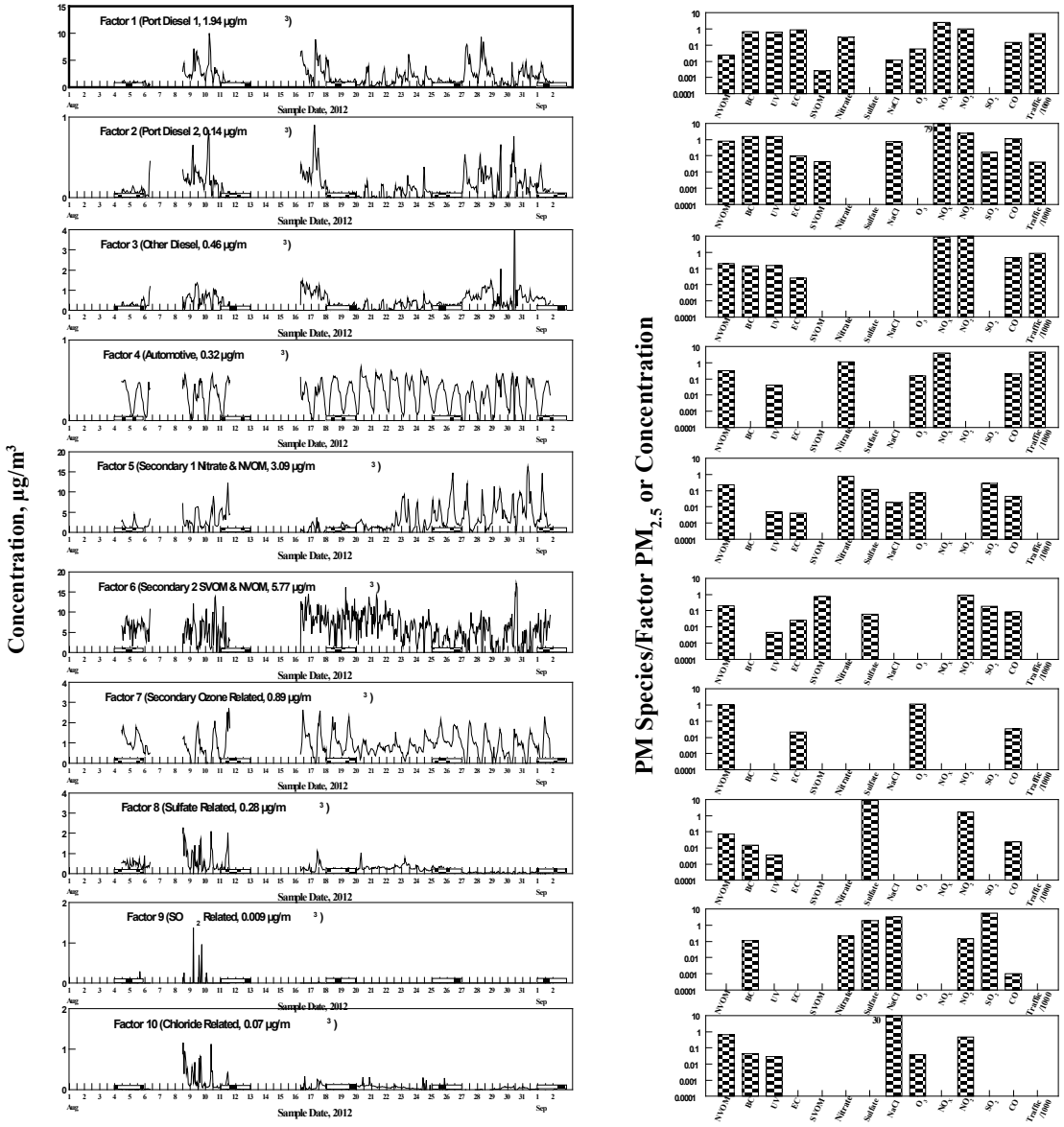

Figure A1.7. Time series plot of the $PM_{2.5}$ concentration for each of the 10 factors identified in the PMF analysis (weekends are marked by the hashed bars under the x axis) and a log bar plot of the factor profile.

each factor. This analysis was greatly aided by the hourly averaged nature of the results that permits better source resolution[314].

Because of the location of the sampling site, mobile sources will provide more factors than usual in their contribution to the $PM_{2.5}$. Mobile sources that affect the site include gasoline combustion emissions from automobiles and light-duty trucks, heavy-duty diesel trucks from the ports and diesel emissions from both heavy and light duty diesel vehicles that do not originate from the ports. It is anticipated that BC will be more associated with diesel emissions. It is also anticipated that a marked weekday – weekend difference will be seen in diesel emissions. Four factors were associated with characteristics of mobile sources. These characteristics are summarized in Table 1.

Table A1.1. Characteristics of the Four Factors Associated with Mobile Sources.

Fac. #	Factor Name	Avg. $\mu g/m^3$	Weekend Reduced	$BC/PM_{2.5}$	$NO_X/PM_{2.5}$	$CO/PM_{2.5}$	% Traffic
1	Port 1	1.94	Yes	0.70	1.3	75	8.3
2	Port 2	0.14	Yes	1.52(0.63)[a]	190(79)[a]	8058 (3360)[a]	0.6
3	Diesel	0.46	Yes	0.15	19.4	1050	14.7
4	Auto	0.32	No	0	12.4	611	76.4
[a] Ratios in ( ) are the values if the mass of Factor 2 was the sum of the carbonaceous components, 0.326 $\mu g/m^3$, see text							

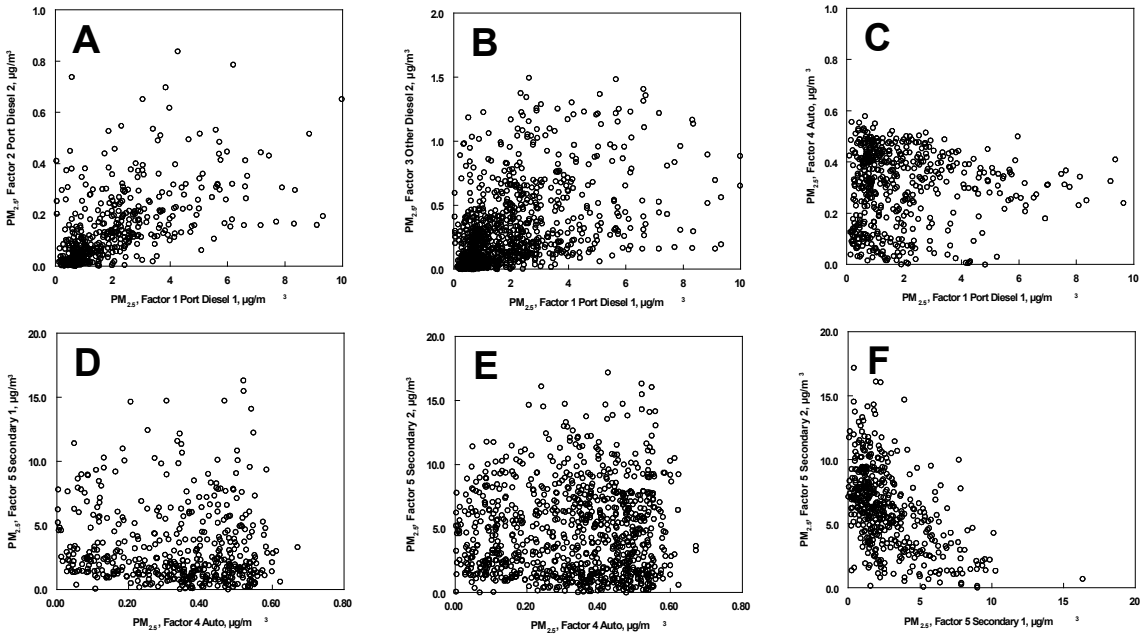

Figure A1.8. G edge analysis plots comparing the results for the three diesel related factors (A, B and C), the Auto related factor to the Secondary 1 and Secondary 2 related factors (D and E) and the two Secondary related factors to each other (F).

Factors 1, 2, and 3 were assumed to be associated with diesel emissions because of the high fraction of the $PM_{2.5}$ present as BC (Table A1.1) and because of the significant reductions in the factor contributions on weekends (Figure A1.7). G-Space edge analysis plots were created for comparison of each set of the diesel factors, Figure A1.8A, B and C. The lack of well-defined edges along the X or Y axes for the three comparisons and poor correlation between any two indicates the 3 diesel factors are independent of each other.

Factor 4 was assumed to be associated with gasoline combustion emission from automobiles because of absence of BC in the profile and the strong correlation with the traffic (Figure A1.9). These relationships included morning and evening rush hour peaks during the week days, and the lack of these peaks but with significant traffic flow on the weekends. To better delineate the differences in the four sources, the average diel patterns for each factor on those days with maximum Factor 1 concentrations (Thursday and Friday) were compared (Figure A1.10).

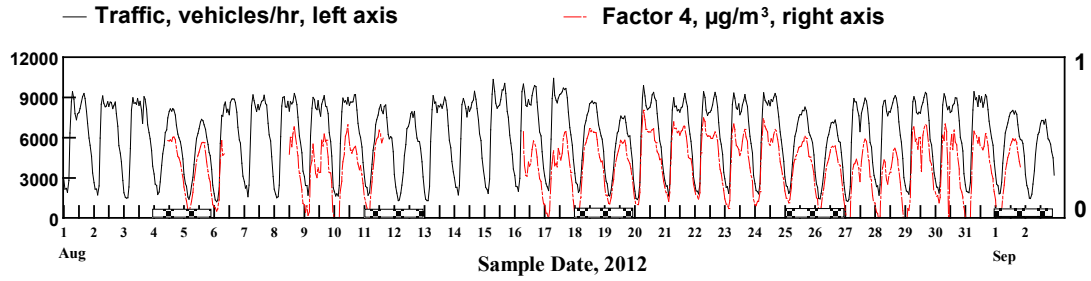

Figure A1.9. Comparison of the hourly averaged traffic count to the concentration of the Auto related Factor 4.

Factor 1, Diesel Port 1, was associated with the main traffic flow from the port had an early morning 6:00 peak and then decreased gradually throughout the day. Factor 2, Diesel Port 2, had a similar pattern but peaked an hour or two earlier. In contrast, Factor 3, the non-port diesel related factor peaked later in the morning after the Auto morning peak at 7:00 am (Figure A1.10). We assume that Factors 1 and 2 are associated with emissions from diesel trucks from the port and that Factor 3 is associated with non-port diesel traffic. The differences in the characteristics of Factor 1 compared to 2 and 3 (Table A1.1) are that the ratio of both NO_X and CO to $PM_{2.5}$ in the factor profile are much lower for Factor 1 than for either Factor 2 or 3, consistent with the Port requirements for lower emitting diesel engines in the Port fleet. These data would then suggest that about 8% of the trucks visiting the Port (Port 2) have higher emissions of CO and NO_X with the CO being comparable to the normal diesel fleet. The

comparably higher amount of NO_x for the Port 2 factor could not be reduced by the EPA-PMF constraint analysis.

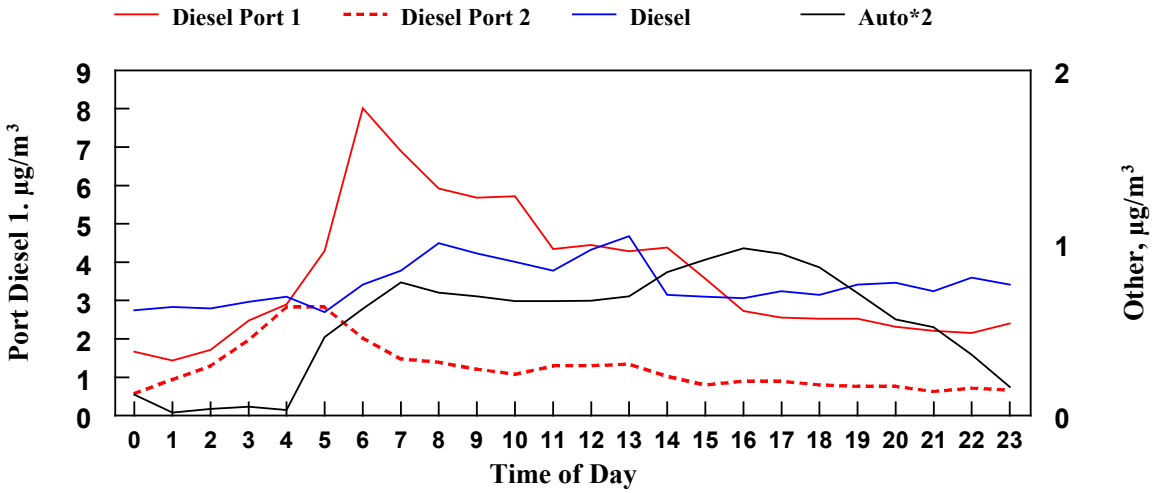

Figure A1.10. Comparison of the average of the diurnal pattern of the four traffic related factors on those days with maximum concentrations from the Diesel Port 1 factor (Thursday and Friday).

Factor 4 is associated with emissions from gasoline burning automobiles. The BC in this factor is very low and the factor is strongly associated with traffic (Table A1.1 and Figure A1.9). The weekday morning and afternoon rush hour events are clearly seen in the data sets. In addition, these rush hour peaks are absent during the weekends.

Factors 5, 6, and 7 are identified in Figure A1.7 as being associated with the formation of secondary $PM_{2.5}$, rather than associated with primary emissions. These factor profiles are generally associated with components expected to be produced by secondary aerosol formation processes, e.g., NVOM, ammonium nitrate, SVOM and (to a lesser extent) ammonium sulfate. The concentrations of the $PM_{2.5}$ associated with these factors also do not have time patterns similar to the patterns associated with the first four, traffic-related, factors. G-space edge analysis plots also indicated that the two

major secondary factors (5 and 6) are not related to each other or to auto factor 4 (Figures A1.8D, E & F). The characteristics of these three factors with respect to the potential secondary material are given in Table A1.2, along with the names with which they are associated in Figure A1.7.

Table A1.2. Characteristics of the Three Factors Associated with Formation of Secondary PM2.5.

Fac. #	Factor Name	Avg. $\mu g/m^3$	NVOM/ $PM_{2.5}$ (%NVOM)	Nitrate/ $PM_{2.5}$ (% Nit.)	SVOM/ $PM_{2.5}$ (%SVOM)	Sulfate /$PM_{2.5}$ (% Sul.)	% Traffic
5	Nitrate & NVOM	3.09	0.23 (22%)	0.79 (72%)	0..00 (11%)	0.11 (12%)	0.0
6	SVOM & NVOM	5.77	0.19 (36%)	0.00 (0%)	0.74 (100%)	0.06 (11%)	0.0
7	Ozone Related[b]	0.89	1.09 (29%)	0.00 (0%)	0.00 (0%)	0.00 (0%)	0.0
	% Species In Other Factors		14% (In mobile, 10%, and refinery, 4%, factors)	29% (In mobile, 28%, and refinery, 1%, factors)	0%	76% (In refinery factors)	

The agreement between factor components and factor mass was very good for the factor in this group having the highest average $PM_{2.5}$ concentration, Port 1 with an average $PM_{2.5}$ concentration of 1.94 $\mu g/m^3$ and a ratio of components to factor mass of 1.04. The component mass to factor mass of Factor 3 (Diesel, 0.46 $\mu g/m^3$) was 0.35 and for Factor 4 (Auto, 0.32 $\mu g/m^3$) was 1.46. These deviations from unity are probably due to the small amount of mass in the factors and uncertainly in the data. The fit for Factor 2 (Port 1, 0.14 $\mu g/m^3$) was particularly high, the ratio being 3.17. If the mass of carbonaceous components in the factor were taken to be a better fit to the data than the

mass assigned by the PMF analysis the average mass for the factor would be 0.326 $\mu g/m^3$ (34% NVOM, 64% BC and 2% SVOM). The ratio of NO_X and CO to factor mass would then be calculated as 79 and 3360, respectively in contrast to the values given in Table A1.2.

Factor 5 (labeled Nitrate & NVOM) is dominated by the presence of NVOM (23% of the factor mass) and ammonium nitrate (79% of the factor mass) and only minor contribution from other particulate species (Figure A1.7 and Table A1.2). The ratio of the mass of factor species to factor mass is 1.15 and reasonable closure is seen between the species mass and factor mass.

Factor 6 (labeled SVOM & NVOM) is dominated by the presence of NVOM (19% of the factor mass) and SVOM (74% of the factor mass). The ratio of the mass of factor species to factor mass is 1.01.

The contributions from Factors 5 and 6 were examined as a function of meteorology. Generally, the nitrate in Factor 5 was high when the organic material in Factor 6 was low and vice versa. The nitrate was high from Aug 23-Sept 2 while the organics were high from Aug 16-23. In both periods, ambient temperatures in the LA Basin were 3-6ºC warmer than normal. In the Aug 16-23 period the night minimums were 21 to 24ºC, warm for the LA Basin. The relative humidity was higher due to a combination of SE monsoonal flow and variable high clouds in the area. There was no stratus in the basin and the mixing heights were low, ranging from 120 to 200 meters increasing to 400 meters at the end of the period. The afternoon sea breeze was quite weak particularly at the beginning of the period when organic concentrations were highest.

There were subtle differences between the two periods. From Aug 23-Sept 2, the ambient maximum surface temperatures were comparable. However, the minima were lower, closer to normal, ranging from 12 to 20.5ºC. The airmass was drier with mostly a

southwestly flow off the Pacific. The mixing heights were comparable. However, the sea breeze was stronger. The lower dewpoints in the deserts led to hotter daytime temperatures.

The relative importance of Factor 5 (the nitrate and NVOM containing secondary factor) is much higher from Aug 23 through the end of the study, less important on Aug 9 and 10 and Aug 23 through 25, and minimal on all other days. These patterns are consistent with the presence of stratus cloud moisture as summarized in the Meteorological section above. Thus, the conversion of precursors to the factor secondary material may be directly related to atmospheric water content. The formation of this factor is also enhanced during the day compared to the night (Figure A1.7). These observations are all consistent with Factor 5 being dominated by ammonium nitrate.

In contrast, Factor 6 contains both NVOM and SVOM, with SVOM being dominant. However, none of the other secondary factors have significant amount of SVOM. The formation of this factor does not show a significant day-night variation and the concentrations of the factor is highest on those days when stratus clouds, and the accompanying moisture, is not present (Figure A1.7 and the Meteorological Section).

Finally, the diel pattern for Factor 7 (Figure A1.7) is consistent with the changes in concentrations of ozone and a 78% of the contribution of ozone to the PMF solution is contained in this factor. The PMF solution described the composition of this factor well, with 9% the factor mass (average of only 0.09 $\mu g/m^3$) being overestimated by the assigned components, NVOM being the most important contributor to the factor mass (Figure A1.7 and Table A1.2).

As outlined in the section **Other Components Used in the PMF Analysis,** the concentration of ozone was estimated from the data at two nearby sites, Long Beach and Compton. The sampling site was located adjacent to the I710 freeway and, while

close to this site, the Compton site is not close to a freeway and the Long Beach site is a couple of blocks from the nearest freeway. It is possible that the ozone at the study site would be more effected by the titration of ozone by higher concentrations of NO at the sampling site. To test the possible impact of this chemistry on the use of ozone in the PMF analysis, the EPA-PMF analysis was performed on the data set omitting ozone from the analysis. Reducing the number of factors to 9 produces a result with 9 factors consistent (the ozone factor was, of course, not present) with the 10-factor solution including ozone. The concentrations of all factors are comparable, except for the concentration of the factor associated with auto emissions, where the average concentration is reduced from 0.32 $\mu g/m^3$ to only 0.03 $\mu g/m^3$, with the difference in mass being present in the Nitrate & NVOM factor. This significant reduction in the mass of the Auto factor does not seem reasonable and suggests that without the ozone present to identify formation of secondary material during the time when the day time peaks in the Auto Factor are present, PMF is not able to sort out these two contribution to total $PM_{2.5}$ mass. Omitting ozone from the analysis but fitting for 10 factor increases the mass in the Auto Factor to 0.73 $\mu g/m^3$ and produces a new factor with an average mass of 3.5 $\mu g/m^3$ with only NVOM material and reduces the mass in the other two secondary factors containing NVOM. We conclude that inclusion of ozone in the analysis is essential to sorting out the presence of primary and secondary material during the day time.

For the species which might be formed by secondary processes, all but 14% of the NVOM, 29% of the ammonium nitrate, and all of the SVOM were associated with the secondary factors. The remainder was generally associated with primary diesel and automotive factors (Table A1.2). None of the secondary factors was strongly associated with the meteorological transport vectors.

The final three factors are very irregular in the factor time pattern and are either dominated by the influence of sulfate, SO_2, or chloride and are so named (Figure A1.7). Possible sources of either the sulfate or SO_2 (Factors 8 and 9, respectively) are either ship traffic from transport of emissions from incoming ships, from ships in the port, or from emissions from nearby refineries, possibly during flare upsets. The meteorological data rule out the importance of the port or ships at sea as important contributors to these two factors. Generally, when episodes for these two factors were present, transport was either from the east, northeast, or west of the sampling site and the transport winds were weak.

SCAQMD keeps logs of locations and significance of refinery upsets (SCAQMD website). Under normal operations, the refinery downwind ambient air quality signal was small/negligible for both SO_2 and sulfate. However, during upset and flare periods at a nearby 3.5 km upwind refinery, the PMF analysis indicated the SO_2, sulfate, and chloride related factor concentrations (8-10) were significant (Figure A1.7). The

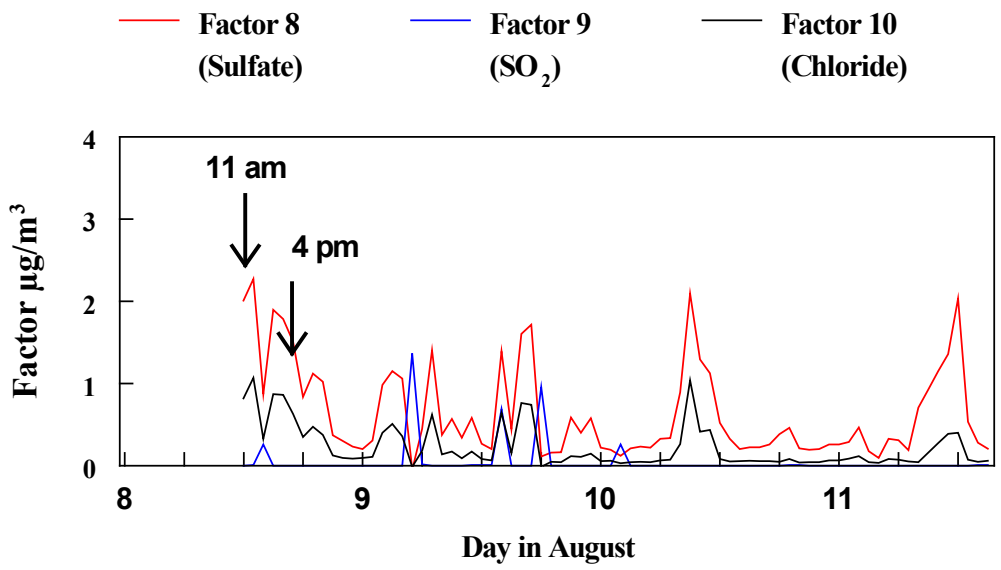

Figure A1.11. Comparison of the diurnal variations in the concentrations of Factor 8 (Sulfate), Factor 9 (SO_2) and Factor 10 (Chloride) on 8 through 11 August. The two downward arrows indicated the times for the streamlines and wind speed data given in Figure 12.

suggested impact by emissions from the refinery is corroborated by the WRF streamline analyses.

An example of this impact occurred Aug 8-11 (Figure A1.11). High concentrations of the three factors were correlated with the lee side stagnation associated with the Palo Verde convergence zone. Figures A1.11 and A1.12 illustrate this condition on Aug 8. The Palo Verde Peninsula and Hills (Figure A1.4B) are about 500 m high, rising next to the Pacific Ocean. Winds can go around both sides of these hills as shown beginning at 1100 PDT on Aug 8 in Figure A1.12A. A convergence/stagnation zone then forms on the lee side of these hills during the morning hours. This location is the general area of the BP/Arco refinery. Later this same day at 1600 PDT, the afternoon westerlies took over, essentially removing the convergence zone (Figure A1.12B). This general pattern was repeated on each day of the Aug 8-11 period. There was a good correlation between these two wind patterns and the pollutant levels. When stagnation conditions prevailed, the pollutant concentrations increased and vice versa when the westerlies took over.

Factors 8 and 10 are dominated by sulfate and chloride, respectively. Figure A1.11 indicates an excellent correlation between these two factors, indicating both are emitted from the refinery under the similar conditions. Sulfur oxides can be emitted

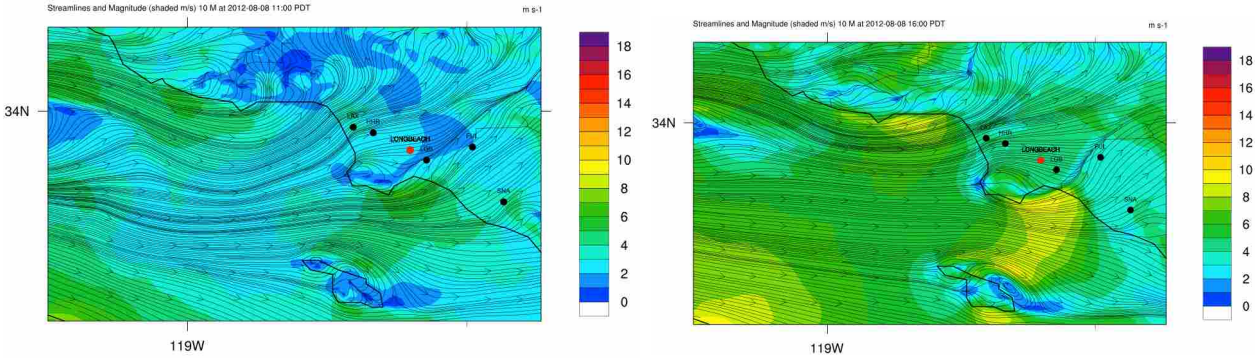

Figure A1.12. Streamlines and wind speed (color shading in m/s) at 10-m above ground level (AGL) for (A) 1300 PDT and (B) 1700 PDT on August 8, 2015 from the inner nest (2 km grid cells) of the WRF simulation

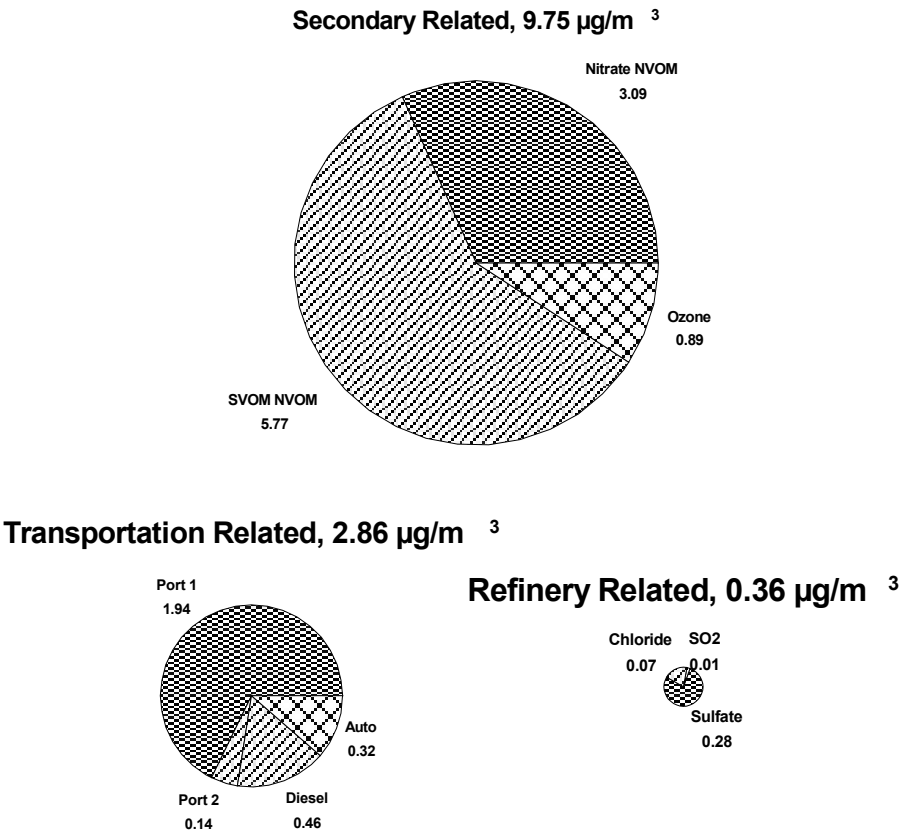

Figure A1.13. Pie charts of the contribution of the three factors contributing to Secondary Related factors, the four factors contributing to Transportation Related factors and the three factors contributing to the Refinery Related factors to total $PM_{2.5}$. The area of each graph and pie section are related to the contribution of each to total $PM_{2.5}$.

from several oil refinery processes including catalytic cracking, the sulfur recovery plant, and the steam boiler, process furnace, or process heater. Chloride is emitted during catalytic reforming. Emissions of chloride and sulfur oxides are comparable[315, 316] (US DHEW, 1960, McIlvaine Company website). Conversion of emitted SO_2 to sulfate in a steam vent can be expected to be rapid. These refinery emission conditions are consistent with Figure A1.11.

The contribution of the three classes of factors identified in this analysis, Transport, Secondary, and Refinery, are compared in the three pie charts in Figure

A1.13. In each case, the area of the circle is proportional to the average total concentrations of the factors represented. Secondary Related factors contributed to 71% of the total $PM_{2.5}$, and Transportation Related and Refinery Related factors to 21% and 8%, respectively. The three factors with the highest contribution to total $PM_{2.5}$ were the SVOM & NVOM secondary factor (44%), Nitrate & NVOM secondary factor (23%) and the Port 1 transportation factor (15%).

A1.7 Conclusions

Utilizing highly time resolved data permitted the resolution of multiple traffic sources because they had different diel patterns. Three traffic sources were attributed to heady-duty diesel emissions, one from traffic not originating from the Long Beach and Los Angeles Ports south of the sampling site and two from traffic originating from these two ports. The two factors associated with traffic from the Ports included 9% of the port traffic with higher emissions of NO_X and CO by about a factor of 5 than the other 91% of traffic from the Ports. It was possible to assess the relative contributions of primary and secondary PM sources on the measured concentrations and to identify specific industrial upset episodes. These results should provide useful input into air quality management plans for this area of Los Angeles. An EPA-PMF analysis of sources of $PM_{2.5}$ during the I710 2012 study were greatly aided by the use of hourly average data. Not specifically highlighted in the discussion, but also evident in the

analysis, was the importance of including highly time resolved measurements of the major $PM_{2.5}$ constituents.

Appendix A2- Chapter 2 Supplementary Information

Supplementary Information for "An Improved Model to Calculate Equilibrium Constants for Formation of Proxy Radical-Water Complexes"

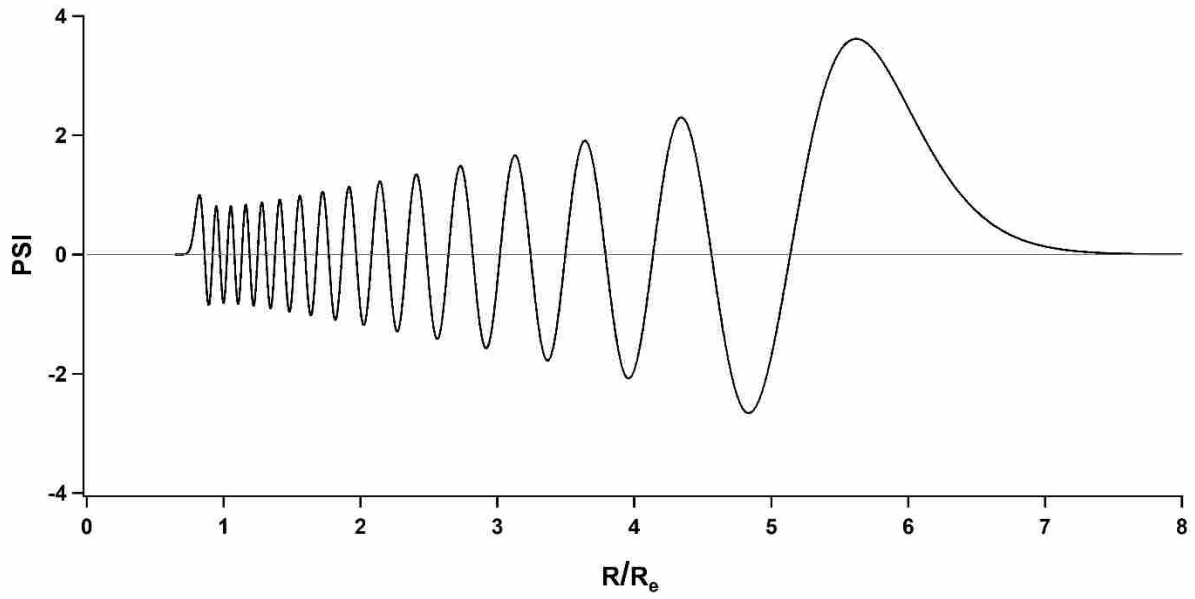

Figure S1. Wavefunction of the Lennard-Jones 6-3 potential for v = 30 (of 52 bound levels) for a dissociation energy 10 times the harmonic frequency. Notice the high probability just inside the classical turning point at approximately R/Re = 6.2. The value of /Re 2 for this state is approximately 25, so this state would have a lower rotational constant by a factor of about 0.04.

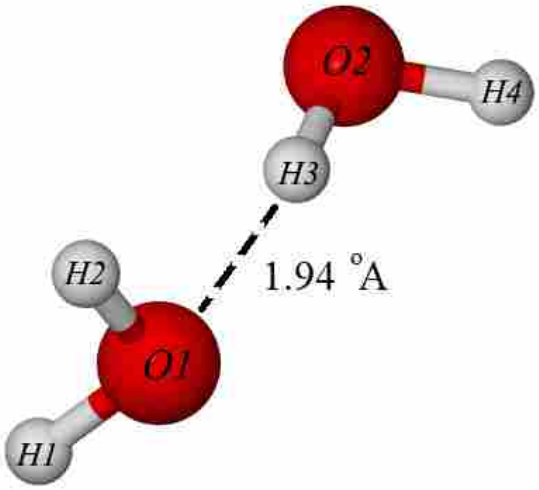

Figure S2 Computed geometry of the water dimer. The molecule on the left is the acceptor, and the molecule on the right is the donor.

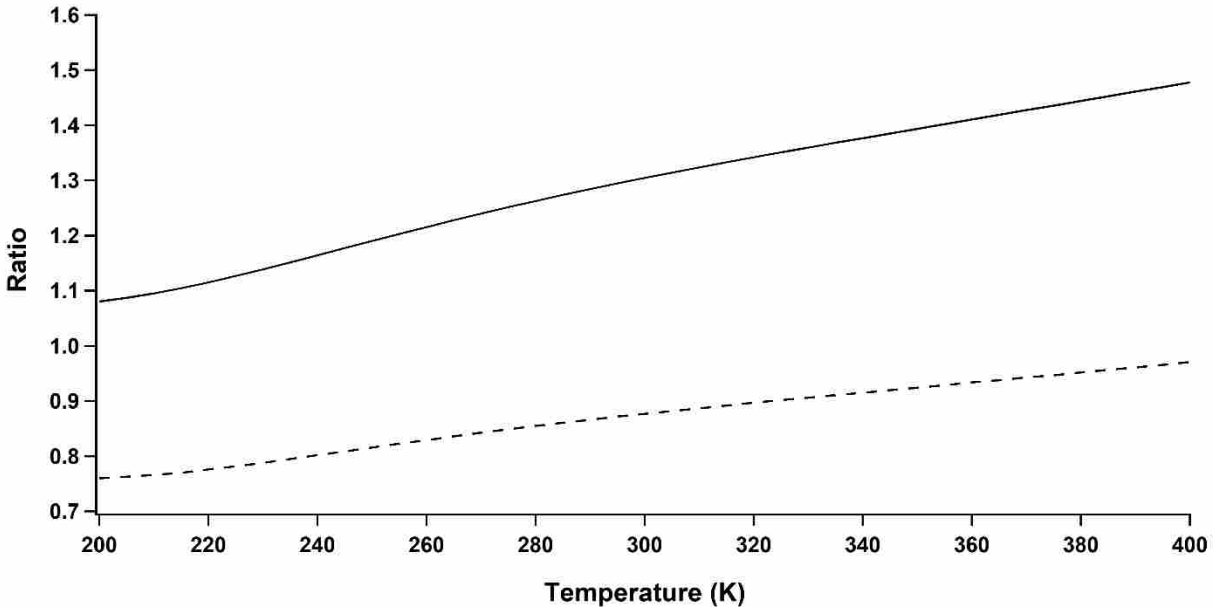

Figure S3 Ratio of the vibrational-rotational partition function using MO6-2X (solid line) and B3LYP DFT (dashed line) options for Gaussian 09 DFT geometry optimizations compared to the experimental values derived from Ref. 27. The calculations use Gaussian harmonic oscillator frequencies, force constants, and masses in the LJ63+5HR model to calculate the partition function. Both methods give results correct to about 30%.

This section explains how output from Gaussian 09 is used in the hindered rotor treatment of soft vibrational modes of radical–water complexes. Gaussian output of each computed normal mode includes the following quantities: frequency in cm^{-1}, reduced mass in amu, and force constant in mdyne/Å. We take the normal mode Hamiltonian to be of the form

$$H=P^2/2\mu+1/2kQ^2 \qquad (8)$$

where Q has the dimensions of length. We seek to transform this to an n-fold hindered rotor Hamiltonian of the form

$$H=p^2/2I+W/2[1-\cos(n\theta)] \qquad (9)$$

where W is the barrier height, I is the moment of inertia, and n is either 1 or 2. The coordinate transformation is given by $Q = a\theta$, where a has dimensions of length, and θ is measured from a reference angle determined by the equilibrium configuration. To match the potential near equilibrium, we note that in Eq. (9) $V(\theta) \approx Wn^2\theta^2/4$, which requires that the parameter a is determined by the harmonic force constant

$$ka^2=n^2W/2 \qquad (10)$$

and the moment of inertia is determined by the effective mass

$$I=\mu a^2 I=\mu a2 \quad (11)$$

Now, to transform the hindered rotor Hamilton to Mathieu's differential equation[317], use the coordinate transformation $2y = n\theta$ to transform to

$$d^2\psi dy^2+(A-2q\cos 2y)\ \psi=0, d2\psi dy2+(A-2q\cos f_0 2y)\psi=0, \quad (12)$$

through which the barrier height parameter, q, is identified.

$$q=2IW\hbar^2 n^2=\mu W^2 k\hbar^2, q=2IW\hbar 2n2=\mu W2k\hbar 2, \quad (13)$$

and the eigenvalue, A, determines the energy of the state using

$$E=W2+An^2\hbar^2 8IE=W2+An2\hbar 28I \quad (14)$$

In Eq. (12) and (14), A is the Mathieu eigenvalue, which comes in 4 types[317]. Eigenvalues a_i where i is even have eigenfunctions which are symmetric with period π. Eigenvalues b_i where i is even have eigenfunctions which are antisymmetric with period π. Both of these types of eigenvalues are allowed for both $n = 1$ and $n = 2$. Eigenvalues a_i where i is odd have eigenfunctions which are symmetric with period 2π. Eigenvalues b_i where i is odd have eigenfunctions which are antisymmetric with period 2π. These types of eigenvalues are not allowed for $n = 1$, only for $n = 2$. The order of the eigenvalues is given by: a_0, b_1, a_1, b_2, a_2, b_3, a_3, b_4, a_4, … [317]. To calculate the partition function, take calculated harmonic frequencies, reduced masses, and force constants from a Gaussian calculation and estimated barrier heights, calculate

the *a* parameter using Eq. (1.), the *I* parameter using Eq. (11), and the *q* parameter using Eq. (13). Then calculate the Mathieu equation eigenvalues using Refs[146, 147] and order them as listed above, retaining all those whose energy given by Eq. (14) is below the dissociation energy of the complex. This approximate treatment assumes a simple cosine form of the potential and that the effective mass (*G*-matrix element) of each hindered rotor mode is constant at its value at the equilibrium geometry.

Equilbrium Geometry of Water Molecule

b3lyp/aug-cc-pVDZ opt=(calcall,noraman) scf=(qc,fulllinear) nosymm
Gaussian 09: EM64L-G09RevB.01 12-Aug-2010
19-Jul-2016

Center Number	Atomic Number	Atomic Type	Coordinates (Angstroms) X	Y	Z
1	8	0	-2.596175	1.240468	0.000000
2	1	0	-1.632126	1.280504	0.000000
3	1	0	-2.880245	2.162589	0.000000

Distance matrix (angstroms):

		1	2	3
1	O	0.000000		
2	H	0.964880	0.000000	
3	H	0.964885	1.528357	0.000000

Rotational constants (GHZ): 813.5451119 429.3509703 281.0342620
Rotational temperatures (Kelvin) 39.04396 20.60557 13.48750

Harmonic frequencies (cm**-1), reduced masses (AMU), force constants (mDyne/A):

	1	2	3
	A	A	A
Frequencies --	1618.7449	3794.4988	3904.3074

Red. masses -- 1.0828 1.0450 1.0821
Frc consts -- 1.6717 8.8653 9.7186

Equilibrium Geometry of Water Dimer

b3lyp/aug-cc-pVDZ opt=(calcall,noraman) scf=(qc,fulllinear) nosymm
Gaussian 09: EM64L-G09RevB.01 12-Aug-2010
26-Jul-2016

Center Number	Atomic Number	Atomic Type	Coordinates (Angstroms) X	Y	Z
1	8	0	1.926626	0.493054	-3.188792
2	1	0	1.606197	-0.026831	-2.431578
3	1	0	2.345930	-0.148125	-3.773448
4	8	0	0.873697	-0.834461	-0.821959
5	1	0	1.261716	-0.435785	-0.032904
6	1	0	-0.073107	-0.658572	-0.753058

Distance matrix (angstroms):

		1	2	3	4	5
1	O	0.000000				
2	H	0.972794	0.000000			
3	H	0.963716	1.537053	0.000000		
4	O	2.910817	1.944144	3.368949	0.000000	
5	H	3.356259	2.457549	3.905117	0.965458	0.000000
6	H	3.355291	2.456947	3.903210	0.965465	1.532974

		6
6	H	0.000000

Rotational constants (GHZ): 215.0252280 6.4093947 6.4078965
Rotational temperatures (Kelvin) 10.31957 0.30760 0.30753

	1	2	3
	A	A	A
Frequencies --	135.9863	158.0129	162.9774
Red. masses --	1.0685	1.6513	1.0624

Frc consts --	0.0116	0.0243	0.0166

	4	5	6
	A	A	A
Frequencies --	187.2245	360.6935	634.4349
Red. masses --	2.0372	1.0986	1.0409
Frc consts --	0.0421	0.0842	0.2469

	7	8	9
	A	A	A
Frequencies --	1617.3464	1637.6701	3672.8179
Red. masses --	1.0837	1.0767	1.0552
Frc consts --	1.6702	1.7014	8.3862

	10	11	12
	A	A	A
Frequencies --	3789.4211	3874.3539	3895.5631
Red. masses --	1.0450	1.0729	1.0822
Frc consts --	8.8411	9.4883	9.6765

Equilibrium Geometry of Hydroperoxy Radical

b3lyp/aug-cc-pVDZ opt=(calcall,noraman) scf=(qc,fulllinear) nosymm
Gaussian 09: EM64L-G09RevB.01 12-Aug-2010
3-Aug-2016

Center Number	Atomic Number	Atomic Type	Coordinates (Angstroms) X	Y	Z
1	8	0	0.388873	1.195421	1.493505
2	1	0	0.960155	0.400247	1.517101
3	8	0	1.000679	2.044898	0.676427

Distance matrix (angstroms):

		1	2	3
1	O	0.000000		
2	H	0.979398	0.000000	
3	O	1.327981	1.847499	0.000000

Rotational constants (GHZ): 616.5472194 33.7158091 31.9676614
Rotational temperatures (Kelvin) 29.58956 1.61810 1.53420

	1	2	3
	A	A	A
Frequencies --	1164.3761	1435.1314	3586.5474
Red. masses --	12.0455	1.1438	1.0687
Frc consts --	9.6219	1.3880	8.0997

Equilbrium Geometry for Hydroperoxy-Water Complex

b3lyp/aug-cc-pVDZ opt=(calcall,noraman) scf=(qc,fulllinear) nosymm
Gaussian 09: EM64L-G09RevB.01 12-Aug-2010
26-Jul-2016

Center Number	Atomic Number	Atomic Type	Coordinates (Angstroms) X	Y	Z
1	8	0	2.020074	0.089054	-3.203443
2	8	0	1.359234	-0.645544	-2.317455
3	1	0	2.471623	-0.589834	-3.775340
4	8	0	2.859929	-2.286289	-4.118741
5	1	0	2.268861	-2.559714	-3.400037
6	1	0	2.540918	-2.740032	-4.908335

Distance matrix (angstroms):

		1	2	3	4	5	6
1	O	0.000000					
2	O	1.327147	0.000000				
3	H	0.995917	1.834650	0.000000			
4	O	2.680556	2.861601	1.773884	0.000000		
5	H	2.667680	2.379801	2.015538	0.969875	0.000000	
6	H	3.343899	3.534956	2.431426	0.964940	1.543208	0.000000

Rotational constants (GHZ): 32.2690365 5.9080602 5.0462611

Rotational temperatures (Kelvin) 1.54867 0.28354 0.24218

	1	2	3
	A	A	A
Frequencies --	108.4895	200.5141	262.2394
Red. masses --	3.1114	1.1013	3.6037
Frc consts --	0.0216	0.0261	0.1460

	4	5	6
	A	A	A
Frequencies --	301.2880	471.4750	686.9162
Red. masses --	1.3452	1.2964	1.0635
Frc consts --	0.0719	0.1698	0.2957

	7	8	9
	A	A	A
Frequencies --	1191.7047	1564.7881	1612.3135
Red. masses --	14.3274	1.1040	1.0801
Frc consts --	11.9882	1.5927	1.6542

	10	11	12
	A	A	A
Frequencies --	3294.7624	3746.4153	3874.6854
Red. masses --	1.0683	1.0484	1.0788
Frc consts --	6.8324	8.6695	9.5427

Equilibrium Geometry of HEP radical, lowest energy conformation

b3lyp/aug-cc-pVDZ freq=anharmonic geom=check guess=read nosymm
Gaussian 09: EM64L-G09RevB.01 12-Aug-2010
27-Sep-2016

Center Number	Atomic Number	Coordinates (Angstroms) X	Y	Z
1	6	-0.061432	0.910957	0.782513
2	1	0.705371	1.659895	1.049117
3	1	-0.866918	0.972968	1.528178
4	6	0.551322	-0.479198	0.865755

5	1	-0.099288	-1.237915	0.412442
6	1	0.802782	-0.748645	1.899438
7	8	1.845509	-0.542002	0.183058
8	8	1.734833	-0.302634	-1.109540
9	8	-0.651527	1.193697	-0.474267
10	1	-0.005885	0.965097	-1.159256

Interatomic distances:

		1	2	3	4	5
1	C	0.000000				
2	H	1.104524	0.000000			
3	H	1.099395	1.781421	0.000000		
4	C	1.521489	2.152457	2.135180	0.000000	
5	H	2.180834	3.074107	2.592706	1.097469	0.000000
6	H	2.179143	2.556091	2.426867	1.097422	1.806730
7	O	2.471206	2.626466	3.385519	1.464561	2.078256
8	O	2.877366	3.093721	3.918396	2.309473	2.560308
9	O	1.416916	2.092657	2.026055	2.457861	2.646499
10	H	1.943318	2.421888	2.822010	2.548948	2.707807

		6	7	8	9	10
6	H	0.000000				
7	O	2.018896	0.000000			
8	O	3.181445	1.319225	0.000000		
9	O	3.394434	3.111256	2.887437	0.000000	
10	H	3.598119	2.738761	2.153999	0.968670	0.000000

Rotational temperatures (Kelvin) 0.42330 0.19579 0.14642
Rotational constants (GHZ): 8.82012 4.07967 3.05091

	1	2	3
	A	A	A
Frequencies --	85.7263	167.3243	329.3932
Red. masses --	4.7190	4.9231	2.1870
Frc consts --	0.0204	0.0812	0.1398

	4	5	6
	A	A	A
Frequencies --	398.3672	458.3005	549.7264
Red. masses --	5.0648	1.1460	2.1348
Frc consts --	0.4736	0.1418	0.3801

	7	8	9
	A	A	A
Frequencies --	795.9505	919.9048	960.8499
Red. masses --	3.3120	2.5057	2.1000
Frc consts --	1.2363	1.2493	1.1423

	10	11	12
	A	A	A
Frequencies --	1080.0795	1106.5028	1165.9243
Red. masses --	2.4795	3.2882	4.9505
Frc consts --	1.7042	2.3720	3.9650

	13	14	15
	A	A	A
Frequencies --	1212.2830	1264.4977	1349.1838
Red. masses --	1.1182	1.2748	1.3282
Frc consts --	0.9682	1.2010	1.4244

	16	17	18
	A	A	A
Frequencies --	1363.8102	1424.1811	1445.8708
Red. masses --	1.2517	1.2480	1.1029
Frc consts --	1.3717	1.4914	1.3585

	19	20	21
	A	A	A
Frequencies --	1469.8634	3004.1336	3070.1907
Red. masses --	1.0828	1.0681	1.0604
Frc consts --	1.3784	5.6792	5.8893

	22	23	24
	A	A	A
Frequencies --	3086.3711	3141.5547	3752.7782
Red. masses --	1.0914	1.1103	1.0660
Frc consts --	6.1255	6.4560	8.8449

X matrix of Anharmonic Constants (cm-1)
Note: numbering of normal modes is reversed from normal mode numbering

	1	2	3	4	5
1	-98.258				
2	0.862	-36.368			
3	-4.270	-14.655	-46.916		
4	-0.217	-113.370	-41.060	-25.833	
5	-2.685	-0.964	-30.731	-4.245	-60.121
6	0.174	-0.551	-13.339	-2.026	11.032
7	-0.145	-21.318	-1.080	-5.058	-0.030
8	-4.589	-1.368	-2.786	-0.507	10.319
9	-5.425	-2.159	-0.895	1.521	3.465
10	-2.782	-7.108	-2.590	2.291	2.029
11	-2.097	-5.689	-2.303	-6.647	-0.342
12	-5.781	-1.626	-2.481	-1.822	-5.089
13	-1.137	-2.040	-0.461	-1.224	-0.004
14	0.029	-2.182	1.349	-1.682	1.321
15	0.248	-1.388	1.110	-1.970	-1.942
16	-1.982	0.114	-4.590	-1.084	0.227
17	-2.100	-0.953	0.146	-1.112	-1.115
18	0.771	0.414	-1.828	-0.293	0.796
19	0.830	-0.418	-0.489	-0.377	0.569
20	12.504	1.078	-5.437	-0.217	5.865
21	0.008	-0.492	0.472	-0.156	0.723
22	1.105	-0.962	-0.568	-0.713	0.916
23	-1.422	0.292	0.583	0.372	1.307
24	6.612	-1.890	1.053	-0.164	3.841

	6	7	8	9	10
6	-2.480				
7	-0.639	-6.479			
8	-3.104	-2.271	-6.819		
9	-0.814	-1.522	-8.488	-5.605	
10	-0.984	-0.272	-4.375	-8.415	-3.974
11	-0.968	-0.984	-4.336	-2.534	-4.149
12	-1.338	-0.582	-8.394	-4.750	-2.244
13	-0.234	-1.436	-1.131	-1.682	-4.697
14	-2.272	-3.033	-5.910	-3.884	-1.629
15	-5.880	-3.814	-3.067	-2.846	-1.844
16	-4.853	-1.542	-1.603	-0.888	-3.030
17	-1.921	-3.321	-1.987	-3.458	-2.643
18	-2.208	-1.974	-1.058	-0.477	-2.503
19	-0.760	-1.846	-0.392	0.638	-0.159

20	-0.072	-1.900	-2.356	0.774	0.156
21	-1.032	0.746	-1.514	0.643	-0.273
22	0.344	1.154	1.603	1.500	0.473
23	-1.238	-0.336	0.208	0.485	0.002
24	-2.233	1.103	-1.666	2.915	1.106

	11	12	13	14	15
11	-1.611				
12	-2.879	-1.937			
13	-3.487	-0.595	-6.150		
14	-1.305	-5.329	-2.525	-3.880	
15	-1.239	-2.663	-0.907	-4.648	-3.444
16	-3.606	-0.180	-1.551	-1.622	-3.152
17	0.013	-1.216	-1.030	-4.145	-2.937
18	-3.853	-0.723	-1.797	-2.611	-3.910
19	0.531	1.049	-1.640	-0.327	-0.887
20	6.996	6.731	-1.752	1.347	5.651
21	-0.806	-0.564	-1.106	-1.267	-0.576
22	-0.145	0.843	0.252	-0.741	-3.495
23	2.525	-0.227	-0.016	-0.503	-2.275
24	-3.062	0.002	0.426	-1.943	-1.884

	16	17	18	19	20
16	-2.339				
17	-3.168	-1.942			
18	-5.491	-2.388	-2.640		
19	1.528	0.570	-1.805	-0.428	
20	10.473	-4.050	2.897	-4.095	-30.619
21	1.113	-0.574	-1.973	-1.042	1.558
22	-0.670	-0.328	-1.300	4.080	4.445
23	0.562	-0.109	-1.672	-4.041	-12.043
24	-1.514	0.264	-1.950	5.017	-7.288

	21	22	23	24
21	-0.676			
22	-1.906	-0.010		
23	3.120	1.498	-1.955	
24	0.885	-1.875	-5.471	-1.719

Geometry of HEP radical, lowest excited energy conformation

b3lyp/aug-cc-pVDZ opt=(calcall,noraman) scf=(qc,fulllinear) nosymm
Gaussian 09: EM64L-G09RevB.01 12-Aug-2010

19-Jul-2016

Center Number	Atomic Number	Atomic Type	Coordinates (Angstroms) X	Y	Z
1	6	0	-2.850408	1.301556	0.056602
2	1	0	-2.502920	1.778681	0.988648
3	1	0	-3.948210	1.285371	0.075554
4	6	0	-2.351299	-0.128752	-0.005440
5	1	0	-2.571418	-0.605416	-0.967864
6	1	0	-2.737788	-0.734926	0.825602
7	8	0	-0.893954	-0.074926	0.132617
8	8	0	-0.329781	-1.236812	-0.120060
9	8	0	-2.481584	2.065346	-1.084651
10	1	0	-1.520228	2.154245	-1.101720

Distance matrix (angstroms):

		1	2	3	4	5
1	C	0.000000				
2	H	1.103225	0.000000			
3	H	1.098085	1.779314	0.000000		
4	C	1.516160	2.156270	2.134579	0.000000	
5	H	2.182638	3.084891	2.561123	1.096322	0.000000
6	H	2.179748	2.529816	2.471698	1.098841	1.805816
7	O	2.393364	2.599504	3.343971	1.464859	2.075178
8	O	3.581631	3.878784	4.415054	2.308131	2.478380
9	O	1.421923	2.093132	2.026186	2.448619	2.674823
10	H	1.959124	2.340165	2.834786	2.665443	2.956120

		6	7	8	9	10
6	H	0.000000				
7	O	2.077391	0.000000			
8	O	2.635273	1.316099	0.000000		
9	O	3.399446	2.929688	4.057701	0.000000	
10	H	3.680262	2.623930	3.725599	0.965608	0.000000

Rotational constants (GHZ): 13.9191405 2.7671052 2.5086211
Rotational temperatures (Kelvin) 0.66801 0.13280 0.12039

	1	2	3
	A	A	A
Frequencies --	55.0481	141.6000	264.7537
Red. masses --	9.0547	4.1763	1.8529
Frc consts --	0.0162	0.0493	0.0765

	4	5	6
	A	A	A
Frequencies --	346.2859	404.0647	543.7453
Red. masses --	1.2624	3.6647	3.3533
Frc consts --	0.0892	0.3525	0.5841

	7	8	9
	A	A	A
Frequencies --	807.6011	881.1619	994.4075
Red. masses --	2.1123	2.2114	2.8137
Frc consts --	0.8117	1.0116	1.6393

	10	11	12
	A	A	A
Frequencies --	1083.6034	1091.9567	1188.4459
Red. masses --	1.9984	2.7883	2.8578
Frc consts --	1.3825	1.9588	2.3781

	13	14	15
	A	A	A
Frequencies --	1213.1357	1232.1482	1348.3011
Red. masses --	1.6626	1.2696	1.3224
Frc consts --	1.4416	1.1357	1.4164

	16	17	18
	A	A	A
Frequencies --	1371.0995	1406.4287	1453.2708
Red. masses --	1.2122	1.3326	1.0946
Frc consts --	1.3426	1.5530	1.3621

	19	20	21
	A	A	A
Frequencies --	1467.2111	3020.0926	3063.3918
Red. masses --	1.0839	1.0679	1.0585

Frc consts -- 1.3748 5.7387 5.8523

	22	23	24
	A	A	A
Frequencies --	3102.5030	3138.6847	3808.4491
Red. masses --	1.0961	1.1089	1.0666
Frc consts --	6.2161	6.4362	9.1149

missing here: x matrix output

Geometry of HEP-water complex (lowest energy conformation - conf. #1)

b3lyp/aug-cc-pVDZ opt=(calcall,noraman) scf=(qc,fulllinear) nosymm
Gaussian 09: EM64L-G09RevB.01 12-Aug-2010
18-Jul-2016

Center Number	Atomic Number	Atomic Type	Coordinates (Angstroms) X	Y	Z
1	6	0	0.019924	-0.014844	0.695285
2	1	0	-0.322364	0.874234	0.141115
3	1	0	-0.853805	-0.456922	1.197221
4	6	0	0.991385	0.425890	1.784497
5	1	0	1.413273	-0.431626	2.321840
6	1	0	0.528510	1.142673	2.475575
7	8	0	2.173162	1.074228	1.208730
8	8	0	1.877583	2.231584	0.652748
9	8	0	0.558330	-0.996872	-0.163582
10	1	0	1.150797	-0.558653	-0.801725
11	8	0	2.264876	0.615869	-1.834823
12	1	0	2.466396	1.392622	-1.291608
13	1	0	2.081178	0.952941	-2.719172

Distance matrix (angstroms):

		1	2	3	4	5
1	C	0.000000				
2	H	1.102146	0.000000			
3	H	1.100352	1.780384	0.000000		

4	C	1.524587	2.151198	2.128139	0.000000
5	H	2.181928	3.077867	2.530820	1.096385	0.000000
6	H	2.183561	2.499150	2.470564	1.098007	1.812418
7	O	2.467010	2.721663	3.392209	1.465758	2.020901
8	O	2.915329	2.635135	3.871046	2.307972	3.177128
9	O	1.411351	2.090335	2.034074	2.450877	2.688448
10	H	1.953367	2.261043	2.832766	2.771873	3.137146
11	O	3.440793	3.265715	4.479994	3.841529	4.370391
12	H	3.451656	3.177830	4.542997	3.545793	4.182578
13	H	4.104131	3.736904	5.093130	4.663525	5.270192

		6	7	8	9	10
6	H	0.000000				
7	O	2.077128	0.000000			
8	O	2.515636	1.317557	0.000000		
9	O	3.397601	2.963170	3.581864	0.000000	
10	H	3.744656	2.784504	3.229417	0.974823	0.000000
11	O	4.676753	3.079240	2.991411	2.882062	1.920408
12	H	4.243765	2.537529	2.197971	3.259270	2.403801
13	H	5.425143	3.930851	3.611956	3.556948	2.612877

		11	12	13
11	O	0.000000		
12	H	0.969040	0.000000	
13	H	0.964072	1.542612	0.000000

Rotational constants (GHZ): 3.2208005 2.9263491 1.7315404
Rotational constants (GHZ): 3.22080 2.92635 1.73154

	1	2	3
	A	A	A
Frequencies --	66.8632	100.5385	106.3835
Red. masses --	4.0279	7.7110	4.4161
Frc consts --	0.0106	0.0459	0.0294

	4	5	6
	A	A	A
Frequencies --	154.3897	162.4635	194.0686
Red. masses --	5.5633	1.2319	3.4642
Frc consts --	0.0781	0.0192	0.0769

	7	8	9

	A	A	A
Frequencies --	269.5284	284.9710	413.2710
Red. masses --	1.3321	2.1926	1.0976
Frc consts --	0.0570	0.1049	0.1105

	10	11	12
	A	A	A
Frequencies --	449.7044	561.0418	668.0746
Red. masses --	2.1679	3.3042	1.0580
Frc consts --	0.2583	0.6128	0.2782

	13	14	15
	A	A	A
Frequencies --	801.3369	872.9150	966.1067
Red. masses --	3.3218	2.2457	2.2646
Frc consts --	1.2568	1.0082	1.2454

	16	17	18
	A	A	A
Frequencies --	1084.0211	1113.0981	1163.7123
Red. masses --	2.8618	2.9344	3.6277
Frc consts --	1.9814	2.1421	2.8945

	19	20	21
	A	A	A
Frequencies --	1245.6440	1260.8008	1350.3474
Red. masses --	1.2548	1.2115	1.3210
Frc consts --	1.1471	1.1347	1.4192

	22	23	24
	A	A	A
Frequencies --	1378.7321	1437.7938	1449.9834
Red. masses --	1.2987	1.1186	1.1420
Frc consts --	1.4545	1.3625	1.4147

	25	26	27
	A	A	A
Frequencies --	1464.8101	1621.1083	3023.3722
Red. masses --	1.0889	1.0818	1.0608
Frc consts --	1.3766	1.6750	5.7129

	28	29	30
	A	A	A
Frequencies --	3068.0876	3080.4631	3148.4134
Red. masses --	1.0650	1.0950	1.1095
Frc consts --	5.9068	6.1219	6.4796

	31	32	33
	A	A	A
Frequencies --	3626.6180	3743.4533	3881.1274
Red. masses --	1.0676	1.0499	1.0784
Frc consts --	8.2728	8.6682	9.5708

X matrix of Anharmonic Constants (cm-1)
Note: Numbering of modes is the reverse of the numbering of normal modes above

	1	2	3	4	5
1	-64.282				
2	-105.244	-66.798			
3	-6.547	-12.158	-120.083		
4	0.065	0.402	-0.145	-39.671	
5	-0.127	-0.197	-4.703	-18.280	-33.801
6	-0.079	-0.045	-1.481	-95.717	-48.270
7	-0.191	0.520	-6.029	-2.275	-76.126
8	-18.133	-16.370	-1.025	-0.067	0.079
9	-0.047	0.010	-1.046	-0.745	-15.416
10	0.231	0.978	5.323	-6.140	-1.594
11	0.178	0.757	2.385	-15.901	-1.921
12	-0.027	0.067	-1.767	-1.084	-2.828
13	0.009	0.041	-0.958	-8.932	-2.017
14	-0.428	-1.406	-2.129	-6.291	-2.483
15	0.225	0.888	1.516	-1.240	-2.865
16	0.030	0.448	-0.330	-3.204	-0.329
17	0.008	0.125	0.419	-2.551	1.399
18	0.069	-0.377	2.242	-1.122	0.961
19	-0.324	-0.977	-1.041	0.331	-4.029
20	-0.241	-0.685	-0.884	-2.136	0.081
21	0.007	0.101	-0.530	0.898	-1.934
22	5.496	4.777	70.303	-0.095	-0.512
23	0.550	1.642	2.433	0.081	-0.423

24	-0.064	0.163	0.579	-1.287	-0.040
25	8.186	21.733	28.623	-1.131	0.443
26	-0.474	8.323	0.180	-0.349	-0.472
27	-2.102	15.184	-3.019	-0.479	0.028
28	0.831	2.229	10.271	-0.080	0.819
29	8.329	11.524	36.085	-0.398	0.328
30	0.029	1.491	8.117	-0.267	0.503
31	2.430	4.560	11.492	-0.734	0.275
32	2.112	4.223	-0.642	-0.338	-0.083
33	-0.191	0.582	2.965	-0.139	-0.668

	6	7	8	9	10
6	-25.319				
7	-20.182	-44.388			
8	0.084	0.084	-16.021		
9	-3.893	3.853	-0.231	-0.885	
10	-1.490	-0.080	-0.201	-2.751	-6.390
11	-4.305	-0.049	-0.313	-1.420	-15.538
12	-1.264	12.626	-0.046	-2.022	-2.159
13	3.182	-0.614	-0.011	-1.108	-1.300
14	-8.044	0.035	-0.002	-0.553	-2.195
15	-1.149	-6.624	-0.106	-1.443	-3.231
16	-1.484	-1.464	-0.121	-0.851	-0.877
17	-2.055	-0.537	0.019	-3.064	-3.997
18	-0.299	0.881	0.059	-3.828	-4.743
19	-0.843	-1.635	0.008	-5.513	-1.028
20	-3.089	0.052	0.136	-1.383	-1.585
21	0.175	-1.019	-0.053	-2.242	-5.067
22	0.561	3.924	0.364	-0.781	1.005
23	0.101	-1.931	0.049	-1.815	0.489
24	-0.870	1.096	0.358	-0.756	-0.433
25	-0.397	1.246	2.978	-0.416	-3.217
26	-0.268	-0.156	0.305	-0.503	-1.044
27	-0.133	-0.939	1.808	-0.407	-0.218
28	0.315	0.589	-0.734	-0.830	-0.157
29	-0.036	2.405	-2.621	0.167	-3.324
30	0.149	0.673	0.065	-0.833	-0.988
31	-0.300	1.773	-0.048	-0.142	-1.810
32	0.028	-1.214	-0.983	-0.036	-0.935
33	-0.244	0.755	-0.007	0.050	0.159

	11	12	13	14	15

11	-4.294				
12	-1.446	-9.204			
13	-0.591	-5.113	-4.632		
14	-1.270	-1.786	-6.071	-2.920	
15	-2.820	-8.430	-2.210	-0.927	-1.649
16	-0.412	-1.610	-4.805	-2.485	-3.414
17	-3.914	-2.805	0.000	-1.701	-2.948
18	-2.842	-5.343	-3.379	-1.962	-3.782
19	-1.316	-1.420	-3.946	-5.357	-0.826
20	-2.144	-2.872	-0.654	0.850	-1.054
21	-3.667	-0.423	-5.640	-5.035	-2.332
22	3.819	1.807	0.958	1.856	0.607
23	0.127	-0.435	-4.066	0.550	3.057
24	-0.509	-0.176	1.134	-1.326	-1.050
25	-1.815	-0.473	0.146	1.430	-1.622
26	-0.520	0.175	0.366	0.423	-0.574
27	0.557	-0.941	-0.347	0.298	0.065
28	-0.644	-0.080	-0.440	1.753	-2.260
29	-1.526	-0.153	0.054	1.885	-1.410
30	-0.476	-0.148	-0.163	-0.478	0.013
31	-0.817	0.652	-0.256	-0.500	0.359
32	-0.722	-0.025	0.349	1.152	-1.299
33	-0.485	-0.208	0.513	0.376	0.680

	16	17	18	19	20
16	-5.459				
17	-1.958	-2.906			
18	-1.438	-6.220	-3.357		
19	-0.881	-1.088	-3.002	-3.095	
20	-0.217	-3.293	-4.483	-3.142	-1.208
21	-1.242	-1.845	-2.470	-7.650	-0.855
22	0.139	-2.134	-0.370	1.696	1.089
23	-1.070	-0.593	-2.074	-1.445	0.036
24	-0.846	-2.858	-1.330	-1.957	-1.861
25	-1.054	-0.781	-0.081	0.970	0.516
26	0.181	-0.579	-1.939	-0.106	-1.092
27	-1.567	0.089	1.097	-0.564	-0.295
28	0.265	-0.420	0.459	-0.011	-0.864
29	-0.331	-0.536	-1.398	1.063	-0.099
30	0.411	0.125	-1.347	0.328	-0.088
31	0.301	-0.648	0.212	-0.185	0.051

32	-0.716	-0.147	0.241	0.067	1.409
33	0.142	-0.722	-0.324	-0.281	-0.178
	21	22	23	24	25
21	-3.342				
22	4.508	-56.555			
23	0.674	-9.302	-0.669		
24	-1.467	-2.684	2.665	-1.029	
25	-0.879	-39.059	-3.176	-12.345	-46.280
26	-0.552	-2.386	0.956	0.012	-3.232
27	-1.070	10.837	0.374	-1.071	-7.338
28	-0.096	-11.169	-1.334	-1.251	-4.271
29	-0.241	-52.478	-2.523	-2.912	-44.613
30	-1.285	-9.982	-2.304	2.595	-6.096
31	-0.200	-15.191	0.221	-1.883	-19.014
32	-0.073	3.491	-2.260	0.744	-8.161
33	-0.503	-4.165	0.478	-1.252	-3.306
	26	27	28	29	30
26	-2.241				
27	-16.202	-6.907			
28	-1.742	-2.160	-1.895		
29	-0.408	9.187	-4.153	-18.223	
30	-4.498	-0.567	-4.216	-2.148	-0.775
31	1.699	3.117	-0.406	-12.561	-2.998
32	-3.380	-6.317	0.547	-2.495	-5.178
33	-1.973	-2.357	-0.301	4.414	0.203
	31	32	33		
31	-0.728				
32	-1.382	-3.240			
33	2.576	-1.283	-0.142		

Equilibrium Geometry of HEP-water complex, 1st excited conformation (conf. #2, #256)

b3lyp/aug-cc-pVDZ freq=anharmonic geom=check guess=read nosymm
Gaussian 09: EM64L-G09RevB.01 12-Aug-2010
26-Sep-2016

Center	Atomic	Coordinates (Angstroms)		
Number	Number	X	Y	Z

1	6	-2.655070	1.139493	-0.172259
2	1	-2.099949	1.887521	0.419319
3	1	-3.726625	1.378842	-0.093786
4	6	-2.456402	-0.240541	0.451495
5	1	-2.883909	-1.038735	-0.164321
6	1	-2.844182	-0.266938	1.479308
7	8	-1.026276	-0.514661	0.584427
8	8	-0.574259	-1.309169	-0.365976
9	8	-2.314725	1.189021	-1.538267
10	1	-1.342926	1.194311	-1.635174
11	8	0.539187	1.002896	-1.695773
12	1	0.626186	0.113701	-1.315893
13	1	0.965211	0.959939	-2.559950

Interatomic distances:

	1	2	3	4	5
1 C	0.000000				
2 H	1.103481	0.000000			
3 H	1.100762	1.779917	0.000000		
4 C	1.527427	2.157949	2.129131	0.000000	
5 H	2.190230	3.085159	2.561215	1.095037	0.000000
6 H	2.177495	2.513793	2.441705	1.098849	1.816250
7 O	2.441673	2.636383	3.367078	1.462215	2.070284
8 O	3.219200	3.628119	4.151735	2.313587	2.334156
9 O	1.408640	2.089539	2.028797	2.454154	2.678543
10 H	1.965921	2.296642	2.844635	2.766372	3.086184
11 O	3.541614	3.495885	4.572182	3.889788	4.269800
12 H	3.623091	3.686355	4.694794	3.570924	3.869754
13 H	4.340477	4.373975	5.317026	4.713533	4.954741

	6	7	8	9	10
6 H	0.000000				
7 O	2.041314	0.000000			
8 O	3.105458	1.318646	0.000000		
9 O	3.392035	3.011389	3.262582	0.000000	
10 H	3.753534	2.819128	2.910176	0.976633	0.000000
11 O	4.810489	3.154832	2.890288	2.864309	1.892792
12 H	4.472302	2.595513	2.089969	3.139223	2.268713
13 H	5.686150	4.003445	3.511743	3.443007	2.497526

	11	12	13

11	O	0.000000		
12	H	0.970848	0.000000	
13	H	0.964440	1.542315	0.000000

	1	2	3
	A	A	A
Frequencies --	67.8709	92.2393	117.7660
Red. masses --	3.9320	8.3220	4.7966
Frc consts --	0.0107	0.0417	0.0392

	4	5	6
	A	A	A
Frequencies --	144.0318	189.7728	226.5956
Red. masses --	5.7080	3.0532	1.1974
Frc consts --	0.0698	0.0648	0.0362

	7	8	9
	A	A	A
Frequencies --	308.6176	331.2140	417.5601
Red. masses --	3.0194	1.1844	1.0638
Frc consts --	0.1694	0.0766	0.1093

	10	11	12
	A	A	A
Frequencies --	479.4506	504.6736	705.9296
Red. masses --	3.9056	2.1676	1.0524
Frc consts --	0.5290	0.3253	0.3090

	13	14	15
	A	A	A
Frequencies --	806.0844	887.9048	960.0680
Red. masses --	3.1710	2.2127	2.4606
Frc consts --	1.2140	1.0278	1.3362

	16	17	18
	A	A	A
Frequencies --	1085.4094	1111.8399	1171.6869
Red. masses --	2.7673	3.0218	3.4068
Frc consts --	1.9208	2.2009	2.7556

	19	20	21
	A	A	A
Frequencies --	1243.5488	1276.8607	1340.1608
Red. masses --	1.1638	1.4020	1.2809
Frc consts --	1.0604	1.3467	1.3555

	22	23	24
	A	A	A
Frequencies --	1382.0091	1433.5062	1454.9353
Red. masses --	1.2864	1.0966	1.1528
Frc consts --	1.4476	1.3277	1.4378

	25	26	27
	A	A	A
Frequencies --	1462.8214	1623.4459	3010.5287
Red. masses --	1.0852	1.0791	1.0631
Frc consts --	1.3681	1.6757	5.6766

	28	29	30
	A	A	A
Frequencies --	3064.2388	3074.7302	3154.3563
Red. masses --	1.0699	1.0883	1.1087
Frc consts --	5.9186	6.0619	6.4994

	31	32	33
	A	A	A
Frequencies --	3584.0811	3714.9350	3871.7190
Red. masses --	1.0684	1.0523	1.0760
Frc consts --	8.0860	8.5564	9.5034

Rotational temperatures (Kelvin) 0.16105 0.13480 0.08246
Rotational constants (GHZ): 3.35566 2.80874 1.71828

X matrix of Anharmonic Constants (cm-1)
note: numbering of modes is reversed from numbering of normal modes above

	1	2	3	4	5
1	-70.060				
2	-78.201	-76.122			
3	-6.300	-22.298	-119.417		

4	0.048	0.470	0.061	-42.947	
5	-0.021	0.005	-4.488	-27.716	-30.508
6	0.073	0.535	-2.030	-74.116	-75.948
7	-0.030	0.290	-5.323	-2.158	-50.371
8	-17.958	-15.804	-1.613	-0.109	-0.114
9	0.039	-0.068	-0.645	-0.605	-12.902
10	0.859	1.150	13.408	-0.901	-1.665
11	0.002	0.048	0.543	-22.369	-3.090
12	-0.127	-0.541	-2.095	-0.986	-2.194
13	-0.072	-0.503	-1.421	-8.382	-1.845
14	0.065	0.440	-0.046	-6.542	-3.342
15	0.164	0.037	2.389	-2.830	-2.543
16	-0.134	-0.492	-0.354	-2.168	-0.715
17	0.029	0.170	0.114	-2.507	0.803
18	-0.010	-0.781	2.349	-2.000	0.633
19	-0.140	-1.286	-0.462	0.388	-3.626
20	0.060	0.339	-0.418	-1.001	-0.570
21	0.131	0.560	0.173	1.200	-1.826
22	2.859	10.127	60.526	-0.326	-0.960
23	0.295	2.043	0.082	-0.507	-0.157
24	-0.039	-0.599	1.596	0.082	-0.296
25	4.436	22.049	20.216	-0.859	-0.851
26	-1.159	18.323	18.559	-0.331	0.461
27	0.075	1.147	0.979	-0.028	-0.292
28	-2.633	21.568	19.655	-0.427	-0.184
29	-0.610	1.498	13.470	0.052	0.693
30	4.435	5.455	5.979	-0.430	-0.025
31	0.908	3.012	6.181	0.079	0.313
32	-0.174	6.784	2.930	-0.628	-0.012
33	-0.704	2.000	2.957	0.334	-1.076

	6	7	8	9	10	
6	-23.506					
7	-25.238	-50.674				
8	0.014	-0.065	-17.481			
9	-5.749	4.465	-0.044	-1.358		
10	-0.650	0.653	-0.472	-3.642	-14.248	
11	-5.941	-0.272	-0.147	-0.579	-4.289	
12	-1.702	15.819	0.040	-1.148	-3.602	
13	2.196	-0.684	-0.015	-0.982	-0.875	
14	-6.410	-0.512	0.037	-0.250	-3.226	

15	-1.414	-5.754	-0.278	-1.741	-9.033
16	-2.137	-0.403	-0.014	-0.880	-1.298
17	-1.228	-0.818	-0.033	-2.774	-3.317
18	-0.180	1.146	0.036	-4.230	-8.200
19	-1.519	-0.261	0.003	-4.723	-2.146
20	-2.031	-1.775	0.200	-2.255	-1.374
21	-0.876	-0.554	-0.134	-2.296	-1.237
22	-0.287	2.069	3.394	-0.020	15.038
23	-0.924	-0.021	0.231	-1.847	0.488
24	0.350	0.542	-0.326	-0.488	0.183
25	-0.712	0.608	1.416	-0.081	-7.069
26	-0.079	0.257	-3.250	-0.022	-5.994
27	-0.166	0.005	0.202	0.370	-1.051
28	-0.535	-0.262	-8.549	-0.694	-9.417
29	0.262	0.775	0.090	-0.002	-4.866
30	-0.490	0.493	-1.066	-0.130	-1.688
31	0.075	0.499	-0.068	0.211	-2.062
32	-0.584	-0.495	-0.332	-0.704	-2.007
33	-0.528	0.676	-0.576	-0.160	-3.142

	11	12	13	14	15
11	-5.640				
12	-1.260	-10.047			
13	-0.614	-3.973	-4.503		
14	-1.472	-2.166	-7.063	-2.389	
15	-1.678	-9.742	-2.175	-1.964	-2.519
16	-1.084	-1.540	-3.092	-5.601	-1.641
17	-3.713	-2.946	-0.965	-2.147	-3.229
18	-2.336	-6.786	-2.213	-1.170	-3.283
19	-1.776	-1.770	-4.291	-4.206	-1.890
20	-0.514	-3.729	-1.672	-2.199	-0.775
21	-2.854	-0.800	-2.038	-5.358	-1.337
22	4.646	-0.208	0.876	0.085	-1.613
23	1.224	-1.772	0.182	-1.807	0.579
24	-0.346	-0.177	0.078	0.036	-0.997
25	-0.498	0.302	0.864	0.454	-1.093
26	-0.460	0.328	0.405	-0.469	-1.128
27	0.551	-1.634	0.704	-1.115	-0.261
28	-0.946	-0.101	0.077	0.028	-0.890
29	-0.269	-0.033	0.151	0.646	-3.692
30	0.011	0.142	0.293	-0.935	0.945

31	-0.366	-0.207	0.502	0.214	-0.390
32	-0.537	-0.035	-0.232	-0.738	-0.852
33	0.795	-1.947	-0.458	-1.063	-0.768

	16	17	18	19	20
16	-3.820				
17	-6.478	-2.501			
18	-2.935	-4.983	-3.397		
19	-1.550	-1.040	-4.248	-3.283	
20	-1.446	-2.916	-3.564	-3.019	-1.624
21	-1.563	-2.158	-2.610	-5.924	-2.058
22	0.371	-0.772	0.094	2.264	0.104
23	-0.776	-0.873	0.036	-0.090	-0.537
24	-1.947	-1.089	-2.760	-2.405	0.921
25	-0.282	-0.572	1.159	1.825	0.728
26	0.042	-0.419	-0.026	0.778	0.013
27	-0.013	-0.287	1.056	-1.048	-0.750
28	0.201	-0.504	-0.373	0.689	0.353
29	0.039	-0.395	-0.984	0.060	-0.051
30	0.247	-0.334	-0.893	0.623	-0.867
31	0.118	-0.597	-0.917	0.574	0.236
32	-0.370	-0.560	0.309	0.732	-0.556
33	-0.578	-0.201	-0.123	0.328	0.160

	21	22	23	24	25
21	-3.087				
22	-0.691	-35.820			
23	-3.210	-1.159	-1.825		
24	-1.279	-3.684	3.079	-2.623	
25	-1.200	-35.528	-0.996	-5.831	-19.812
26	-0.755	-19.388	-1.470	-1.185	-31.147
27	-0.179	-1.809	-0.032	2.302	-1.180
28	-1.178	-14.386	-1.405	-1.967	-61.775
29	-0.198	-14.990	-0.537	-0.467	-5.397
30	-0.286	-4.318	-2.829	2.120	-11.546
31	-0.347	-4.281	-0.659	0.328	-3.397
32	-0.045	-6.824	-3.765	0.867	-9.133
33	-0.154	-5.919	-1.651	0.702	-1.918

	26	27	28	29	30
26	-7.822				
27	-1.029	-0.378			
28	-62.131	-1.426	-44.350		

29	-9.076	0.149	-22.871	-4.683	
30	-8.622	-1.915	-22.520	-3.345	-3.478
31	-4.009	-0.104	-5.447	-4.184	-4.317
32	-7.604	-0.955	-19.287	-4.455	-7.503
33	-4.730	0.084	-24.361	-6.050	-3.497

	31	32	33
31	0.333		
32	-4.252	-0.801	
33	-1.005	-5.480	-1.782

Equilbrium Geometry of HEP-water complex, 2nd excited conformation (conf. #3, #248)

b3lyp/aug-cc-pVDZ freq=anharmonic geom=check guess=read nosymm
Gaussian 09: EM64L-G09RevB.01 12-Aug-2010
27-Sep-2016

Center Number	Atomic Number	Coordinates (Angstroms) X	Y	Z
1	6	-0.055251	0.905000	0.783159
2	1	0.712982	1.657664	1.024373
3	1	-0.858503	0.977774	1.527671
4	6	0.544884	-0.488813	0.867777
5	1	-0.120514	-1.243870	0.431139
6	1	0.801386	-0.752405	1.901194
7	8	1.835517	-0.568729	0.175669
8	8	1.741937	-0.224727	-1.094005
9	8	-0.652023	1.180894	-0.484449
10	1	0.004434	0.946588	-1.159793
11	8	-2.650343	-0.799692	-0.165559
12	1	-2.147389	-0.027863	-0.483928
13	1	-3.509772	-0.750832	-0.597620

Interatomic distances:

		1	2	3	4	5
1	C	0.000000				
2	H	1.102211	0.000000			

3	H	1.097638	1.784691	0.000000		
4	C	1.519880	2.158736	2.134440	0.000000	
5	H	2.178490	3.076612	2.585094	1.097049	0.000000
6	H	2.175045	2.566138	2.426576	1.096916	1.803468
7	O	2.473040	2.633859	3.387821	1.466674	2.084979
8	O	2.833710	3.014908	3.883488	2.313280	2.614085
9	O	1.427966	2.089759	2.032860	2.459476	2.645805
10	H	1.944314	2.403799	2.822782	2.542342	2.710127
11	O	3.246620	4.332030	3.039260	3.372522	2.636926
12	H	2.617783	3.646601	2.592116	3.047608	2.534610
13	H	4.072106	5.124779	3.812370	4.319291	3.576102

	6	7	8	9	10
6 H	0.000000				
7 O	2.020050	0.000000			
8 O	3.183441	1.318774	0.000000		
9 O	3.397254	3.112040	2.842248	0.000000	
10 H	3.590453	2.726263	2.096479	0.970528	0.000000
11 O	4.023448	4.504744	4.526005	2.831553	3.329540
12 H	3.861223	4.073223	3.941803	1.922814	2.456969
13 H	4.982987	5.404004	5.301286	3.451246	3.942958

	11	12	13
11 O	0.000000		
12 H	0.974700	0.000000	
13 H	0.963163	1.546511	0.000000

	1	2	3
	A	A	A
Frequencies --	38.9389	70.2566	96.0895
Red. masses --	7.1377	6.0674	3.7392
Frc consts --	0.0064	0.0176	0.0203

	4	5	6
	A	A	A
Frequencies --	143.5970	161.4133	207.8826
Red. masses --	1.1328	4.5826	5.0481
Frc consts --	0.0138	0.0703	0.1285

	7	8	9
	A	A	A
Frequencies --	329.2734	387.5026	404.2488

Red. masses --	2.2076	1.2948	2.7192
Frc consts --	0.1410	0.1146	0.2618

	10	11	12
	A	A	A
Frequencies --	498.1959	560.6791	656.7100
Red. masses --	1.1122	2.1876	1.0776
Frc consts --	0.1626	0.4052	0.2738

	13	14	15
	A	A	A
Frequencies --	796.8494	918.3073	963.9114
Red. masses --	3.3847	2.7057	1.9870
Frc consts --	1.2663	1.3443	1.0877

	16	17	18
	A	A	A
Frequencies --	1079.0460	1092.1985	1170.1142
Red. masses --	2.6391	2.9481	5.2047
Frc consts --	1.8105	2.0721	4.1985

	19	20	21
	A	A	A
Frequencies --	1213.2847	1264.1626	1350.0658
Red. masses --	1.0968	1.2707	1.2925
Frc consts --	0.9513	1.1965	1.3880

	22	23	24
	A	A	A
Frequencies --	1369.0213	1429.7959	1453.9726
Red. masses --	1.2798	1.2486	1.1026
Frc consts --	1.4132	1.5039	1.3734

	25	26	27
	A	A	A
Frequencies --	1470.7728	1638.9810	3029.4339
Red. masses --	1.0751	1.0746	1.0668
Frc consts --	1.3702	1.7008	5.7682

	28	29	30

	A	A	A
Frequencies --	3078.1843	3108.3813	3147.7707
Red. masses --	1.0578	1.0975	1.1104
Frc consts --	5.9052	6.2475	6.4825

	31	32	33
	A	A	A
Frequencies --	3630.4935	3722.4574	3877.8664
Red. masses --	1.0576	1.0654	1.0717
Frc consts --	8.2130	8.6984	9.4952

Rotational temperatures (Kelvin) 0.22505 0.08272 0.08016
Rotational constants (GHZ): 4.68932 1.72369 1.67035

X matrix of Anharmonic Constants (cm-1)
Note: numbering of modes is reversed from that of normal modes above

	1	2	3	4	5
1	-78.241				
2	-0.881	-102.467			
3	-40.962	-13.764	-102.557		
4	-0.167	1.129	0.111	-35.902	
5	0.110	-4.684	2.524	-2.360	-54.019
6	-0.189	0.311	0.101	-126.395	-9.218
7	0.149	-2.892	3.833	-1.309	-46.253
8	-16.100	0.047	-10.978	-0.515	-0.521
9	0.022	0.357	-0.381	-0.704	-17.910
10	-0.012	0.097	0.639	-20.551	-0.370
11	0.047	-4.309	0.028	-1.683	-2.831
12	0.077	-4.483	0.477	-3.335	-0.991
13	0.050	-4.102	-0.306	-5.901	-3.166
14	0.087	-2.205	-0.074	-5.558	-1.732
15	0.049	-5.361	-0.039	-2.157	-2.977
16	0.094	-1.171	0.369	-1.833	-0.305
17	0.051	0.872	-1.344	-3.074	1.546
18	0.045	-0.296	0.041	-0.766	0.978
19	0.132	-1.935	0.523	-0.164	-5.382
20	0.282	-1.932	-0.412	-0.816	0.708
21	0.189	0.716	1.017	0.570	-2.323
22	1.452	11.034	54.816	-0.157	-2.697

23	0.276	0.994	1.486	0.066	-0.780
24	0.515	14.416	22.186	0.562	-4.086
25	-0.715	0.790	10.832	-0.488	-0.752
26	-3.617	2.468	29.938	-1.165	-1.813
27	0.297	2.311	1.298	-1.220	-1.204
28	1.244	0.955	10.998	0.193	-0.751
29	0.899	2.205	5.895	-0.089	-0.299
30	-13.955	0.635	2.949	0.226	-0.711
31	0.594	3.935	3.154	-1.530	-0.578
32	1.204	0.638	2.197	-0.990	-1.233
33	3.588	2.021	7.913	-0.386	-1.334

	6	7	8	9	10
6	-30.289				
7	-1.810	-56.182			
8	-0.845	-0.602	-21.368		
9	-1.034	2.042	0.002	-2.897	
10	-3.568	0.124	-0.022	-0.909	-6.756
11	-0.588	9.622	0.137	-3.433	-2.595
12	3.710	0.964	-0.449	-0.479	-1.382
13	0.614	2.000	-0.329	-1.135	-0.618
14	-6.878	-0.513	-0.871	-0.761	-0.968
15	-2.232	-5.547	-0.354	-1.581	-0.464
16	-1.358	-0.117	-0.187	-0.169	-1.533
17	-3.094	0.294	-0.066	-2.962	-4.166
18	-1.547	-1.584	-0.016	-4.895	-3.539
19	-0.861	-0.519	-0.208	-5.246	-1.589
20	-1.327	-0.450	-0.100	-2.663	-3.139
21	-0.108	0.534	-0.215	-2.311	-1.944
22	-0.250	-2.009	5.743	0.426	-0.795
23	-0.012	0.184	-0.499	-1.533	-1.813
24	0.053	1.030	1.314	0.338	-0.719
25	-0.684	-0.302	-4.612	-0.928	0.542
26	-1.340	-2.066	-16.041	-0.496	-0.760
27	-1.031	0.759	-0.929	-1.155	0.771
28	0.064	-0.421	-1.573	-1.111	-0.604
29	-0.230	-0.213	-1.258	-1.258	-0.629
30	-0.348	0.186	13.202	1.621	-0.124
31	-1.130	1.845	-1.073	-3.045	0.137
32	-1.544	-0.162	-1.837	-0.845	-0.782
33	-1.815	-0.699	-2.990	-1.274	-1.419

	11	12	13	14	15
11	-6.891				
12	-6.252	-4.610			
13	-5.636	-10.674	-3.177		
14	-3.366	-3.438	-3.381	-1.356	
15	-9.853	-4.103	-3.162	-2.364	-2.231
16	-0.850	-2.705	-3.864	-3.881	-0.438
17	-5.250	-2.077	-1.756	-1.017	-4.445
18	-4.390	-3.264	-2.693	-1.979	-3.327
19	-1.754	-1.274	-2.981	-2.975	0.056
20	-2.244	-3.188	-2.628	-0.635	-1.734
21	-1.534	-0.725	-2.398	-4.118	-1.076
22	2.537	1.607	2.105	1.780	1.378
23	-0.287	0.724	-0.181	0.628	-0.081
24	0.848	1.273	1.836	5.658	6.689
25	-1.913	0.528	-0.324	0.476	-0.116
26	-0.473	-0.388	-0.857	0.398	-0.362
27	0.306	1.424	0.371	-0.042	0.516
28	0.118	0.035	0.061	0.519	0.661
29	0.692	0.153	0.144	-0.221	-0.183
30	0.340	-1.015	0.275	-0.145	0.120
31	-1.536	1.376	-0.070	-1.635	-1.147
32	-0.119	0.990	-1.017	0.458	0.595
33	-1.708	-0.072	-1.018	0.888	-1.281

	16	17	18	19	20
16	-6.378				
17	-1.322	-3.232			
18	-1.049	-5.482	-3.517		
19	-2.059	-1.602	-2.937	-2.060	
20	-0.971	-4.516	-3.973	-3.083	-1.798
21	-1.993	-2.950	-3.301	-4.206	-3.004
22	-0.158	0.489	-0.018	-0.027	0.214
23	-1.851	-0.802	-0.756	0.288	1.149
24	-0.538	1.372	1.302	-3.123	-1.374
25	-0.796	-0.374	0.060	-0.256	-0.783
26	-0.536	0.824	-0.173	0.844	0.121
27	0.419	-0.804	-2.430	-1.183	-0.509
28	-0.604	-0.196	-0.760	0.895	0.020
29	0.162	-0.150	-0.962	1.114	-0.009
30	0.668	2.745	1.707	1.742	0.101

31	0.588	-1.333	-0.797	-1.932	-0.795
32	0.517	-0.200	0.116	0.232	-0.430
33	0.011	-0.037	-0.266	0.432	-0.591

	21	22	23	24	25
21	-2.678				
22	-2.084	-36.343			
23	-1.961	-1.044	0.146		
24	0.810	-56.200	-4.109	-16.332	
25	-0.741	-4.662	0.669	-8.566	-1.037
26	0.647	-13.512	-0.726	-8.285	-17.083
27	-2.013	-0.168	4.304	4.236	-2.518
28	-1.147	-19.217	-1.653	-6.015	-1.854
29	-2.901	-9.976	-1.971	-4.506	-0.093
30	1.336	-19.516	2.407	-24.919	13.273
31	-0.899	-1.430	2.530	-1.654	-1.310
32	0.473	2.293	0.368	1.486	-0.127
33	-0.123	2.082	0.460	6.050	0.563

	26	27	28	29	30
26	-15.348				
27	-3.410	-0.647			
28	-2.470	-0.181	-3.668		
29	1.813	-1.137	-9.074	-1.472	
30	25.303	2.942	3.762	-1.247	-56.624
31	0.391	2.465	-1.464	-2.387	4.624
32	-3.513	0.480	0.147	-1.303	17.724
33	5.717	1.072	-2.853	-1.263	32.185

	31	32	33
31	-0.465		
32	-2.103	-0.522	
33	6.448	5.946	3.806

Geometry of HEP-water complex, 3rd excited conformation (conf. #4, #244)

b3lyp/aug-cc-pVDZ freq=anharmonic geom=check guess=read nosymm
Gaussian 09: EM64L-G09RevB.01 12-Aug-2010
27-Sep-2016

Center	Atomic	Coordinates (Angstroms)		
Number	Number	X	Y	Z

1	6	-0.476569	-1.440996	0.386755
2	1	-0.693769	-1.093803	1.411495
3	1	-0.473049	-2.540805	0.404900
4	6	0.918651	-0.995660	-0.018039
5	1	1.119530	-1.188394	-1.078481
6	1	1.695709	-1.446164	0.614111
7	8	1.005928	0.458683	0.177037
8	8	2.163854	0.947013	-0.216206
9	8	-1.478835	-1.039329	-0.525711
10	1	-1.694939	-0.103390	-0.360560
11	8	-1.672053	1.721268	0.186116
12	1	-0.712828	1.852719	0.190015
13	1	-2.033640	2.436411	-0.350369

Interatomic distances:

		1	2	3	4	5
1	C	0.000000				
2	H	1.103545	0.000000			
3	H	1.099965	1.776447	0.000000		
4	C	1.519480	2.157104	2.122069	0.000000	
5	H	2.181343	3.081717	2.562371	1.096375	0.000000
6	H	2.184150	2.543538	2.438344	1.098356	1.806460
7	O	2.418793	2.612100	3.352047	1.469961	2.074148
8	O	3.610815	3.870446	4.416323	2.315984	2.528655
9	O	1.413671	2.090948	2.032750	2.451035	2.660690
10	H	1.957574	2.263501	2.831950	2.782862	3.100626
11	O	3.386642	3.222300	4.432916	3.759671	4.225905
12	H	3.308033	3.189728	4.405306	3.289114	3.770277
13	H	4.242889	4.166753	5.270537	4.539337	4.859202

		6	7	8	9	10
6	H	0.000000				
7	O	2.072503	0.000000			
8	O	2.576020	1.316776	0.000000		
9	O	3.397416	2.985287	4.160593	0.000000	
10	H	3.774854	2.810627	4.001809	0.974658	0.000000
11	O	4.643019	2.960708	3.933894	2.857433	1.904929
12	H	4.106524	2.213059	3.043127	3.076194	2.256997
13	H	5.469247	3.664498	4.455925	3.524106	2.562306

		11	12	13

11 O 0.000000
12 H 0.968198 0.000000
13 H 0.964361 1.541835 0.000000

Rotational temperatures (Kelvin) 0.16087 0.11601 0.07221
Rotational constants (GHZ): 3.35189 2.41732 1.50457

	1	2	3
	A	A	A
Frequencies --	54.6887	59.3235	101.3463
Red. masses --	4.2048	5.0168	4.3851
Frc consts --	0.0074	0.0104	0.0265

	4	5	6
	A	A	A
Frequencies --	133.9206	173.0382	195.6424
Red. masses --	5.3686	1.0936	3.5372
Frc consts --	0.0567	0.0193	0.0798

	7	8	9
	A	A	A
Frequencies --	269.5032	287.9063	369.0524
Red. masses --	1.9618	1.4773	1.0933
Frc consts --	0.0840	0.0721	0.0877

	10	11	12
	A	A	A
Frequencies --	396.4367	537.7032	657.5747
Red. masses --	3.8332	3.1814	1.0529
Frc consts --	0.3549	0.5419	0.2683

	13	14	15
	A	A	A
Frequencies --	801.0714	882.6699	1001.0654
Red. masses --	2.3814	2.1732	3.0449
Frc consts --	0.9004	0.9976	1.7978

	16	17	18
	A	A	A
Frequencies --	1085.2926	1105.3921	1195.1058

Red. masses --	1.9406	3.6421	6.3752
Frc consts --	1.3467	2.6220	5.3649

	19	20	21
	A	A	A
Frequencies --	1210.7907	1267.1833	1351.3434
Red. masses --	1.2248	1.1415	1.3024
Frc consts --	1.0579	1.0800	1.4013

	22	23	24
	A	A	A
Frequencies --	1390.4158	1445.8106	1458.5607
Red. masses --	1.3938	1.1008	1.1448
Frc consts --	1.5876	1.3557	1.4350

	25	26	27
	A	A	A
Frequencies --	1461.7341	1611.2323	3012.9473
Red. masses --	1.0776	1.0809	1.0651
Frc consts --	1.3565	1.6533	5.6968

	28	29	30
	A	A	A
Frequencies --	3065.1628	3080.2753	3140.6908
Red. masses --	1.0619	1.0937	1.1096
Frc consts --	5.8779	6.1138	6.4488

	31	32	33
	A	A	A
Frequencies --	3623.7004	3763.0250	3884.3321
Red. masses --	1.0678	1.0476	1.0802
Frc consts --	8.2611	8.7401	9.6022

X matrix of Anharmonic Constants (cm-1)
Note: Numbering is reversed over normal mode numbering above

	1	2	3	4	5
1	-57.924				
2	-130.983	-55.662			
3	-6.288	-9.957	-117.560		

4	0.231	0.621	0.016	-40.522	
5	-0.114	-0.335	-4.523	-12.457	-43.374
6	0.213	0.649	-0.756	-103.122	-39.713
7	-0.103	0.434	-6.671	-2.059	-49.924
8	-17.982	-18.496	-0.373	-0.067	0.134
9	0.347	0.331	6.313	-1.094	-10.161
10	0.512	0.371	5.740	-3.948	-6.761
11	0.212	0.151	3.131	-17.950	-1.612
12	0.028	0.132	-1.681	-1.331	0.267
13	-0.013	0.072	-1.038	-7.373	-3.609
14	0.239	0.660	1.152	-1.758	-3.514
15	-0.079	-0.403	0.264	-6.315	-1.013
16	-0.053	0.051	0.146	-0.299	-0.492
17	0.115	0.225	1.996	-0.866	1.822
18	-0.035	-0.512	1.923	-3.869	0.104
19	-0.142	-0.279	-0.668	1.265	-3.881
20	0.037	0.204	-0.097	-2.543	0.075
21	-0.317	-1.102	0.098	1.040	-3.386
22	4.176	4.935	53.419	-0.024	-1.590
23	-0.174	-0.644	-0.008	0.179	-0.061
24	0.215	-0.042	2.226	-0.351	0.172
25	6.483	12.743	19.050	-1.285	-0.009
26	2.293	5.348	14.231	-0.111	0.262
27	0.576	2.377	5.552	-0.076	-0.061
28	1.041	2.580	10.479	-0.184	0.797
29	9.630	16.413	17.279	-0.828	0.285
30	0.143	1.612	3.806	-0.268	1.013
31	3.055	2.741	1.036	-0.508	-0.266
32	0.841	2.760	0.285	1.993	0.759
33	0.241	0.058	2.859	1.807	-0.570

	6	7	8	9	10	
6	-28.286					
7	-9.346	-54.303				
8	-0.059	0.053	-16.913			
9	-1.549	-2.844	-0.407	-5.914		
10	-1.569	4.594	-0.173	-15.252	-5.898	
11	-3.322	0.179	-0.381	-6.099	-10.355	
12	1.146	14.800	-0.053	-0.409	-2.677	
13	3.202	0.964	-0.043	-0.646	-1.312	
14	-3.221	-5.154	-0.436	-3.216	-3.652	

15	-5.228	-2.552	0.197	-0.988	-1.435
16	-1.196	-0.780	0.084	-0.747	-0.408
17	-1.088	3.658	-0.016	-3.854	-4.303
18	-1.426	-3.927	0.175	-2.698	-4.737
19	-1.093	-0.087	-0.051	-2.384	-2.557
20	-4.494	0.698	0.017	-1.208	-1.749
21	0.767	-1.761	0.193	-2.365	-2.118
22	-0.443	3.010	2.342	-1.026	-1.990
23	0.283	-0.164	0.221	0.200	0.279
24	0.109	0.941	0.230	-0.888	-0.530
25	-1.542	1.324	3.142	-1.212	-3.305
26	-0.531	0.685	5.061	-1.388	-1.495
27	-0.031	0.525	3.278	-0.503	-0.005
28	0.220	1.098	0.780	-1.913	-1.975
29	-1.115	0.126	-1.315	-2.311	-1.789
30	0.721	0.420	0.598	-0.377	-0.485
31	-0.667	0.429	0.548	-0.348	-0.058
32	-1.451	-0.696	1.027	0.491	0.243
33	-1.351	0.821	0.655	0.133	-0.028

	11	12	13	14	15
11	-4.775				
12	-1.298	-8.824			
13	-0.565	-7.617	-3.845		
14	-1.968	-8.804	-4.551	-1.805	
15	-1.714	-2.702	-4.133	-3.173	-1.881
16	-0.202	-1.685	-1.545	-0.686	-3.755
17	-2.532	-6.173	-1.883	-4.538	-3.251
18	-4.980	-1.062	-0.766	-1.034	-2.252
19	-2.525	-2.071	-4.194	-3.288	-3.262
20	-1.295	-3.350	-1.220	-2.395	0.457
21	-3.817	1.001	-1.673	-0.648	-2.994
22	-0.402	0.886	0.519	-5.774	-0.021
23	1.618	-0.280	-0.612	0.209	-1.180
24	0.200	-0.612	0.251	-1.036	-1.000
25	-2.670	-0.147	-0.515	-1.982	0.452
26	-0.821	-0.043	0.047	-1.603	1.221
27	-0.327	1.154	-0.168	-0.221	0.837
28	-1.453	0.096	0.060	-0.204	-0.434
29	-1.156	0.230	-0.617	-2.962	-0.019
30	0.099	0.066	0.324	0.545	-1.904

31	0.038	0.546	0.053	0.237	0.727
32	-0.211	0.499	0.149	-1.044	3.072
33	0.728	0.075	-0.197	0.555	-0.527

	16	17	18	19	20
16	-7.406				
17	-0.743	-5.732			
18	0.206	-2.763	-1.856		
19	-2.068	-1.898	-2.041	-4.482	
20	-1.118	-5.421	-0.444	-3.447	-1.322
21	-0.874	-0.168	-5.011	-8.098	-0.836
22	-0.932	-2.138	0.667	-0.168	-0.853
23	-1.325	1.090	-1.438	-2.169	-1.133
24	-1.360	-1.236	-0.400	-0.522	1.616
25	-0.605	-1.501	-0.556	0.174	-0.287
26	-0.598	0.308	-1.273	-0.632	-0.678
27	0.250	-0.617	0.326	-0.673	-0.049
28	0.283	-0.934	0.526	0.109	-1.241
29	-0.527	-0.142	0.204	0.130	-0.714
30	0.012	-1.238	-0.214	0.054	0.339
31	-0.024	-0.403	0.314	0.420	-0.772
32	-1.476	-0.676	1.011	-2.276	-1.296
33	0.146	-0.488	0.065	-1.428	0.130

	21	22	23	24	25
21	-1.616				
22	1.253	-39.598			
23	-3.360	-1.226	-1.602		
24	-1.271	-4.301	0.368	0.154	
25	1.650	-52.933	1.679	-1.675	-21.817
26	3.027	-14.387	2.060	-0.414	-22.214
27	-1.014	-7.400	2.552	-0.193	-7.058
28	0.174	-12.967	0.180	-0.435	-7.682
29	1.085	-11.588	0.733	-0.693	7.978
30	0.421	-5.095	0.282	-1.652	-4.457
31	0.784	-3.932	0.687	0.501	-14.323
32	0.721	-1.820	0.354	1.991	-0.152
33	-0.321	-3.096	-0.379	2.076	0.801

	26	27	28	29	30
26	1.026				
27	4.945	1.004			
28	-1.440	-0.264	-3.238		

29	-18.738	-2.905	-3.936	-1.060	
30	-0.022	0.936	-3.958	-2.743	-1.716
31	2.688	0.047	-0.418	-3.915	-1.199
32	1.721	2.959	-1.415	8.067	0.233
33	2.130	2.228	-2.032	6.451	-0.719

	31	32	33
31	-2.151		
32	-1.279	-0.650	
33	1.126	0.524	-0.632

Appendix A3- Chapter 3 Supplemental Information

Table S1: Rotational Constants of precursors and the HO_2-H_2O-amine, MSA-

Complex	Rotational Constant A (GHz)	Rotational Constant B (GHz)	Rotational Constant C (GHz)
H_2SO_4 (1G)	4.88652	4.86326	4.59113
H_2O (1B)	818.02904	431.82215	282.62809
MSA (1)	4.67744	4.67744	4.33005
TMA (1F)	8.76950	8.76714	4.99065
DMA (1E)	34.29179	9.39972	8.27984
MA (1D)	103.99026	22.83226	21.91809
NH_3 (1C)	293.33601	296.29674	188.4596
HO_2 (1A)	624.23626	34.74679	32.91467
H_2SO_4 (1	4.88652	4.86326	4.59113
H_2SO_4-H_2O(2A)	4.81410	1.92225	1.89750
H_2SO_4-H_2O-TMA(3D)	1.91236	0.55919	0.52548
H_2SO_4-H_2O-DMA(3)	1.81640	0.82585	0.73626
H_2SO_4-H_2O-MA(3)	2.22679	1.10725	0.91336
H_2SO_4-H_2O-NH_3 (3)	3.49607	1.16645	1.07919
MSA-H_2O(2)	4.47886	1.84694	1.81042
MSA-H_2O-TMA(4)	1.93812	0.57213	0.54049
MSA-H_2O-DMA(4)	2.07644	0.73433	0.67879
MSA-H_2O-MA(4)	2.314882	1.048149	0.89933
MSA-H_2O-NH_3 (4)	2.87969	1.39010	1.17465
HO_2-H_2O(2B)	32.85142	6.16792	5.24742
HO_2-H_2O-TMA(5D)	2.38379	1.56439	1.16972
HO_2-H_2O-DMA(5C)	3.01438	1.92762	1.46143
HO_2-H_2O-MA(5B)	3.78779	2.99297	1.93291
HO_2-H_2O-NH_3(5A)	5.72025	4.08932	2.415323

Table S2: Harmonic calculations of Gibbs free energy, Entropy and Enthalpy of the H_2SO_4-H_2O-amine, MSA-H_2O-amine and HO_2-H_2O-amine complexes

Complex	ΔG° (kJ mol^{-1})	ΔH° (kJ mol^{-1})	ΔS° (kJ mol^{-1} K)
HO_2-H_2O (2B)	3.28	-35.55	-0.13
TMA-HO_2(2F)	-14.39	-59.20	-0.15
DMA-HO_2(2E)	-14.59	-59.18	-0.15
MA-HO_2(2D)	-13.06	-55.25	-0.14
NH_3-HO_2(2C)	-10.53	-49.04	-0.13
MSA-H_2O(2H)	-6.41	-48.26	-0.14
MSA-TMA	-17.92	-28.11	-0.04
H_2SO_4-H_2O(2A)	-12.26	-54.49	-0.14
H_2SO_4-TMA	-22.64	-16.82	-0.03
HO_2-H_2O-TMA (5D)	-7.62	-89.24	-0.27
HO_2-H_2O-DMA (5C)	-15.21	-97.08	-0.28
HO_2-H_2O-MA (5B)	-10.95	-93.73	-0.28
HO_2-H_2O-NH_3 (5A)	-6.06	-86.00	-0.27
MSA-H_2O-TMA(4A)	-17.48	-108.10	-0.30
MSA-H_2O-DMA(4B)	-22.02	-111.92	-0.30
MSA-H_2O-MA(4B)	-22.15	-110.31	-0.30
MSA-H_2O-NH_3 (4B)	-15.13	-102.04	-0.29
H_2SO_4-H_2O-TMA(3D)	-19.85	-107.04	-0.29
H_2SO_4-H_2O-DMA(3C)	-57.49	-142.63	-0.29
H_2SO_4-H_2O-MA(3C)	-49.59	-138.96	-0.30
H_2SO_4-H_2O NH_3 (3C)	-37.59	-120.20	-0.28

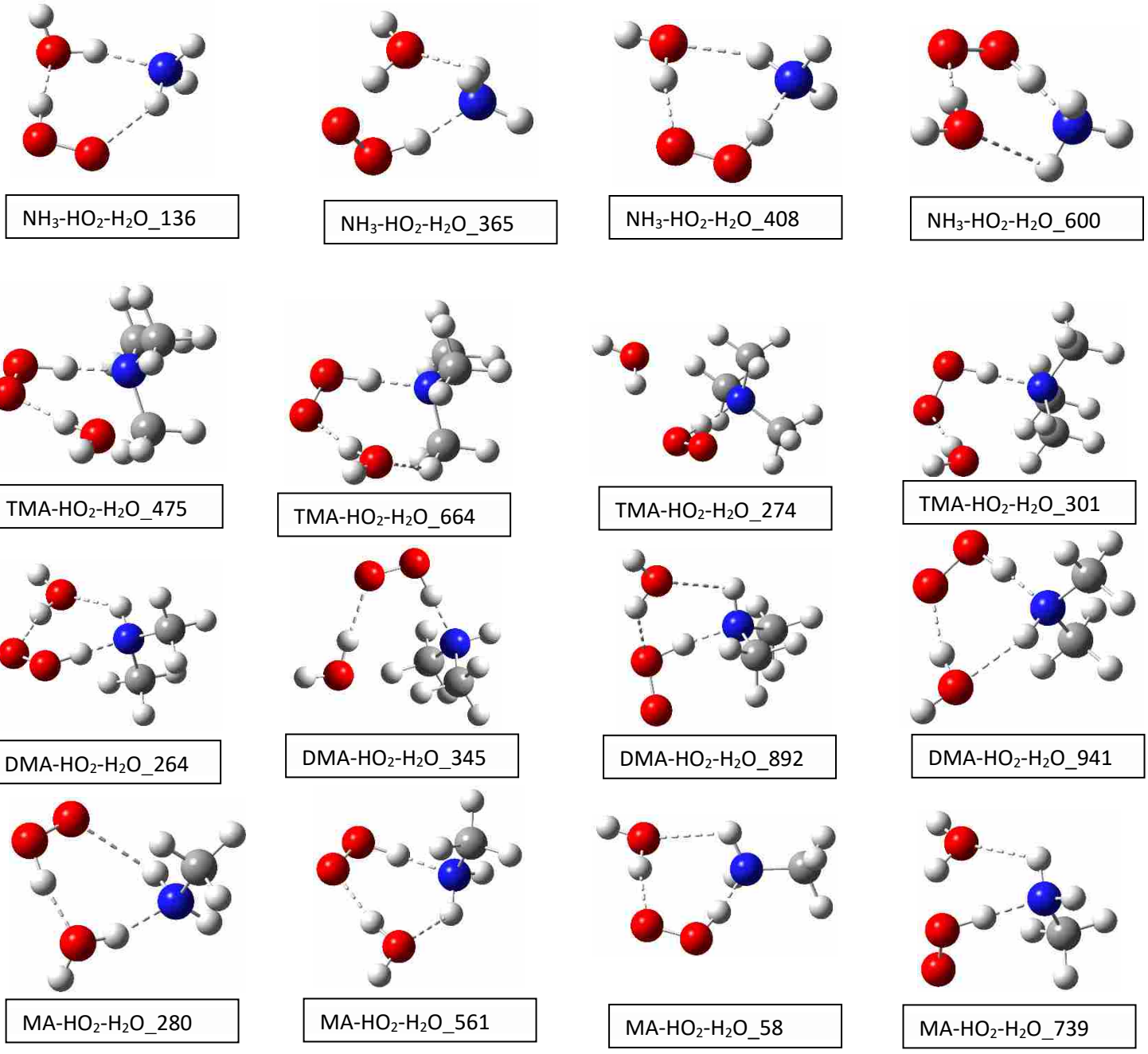

Figure S1: optimized global and local minima's of the HO_2-H_2O-amine complexes

Table S3: Comparison of binding energies calculated using different methods.

Method	Binding Energies (kJ mol^{-1})
CCSD (T)/aug-cc-PVDZ[a]	-50.75
M06-2X/6-311++G (3df,3dp)[318]	-48.70
RI-MP2/aug-cc-pV(T+d)Z[319]	-50.38
B3LYP/cc-pV(T+d)Z[320]	-47.86
PW91/cc-pV(T+d)Z[3]	-46.39
MP2/cc-pV(T+d)Z[3]	-47.990
CCSD(T)/cc-pV(∞+d)Z[3]	-50.52

Appendix A4- Chapter 4 Supplemental Information

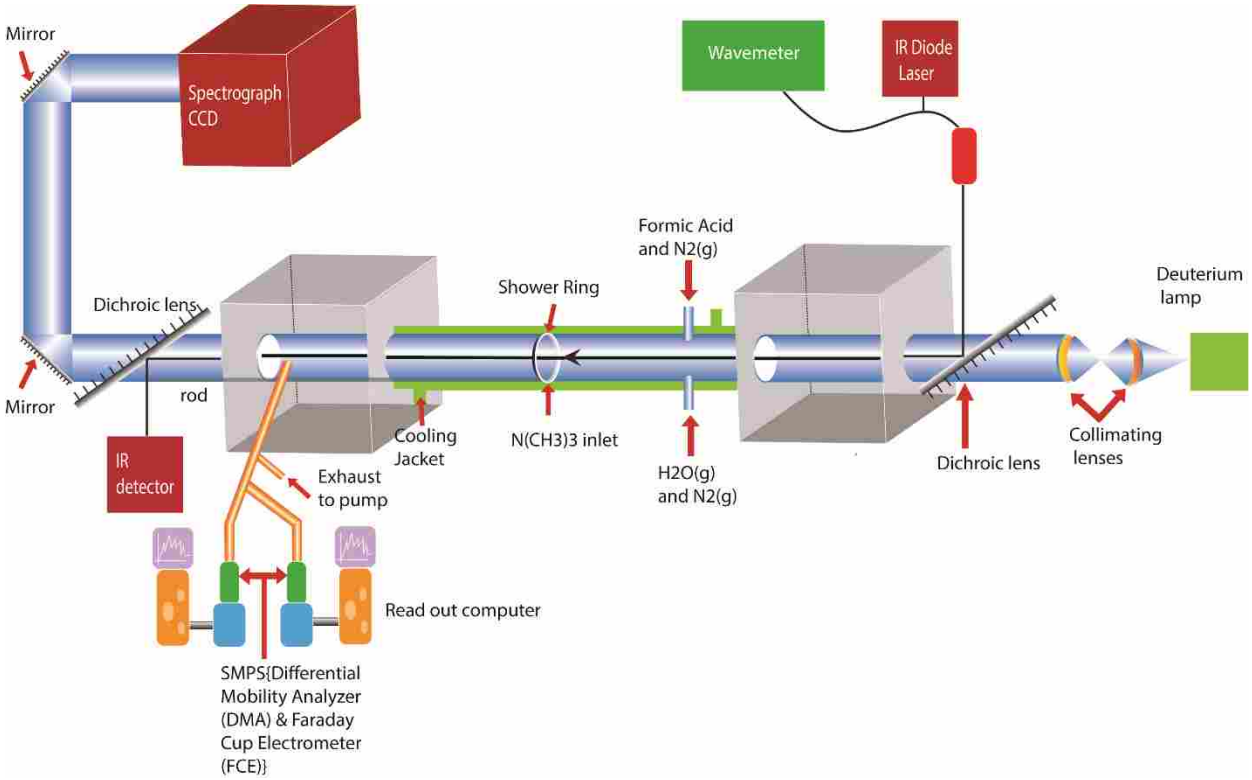

Supplementary Figure 1. Instrument Set-Up for probing the particle formation initiated by formic acid, water vapor and trimethylamine.

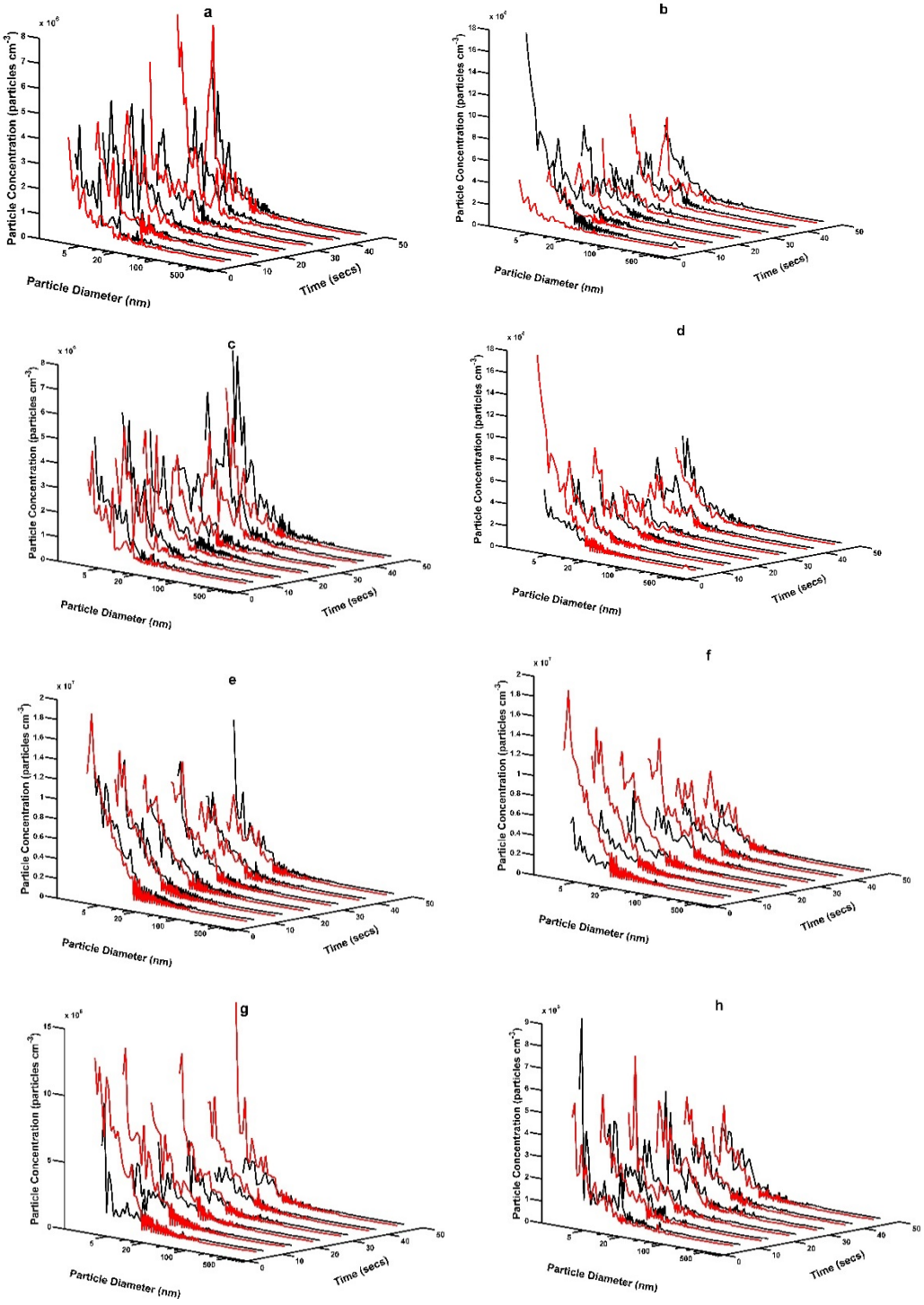

Supplementary Figure 2. Inclusion of TMA into the formic acid water vapor system is shown to increase particle formation. Comparison of particle size distribution measured by an SMPS with different concentrations of formic acid, H_2O and TMA. 3A- concentrations A(red) vs B(black); 3B- concentrations A(red) vs C(black);3C-concentrations B(red) vs D(black); 3D- concentrations C(red) vs D(black) ; 3E- concentrations E(red) vs F(black); 3F- concentrations E(red) vs G(black); 3G- concentrations F(red) vs H(black) ; 3H- concentrations G(red) vs H(black).

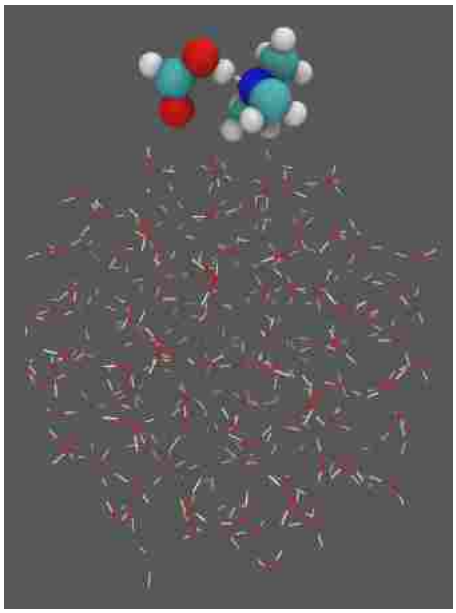

Supplementary Figure 3. Initial interfacial position of the hydrogen-bonded complex of formic acid with trimethylamine on the water droplet. Formic acid and trimethylamine are shown in space-filling representation whereas the water molecules in the droplet are shown in wire representation. Red: O; white: H; blue: N; green: C.

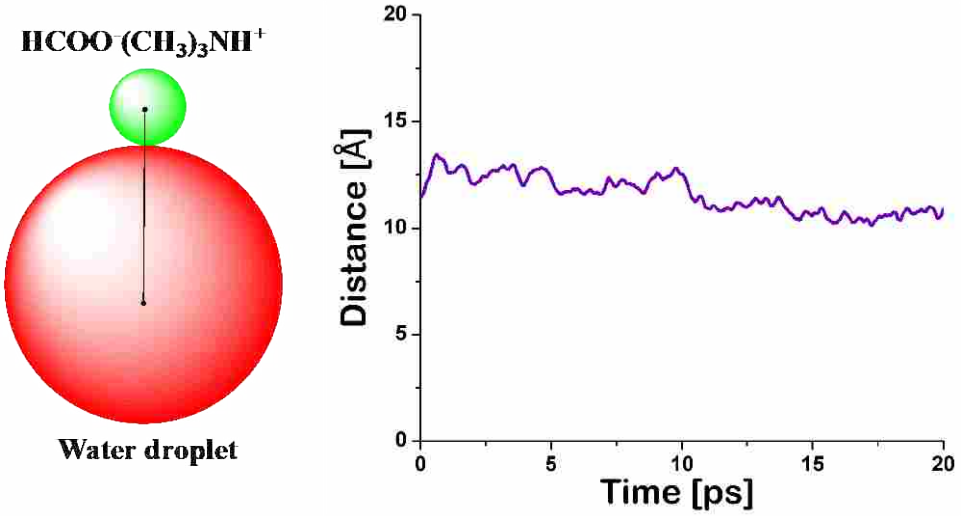

Supplementary Figure 4. The schematics and time evolution between $HCOO^{-}\cdot\cdot(R_1)(R_2)NH_2^{+}$ ion-pairs and water droplets. Left panel: schematics showing the distance between the center of mass of $HCOO^{-}\cdot\cdot(R_1)(R_2)NH_2^{+}$ and that of the water droplet. Right panel: time evolution of the distance between the center of mass of the $HCOO^{-}\cdot\cdot(R_1)(R_2)NH_2^{+}$ ion-pairs and that of the water droplet.

Supplementary Table 1. Particulate phase concentrations (in parts per billion by volume) of formic and acetic acids in different global regions.

Location	Formic Acid (ppbV)	Acetic Acid (ppbV)
[1]USA Virginia (semi-rural)	15.0	9.0
[2]USA Virginia (semi-rural)	25.0	
[2]USA Florida (semi-rural)	20.0	
[3]USA LA (urban)	0.024-0.31	0.035-0.13
[4]Brazil, Amazon	24.5	20.2
[2]W and N Atlantic (marine)	35.0	
[5]Atlantic Ocean	0.697	0.001
[6]Barbados	~24.5	~16.0
[7]Alaska	~110	~270

Initial Concentrations	Formic Acid (ppm)	Water Vapor (ppm)	TMA (ppb)
1	140	630	200
2	140	630	300
3	140	630	400
4	140	1360	200
5	140	1360	300
6	140	1360	400
7	140	1550	200
8	140	1550	300
9	140	1550	400
10	350	630	200
11	350	630	300
12	350	630	400
13	350	1360	200
14	350	1360	300
15	350	1360	400
16	350	1550	200
17	350	1550	300
18	350	1550	400
19	540	630	200
20	540	630	300
21	540	630	400
22	540	1360	200
23	540	1360	300
24	540	1360	400
25	540	1550	200
26	540	1550	300
27	540	1550	400

Supplementary Table 2. Reaction conditions used in experiments for studying the particle formation from formic acid, water vapor and trimethylamine (TMA).

Supplementary Note 1

Table 1 lists the conditions probed for each trial and the measured rate of particle formation whereas **Supplementary Figures 2a-h** compares particle formation as a function of initial formic acid, water vapor and TMA concentrations. **Supplementary Figure 2a** shows that the particle formation occurs even at the lowest concentration of formic acid (140 ppm), water vapor (630 ppm) and TMA (200 ppb) in the reaction cell shown in red compared to increased water concentration (1550 ppm) shown in black. The rate of particle formation under these conditions is measured to be $1\pm.02x10^{6}$ particles cm^{-3} s^{-1}. When compared to **Supplementary Figure 2b**, which compares trials A and C and the only change being the increased concentration of TMA to 400 ppm (shown in black), there is a definite increase in the smaller particles at the shorter reaction times. Increasing the water vapor concentration by a factor of 2.5 results in a 3.1% increase in the number of particles formed with diameters < 20 nm. The rate of particle formation under these conditions and those with higher concentrations could not be determined due to the aggregation of smaller sized particles leading to an increased concentration of larger particles which skewed the calculations needed to determine the rate of particle formation. When trial A (140 ppm formic acid, 630 ppm water vapor, 200 ppb TMA) is compared to trial C (140 ppm formic acid, 630 ppm water vapor, 400 ppb TMA), a shift in the size distribution of smaller particles (<20 nm) and increase in the number of particles > 40 nm is observed. In Figure 2C, trials B (red) and D (black) are shown. The

formic acid and water vapor concentrations were kept constant, but the concentration of TMA was double in trial D compared to B. The total number of particles grown in trial D at 8 s was 36% larger compared to that in B. In addition, evaluation of the particle size distribution shows 3.9% of the total particles in B are > 20 nm in diameter but upon doubling of the concentration of TMA the total number of particles >20 nm in trial D grows to 4.2%. Comparison of the data in **Supplementary Figure 2a-c** indicates that the concentration of water vapor in the system effects particle formation however, an increase in the concentration of TMA increases the rate of particle formation and perturbs the particle size distribution. However, due to the high concentrations of formic acid and TMA in these trials, nucleation was not the only mechanism contributing to particle formation as is discussed later. In **Supplementary Figure 2d**, which illustrates trials C (red) and D (black), the formic acid (140 ppm) and high TMA (400 ppm) concentrations were kept constant but the concentration of water concentration was increased in trial D. This is different than trial A vs B in that the TMA is doubled in trials C and D. The total number of particles grown in trial D at 8 seconds was 29% smaller compared to that in C. In addition, evaluation of the particle size distribution shows, 3.6% of the total particles in C are > 20 nm in diameter but upon increasing the concentration of water concentration, the total number of particles >20 nm in trial D grows to 4.2%. This indicates that there is an increase in the total number of particles due to the increase of water concentration. **Supplementary Figure 2e** shows the comparison of the data from trials E (red) and F

(black). These trials show the effects of changing water vapor concentration while keeping the concentration of formic acid and TMA constant. At early reaction time, <20 seconds, the number of particles <20 nm is observed to increase under the conditions of elevated water in trial F. At reaction times > 20 seconds, the number of particles <20nm in diameter under conditions of elevated water are observed to increase. In trial F, the total number of particles < 1.2-20 nm is 9.1±0.08 x 10^7 particles at a reaction time of 48 seconds. In trial E, the particles <1.2-20 nm is 8.5±0.08 x 10^7 particles at the same reaction time. In **Supplementary Figure 2f**, which shows trials E (red) and G (black), the formic acid (540 ppm) and water concentrations (630 ppm) were kept constant but the TMA concentration was double in trial G compared to E. The total number of particles grown in trial G at 8 seconds was 17% smaller compared to that in E. In addition, evaluation of the particle size distribution shows that 3.1% of the total particles in E are > 20 nm in diameter but upon increasing the concentration of water, the total number of particles >20 nm in trial G grows to 3.3%. In **Supplementary Figure 2g**, which shows trials F (red) and H (black), the formic acid (540 ppm) and water concentrations (630 ppm) were kept constant but the TMA concentration was double in trial H compared to F. The total number of particles grown in trial F at 8 seconds was 4.8% larger compared to that in H. In addition, evaluation of the particle size distribution shows that 4.1% of the total particles in F are > 20 nm in diameter but upon increasing the concentration of water, the total number of particles >20 nm in trial H grows to 4.5%. In **Supplementary Figure 2h**,

which shows trials G (red) and H (black), the formic acid (540 ppm) and TMA (400 ppm) concentrations were kept constant but the water concentration was double in trial H compared to G. The total number of particles grown in trial H at 8 seconds was 70% smaller compared to that in G. In addition, evaluation of the particle size distribution shows that 3.3% of the total particles in G are > 20 nm in diameter but upon increasing the concentration of water, the total number of particles >20 nm in trial H grows to 4.5%. The severe drop in total particles can be accounted to the loss of larger sized particles due to our inability to detect particles >494 nm.

Supplementary Table 3. Total particle concentration, max concentration and diameters under the given conditions as discussed in paper and figure `

Supplementary Table 3. Total particle concentration, max concentration and diameters under the given conditions as discussed in paper and figure `

Conditions	Total Particles (particles cm^{-3})	Max concentration (particles cm^{-3})	$Diameter_{max}$ (nm)	Max $Diameter_{<300}$ nm concentration (particles cm^{-3})	Max $Diameter_{<300}$ (nm)
140 ppm FA, 630 ppm H_2O	$7.2\pm0.3 \times 10^6$	$3.3\pm0.3 \times 10^5$	1.29	$6.8\pm0.02 \times 10^3$	493.95
140 ppm FA, 630 ppm H_2O, 200 ppb TMA, 8 secs	$7.1\pm0.05 \times 10^7$	$3.9\pm0.3 \times 10^6$	1.09	$1.9\pm0.1 \times 10^4$	332.04
140 ppm FA, 630 ppm H_2O, 200 ppb TMA, 48 secs	$4.1\pm0.11 \times 10^8$	$7.3\pm0.9 \times 10^6$	1.54	$4.2\pm0.08 \times 10^4$	377.69

Supplementary Table 4. Total particles at 8 seconds and total particles less than 20 nm in diameters at different reaction conditions.

Supplementary Table 4. Total particles at 8 seconds and total particles less than 20 nm in diameters at different reaction conditions.

Concentrations (particles cm^{-3}), 8 sec	A	B	C	D	E	F	G	H
Total Particles	$7.10\pm0.05 \times 10^7$	$2.89\pm0.11 \times 10^7$	$1.63\pm0.1 \times 10^8$	$4.59\pm0.2 \times 10^7$	$1.89\pm0.3 \times 10^8$	$4.37\pm0.1 \times 10^7$	$1.56\pm0.1 \times 10^8$	$4.59\pm0.1 \times 10^7$
>20 nm	$6.76\pm0.04 \times 10^6$	$9.08\pm0.05 \times 10^5$	$4.69\pm0.06 \times 10^6$	$1.63\pm0.03 \times 10^6$	$5.31\pm0.02 \times 10^6$	$2.13\pm.03 \times 10^6$	$4.49\pm0.02 \times 10^6$	$1.86\pm0.01 \times 10^6$

Supplementary Table 5. Concentrations of particles from fig. 5A, 5B and 5c separated by time and range.

Supplementary Table 5. Concentrations of particles from fig. 5A, 5B and 5c separated by time and range.

	140 ppm FA, 630 ppm H_2O, 200 ppb TMA (**4B,5A**)			140 ppm FA, 630 ppm H_2O, 400 ppb TMA (**5B**)			140 ppm FA, 1550 ppm H_2O, 200 ppb TMA (**5C**)		
	Particle Concentration (particles cm^{-3})			Particle Concentration (particles cm^{-3})			Particle Concentration (particles cm^{-3})		
Time (sec)	2.5-10 nm	10-100 nm	100-500 nm	2.5-10 nm	10-100 nm	100-500 nm	2.5-10 nm	10-100 nm	100-500 nm
8	6.72E+07	5.03E+06	1.33E+04	4.81E+07	1.06E+07	5.36E+05	3.46E+07	4.50E+06	1.96E+05
16	3.29E+07	2.84E+06	1.06E+05	2.28E+07	7.58E+06	1.01E+05	4.37E+07	3.93E+06	1.78E+05
24	4.20E+07	2.55E+06	1.17E+05	2.47E+07	6.65E+06	8.13E+04	3.70E+07	3.59E+06	2.47E+05
32	4.17E+07	3.00E+06	1.26E+05	1.33E+07	4.87E+06	1.71E+05	3.16E+07	3.47E+06	2.70E+05
40	4.07E+07	2.93E+06	1.22E+05	2.23E+07	5.67E+06	3.17E+05	3.79E+07	4.62E+06	2.10E+05
48	5.48E+07	2.54E+06	7.74E+04	1.72E+07	6.53E+06	2.12E+05	4.08E+07	3.30E+06	1.64E+05

Supplementary Table 6 Concentrations of particles from fig. 4A separated by aerodynamic diameter

	Particle Concentration (particles cm^{-3})				
Time (sec)	Total Diameter >300 nm	332.04 nm	377.69 nm	431.16 nm	493.95 nm
8	2.66E+04	1.87E+04	0.00E+00	4.39E+02	7.48E+03
16	1.92E+04	4.26E+03	8.83E+03	3.67E+03	2.41E+03
24	5.83E+04	4.74E+04	3.25E+03	7.66E+02	6.84E+03
32	5.55E+04	8.63E+03	3.10E+03	1.50E+04	2.88E+04
40	4.26E+04	2.21E+03	4.34E+03	2.08E+04	1.53E+04
48	1.07E+05	2.48E+04	4.18E+04	1.55E+04	2.53E+04

References

1. Andreae, M. O.; Talbot, R. W.; Li, S. M. Atmospheric measurements of pyruvic and formic acid. *J. Geophys. Res*. **1987**, *92*, 6635-6641.
2. Andreae, M. O.; Talbot, R. W.; Andreae, T. W.; Harris, R. C. Formic and acetic acid over the central Amazon region, Brazil: 1. Dry season. *J. Geophys. Res.* **1988**, *93*, 1616.
3. Talbot, R. W.; Beecher, K. M.; Harris, R. C.; Browell, E. V.; Gregory, G. L.; Sabacher, D. I.; Becck, S. M. *J. Geophys. Res.* **1986**, *91*, 5173.
4. Talbot, R. W.; Beecher, K. M.; Harris, R. C.; Cofer III, W. R. Atmospheric geochemistry of formic and acetic acids at a mid-latitude temperate site. *J. Geophys. Res*. **1988**, *93*, 1638-1652.
5. Li, S. M.; Winchester, J. W. Geochemistry of organic and inorganic ions of the late winter Arctic aerosol. *Atmos. Environ.* **1989**, *23*, 2401-2416.
6. Kawamura, K.; Steinberg, S.; Kaplan, I. R. Homologous series of C1-C10 monocarboxylic acids and C1-C6 carbonyls in Los Angeles air and motor vehicle exhausts. *Atmos. Environ.* **2000**, *34*, 4175-4191
7. Baboukas, E. D.; Kanakidou, M.; Mihalopoulos, N. Carboxylic acids in gas and particulate phase above the Atlantic Ocean. *J. Geophys. Res.* **2000**, *105*, 14459-14471.

Appendix A5- Chapter 5 Supplemental Information

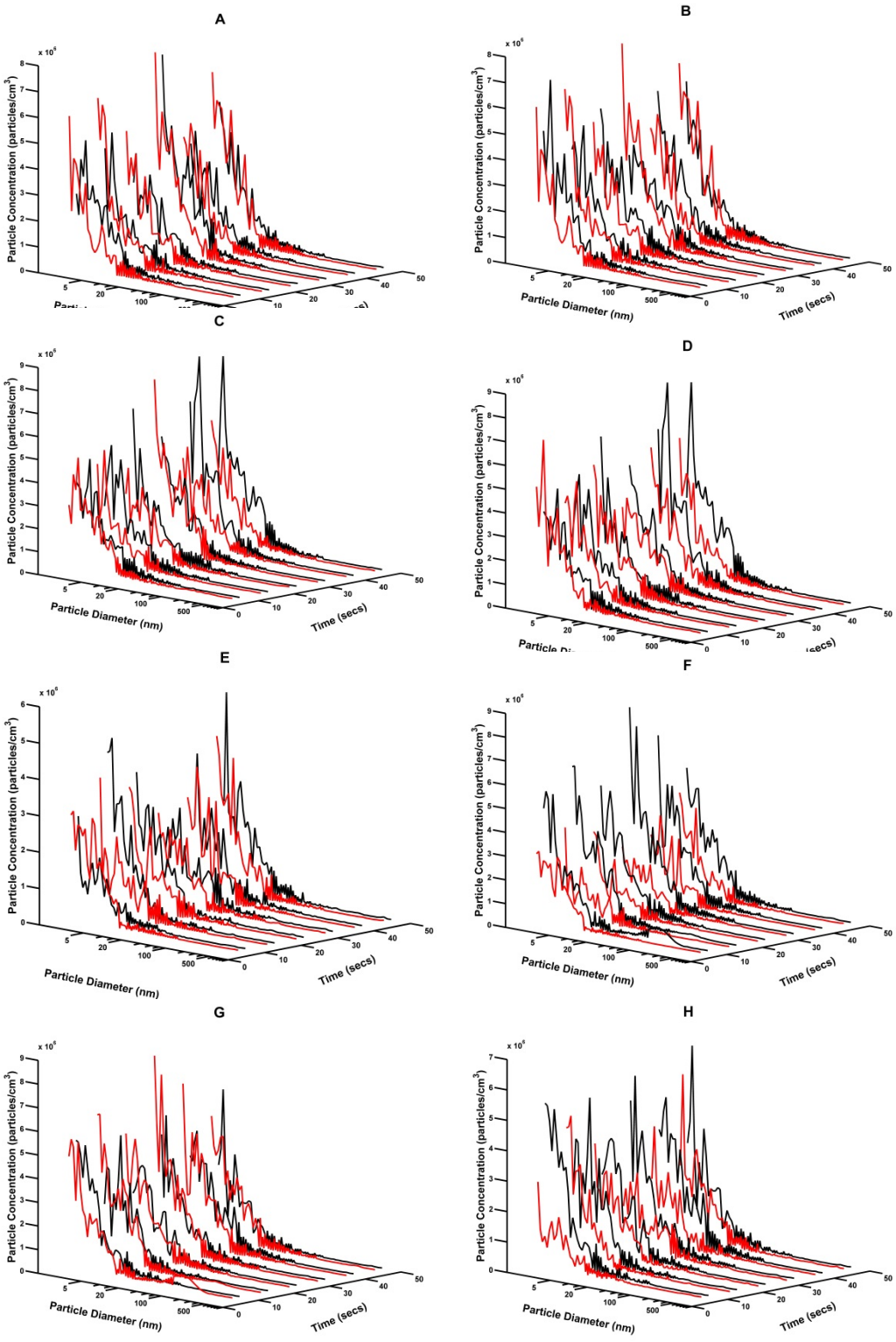

Supplemental Note

Table 1 lists the conditions probed for each trial and the measured rate of particle formation whereas **Figures 3A-5H** compares particle formation as a function of initial acetic acid, water vapor and TMA concentrations. **Figure 3A** shows that particle formation occurs in the reaction cell at the lowest concentration of acetic acid (22 ppm), water vapor (630 ppm) and TMA (35 ppb) shown in red compared to increased water concentration (1550 ppm) shown in black. The rate of particle formation under condition set A is measured to be $1 \pm .02 \times 10^{7}$ particles cm^{-3} s^{-1}. When compared to **Figure 3B**, which compares trials A (red) and C (black) and the only change being the increased concentration of TMA to 75 ppm, there is a definite increase in the smaller particles at the shorter reaction times. Increasing the water vapor concentration by a factor of 2.5 results in a 1.0% increase in the number of particles formed with diameters < 20 nm. The rate of particle formation under these conditions and those with higher concentrations could not be determined due to the aggregation of smaller sized particles leading to an increased concentration of larger particles which skewed the calculations needed to determine the rate of particle formation. When trial A (22 ppm acetic acid, 630 ppm water vapor, 35 ppb TMA) is compared to trial C (22 ppm acetic acid, 630 ppm water vapor, 70 ppb TMA), a shift in the size distribution of smaller particles (<20 nm), 97.1% to 96.2%, and an increase in the number of particles > 40 nm, 0.8% to 1.7%, is observed. In Figure 2C, trials B (red) and D (black) are shown. The acetic acid and water vapor concentrations were kept constant but the concentration of TMA was double in trial D compared to B. Unexpectedly, the total number of particles grown in trial D at 8 s was 5.6% smaller compared to that in B. In addition, evaluation

of the particle size distribution shows 3.4% of the total particles in B are > 20 nm in diameter but upon doubling of the concentration of TMA the total number of particles >20 nm in trial D slightly decreases to 3.0%. Previous research as shown that experiments run in a slow flow reactor cells have two mechanisms competing for particle growth and can be used to explain the decrease in both larger and smaller diameter particles in higher concentration experiments. Comparison of the data in **Figure 3A**, **2B and 2C** indicates that the concentration of water vapor in the system effects particle formation however, an increase in the concentration of TMA increases the rate of particle formation and perturbs the particle size distribution. However, due to the high concentrations of acetic acid and TMA in these trials, nucleation was not the only mechanism contributing to particle formation as was discussed. In **Figure 3D**, which illustrates trials C (red) and D (black), the acetic acid (22 ppm) and high TMA (70 ppm) concentrations were kept constant but the concentration of water vapor was increased in trial D. This is different than trial A vs B in that the TMA is doubled in trials C and D. The total number of particles grown in trial D at 8 s was 1.5% larger compared to that in C. In addition, evaluation of the particle size distribution shows, 3.8% of the total particles in C are > 20 nm in diameter but upon increasing the concentration of water concentration, the total number of particles >20 nm in trial D decreased to 3.0%. This is another indication of two competing mechanism that occur in the slow flow reactor cell. **Figure 3E** shows the comparison of the data from trials E (red) and F (black). These trials show the effects of changing water vapor concentration while keeping the concentration of acetic acid and TMA constant. At early reaction time, <20 s, the number of particles <20 nm is observed to decrease from 97.4% to 87.1% under the conditions of elevated water in trial F. At reaction times > 20s, the number of particles <20nm in diameter

under conditions of elevated water are observed to significantly increase. In trial F, the total number of particles < 1.2-20 nm is 5.6±0.08 x 10^7 particles at a reaction time of 48s. In trial E, the particles <1.2-20 nm is 3.5±0.08 x 10^7 particles at the same reaction time. In **Figure 3F**, which shows trials E (red) and G (black), the acetic acid (73 ppm) and water concentrations (630 ppm) were kept constant but the TMA concentration was double in trial G compared to E. The total number of particles grown in trial G at 8 s was 35.1% smaller compared to that in E. In addition, evaluation of the particle size distribution shows that 2.6% of the total particles in E are > 20 nm in diameter but upon increasing the concentration of water, the total number of particles >20 nm in trial G grows to 4.0%. In **Figure 3G**, which shows trials F (red) and H (black), the acetic acid (73 ppm) and water concentrations (630 ppm) were kept constant but the TMA concentration were again doubled in trial H compared to F. The total number of particles grown in trial F at 8 s was 3.7% larger compared to that in H. In addition, evaluation of the particle size distribution shows that 13.0% of the total particles in F are > 20 nm in diameter but upon increasing the concentration of water, the total number of particles >20 nm in trial H decreases to 3.2% which is a further indication that larger sized particles are being formed but not detected. In **Figure 3H**, which shows trials G (red) and H (black), the acetic acid (73 ppm) and TMA (75 ppm) concentrations were kept constant but the water concentration was doubled in trial H compared to G. The total number of particles grown in trial H at 8 s was 58% larger compared to that in G. In addition, evaluation of the particle size distribution shows that 3.9% of the total particles in G are > 20 nm in diameter but upon increasing the concentration of water, the total number of particles >20 nm in trial H decreases to 3.2%. The severe drop in total particles can be accounted to the loss of larger sized particles due to our inability to detect

particles >494 nm. The dependence of the concentration of TMA on the kinetics of particle formation was measured by changing the TMA concentrations and comparing the changed rates of particle formation.